



**PROCEEDINGS**  
**BOOK OF THE 5<sup>TH</sup>**  
**INTERCONTINENTAL**  
**GEOINFORMATION DAYS**  
**14-15 DECEMBER 2022**  
**New Delhi, INDIA**

MERSIN UNIVERSITY-ENGINEERING FACULTY  
DEPARTMENT OF GEOMATICS ENGINEERING



ISBN: 978-605-72800-1-5

<https://igd.mersin.edu.tr/>

**The proceedings of the  
5<sup>th</sup> Intercontinental Geoinformation Days**



**Editor-in-Chief**

Prof. Dr. Murat Yakar

**Editors**

Asst. Prof. Dr. Ali Ulvi

Asst. Prof. Dr. Lütfiye Kuşak

Asst. Prof. Dr. Fatma BÜNYAN Ünel

Lecturer Lale Karataş

Res. Asst. Aydın Alptekin

ISBN: 978-605-72800-1-5

New Delhi, 2022

## **5<sup>th</sup> Intercontinental Geoinformation Days**

I would like to thank all of the contributing authors and reviewers to the 5<sup>th</sup> Intercontinental Geoinformation (IGD) Symposium, 14-15 December 2022. In this international symposium there are 46 presentations.

Best regards

Prof. Dr. Murat YAKAR



## Technical Program of 5<sup>th</sup> Intercontinental Geoinformation Days

<b>Welcome session 14-December 2022</b>	
11.30-11.45	Welcome and Introduction- Dr. Sangeeta Aggrawal
11.45- 11.55	Prof. Deepshikha Sharma (Chief Guest Speech )
11.55-12.00	Candle Lightning

<b>Session 1 - 14 December 2022</b>	
Keynote speakers (Session Chair Tiwari Ravindra)	
12.00-12.20	Timothy Warner
12.20-12.40	Cornelis F De Hoop
12.40-13.00	Neetu Goswami
13.00-13.20	Shweta Rani
13.20-13.40	Sunil Kumar

<b>Session 2 - Remote Sensing- 14 December 2022</b>	
14.00-14.10	<b>Valorization of phlogopite ore by geochemical analysis and interpolation with Aster satellite images (case of Ampandrandava - South of Madagascar)</b> Miora Harivony Rakotondrabe, Anoop V Mohandas, Lucienne Rakotozafy Randriamanivo
14.10-14.20	<b>Estimation of Wind Erosion Threshold Velocity Based on Spectroscopy Data Using Random Forest Algorithm</b> Monireh Mina, Mahrooz Rezaei, Leila Hossein Abadi, Abdolmajid Sameni
14.20-14.30	<b>GreenMetric Ranking Calculation by Using Satellite Imageries; A Case Study from Turkiye</b> Abdullah Harun İncekara, Elif Başaran, Dursun Zafer Şeker
14.30-14.40	<b>Spatiotemporal prediction of Reference Evapotranspiration in Araban region, Turkey: A Machine Learning Based Approaches</b> Mehmet Irfan Yesilnacar, Jazuli Abdullahi Abdullahi, Ala Tahseen Mohsin, Abdullah Izzeddin Karabulut

<b>Session 3 - Geographic Information Systems - 14 December 2022</b>	
15.00-15.10	<b>Utilizing GIS to select potential sites for biomass-utilizing mills in Louisiana USA</b> Cornelis de Hoop, Anil Kizha, Arif Oguz Altunel
15.10-15.20	<b>Identification of landslide susceptible zones in Idukki district (Southern Western Ghats) employing the REPTree model and geospatial techniques</b> Rajendran Shobha Ajin, Hamza Vijith, Mohan Akshaya, Jayan Bindu Jibitha, Kunnummal Agina Chandran, Romulus Costache
15.20-15.30	<b>Landslide susceptibility assessment employing machine learning ensemble models: a study in the most severely battered district of the Southern Western Ghats</b> Rajendran Shobha Ajin, Hamza Vijith, Megha Krishna Prasad, Jayan Bindu Jibitha, Romulus Costache
15.30-15.40	<b>Assessment of variation in water level of Quetta valley of 2010 &amp; 2020</b> Liaqat Ali

<b>Session 4 - Land Administration- 14 December 2022</b>	
16.00-16.10	<b>Content analysis of real estate valuation courses taught in the relevant departments of vocational schools in Turkey</b> Nuri Erdem
16.10-16.20	<b>Evaluating kernel functions of support vector machines for supervised classification of land use classes</b> Sinan Bulut
16.20-16.30	<b>A Mass Valuation Model Proposal for Residential Property Taxation in Türkiye</b> Ecem Sirkeci, Reha Metin Alkan, Muhammed Oğuzhan Mete
16.30-16.40	<b>The Role of Geomatics Engineering Discipline on Nearly Zero Energy Building Concept for Türkiye</b> Büşra Kartal, Reha Metin Alkan, Mehmet İşiler
16.40-16.50	<b>A Preliminary Research on Methodology for Establishing Legal Infrastructure Regarding Public Law Restrictions Cadastre in Türkiye</b> Mehmet İşiler, Mustafa Yanalak

<b>Session 5 - Remote Sensing- 14 December 2022</b>	
17.00-17.10	<b>Estimation of the ground surface temperature using sebal method and the decision tree from ETM+ (Case Study: Maraş Town)</b> Khalil Valizadeh Kamran
17.10-17.20	<b>Determination of evapotranspiration on Dicle Basin</b> Abdullah Karatoprak, Nizar Polat
17.20-17.30	<b>Implementation of supervised SID algorithm in preparation of map of geological units</b> Parviz Zeaiean Firouzabadi, Parisa Safarbeyranvand, Ali Hosingholizade
17.30-17.40	<b>A quantitative and qualitative assessment from official statistics to spatial statistics: Agricultural greenhouses detection over time integrating of remote sensing and transfer learning-based machine learning approach</b> Fuat Kaya, Gordana Kaplan, Levent Başayığıt
17.40-17.50	<b>Approximation of COVID-19 effect on land surface temperature using MODIS data over YSR district, India</b> Jagadish Kumar Mogaraju

<b>Session 6 - Survey &amp; Geodesy- 14 December 2022</b>	
18.00-18.10	<b>Evaluation of the TEC Prediction Performance of NeQuick2 Model</b> Salih Alcaay, Sermet Ogutcu, Gurkan Oztan, Behlül Numan Ozdemir
18.10-18.20	<b>Zenith Tropospheric Delay Estimation Using a Low-Cost GNSS</b> Ceren Konukseven, Sermet Ogutcu, Salih Alcaay
18.20-18.30	<b>Near-Real-Time Precise Point Positioning Technique with Single-Frequency Raw GNSS Observations on Android Smartphones</b> Hüseyin Pehlivan, Barış Karadeniz, Barışcan Arı
18.30-18.40	<b>Using the particle swarm optimization for geoid determination</b> Ulku Kirici Yildirim, Yasemin Sisman

<b>Welcome session -15 December 2022</b>	
11.00-11.15	Welcome and Introduction- Dr. Sangeeta Aggrawal
11.15- 11.25	Welcome and Introduction – Deepshikha Sharma
11.25-11.30	Candle Lighting

<b>Session 7 - 15 December 2022</b>	
Keynote speakers	
11.40-12.00	Dr. Kiran S Sharma
12.00-12.20	Dr. Prashant Yadav
12.20-12.40	Bhanu Srivastva
12.40-13.00	Dr. Khin Mar Yee
13.00-13.20	Dr. Manoj Mishra

<b>Session 8 - Geographic Information systems- 15 December 2022</b>	
13.30-13.40	<b>MCDM: A New Quantum GIS Plug-In for Multi Criteria Decision Making Analysis</b> Emre Yılmaz, Süleyman Sefa Bilgiliolu
13.40-13.50	<b>Environmental risk and hazards assessment using GIS technology</b> Mirnukh Ismayilov, Latifa Kazimova
13.50-14.00	<b>Analysis of Google Point of Interest Data Based on Scoring Key Criteria for Local Restaurants</b> Fatemeh Rajabi, Farhad Hosseinali, Hamidreza Rabiei-Dastjerdi, Mahdi Rajabi
14.00-14.10	<b>Investigation of Spatial Change on Badlands Topography Around Kuyulu Village (Adiyaman) with Remote Sensing and Geographic Information Systems</b> Sezgin Abukan, ibrahim halil Yildirim, Ahmet Serdar Aytaç, Nizar Polat

<b>Session 9 - Remote Sensing- 15 December 2022</b>	
14.30-14.40	<b>Aircraft detection using optical remote sensing images and YOLOv7 based deep learning method</b> Roya Talebi
14.40-14.50	<b>Calculation of daily land surface temperature values using Google Earth Engine</b> Mehmet Numan Fırat, Yunus Kaya, Nizar Polat
14.50-15.00	<b>Calculation of glacial area change at Cilo mountain with Google Earth Engine</b> Gonca Abdioğlu, Yunus Kaya, Nizar Polat
15.00-15.10	<b>Automated vehicle detection and instance segmentation from high-resolution UAV imagery using YOLOv7 model</b> Esra Yildirim, Umut Gunes Sefercik, Taskin Kavzoglu

<b>Session 10 - Geographic Information Systems- 15 December 2022</b>	
15.30-15.40	<b>Determination of Rainwater Harvesting Potential in GIS Using UAV Imagery with Machine Learning Classification</b> Abdulkadir Memduhoglu
15.40-15.50	<b>Evaluation of Cutaneous Leishmaniasis cases in Şanlıurfa in 2019-2022 using Geographic Information Systems</b> Ceren Arkant, Abdullah İzzeddin Karabulut, Yaşar Koçer, Mehmet İrfan Yeşilnacar
15.50-16.00	<b>Landslide Susceptibility Analysis with AHP and FUCOM; a case Study of Taşova</b> Melike Öcül, Aziz Şişman
16.00-16.10	<b>Use Of GIS In Macro Planning, Interdisciplinary Collaboration: Konya - Isparta Environmental Master Plans</b> İrem Yurday, Mehmet Tunçer
16.10-16.20	<b>The ultimate vertical accuracy assessment of the third generation Turkish 1:25000 quad maps; under canopy vs. no canopy</b> Arif Oguz Altunel, Oytun Emre Sakici

<b>Session 11 - Remote Sensing- 15 December 2022</b>	
16.30-16.40	<b>Analysis of three hydro-meteorological parameters for the East Mediterranean Basin with GLDAS data</b> Cihangir Koycegiz, Meral Buyukyildiz
16.40-16.50	<b>Classification of Jilin-1 GP01 hyperspectral image using machine learning techniques with explainable artificial intelligence</b> Elif Ozlem Yilmaz, Taskin Kavzoglu
16.50-17.00	<b>Measuring changes in spatio-temporal LST variations and evaluating their relationship between greenhouses and their surroundings</b> Serdar Selim, Buket Eyileten
17.10-17.20	<b>Scene Classification of Google Earth Images with Different Deep Learning Models</b> Şaziye Özge Atik

<b>Session 12 - Close-Range and Aerial Photogrammetry &amp; Lidar- 15 December 2022</b>	
17.30-17.40	<b>3D Modeling of Cultural Heritage Commagene Kingdom Funerary Monument</b> Cem Erol, Nizar Polat
17.40-17.50	<b>Automatic Building Extraction using Kernel-based Deep Learning Approach from VHR Imagery</b> Tolga Bakirman, Mahmut Oguz Selbesoglu
17.50-18.00	<b>Comparison of CSF and SMRF Filtering methods for Airborne LiDAR point cloud data</b> Ramazan Alper Kuçak
18.00-18.10	<b>Point Cloud Classification Using Machine Learning Algorithms and Selection of Relevant Features</b> Muhammed Enes Atik, Zaide Duran
18.10-18.20	<b>Documentation of stone material deterioration on the facades of historical masonry buildings by terrestrial laser scanning: A case study of a Masion located in Mardin Province</b> Lale Karataş, Aydın Alptekin, Murat Yakar
18.20-18.30	<b>Can we “see” the neighborhood built environments from a UAV?</b> Xin Hong
18.30-18.40	<b>Development of Open-Source Applications Using WebGIS Technology</b> Mehmet Alper Şahin, Murat Yakar, Ali Ulvi, Abdurahman Yasin Yiğit

18.40	<b>Valedictorian Session</b>
-------	------------------------------

Content	Page
<b>Valorization of phlogopite ore by geochemical analysis and interpolation with Aster satellite images (case of Ampandrandava - South of Madagascar)</b> Miora Harivony Rakotondrabe, Anoop V Mohandas, Lucienne Rakotozafy Randriamanivo Ononamandimby Antsonantenainarivony	1
<b>Estimation of Wind Erosion Threshold Velocity Based on Spectroscopy Data Using Random Forest Algorithm</b> Monireh Mina, Mahrooz Rezaei, Leila Hossein Abadi, Abdolmajid Sameni	5
<b>GreenMetric ranking calculation by using satellite imageries: A Case Study from Türkiye</b> Abdullah Harun Incekara, Elif Yaprak Basaran, Dursun Zafer Seker	10
<b>Spatiotemporal prediction of reference evapotranspiration in Araban region, Turkey: A machine learning based approaches</b> Mehmet Irfan Yesilnacar, Jazuli AbdullahiAla Tahsin, Abdullah İzzeddin Karabulut	14
<b>Utilizing GIS to select potential sites for biomass-utilizing mills in Louisiana USA</b> Cornelis F. de Hoop, Anil Raj Kizha, Arif Oguz Altunel	18
<b>Identification of landslide susceptible zones in Idukki district (Southern Western Ghats) employing the REPTree model and geospatial techniques</b> Rajendran Shobha Ajin, Hamza Vijith, Mohan Akshaya, Jayan Bindu Jibitha, Kunnummal Agina Chandran, Romulus Costache	22
<b>Landslide susceptibility assessment employing machine learning ensemble models: a study in the most severely battered district of the Southern Western Ghats</b> Rajendran Shobha Ajin, Hamza Vijith, Megha Krishna Prasad, Jayan Bindu Jibitha, Romulus Costache	26
<b>Assessment of variation in water table of Quetta valley of 2010 &amp; 2020</b> Liaqat Ali	30
<b>Content analysis of real estate valuation courses taught in the relevant departments of vocational schools in Turkey</b> Nuri Erdem	33
<b>Evaluating kernel functions of support vector machines for supervised classification of land use classes</b> Sinan Bulut	37
<b>A Mass Valuation Model Proposal for Residential Property Taxation in Türkiye</b> Ecem Sirkeci, Reha Metin Alkan, Muhammed Oğuzhan Mete	41
<b>The role of geomatics engineering discipline on nearly zero energy building concept for Türkiye</b> Büşra Kartal, Reha Metin Alkan, Mehmet İşiler	45
<b>A preliminary research on methodology for establishing legal infrastructure regarding public law restrictions cadastre in Türkiye</b> Mehmet İşiler, Mustafa Yanalak	48
<b>Estimation of the ground surface temperature using Sebal method and the decision tree from ETM+ (Case study: Maraş Town)</b> Khalil Valizadeh Kamran	52
<b>Determination of evapotranspiration on Dicle Basin</b> Abdullah Karatoprak, Nizar Polat	57
<b>Implementation of supervised SID algorithm in preparation of map of geological units</b> Parviz Zeaiean Firouzabadi, Parisa Safarbeyranvand, Ali Hosingholizade	60

---

<b>A quantitative and qualitative assessment from official statistics to spatial statistics: Agricultural greenhouses detection over time integrating of remote sensing and transfer learning-based machine learning approach</b> Fuat Kaya, Gordana Kaplan, Levent Başayığıt	64
<b>Approximation of COVID-19 effect on land surface temperature using MODIS data over YSR district, India</b> Jagadish Kumar Mogaraju	69
<b>Evaluation of the TEC prediction performance of NeQuick2 model</b> Salih Alcay, Sermet Ogutcu, Gurkan Oztan, Behlul Numan Ozdemir	74
<b>Zenith Tropospheric Delay Estimation Using a Low-Cost GNSS</b> Ceren Konukseven, Sermet Ogutcu, Salih Alcay	78
<b>Near-Real-Time Precise Point Positioning Technique with Single-Frequency Raw GNSS Observations on Android Smartphones</b> Hüseyin Pehlivan, Barış Karadeniz, Barışcan Arı	82
<b>Using the particle swarm optimization for geoid determination</b> Ulku Kirici Yildirim, Yasemin Sisman	86
<b>MCDM: A new Quantum GIS Plug-In for multi criteria decision making analysis</b> Emre Yılmaz, Süleyman Sefa Bilgilioğlu	90
<b>Environmental risk and hazards assessment using GIS technology</b> Ismayilov Mirnukh, Kazimova Latifa	94
<b>Analysis of Google Point of Interest Data Based on Scoring Key Criteria for Local Restaurants</b> Fatemeh Rajabi, Farhad Hosseinali, Hamidreza Rabiei-Dastjerdi, Mahdi Rajabi	97
<b>Investigation of spatial change on badlands topography around Kuyulu Village (Adıyaman) with remote sensing and geographic information systems</b> Sezgin Abukan <sup>1</sup> , Halil İbrahim Yıldırım <sup>1</sup> , A. Serdar Aytaç <sup>2</sup> , Nizar Polat	101
<b>Aircraft detection using optical remote sensing images and YOLOv7 based deep learning method</b> Roya Talebi	105
<b>Calculation of daily land surface temperature values using Google Earth Engine</b> Mehmet Numan Fırat, Yunus Kaya, Nizar Polat	108
<b>Calculation of glacial area change at Cilo mountain with Google Earth Engine</b> Gonca Abdioğlu, Yunus Kaya, Nizar Polat	112
<b>Automated vehicle detection and instance segmentation from high-resolution UAV imagery using YOLOv7 model</b> Esra Yildirim, Umut Gunes Sefercik, Taskin Kavzoglu	116
<b>Determination of rainwater harvesting potential in GIS using UAV imagery with machine learning classification</b> Abdulkadir Memduhoglu	120
<b>Evaluation of Cutaneous Leishmaniasis cases in Şanlıurfa in 2019-2022 using geographic information systems</b> Ceren Arkant, Abdullah İzzeddin Karabulut, Yaşar Koçer, Mehmet İrfan Yeşilnacar	124
<b>Landslide Susceptibility Analysis with AHP and FUCOM; a case Study of Taşova</b> Melike Öcül, Aziz Şişman	128
<b>Use of GIS in macro planning, interdisciplinary collaboration: Konya – Isparta environmental master plans</b> İrem Yurday, Mehmet Tunçer	134

---

---

<b>The ultimate vertical accuracy assessment of the third generation Turkish 1:25000 quad maps; under canopy vs. no canopy</b>	136
Arif Oguz Altunel, Oytun Emre Sakici	
<b>Analysis of three hydro-meteorological parameters for the East Mediterranean Basin with GLDAS data</b>	141
Cihangir Koycegiz, Meral Buyukyildiz	
<b>Classification of Jilin-1 GP01 hyperspectral image using machine learning techniques with explainable artificial intelligence</b>	145
Elif Ozlem Yilmaz, Taskin Kavzoglu	
<b>Measuring changes in spatio-temporal LST variations and evaluating their relationship between greenhouses and their surroundings</b>	149
Serdar Selim, Buket Eyileten	
<b>Scene classification of Google Earth Images with different deep learning models</b>	153
Şaziye Özge Atik	
<b>3D modeling of cultural heritage: Commagene Kingdom funerary monument</b>	156
Cem Erol, Nizar Polat	
<b>Automatic Building Extraction using Kernel-based Deep Learning Approach from VHR Imagery</b>	160
Tolga Bakirman, Mahmut Oğuz Selbesoğlu	
<b>Comparison of CSF and SMRF filtering methods for airborne LiDAR point cloud data</b>	164
Ramazan Alper Kuçak	
<b>Point cloud classification using machine learning algorithms and selection of relevant features</b>	168
Muhammed Enes Atik, Zaide Duran	
<b>Documentation of stone material deterioration on the facades of historical masonry buildings by terrestrial laser scanning: A case study of a Mansion in Mardin</b>	172
Lale Karataş, Aydın Alptekin, Murat Yakar	
<b>Can we “see” the neighborhood-built environments from a UAV?</b>	176
Xin Hong	
<b>Development of Open-Source Applications Using WebGIS Technology</b>	179
Mehmet Alper Şahin, Murat Yakar, Ali Ulvi, Abdurahman Yasin Yiğit	

---



## 5<sup>th</sup> Intercontinental Geoinformation Days

igd.mersin.edu.tr



### Valorization of phlogopite ore by geochemical analysis and interpolation with Aster satellite images (case of Ampandrandava - South of Madagascar)

Miora Harivony Rakotondrabe<sup>1</sup>, Anoop V Mohandas<sup>2</sup>, Lucienne Rakotozafy Randriamanivo<sup>3</sup>  
Ononamandimby Antsonantenainarivony<sup>1</sup>

<sup>1</sup>Institut d'Enseignement Supérieur d'Antsirabe Vakinakaratra, Antsirabe, Madagascar

<sup>2</sup>Geological Survey of India, Hyderabad, India

<sup>3</sup>Institut National des Sciences et Technique Nucléaires - Madagascar, XRF-Environnement, Antananarivo, Madagascar

#### Keywords

Aster  
ACP  
Fluorescence-X  
Phlogopite  
Ampandrandava

#### Abstract

Phlogopite is one of the oldest industrial minerals exploited in southern Madagascar. From Ihosy to Fort Dauphin, there are several types of farmers who live from the artisanal exploitation of phlogopite with various underground mica mines abandoned before 1940. Currently, it is exploited almost everywhere in the south of Madagascar. This irrational exploitation, without specific characterization makes this mineral cheap, likewise destroys the environment and leads to waste of the deposit. Ampandrandava is one of those former semi-mechanized underground mines still in operation, and is the only underground mine on the island. With a depth of at least 100m, this mine is characterized by its different minerals and unique phlogopite. In order to develop this mineral and to include this mine among the mining heritage in Madagascar, it is important to characterize its products and value the mine and the existing minerals in the town. The analysis of the samples and the interpretation of the geochemical data of this mineral associated with analyzes of ASTER satellite images will allow us to know its mineral specification as well as the value of the mine. The results of this process will show a correlation to the distribution of this mineral in the study area. The interpolation with the relevant lithological information and the mineralization indices shows a homogeneity of the results obtained. However, these results provide a new layer of information that can be used for the detection of favorable lineaments for a new exploitation.

#### 1. Introduction

The Ampandrandava mine is the only oldest underground mica mine in Madagascar. It is one of the legends of geological and mining works in Madagascar known by its minerals and its mica deposit with an underground exploitation going down to -181m with multiple mica deposits in the surroundings.

This work aims at the geochemical characterization of the various minerals of phlogopite in the mine of Ampandrandava and its surroundings in order to their valorization.

Analyses and interpretation of geochemical data and satellite imagery have been used for mineral specificity and mineral resource development in the district.

Satellite image data are widely used in various aspects in the field of geoscience. The use and exploitation of ASTER images in the exploitation of a mineral takes an important place. Deposits can be identified through the detection of rocks hydrothermally by their spectral signatures. The use of remote sensing

data, more specifically ASTER images in the field of geological mapping.

#### 2. Localization

Ampandrandava is located 12Km from Beraketa in the Anosy region, district of Amboasary Sud.

#### 3. Method

The methodological approach used in this work consisted of field work, sampling, laboratory work and finally the analysis of satellite images.

##### 3.1. Works geological

The study area is mainly formed by leptynites, pyroxene gneisses. We also find pyroxenite with diopsidi and phlogopite. Pyroxene is the parent rock carrying phlogopite mineralization in the region.

#### \* Corresponding Author

\*(rakmiora@gmail.com) ORCID ID 0000-0002-4625-1193  
(anoopmohval@gmail.com) ORCID ID 0000 - 0001 - 7702 - 018X

#### Cite this study

Miora H. Rakotondrabe, Anoop V. Mohandas & Lucienne R. Randriamanivo (2022). Valorisation of phlogopite ore by geochemical analysis and interpolation with Aster satellite images (case of Ampandrandava - South of Madagascar). 5<sup>th</sup> Intercontinental Geoinformation Days (IGD), 1-4, Netra, India

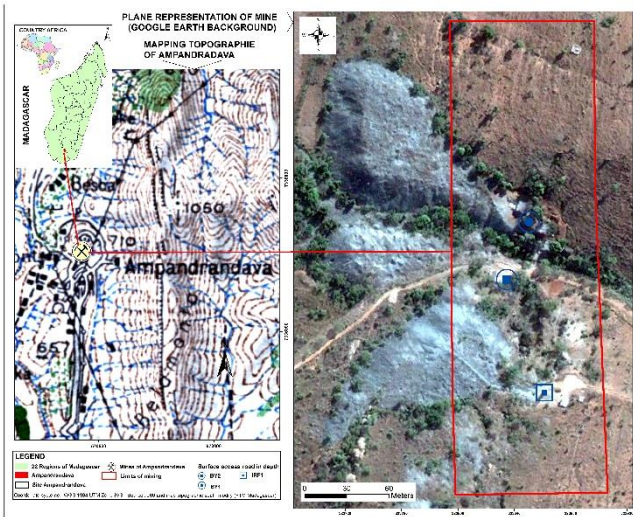


Figure 1. Localization map Ampandrandava

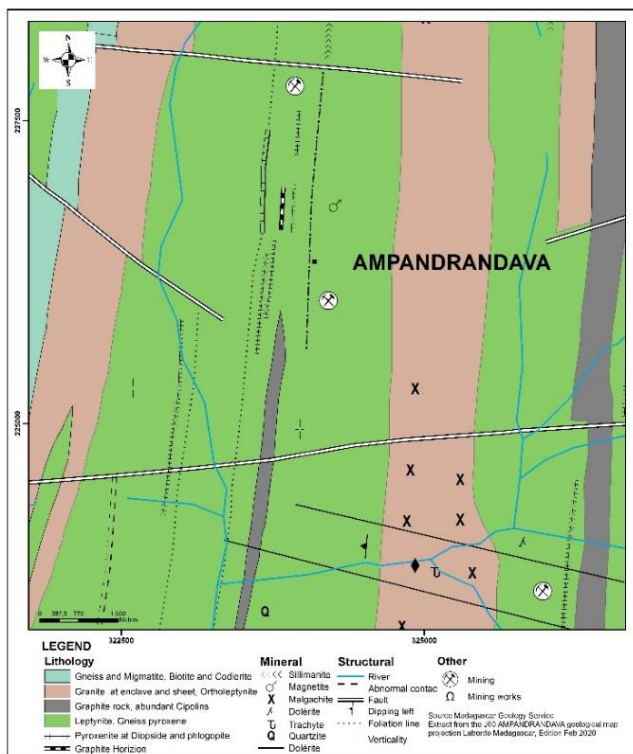


Figure 2. Geological map of Ampandrandava

Figure 3 shows the cross section different levels of the mine going from +15 m to -181m above sea level.

### 3.2. Geochemical analysis

Some phlogopite samples from the Ampandrandava underground mine were analyzed by direct excitation X-ray spectrometry. X-ray fluorescence spectrometry (FX, or XRF for X-ray fluorescence) is a non-destructive technique used to quantify the elemental composition of solid and liquid samples for elemental analysis. This method is a quantitative analysis of the chemical elements present in the mineral.

### 3.3. Mapping and processing

The data used are ASTERS (L1T) satellite images. The analysis of ASTER data aims to describe the lithology,

based on the relationship between the absorption or spectral emittance and the mineral composition of the rock units studied. The composition of the different bands contains a large volume of information, including geological, topographical and roughness information. In the present work, the main image processing techniques performed are: mineral index, spectral analysis and classification.

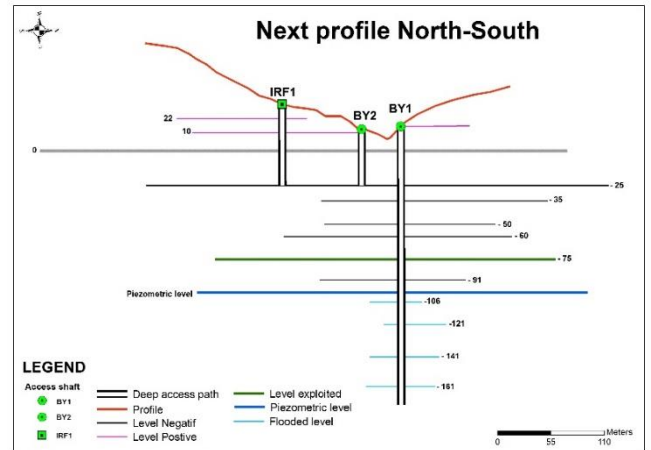


Figure 3. Cross section (North South)

## 4. Results

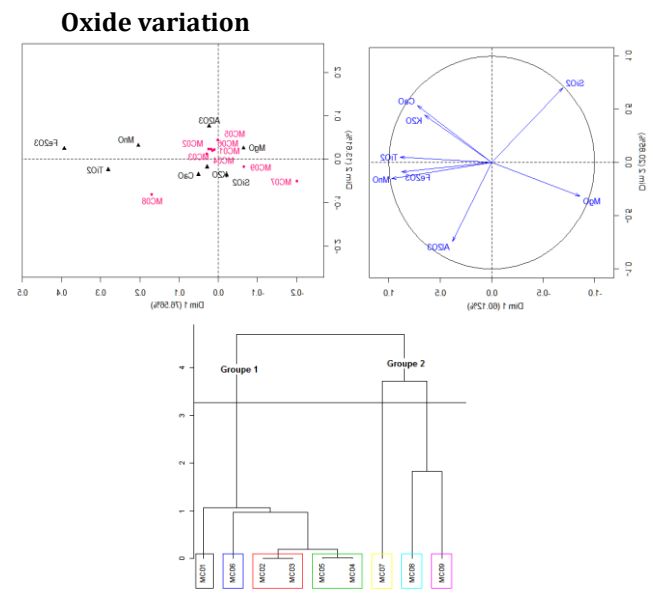
### 4.1. Level -75 structural map

In the NS pyroxenite banks we find eruptive rocks (phlogopite vein associated with anhydrite, calcite, pyrite, diopsidites and pegmatite).

According to the structural exploitation map of level -75, from East to West we have eight layers carrying named mineralization: Alpha, Baltazar, Bravo, Charly, Delta, Echo, foxtrot and Golf.

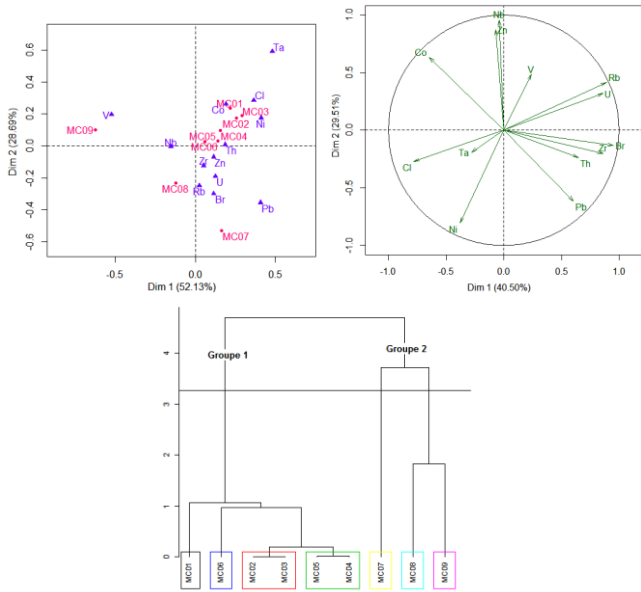
### 4.2. Geochemical analyzes

The XRF geochemical analysis made it possible to know the distribution of the chemical elements on some phlogopite samples of the level -75.



- the Ampandrandava phlogopites are highly rich in [SiO<sub>2</sub>> 35%, Al<sub>2</sub>O<sub>3</sub>> 10% and MgO> 25%] a with an abundance of [CaO> 10% and K<sub>2</sub>O> 10%] b, they are of aluminous-magnesian type;
- high probability of talc in the phlogopite mineral due to the abundance of MgO.

**Variation of minor trace elements**



- four elements of this classification are present in this mineral, the majority of which is lithophilic;
- presence of trace element: U and Th in this mineral of phlogopite.

**4.3. Isotainer map of the chemical elements in level -75**

The distribution of some chemical elements are present in the isotene map.

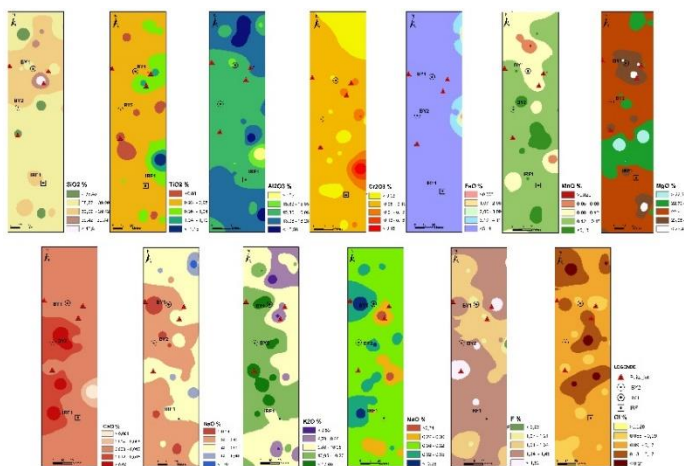


**Figure 5. Isotainer map of the chemical elements in level -75**

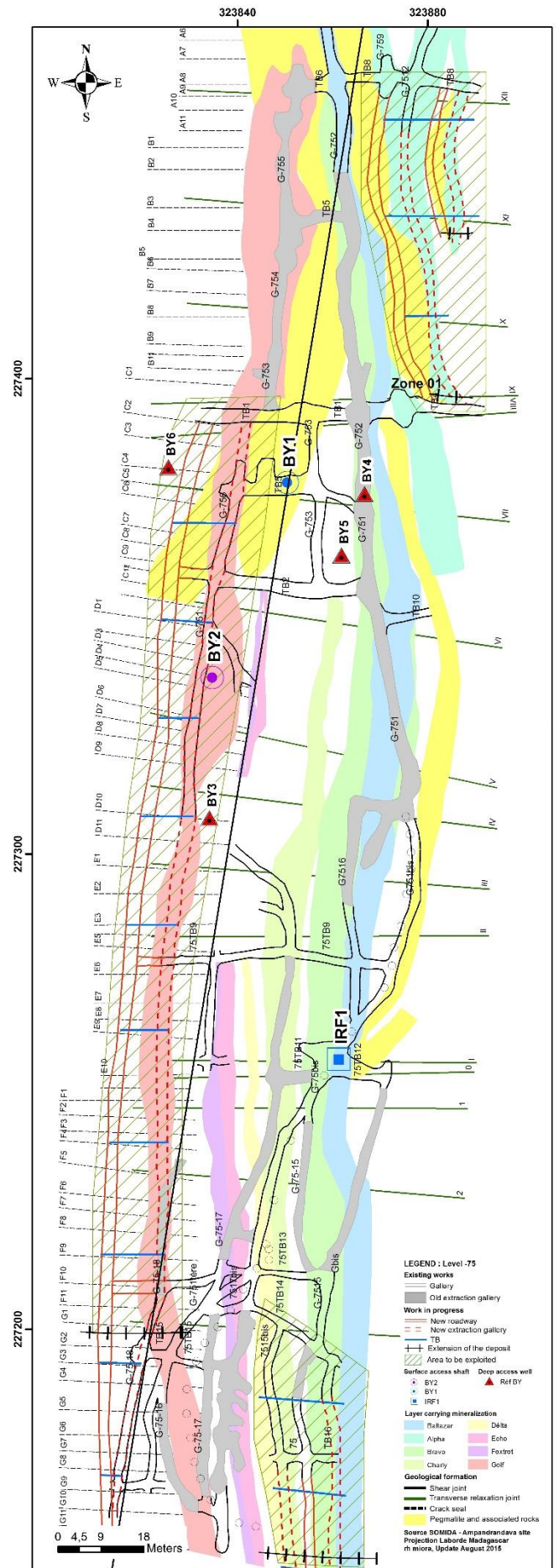


**Figure 4. Cross section (North South)**

Geochemical analysis of the -75 level phlogopite samples shows that the Ampandrandava phlogopites are rich in SiO<sub>2</sub>, Al<sub>2</sub>O<sub>3</sub>, MgO and K<sub>2</sub>O including SiO<sub>2</sub>> 35%, Al<sub>2</sub>O<sub>3</sub>> 15%, MgO> 20%.

This phlogopite is of the magnesium aluminous type with a high resistivity at a temperature + 500 ° C. This resistivity is due to several factors including: depth exploitation, high intensity metamorphism zone.

#### 4.4. Aster image processing

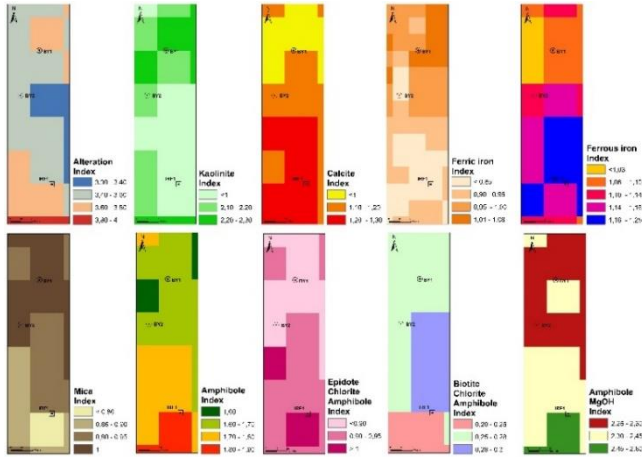


Figure 6. Maps produced form Aster data

The distribution of minerals and chemical elements in these analyzes of the aster images gives us an idea of the outcrops on the surface. This variance is due to the absorption spectrum including 0.48µm <Fe<sup>3+</sup> <0.80µm, 0.40µm <Fe<sup>2+</sup><0.55µm.

Hydrothermal alteration minerals containing Al(OH) radicals, alunite, muscovite and kaolinite have a strong absorption spectrum, don't 2.14µm-2.28µm.

The ratios between bands 4, 5,6 and 7 of VNIR and SWIR provide the mineral distribution associated with the parent rock carrying mineralization.

#### 5. Discussion

Drilling in certain levels of the mine is important for the confirmation and extension of the deposit. The geochemical analysis which allowed us to make the distribution of the chemical elements in the -75 levels will be advantageous accompanied by dreams.

The correlation between processed aster image and geochemical analysis is complex given the depth of investigation. However, it allows us to understand the

variation of minerals on the surface and on an investigation depth or outcrop (dike, fault, foliation).

The Ampandrandava phlogopite deposit is not thick, but in-depth investigation remains the main mining problem.

#### 6. Conclusion

The Ampandrandava mine is the only functional underground mine in Madagascar today. It is unique for its phlogopite which is the most demanded on the international market with its various minerals: anhydrite, apatite, calcite, pyrite, gypsum, diopside, pegmatite etc. Many deposits are mined artisanally in the south because of the high demand for phlogopite. The Ampandrandava mine production is the most solicited because of its geochemical and physical properties. The analysis of the Aster data allowed us to make a classification of the minerals and to make a lithology mapping of a given region. With the combination of the bands as well as the ratios, the analyses and the corrections brought to the satellite images, it describes us important geological information.

#### References

- Amin Beiranvand Pour, Mazlan Hashim, (2012). The application of ASTER remote sensing data to porphyry copper and epithermal gold deposits, Journal Elsevier.
- Barnaby, W., Rockwell, Daniel H. Knepper, Jr, Jhon, D. Horton, (2012). Télédétection spectrale, en complément du projet d'évaluation des ressources minérales PRISM-II, République Islamique de Mauritanie, Journal USGS.
- Miora, H. Rakotondrabe, Anoop V Mohandas, Eddy, H. Rasolomanana, Virtual Symposium, 2-4 Dec, 2020 - IEEE InGARSS 2020, Analysis of geochemical data of mica for the development of mineral resources: case of southern Madagascar, Beraketa, [https://www.ingarss2020.org/view\\_paper.php?PaperNum=1062](https://www.ingarss2020.org/view_paper.php?PaperNum=1062), 5p
- Miora H. Rakotondrabe, Eddy H. Rasolomanana, Lucienne R. Randriamanivo, Nirina H. Ravoson, Madamines - Madarevues (2019). Characterization of Ampandrandava phlogopite by fluorescence-X methods and valorization of the deposit (Southern Madagascar), <http://madarevues.recherches.gov.mg/?-Madamines-19p>.



## 5<sup>th</sup> Intercontinental Geoinformation Days

igd.mersin.edu.tr



### Estimation of Wind Erosion Threshold Velocity Based on Spectroscopy Data Using Random Forest Algorithm

Monireh Mina <sup>1</sup>, Mahrooz Rezaei <sup>\*2</sup>, Leila Hossein Abadi <sup>3</sup>, Abdolmajid Sameni <sup>1</sup>

<sup>1</sup>Shiraz University, School of agriculture, Department of soil science, shiraz, Iran

<sup>2</sup>Wageningen University & Research P.O. Box 47, AA, 6700, Meteorology and Air Quality Department, Wageningen, the Netherlands

<sup>3</sup>Shahid Beheshti University, Remote Sensing and GIS Center, Tehran, Iran

#### Keywords

Random Forest  
Reflectance  
Soil Erosion  
Vis – NIR  
Wind Tunnel

#### Abstract

Threshold Velocity (TV) of soil is considered a great indicator in order to assess Potential wind erosion (PWE). However, TV is difficult to measure and some techniques such as wind tunnels can be quite time-consuming and hard. To deal with this challenge, spectroscopy could be considered as an advantageous method to estimate TV. In the current research, the potential of Vis-NIR spectroscopy in TV estimation with the help of machine learning algorithm namely Random Forest (RF) was assessed. For this reason, in the Fars Province, Iran, 100 in-situ wind tunnel tests were executed, and soil samples spectral reflectance were examined with the help of spectroscopy apparatus. Results showed that outputs of TV estimation with the aid of RF model were ( $R^2 = 0.74$ ,  $RMSE = 0.65 \text{ m s}^{-1}$ ,  $RPD = 1.78$ , and  $RPIQ = 2.83 \text{ m s}^{-1}$ ). This study has shown the utilization of the reflectance spectroscopy with the assist of machine learning algorithm is a reassuring method for worldwide evaluation of wind erosion phenomena.

#### 1. Introduction

Alarming danger of Wind erosion is considered as one of the primary sources of deterioration of lands especially in arid also in semi-arid areas (Chappell et al., 2018). This particular issue is a concerning one worldwide (Pásztor et al., 2016). The occurrence of wind erosion happens when intense winds and surface of soil, which has already been exposed to erosion, exist at the same time (Chappell et al., 2018). Determining the threshold velocity parameter (TV) is known to be a critical part for assessing wind erosion because wind velocity ought to be immense to a degree that carries a considerable amount of soil particles.

TV is used as an important hallmark for assessing wind erosion risk and determining soil susceptibility and it is frequently used in many researches (Kouchami-Sardoo et al., 2019). TV is remarkably associated with soil properties (Mina et al., 2022) and the intensity of wind erosion (Visser et al., 2004). In some research, attention was drawn to the distribution of fundamental (textural) particles (Pásztor et al., 2016; Van Pelt et al., 2017) and secondary (aggregate) ones (Rezaei et al., 2022). Also, some focused-on roughness of the surface

(Yan et al., 2015), calcium carbonate substance (Kheirabadi et al., 2018), gypsum content (Kouchami-Sardoo et al., 2019), and soil moisture (Sirjani et al., 2019). These factors are reported as the highest rank in terms of influence in soil erosion assessment repeatedly. One of the important obstacles in wind erosion management is the issue of measuring or predicting the TV accurately in arid and in semi-arid regions (Okin, 2005). During the past half century, some researches take advantage of portable wind tunnel method in order to compute wind erosion in natural environment for different reasons (Zobeck and Van Pelt., 2014).

Estimating TV indirectly would be quite beneficial because of the many difficulties in measuring this parameter directly. Significant wind erosion needs to be dealt with especially in vast areas which are susceptible to wind erosion for example, in aeolian sediment transport (Li et al., 2015). The technique of Visible-near infrared spectroscopy (Vis-NIRS) has a great capability for soil analysis, and it can be used alternatively in such matter (de Santana et al., 2018).

Detecting the most Significant wavelengths which are highly linked to the desired variables obtained from the wavelengths of each spectral curve, is determined by this

#### \* Corresponding Author

monireh.mina@gmail.com  
\*mahrooz.rezaei@wur.nl  
leilahosseinabadi1993@gmail.com  
majid.baba@gmail.com

#### Cite this study

Mina M, Rezaei M, Hossein Abadi L, Sameni A (2022). Estimation of Wind Erosion Threshold Velocity Based on Spectroscopy Data Using Random Forest Algorithm. 5<sup>th</sup> Intercontinental Geoinformation Days (IGD), 5-9, Netra, India

method. This technology is a promising, fast, non-destructive soil sensing technique that made the estimation of various properties of soil possible by field or laboratory measurement (Kim et al., 2014). Selecting the proper calibration method and its performance is directly linked to the calibration ultimate successful outcome (Mouazen et al., 2010). In most researches, Partial Least Square Regression (PLSR) method has been implemented for linear multivariate calibration. However, the complication in the link between the spectra and wind erosion soil characteristics cannot be denied and considering PLSR method may be insufficient. Therefore, employing other chemometric methods, which follow the principles of non-linear procedures, is extremely important. Complex non-linear systems apply Random Forest (RF), which is an impressive yet commonly-used machine learning method for modelling data (Nawar et al., 2016; de Santana et al., 2018). The only literature investigated the relationship between threshold velocity of wind and near and infrared spectral reflectance (350-2500nm) was practiced by Li et al. in 2015. They have employed PLSR method for TV estimation. Despite the fact that they used 31 samples ( $R^2 = 0.76$ ,  $RMSE = 0.12$ ), Their outcome indicated that the visible range (400–700 nm) and near infrared (1100–2500 nm) could be used as indicative wavelengths for TV estimation. Ostovari et al. (2018) investigated the performance of PLSR method in estimating soil erodibility (K) in lands which were affected by water erosion and they used 40 samples. Their results demonstrated a successful prediction for K-factor with  $R^2 = 0.56$ . Some researchers have used soil reflectance spectra for predicting soil properties which were affected by erosion as well as using this method for investigating the link between soil erosion and soil spectra. Wang et al. (2016) discovered that some factors including Soil Organic Matter (SOM), water-stable aggregates (WSA), and geometric mean diameter can have a noticeable effect on erodibility of soil.

For this purpose, they have implemented hyperspectral visible and near-infrared reflectance spectroscopy method. Moreover, They evidenced that a spectral analytical method is applicable for complex datasets analysis and they shed some light on dynamic variation association to erodibility estimation. There have been many researches in this field, most of which have investigated on soil particle size (Shi et al., 2020),  $CaCO_3$  (Bilgili et al., 2010), the soil organic matter (Nawar et al., 2016; Ostovari et al., 2018) and soil moisture (Mirzaei et al., 2022) and Cation Exchange Capacity (CEC) (Ng et al., 2019; Mina et al., 2022). In order to discover how soil is resisting to environmental highly erosive forces, some criterions including the stability of soil aggregation and distribution of aggregate soil size were determined and estimated by Vis-NIR spectroscopic technique (Shi et al., 2020). Indeed, in Italy (Conforti et al., 2013) and in Czech Republic (Žižala et al., 2017) have used SOM as an initial indicator for determination of water-induced soil erosion areas. Schmid et al., (2012) classified soil eroded spots in Spain using land surface's spectral properties with the help of important soil features such as physical, chemical, and

morphological ones which were all associated with soil loss.

To our understanding, there is no research on the applicability of Vis-NIR spectroscopy coupled to RF model for wind erosion prediction. Conducting such researches are markedly and extremely vital for wind erosion controlling scenarios and conserving of soil in large areas especially the ones which are susceptible to wind erosion and emission of dust for example, Iran. The application of Remote Sensing (RS) techniques in wind erosion field is emphasized in this research and its results can be used for evaluating policies at local and worldwide scales in order to manage soil erosion.

Therefore, some purposes of this study were 1) to measure the TV using extensive wind tunnel test, 2) evaluation of the possibility of employing reflectance spectroscopy method in TV estimation.

## 2. Method

### 2.1. Study Area

Fars province, which is an arid and semi- arid region, in Iran is situated in the south-central part of the county and was our study (Abbasi et al., 2021). In most parts of this province, wind erosion happens regularly and one reason is climate condition. In this area, many critical wind erosion regions exist (Mina et al., 2022). The average amount of the annual rainfall is within the range of 100 mm in the south parts and nearly 400 mm in the north parts (Ostovari et al., 2018). There are many seasonal and empty agricultural fields, rangelands, lakes and dried riverbeds. The slope was less than 1% and poor vegetation condition was recognizable in these areas.

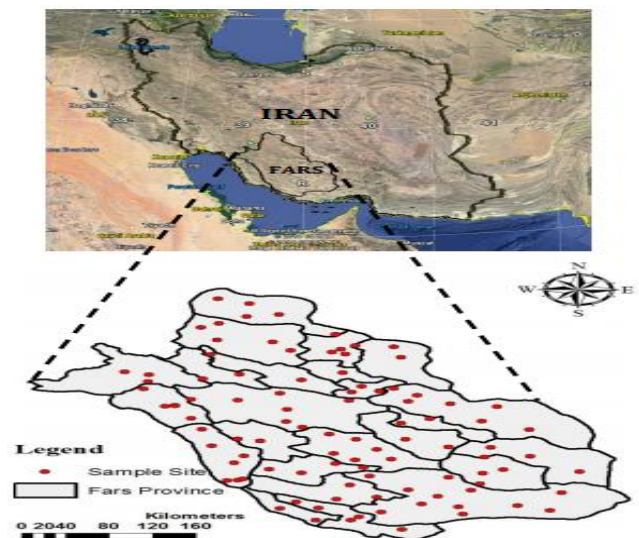


**Figure 1.** Locations of Fars province.

### 2.2. Soil Sampling and Wind Tunnel Experiments

In 100 study sites soil samples were selected from the topsoil (3 cm) in the summer of 2019. Then, a comprehensive in-situ wind tunnel experiment was done in 100 sites. Three different sites were chosen in order to practice wind tunnel experiment considering local soil variability. After the determination of the proper test points, we have placed wind tunnel on intact soil in the

prevailing wind direction. We have implemented observational method to measure TV. The comprehensive detail of the wind tunnel is described in Mina et al. (2022).

### 2.3. Spectral Reflectance Measurement

We have used spectrophotometer apparatus (Metrohm, NIRS XDS) within the range of Vis-NIR (400-2500 nm) with 0.5 nm spectral resolution for measuring spectral reflectance of samples. Twenty replicates were considered for each sample. Figure. 2. provides the spectral reflectance in detail. Reduction of noise was done and the reflectance spectra range were between 450-2450 nm. For the aim of eliminating turbulence and increasing spectral data quality, various pre-processing techniques have been done. For that matter, firstly, Savitzky and Goly filter (SG) (Savitzky and Golay, 1964) was performed on spectral data. Then, Standard Normal Variate (SNV) technique for each parameter were done. Finally, For spectral data processing we have used Unscrambler X v. 10.4 software (Camo Software AS, Oslo, Norway).

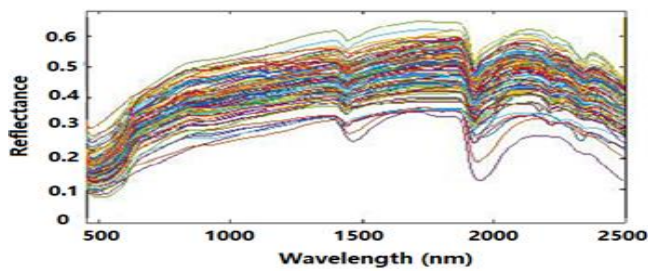


**Figure 2.** The raw spectral reflectance data of the soil samples.

### 2.4. Model Evaluation

For the prediction of TV based on soil spectral reflectance, RF model was used. RF regression is famously used for many data analysis and many statistical purposes. Evaluation step contained using four statistical criteria including Ratio of Performance to the Interquartile range (RPIQ), coefficient of determination (R<sup>2</sup>), the Ratio of Predicted Deviation (RPD), and Root Mean Square Error (RMSE) to examine the accuracy of the model. To perform Statistical analysis and model the data we have used Machine Learning (ML) toolbox in MATLAB 2019b.

In Equations 1-4,  $P_i$  and  $O_i$  are the estimated and measured values of the parameter, respectively, and  $n$ : is the number of observations. SD is the standard deviation of the measured values,  $Q_1$  is the first quartile of the samples, and  $Q_3$  is the third quartile of them. The estimations were categorized in the following order: very poor with  $RPD < 1$ , weak with  $RPD = 1-1.4$ , moderate with  $RPD = 1.4-1.8$ , good with  $RPD = 1.8-2$ , very good with  $RPD = 2.5-2$ , and excellent with  $RPD > 2.5$  (Lacerda et al., 2016). The same classification principle was applied for RPIQ analysis.

$$R^2 = \frac{\left[ \frac{\sum_{i=1}^n (O_i - \bar{O})(P_i - \bar{P})}{\sum_{i=1}^n (O_i - \bar{O}) \sum_{i=1}^n (P_i - \bar{P})} \right]^2}{1} \quad (1)$$

$$RMSE = \sqrt{\frac{\sum_{i=1}^n (P_i - O_i)^2}{n}} \quad (2)$$

$$RPD = \frac{SD}{RMSE} \quad (3)$$

$$RPIQ = \frac{IQ}{RMSE} \quad (4)$$

$$IQ = Q_3 - Q_1$$

## 3. Results and Discussion

Statistical summary for TV is shown in Table 1. Average TV ranged from 1.50 to 12.5 m s<sup>-1</sup>, presenting a noticeable potential of wind erosion in the region.

**Table 1.** TV Statistical analysis. Q1: First quartile, Q3: Third quartile, SD: Standard Deviation, CV: Coefficient of Variation

Soil parameter	Threshold Velocity
Unit	m s <sup>-1</sup>
Range	1.5-12.5
Q1-Q3	6 - 8
Mean $\pm$ SD	7.21 $\pm$ 1.98
CV (%)	28

Represented soil spectra revealed three specific absorption bands at 1414, 1915, and 2212 nm (Figure. 2).

Results of predictive model for TV estimation model using spectral reflectance are presented in Table 2. Figure. 3 also shows its scatter plot demonstrating predicted versus measured TV using RF technique. The parameter concentration area is distributed along the adjusted regression line in the validation group. Consequently, results clearly showed the estimation acceptance and it was due to the overall consistency of the predicted and measured values. Overestimation and underestimation predicted values considering RMSE and RPD factors were not great enough to consider the regression model invalid.

For the purpose of assessing model performance, we have used datasets which were not involved in the calibration as an external validation set. According to Table 2, the RF model showed R<sup>2</sup> (0.74) and RMSE (0.65), with RPD of 1.78 and RPIQ = 2.83 stating prediction excellency.

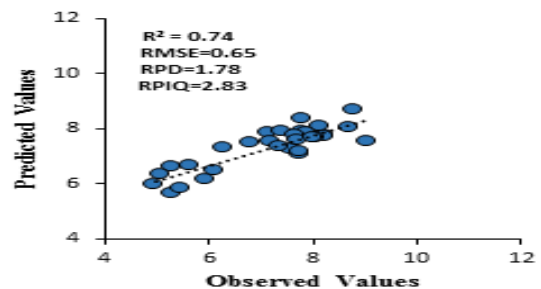


**Figure 3.** Scatter plot of predicted versus measured TV by RF model

**Table 2.** Prediction results for TV ( $\text{m s}^{-1}$ ) using RF model

Model	Calibration		Validation			
	R <sup>2</sup>	RMSE	R <sup>2</sup>	RMSE	RPD	RPIQ
RF	0.91	0.62	0.74	0.65	1.78	2.83

#### 4. Discussion

According to the TV value, the lowest TV was noticed in the southwest part of the province containing sandy texture and it had very poor vegetation cover. Additionally, this area is famous for its susceptibility to wind erosion and it is a critical part of this province (Rezaei et al., 2016). Meanwhile, the highest TV was found in the northwest and north parts of the province and in these regions, soils were largely contained of clay loam texture and they were under rangeland (Sirjani et al. 2019).

They also showed free and hygroscopic water characteristic at 1414 nm, hydroxyl groups at 1915 nm, magnesium and aluminium metals clay minerals networks, the bonding of hydroxides with iron at 2212 nm (Clark et al., 1990). Research has illustrated that the absorption peaks which is around 2341 nm are linked to CO<sub>3</sub> groups in minerals which contain carbonate (Lagacherie et al., 2008). Furthermore, spectral curves show a peak at wavelengths in range of 500-700 nm which can be considered as a characteristic of goethite and hematite of soil (de Santana et al., 2018).

PLSR performance in TV prediction was ( $R^2 = 0.76$ , RMSE = 0.12) in a research by Li et al. (2015). This difference in accuracy factors might be due to the fact that we have used more samples than them. They examined 31 samples and we had 100 samples.

Our results indicate that the data mining technique (RF) revealed better results compare to the other one. One reason could be its ability to include nonlinear interactions and relationships, and it was mentioned in other researches as well (Brown et al., 2006; Mouazen et al., 2010; Vohland et al., 2011). The superiority of RF performance over PLSR was also reported by de Santana et al (2018), and they have quantified clay content in their research. They also emphasized on this better performance and they associated it to the lower number of outliers excluded from RF in calibration and validation sets in comparison with PLSR.

Generally, the complexity of prediction model has increased with an increase in sample's number and also variability. ML calibration models can improve prediction accuracy assessment. In overall, the TV factor, considered as a soil property, which has no well-known spectral characteristic, ML algorithms can result in better performance in terms of assessment.

#### 5. Conclusion

In the presented research, we examined the utilization of reflection spectroscopy for TV estimation in wind erosion estimation challenges. All in all, the results illustrated that between the TV factor and soil spectral reflectance a clear correlation has been noticed. Representative soil spectra demonstrated specific absorption bands at 1414, 1915, 2212, and 2341 nm. Our results have stated that spectral reflectance is a sufficient

tool even in large areas. Hence, soil spectral reflections could be mentioned as an effective method in soil analysis. Other sources including remotely-sensed data can provide these spectra too. Lastly, to have a comprehensive knowledge of its application more studies should be done including the developed PSTD method with the help of satellite imageries for monitoring TV spatial distribution, and data mining techniques such as support vector regression and artificial neural networks could be useful for future projects.

#### References

- Abbasi, S., Rezaei, M., Keshavarzi, B., Mina, M., Ritsema, C., & Geissen, V. 2021. Investigation of the 2018 Shiraz dust event: Potential sources of metals, rare earth elements, and radionuclides; health assessment. *Chemosphere*, 279, 130533.
- Bilgili, A. V., Van Es, H. M., Akbas, F., Durak, A., & Hively, W. D., 2010. Visible-near infrared reflectance spectroscopy for assessment of soil properties in a semi-arid area of Turkey. *Journal of Arid Environments*. 74(2), 229-238.
- Brown, D. J., Shepherd, K. D., Walsh, M. G., Mays, M. D., & Reinsch, T. G., 2006. Global soil characterization with VNIR diffuse reflectance spectroscopy. *Geoderma*. 132(3-4), 273-290.
- Campbell, P. M. D. M., Filho, E. I. F., Francelino, M. R., Demattê, J. A. M., Pereira, M. G., Guimarães, C. C. B., & Pinto, L. A. D. S. R., 2018. Digital Soil Mapping of Soil Properties in the "Mar de Morros" Environment Using Spectral Data. *Revista Brasileira de Ciência do Solo*. 42.
- Clark, R. N., Swayze, G. A., Singer, R. B., & Pollack, J. B., 1990. High-resolution reflectance spectra of Mars in the 2.3- $\mu\text{m}$  region: Evidence for the mineral scapolite. *Journal of Geophysical Research: Solid Earth*. 95(B9), 14463-14480.
- Conforti, M., Buttafuoco, G., Robustelli, G., & Scarciglia, F., 2013. Studying the relationship between water-induced soil erosion and soil organic matter using Vis-NIR spectroscopy and geomorphological analysis: A case study in southern Italy. *Catena*. 110, 44-58.
- de Santana, F. B., de Souza, A. M., & Poppi, R. J., 2018. Visible and near infrared spectroscopy coupled to random forest to quantify some soil quality parameters. *Spectrochimica Acta Part A: Molecular and Biomolecular Spectroscopy*. 191, 454-462.
- Kheirabadi, H., Mahmoodabadi, M., Jalali, V., & Naghavi, H., 2018. Sediment flux, wind erosion and net erosion influenced by soil bed length, wind velocity and aggregate size distribution. *Geoderma*. 323, 22-30.
- Kim, I., Pullanagari, R. R., Deurer, M., Singh, R., Huh, K. Y., & Clothier, B. E., 2014. The use of visible and near-infrared spectroscopy for the analysis of soil water repellency. *European Journal of Soil Science*. 65(3), 360-368.
- Kouchami-Sardoo, I., Shirani, H., Esfandiarpour-Boroujeni, I., Álvaro-Fuentes, J., & Shekofteh, H., 2019. Optimal feature selection for prediction of wind erosion threshold friction velocity using a modified evolution algorithm. *Geoderma*. 354, 113873.

- Kouchami-Sardoo, I., Shirani, H., Esfandiarpour-Boroujeni, I., Besalatpour, A. A., & Hajabbasi, M. A., 2020. Prediction of soil wind erodibility using a hybrid Genetic algorithm–Artificial neural network method. *Catena*. 187, 104315.
- Lacerda M.P.C., Demattê J.A.M., Sato, M.V., Fongaro, C.T., Gallo, B.C., & Souza A.B., 2016. Tropical texture determination by proximal sensing using a regional spectral library and its relationship with soil classification. *Remote Sensing*. 8, 701.
- Lagacherie, P., Baret, F., Feret, J. B., Netto, J. M., & Robbez-Masson, J. M., 2008. Estimation of soil clay and calcium carbonate using laboratory, field and airborne hyperspectral measurements. *Remote Sensing of Environment*. 112(3), 825-835.
- Li, J., Flagg, C., Okin, G. S., Painter, T. H., Dintwe, K., & Belnap, J., 2015. On the prediction of threshold friction velocity of wind erosion using soil reflectance spectroscopy. *Aeolian Research*. 19, 129-136.
- Mina, M., Rezaei, M., Sameni, A., Moosavi, A. A., & FALLAH SHAMSI, R. A. S. H. I. D. (2022). Using Soil Pedotransfer and Spectrotransfer Functions to Estimate Cation Exchange Capacity in Calcareous Soils, Fars Province. *Iranian Journal of Soil and Water Research*, 52(11),2911-2922.
- Mina, M., Rezaei, M., Sameni, A., Moosavi, A. A., & Ritsema, C. (2021). Vis-NIR spectroscopy predicts threshold velocity of wind erosion in calcareous soils. *Geoderma*, 401, 115163.
- Mina, M., Rezaei, M., Sameni, A., Ostovari, Y., & Ritsema, C. (2022). Predicting wind erosion rate using portable wind tunnel combined with machine learning algorithms in calcareous soils, southern Iran. *Journal of Environmental Management*, 304, 114171.
- Mirzaei, S., Bolorani, A. D., Bahrami, H. A., Alavipanah, S. K., Mousivand, A., & Mouazen, A. M. 2022. Minimising the effect of moisture on soil property prediction accuracy using external parameter orthogonalization. *Soil and Tillage Research*, 215, 105225.
- Mouazen, A. M., Kuang, B., de Baerdemaeker, J., & Ramon, H., 2010. Comparison among principal component, partial least squares and back propagation neural network analyses for accuracy of measurement of selected soil properties with visible and near infrared spectroscopy. *Geoderma*. 158(1-2), 23-31.
- Nawar, S., Buddenbaum, H., Hill, J., Kozak, J., & Mouazen, A. M., 2016. Estimating the soil clay content and organic matter by means of different calibration methods of vis-NIR diffuse reflectance spectroscopy. *Soil and Tillage Research*. 155, 510-522.
- Ng, W., Minasny, B., Montazerolghaem, M., Padarian, J., Ferguson, R., Bailey, S., & McBratney, A. B., 2019. Convolutional neural network for simultaneous prediction of several soil properties using visible/near-infrared, mid-infrared, and their combined spectra. *Geoderma*. 352, 251-267.
- Okin, G.S., 2005. Dependence of wind erosion and dust emission on surface heterogeneity: Stochastic modeling. *Journal of Geophysical Research: Atmospheres*. 110, D11.
- Ostovari, Y., Ghorbani-Dashtaki, S., Bahrami, H. A., Abbasi, M., Dematte, J. A. M., Arthur, E., & Panagos, P., 2018. Towards prediction of soil erodibility, SOM and CaCO<sub>3</sub> using laboratory Vis-NIR spectra: A case study in a semi-arid region of Iran. *Geoderma*. 314, 102-112.
- Pásztor, L., Négyesi, G., Laborczi, A., Kovács, T., László, E., & Bihari, Z., 2016. Integrated spatial assessment of wind erosion risk in Hungary. *Natural Hazards and Earth System Sciences*. 16(16), 2421-2432.
- Rezaei, M., Mina, M., Ostovari, Y., & Riksen, M. J. 2022. Determination of the threshold velocity of soil wind erosion using a wind tunnel and its prediction in calcareous soils of Iran. *Land Degradation & Development*.
- Rezaei, M., Sameni, A., Fallah Shamsi, S. R., & Bartholomeus, H., 2016. Remote sensing of land use/cover changes and its effect on wind erosion potential in southern Iran. *PeerJ*. 4, e1948.
- Schmid, T., Palacios-Orueta, A., Chabrilat, S., Bendor, E., Plaza, A. Rodriguez, M., Huesca, M., Pelayo, M., Pascual, C., Escribano, P., Cicuendez, V., 2012. Spectral characteristic of land surface composition to determination soil erosion within semiarid rainfed cultivated areas. IGARSS 2012. 7082-7084.
- Shi, P., Castaldi, F., van Wesemael, B., & Van Oost, K., 2020. Vis-NIR spectroscopic assessment of soil aggregate stability and aggregate size distribution in the Belgian Loam Belt. *Geoderma*. 357, 113958.
- Sirjani, E., Sameni, A., Moosavi, A. A., Mahmoodabadi, M., & Laurent, B., 2019. Portable wind tunnel experiments to study soil erosion by wind and its link to soil properties in the Fars province, Iran. *Geoderma*. 333, 69-80.
- Van Pelt, R. S., Hushmurodov, S. X., Baumhardt, R. L., Chappell, A., Nearing, M. A., Polyakov, V. O., & Strack, J. E., 2017. The reduction of partitioned wind and water erosion by conservation agriculture. *Catena*. 148, 160-167.
- Visser, S. M., Sterk, G., & Ribolzi, O., 2004. Techniques for simultaneous quantification of wind and water erosion in semi-arid regions. *Journal of Arid Environments*. 59(4), 699-717.
- Vohland, M., Besold, J., Hill, J., & Fründ, H. C., 2011. Comparing different multivariate calibration methods for the determination of soil organic carbon pools with visible to near infrared spectroscopy. *Geoderma*. 166(1), 198-205.
- Wang, G., Fang, Q., Teng, Y., & Yu, J., 2016. Determination of the factors governing soil erodibility using hyperspectral visible and near-infrared reflectance spectroscopy. *International Journal of Applied Earth Observation and Geoinformation*. 53, 48-63.
- Yan, Y., Wu, L., Xin, X., Wang, X., & Yang, G., 2015. How rain-formed soil crust affects wind erosion in a semi-arid steppe in northern China. *Geoderma*, 249, 79–86.
- Žižala, D., Zádorová, T., & Kapička, J., 2017. Assessment of soil degradation by erosion based on analysis of soil properties using aerial hyperspectral images and ancillary data, Czech Republic. *Remote Sensing*. 9(1), 28.
- Zobeck, T. M., & Van Pelt, R. S., 2014. Wind erosion. Publications from USDA-ARS /UNL Faculty. 1409.

5<sup>th</sup> Intercontinental Geoinformation Days

igd.mersin.edu.tr



## GreenMetric ranking calculation by using satellite imageries: A Case Study from Türkiye

Abdullah Harun Incekara\*<sup>1</sup>, Elif Yaprak Basaran<sup>2</sup>, Dursun Zafer Seker<sup>3</sup><sup>1</sup> Tokat Gaziosmanpasa University, Faculty of Engineering and Architecture, Department of Geomatics Engineering, Tokat, Türkiye<sup>2</sup> Tokat Gaziosmanpasa University, Faculty of Engineering and Architecture, Department of Architecture, Tokat, Türkiye<sup>3</sup> Istanbul Technical University, Faculty of Civil Engineering, Department of Geomatics Engineering, Istanbul, Türkiye**Keywords**Remote sensing  
GreenMetric  
Higher Education**Abstract**

GreenMetric (GM) is universally used to determine the sustainability levels of universities. In this study, it is recommended to use satellite imageries in calculating the scores of the setting and infrastructure category, which is the first category of GM. Also, it is suggested to use thematic maps derived from satellite imageries as evidence presented to the system for the calculated scores. For this purpose, a Sentinel-2B satellite image of the Tokat Gaziosmanpasa University Tasliciftlik Campus area from Turkey was exposed to digital image processing techniques to derive statistical values regarding greenery. Score calculations were made by using numerical information derived from the satellite image, and the values of the attributes such as population on the campus. Based on these data and information, the total score of the setting and infrastructure category was calculated as 925, and those officially claimed was 825. Considering the controversial evidence presented to the GM system for the first category, it has been determined that thematic maps are more consistent and reliable. The results proved that the use of satellite imagery in calculations for the first category of GM could set a standard.

**1. Introduction**

Universities represent much more than closed areas where students receive occupational education from academic staff. A university is a complete living space with its facilities and the environment it provides (Alshuwaikhat and Abubakar, 2008). Universities, which are no different from a small cities with their versatile nature, have to be sustainable in line with their goals. Many universities around the world are trying to improve themselves and increase their popularity for this purpose.

The educational aspect of sustainability was first alleged at the Stockholm Conference in 1972. Studies on the sustainability of universities have been discussed in the literature mostly in the field of social sciences (Velazquez et al., 2006; Alshuwaikhat and Abubakar, 2008; Lozano et al., 2013; Lauder et al., 2015; Ragazzi and Ghidini, 2017). Various metrics were used to determine the sustainability levels of universities. However, this is now determined by GreenMetric (GM) at a universal level. The emergence and development process of GM was examined in detail by Suwartha and Sari (2013). The ranking of the participating universities is carried out according to the total score obtained from different

categories with various criteria. Universities also upload documents proving the values they present to the system.

GM consists of six main categories. These are setting and infrastructure (SI), energy and climate change (EC), waste (WS), water (WR), transportation (TR), and education and research (ED), respectively (GM Guideline, 2019). The scores obtained separately from each category constitute the total score and then, universities are ranked in terms of being a green campus. The percentage of each category in the total score is presented in Figure 1.

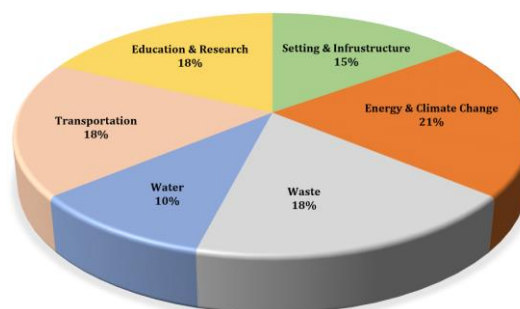


**Figure 1.** The six categories used in the ranking and their distributions as a percentage.

\* Corresponding Author

\*(abdullah.incekara@gop.edu.tr) ORCID ID 0000-0001-9166-7537

Cite this study

Incekara, A.H., Basaran, E.Y. & Seker, D.Z. (2022). GreenMetric Ranking Calculation by Using Satellite Imageries; A Case Study from Türkiye. 5<sup>th</sup> Intercontinental Geoinformation Days (IGD), 10-13, Netra, India

The first among six categories provide information about the university’s opinion on the environment (GM Guideline, 2018; GM Guideline 2019). SI has its sub-categories as presented in Table 1. Scores of each indicator affect the final score depending on the percentile ranges specified in the guide.

There are a total of 5 percentiles or areal slice for each indicator and since it is not possible to show the scores corresponding to 30 slice spacings in a table form in this study, the readers are recommended to refer to the GM guideline. Calculation for SI-5 is based on slicing in square meters. For others, ranges created according to percentiles are used. For example, if the calculated proportional value for SI-1 is between 1% and 80%, 300 point is multiplied by a coefficient of 0.25. This coefficient is 0.50 for the percentile value between 80 and 90, and 0.75 for the 90 to 95 value. If the percentile is greater than 95%, it is directly multiplied by 1. If the calculated proportional value corresponds to the first of 5 percentiles, zero point is taken regardless of which category it is. The coefficient values corresponding to these percentiles are not the same in each category. Therefore, it is necessary to calculate separately for each sub-category.

Details of other indicators related to other categories can be reached through GM guidelines. In the last published guide, the number of sub-indicators in the SI category has increased (GM Guideline, 2021). Therefore, the maximum scores of the indicators discussed in this study were also updated. However, it is immaterial which of the guidelines for the last 4 years has been used to determine the possible contribution of satellite imagery to the GM ranking.

No	Category SI	Max. Points
SI-1	The ratio of open space area to the total area	300
SI-2	Total area on campus covered in forest vegetation	200
SI-3	Total area on campus covered in planted vegetation	300
SI-4	Total area on campus for water absorption besides the forest and planted vegetation	200
SI-5	The total open space area divided by the total campus population	300
SI-6	Percentage of university budget for sustainability efforts within a year	200
<b>TOTAL</b>		<b>1500</b>

## 2. Methodology Used

In this study, sub-categories of SI were determined using image processing techniques. The aim of this study is that the techniques used at a basic level can take GM, which is mostly handled by social sciences, a little further. The selected study area was Tokat Gaziosmanpasa University (TOGU) located in Turkiye. The names of the main campus where they joined the GM is Tasliciftlik. The methodology applied for the study area was briefly visualized in Fig. 2.

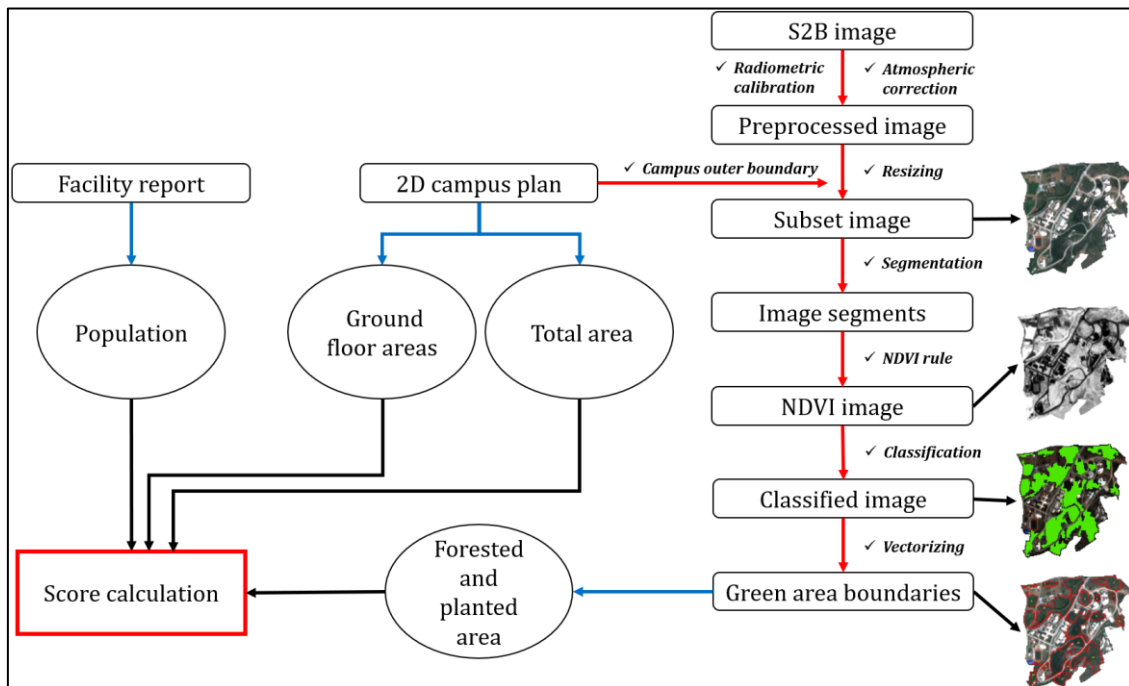


**Figure 2.** Applied workflow

Sentinel 2 satellite image was used to derive information about the greenery level of the university. Satellite imagery used in this study was S2B image with the acquiring date of April 24. The reason why the image used belongs to 2018 is that the guide referenced in the

study belongs to 2019. Object-oriented classification technique was applied to the pre-processed satellite image which covered only the current campus area. The rule created based on Normalize Difference Vegetation Index (NDVI) (Rouse et al., 1973) value was applied to

produced segments. Thus, green and non-green areas were separated from each other to determine the level of greenery. The study area and its NDVI image for TOGU is presented in Fig. 3. The status of green area on campus and the enclosed outer boundaries of green areas on campus are presented in Fig. 4. The extent of the area covered by each green area became evident in this fully scaled dataset.

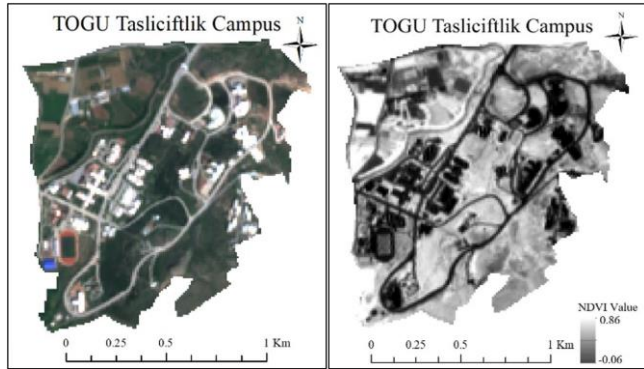


Figure 3. Study area and NDVI image

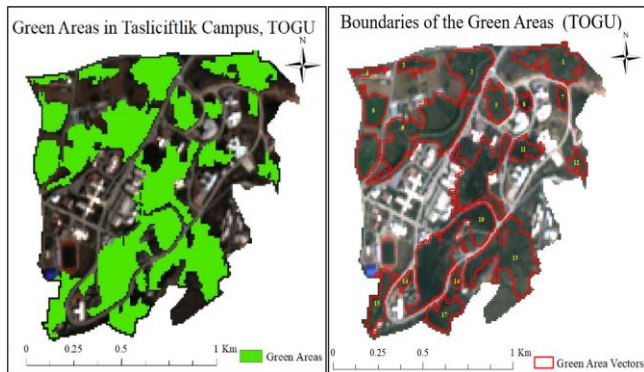


Figure 4. Green areas and outer boundaries of the green areas

### 2.1. Score calculations

Recommendations for GM score calculation are limited in the literature. The effect of campus morphology (Marrone et al., 2018) on the calculated score and the evaluation of data envelopment analysis (Marti, 2019) in calculations are a few of them. However, most of the studies have already researched evaluating the current situation rather than taking GM forward with new ideas.

Green areas in GM are evaluated in two different sub-categories as forested and planted. In this study, SI-2 and

SI-3 were evaluated together in a single category, as the university's relationship with greenery was determined by sustainability. In other words, the total amount of green space was evaluated regardless of its type. The calculation was made over 500 points with the combined sub-category. Also, it is the satellite image used in the majority of the score calculation in the SI category. For SI-4, structures such as roads and walkways that are shown as water-absorbing surfaces other than green areas by GM were not considered in the same concept. These are not structures created specifically to absorb water, but for transportation purposes. Except for the forest and planted vegetation areas, which are already natural water absorption surfaces, a separate surface is generally not constructed. Therefore, the university's relationship with greenery was handled through more realistic parameters and the score was calculated in this way.

The ones required to calculate the scores of the sub-categories mentioned in Table 1 are presented in Table 2. Ground floor areas of buildings were extracted from the scaled ownership status plans of the campuses. The difference between the total area and total campus ground floor area of buildings gives the open space area. The population values involving the academic and administrative staff and students on the campuses were obtained from the annual facility report published by the university (Url-1).

Table 2. Values required for calculations

Information	Value
Total area (m <sup>2</sup> )	1,448,599
Total campus ground floor area of buildings (m <sup>2</sup> )	78074
Open space area (m <sup>2</sup> )	1,370,525
Green area (Forested + Planted) (m <sup>2</sup> )	549000
Population (m <sup>2</sup> )	37187

### 3. Results and Discussion

The scoring is presented in Table 3. SI-4 is not an indicator that can be extracted from a Sentinel image due to its spatial resolution. However, main water absorption surfaces are generally forested and planted vegetation areas. Apart from these, no specific surface or structure is usually created for absorption. Thus, the percentile selected for TOGU corresponds to zero points. SI-6 is the indicator related to the budget and the percentile used for SI-6 is the value submitted by TOGU to the system.

Table 3. Score calculations for TOGU

SI Id	Calculation	Percentile	Range Score
SI-1	$(1,370,525 \text{ m}^2 / 1,448,599 \text{ m}^2) * 100$	> 90% and 95%	$0.75 * 300 = 225$
SI-2&3	$(549000 \text{ m}^2 / 1,448,599 \text{ m}^2) * 100$	> 35%	$1 * 500 = 500$
SI-4	-	-	-
SI-5	$(1,370,525 \text{ m}^2 / 37187)$	> 20 - 40 m <sup>2</sup>	$0.5 * 300 = 150$
SI-6	-	> 1% - 3%	$0.25 * 200 = 50$
<b>Total Score</b>			<b>925</b>

The score calculated for TOGU based on information derived from satellite image was 925. In contrast, the

official score depending on the evidence presented by the university was 825. There may be various reasons for the

differences between the scores calculated in the study and the officially announced ones. The 2<sup>nd</sup> and 3<sup>rd</sup> of sub-categories were combined and considered as a single category. This category recommended by the authors is used to evaluate the green area as a single category representing greenery rather than separating it as forested and planted vegetation. A score difference may have occurred due to the percentile range corresponding to the proportional value calculated with the combined category.

Another possible reason is the image data used directly in the study. There are sample evidence templates on the GM official website for the metric values to be submitted. A composite section from the template with examples of what the evidence might look like is presented in Figure 5. Most of the universities superficially form polygons on Google Earth when calculating areal values. Moreover, sample evidence in these templates for building floor areas and planted vegetation areas does not give any information about how the values presented to the system are calculated. An ordinary photograph of the relevant building or planted vegetation area is demonstrated as evidence and the corresponding areal value is written below. Therefore, it is expected that there will be a difference between the scores calculated with the data submitted to the system but whose reliability is controversial, and the values calculated more consistently with more professional evidence in this study.

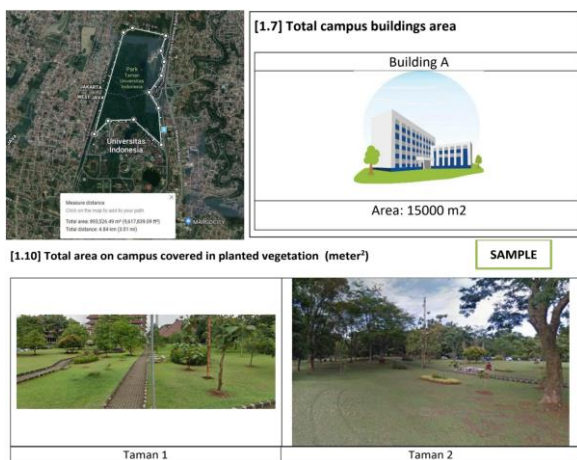


**Figure 5.** Sample pieces of evidence accepted by GM

#### 4. Conclusions

In the study, the possible contribution of satellite images to the GM rating system was examined. Depending on the image type used, two indicators related to greenery were gathered under a single heading. The resulting products produced using satellite imagery proved to be more reliable and consistent evidence for the values presented to GM. There should be a standard for the evidence to be presented and the thematic map in Fig.4 is the suggested evidence for the greenery of the campus in this study.

The image processing steps used are simple but effective in terms of the scope of the study. Therefore, thematic maps can be requested as evidence in the next GM guidelines. Although satellite images were used

specifically for the SI category in the study, it is also possible to evaluate them in subcategories of other main categories. One of the indicators under the transportation category is related to the ratio of the ground parking area to the total campus area. To produce similar information to the SI category, satellite imageries can be used with classifications where the number of classes is more than one.

#### References

- Alshuwaikhat, H.M., Abubakar, I., 2008. An integrated approach to achieving campus sustainability: assessment of the current campus environmental management practices. *J. Clean. Prod.* 16, 1777–1785. <https://doi.org/10.1016/j.jclepro.2007.12.002>
- Dagiliūtė, R., Liobikienė, G., Minelgaitė, A., 2018. Sustainability at universities: Students' perceptions from Green and Non-Green universities. *J. Clean. Prod.* 181,473–482. <https://doi.org/10.1016/j.jclepro.2018.01.213>
- GM Guideline 2018. Universities, impacts and sustainable development goals.
- GM Guideline, 2019. Sustainable university in a changing world: Lessons, Challenges and Opportunities.
- Lauder, A., Sari, R.F., Suwartha, N., Tjahjono, G., 2015. Critical review of a global campus sustainability ranking: GreenMetric. *J. Clean. Prod.* 108, 852–863. <https://doi.org/10.1016/j.jclepro.2015.02.080>
- Lozano, R., Lukman, R., Lozano, F.J., Huisingh, D., Lambrechts, W., 2013. Declarations for sustainability in higher education: Becoming better leaders, through addressing the university system. *J. Clean. Prod.* 48, 10–19. <https://doi.org/10.1016/j.jclepro.2011.10.006>
- Marrone, P., Orsini, F., Asdrubali, F., Guattari, C., 2018. Environmental performance of universities: Proposal for implementing campus urban morphology as an evaluation parameter in Green Metric. *Sustain. Cities Soc.* 42, 226–239. <https://doi.org/10.1016/j.scs.2018.07.012>
- Ragazzi, M., Ghidini, F., 2017. Environmental sustainability of universities: Critical analysis of a green ranking. *Energy Procedia* 119, 111–120. <https://doi.org/10.1016/j.egypro.2017.07.054>
- Rouse, J.W., Hass, R.H., Schell, J.A., Deering, D.W., 1973. Monitoring vegetation systems in the great plains with ERTS. *Third Earth Resour. Technol. Satell. Symp.* 1, 309–317. <https://doi.org/citeulike-article-id:12009708>
- Suwartha, N., Sari, R.F., 2013. Evaluating UI GreenMetric as a tool to support green universities development: Assessment of the year 2011 ranking. *J. Clean. Prod.* 61, 46–53. <https://doi.org/10.1016/j.jclepro.2013.02.034>
- Velazquez, L., Munguia, N., Platt, A., Taddei, J., 2006. Sustainable university: what can be the matter? *J. Clean. Prod.* 14, 810–819. <https://doi.org/10.1016/j.jclepro.2005.12.008>
- URL-1: <https://strategi.gop.edu.tr/dosyasayfasi.aspx?birimi d=7&dil=tr&menuid>



## 5<sup>th</sup> Intercontinental Geoinformation Days

igd.mersin.edu.tr



# Spatiotemporal prediction of reference evapotranspiration in Araban region, Turkey: A machine learning based approaches

Mehmet Irfan Yesilnacar<sup>1</sup>, Jazuli AbdullahiAla Tahsin<sup>2</sup>, Abdullah İzzeddin Karabulut<sup>3</sup>

<sup>1</sup>Harran University, Environmental Engineering Department, Haliliye, Sanliurfa, Türkiye

<sup>2</sup>Baze University, Faculty of Engineering, Civil Engineering Department, Abuja, Nigeria

<sup>3</sup>Harran University, Environmental Engineering Department, Urfa, Türkiye

<sup>3</sup>Harran University, Remote Sensing and Geographic Information Systems, Urfa, Türkiye

### Keywords

Meteorological variables  
Artificial neural network  
Evapotranspiration  
Climate change mitigation  
Turkey

### Abstract

Accurate prediction of Reference Evapotranspiration ( $ET_0$ ) is crucial for climate change mitigation, water resources management and agricultural activities. Therefore, this study aimed at investigating the applicability of a recently developed Machine Learning (ML) model called Gaussian Process Regression (GPR), for the prediction of  $ET_0$  in Araban station, Gaziantep region Turkey. Artificial Neural Network (ANN) was also developed for comparison. Several meteorological variables including temperatures  $T_{min}$ ,  $T_{max}$  and  $T_{mean}$  (minimum, maximum and mean), surface pressure (PS), wind speed ( $U_2$ ) and relative humidity (RH) from 1990 – 2021 were used as the inputs. Determination coefficient ( $R^2$ ), root mean square error (RMSE) and mean absolute deviation (MAD) were used as performance evaluation criteria. The obtained results revealed that GPR led to better performance with  $MAD = 0.0174$ ,  $RMSE = 0.0236$  and  $R^2 = 0.9940$  in the validation step. The general results demonstrated that GPR could be employed successfully to accurately predict  $ET_0$  in Araban station and thus, could be useful to decision makers and designers of water resources structures.

## 1. Introduction

Evapotranspiration (ET) plays a vital role in water resources management and planning and is amongst the most important components of hydrologic water cycle (Abdullahi et al. (2019). ET can be instrumentally measured or by reference evapotranspiration ( $ET_0$ ) calculation (Gocic et al. 2015). The  $ET_0$  serve as the basis for computing crop evapotranspiration ( $ET_c$ ) as well as irrigation water requirement of crops (Dai et al. 2009). Penman Monteith model by Food and Agricultural Organization of United Nations (FAO) has been accepted as the main method for estimating  $ET_0$  in hourly, daily and monthly scales (Allen et al. 1998).

For the past decades, artificial neural network (ANN) has been given significant attention in numerous fields of study including  $ET_0$ . Dimitriadou and Nikolakopoulos (2022) applied for  $ET_0$  prediction at Peloponnese Peninsula, Greece. Farooque et al. (2022) employed ANN for daily  $ET_0$  forecasting for sustainable irrigation scheduling. Under climate change scenarios, Maqsood et

al. (2022) projected  $ET_0$  using ANN. Despite the nonlinearity of ANN and its ability to deal with nonlinear aspect of  $ET_0$ , it has some limitations which include over-fitting, time delay in choosing the best befitting structure etc. To overcome these and other issues, a recently developed model called Gaussian Process Regression (GPR) was employed in this study to predict  $ET_0$  at Araban station, Gaziantep region in Turkey.

## 2. Method

### 2.1. Study area

Araban is bordered from North by Adiyaman district with latitudes ( $37^{\circ}22'$  and  $37^{\circ}31'$ ), from South by Gaziantep district and Urfa left on its east side and Kahramanmaraş district on the west side, the climate of Araban is designated as semi -arid region. Fig. 1 shows the study area.

### \* Corresponding Author

(e-mail) ORCID ID xxxx - xxxx - xxxx - xxxx  
(e-mail) ORCID ID xxxx - xxxx - xxxx - xxxx  
(e-mail) ORCID ID xxxx - xxxx - xxxx - xxxx

### Cite this study

Yesilnacar M, I, Tahsin J. A, & Karabulut A. I. (2022). Spatiotemporal prediction of reference evapotranspiration in Araban region, Turkey: A machine learning based approaches. 5<sup>th</sup> Intercontinental Geoinformation Days (IGD), 14-17, Netra, India



Figure 1. Study location in Turkey

## 2.2. Data Normalization and global statistical indicators

The data used in this study including temperatures  $T_{min}$ ,  $T_{max}$  and  $T_{mean}$  (minimum, maximum and mean), surface pressure (PS), wind speed ( $U_2$ ) and relative humidity (RH) from 1990 – 2021 were obtained from Turkey meteorological organization and divided into 70% training (269) and 30% validation (115). Determination coefficient ( $R^2$ ), root mean square error (RMSE) and mean absolute deviation (MAD) were used as performance indicator and information regarding them can be found from Ibrahim et al. (2022) study.

## 2.3. Artificial neural network (ANN)

ANNs and the neural network analysis process share a number of features. Among feed-forward ANN models, multi-layered structures are the most widespread. The simple network design of the ANN is composed of input, hidden, and output layers. The number of inputs depends on how many nodes are present at the input layer, where the input group transferred to the network. Detail information on ANN can be found in Elbeltagi et al (2022a) study.

## 2.4. A Gaussian process regression (GPR)

A relatively new machine learning approach is the Gaussian process regression (GPR) model Elbeltagi et al. (2022b) state that the stochastic process explained by the multivariable Gaussian probability distribution

(GPD) and the unbiased forecasting based on the linear combination of prior experimental observation are the two key characteristics of GPR. Detail information regarding GPR can be found in Elbeltagi et al (2022b).

## 2.5. Reference evapotranspiration ( $ET_0$ )

According to Allen et al. (1998), For estimating  $ET_0$  the most common used energy balance physical-based equation is the Penman-Monteith equation (FAO56-PM) as it proposed by the food and agriculture organization (FAO).

The (FAO56-PM) equation's performance is widely acknowledged as the most expert equation for estimating  $ET_0$  (Sobh et al. 2022). Detail information can be found in Allen et al. (1998).

## 3. Results

In this study, the recently developed GPR model was applied to predict  $ET_0$  and compared with ANN model. Hence, the results are presented accordingly. For machine learning applications, the input size has a great role to play in determining highest performance. Therefore, 2 different input combination were developed given as:

$$M1=f(R_H, P, T_{mean}, T_{max}) \quad (1)$$

$$M2=f(T_{min}, P_s, U_2) \quad (2)$$

Where M1 and M2 are the developed models for  $ET_0$  prediction. The results of the  $ET_0$  prediction are shown in Tables 1 and 2.

Table 1. Results of the predicted  $ET_0$  based on ANN and GPR in the training phase

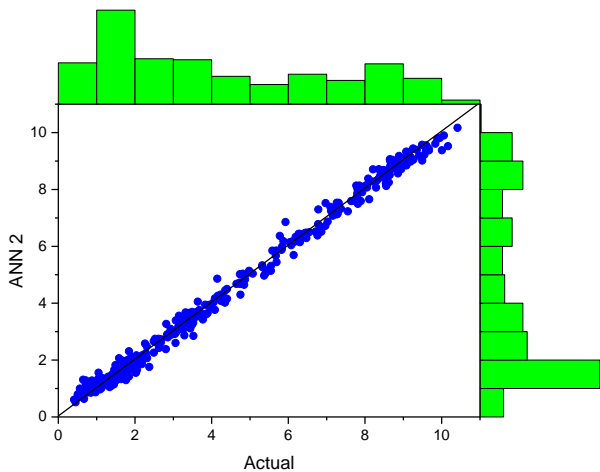
Model type	Model NO.	MAD	RMSE	$R^2$
ANN	M1	0.0286	0.0401	0.9813
	M2	0.0283	0.0397	0.9817
GPR	M1	0.0173	0.0224	0.9941
	M2	0.0241	0.0311	0.9888

Table 2. Results of the predicted  $ET_0$  based on ANN and GPR in the validation phase

Model type	Model NO.	MAD	RMSE	$R^2$
ANN	M1	0.0299	0.0412	0.9816
	M2	0.0299	0.0412	0.9816
GPR	M1	0.0174	0.0236	0.994
	M2	0.0244	0.0323	0.9887

The performances of ANN and GPR models as presented in Tables 1 and 2 show good performance of the applied models in predicted  $ET_0$  at Araban region Turkey. It can be seen that a goodness of fit performance with  $R^2$  up to 0.9887 in the validation phase. It can be observed from Tables 3 and 4 that using any of the proposed modeling combination, accurate predictions were achieved.

Figures 2 and 3 shows the scatter plots and histogram of the actual versus predicted  $ET_0$  values for both ANN and GPR.



**Figure 2.** Graphical comparison of the observed and predicted  $ET_0$  values for the best ANN model

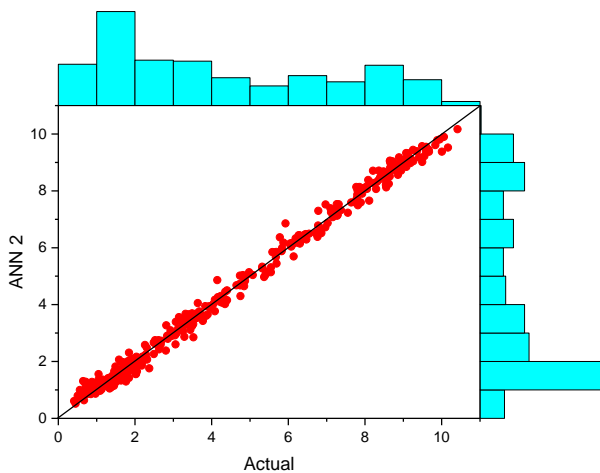


**Figure 3.** Graphical comparison of the observed and predicted  $ET_0$  values for the best GPR model

#### 4. Discussion

As seen in Tables 1 and 2, using different input combinations, different performances are achieved for both ANN and GPR models. For ANN models, similar performances are obtained. Although, there is slight difference between the M1 and M2 in the training step, the results are same in the validation step with RMSE and R2 values of 0.0412 and 0.9816, respectively. This shows that the accurate prediction of  $ET_0$  by machine learning (ML) does not depend on the quantity of inputs used, rather on the quality of inputs. As such, M2 with 3 inputs can appropriately predict the behavior of the  $ET_0$  with less computational difficulties and less time consuming. The improved performance of M2 could be attributed to inclusion of  $U_2$  as input. According to Nourani et al. (2020), despite having less influence on  $ET_0$  prediction when single input single output prediction is considered,  $U_2$  significantly improve performance when combined with other variables as  $ET_0$  inputs.

#### 5. Conclusion

This study was performed to assess the possibility of employing a recently developed model called gaussian process regression (GPR) to improve performance of machine learning (ML) based artificial neural network (ANN) for the spatiotemporal prediction of reference evapotranspiration ( $ET_0$ ) in Araban, Gaziantep region, Turkey. To achieve this, 2 different input combination models were developed using  $R_H$ ,  $P$ ,  $T_{mean}$  and  $T_{max}$  as M1 and  $T_{min}$ ,  $P_s$  and  $U_2$  as M2 for both ANN and GPR models for data that spanned from 1990 - 2021.

The obtained results showed that the ML models are sophisticated tools for ascertaining the stochastic phenomena surrounding  $ET_0$ . Both M1 and M2 can lead to high performance but M2 slightly outperform M1. However, when less simulation difficulties as well as less time consuming are more important, M1 is preferable. The general results indicated and improved GPR performance over ANN.

#### References

- Abdullahi, J., Elkiran, G., & Nourani, V. (2019, August). Artificial intelligence based and linear conventional techniques for reference evapotranspiration modeling. In International Conference on Theory and Application of Soft Computing, Computing with Words and Perceptions (pp. 197-204).
- Allen RG, Pereira LS, Raes D & Smith M (1998) Crop Evapotranspiration: Guidelines for computing crop water requirements FAO Irrigation and Drainage Paper 56.
- Dai, X., Shi, H., Li, Y., Ouyang, Z., & Huo, Z. (2009). Artificial neural network models for estimating regional reference evapotranspiration based on climate factors. *Hydrological Processes: An International Journal*, 23(3), 442-450.
- Dimitriadou, S., & Nikolakopoulos, K. G. (2022). Artificial neural networks for the prediction of the reference evapotranspiration of the Peloponnese Peninsula, Greece. *Water*, 14(13), 2027.
- Elbeltagi, A., Kushwaha, N. L., Rajput, J., Vishwakarma, D. K., Kulimushi, L. C., Kumar, M., ... & Abd-Elaty, I. (2022a). Modelling daily reference evapotranspiration based on stacking hybridization of ANN with meta-heuristic algorithms under diverse agro-climatic conditions. *Stochastic Environmental Research and Risk Assessment*, 1-24.
- Elbeltagi, A., Salam, R., Pal, S. C., Zerouali, B., Shahid, S., Mallick, J., & Islam, A. R. M. (2022b). Groundwater level estimation in northern region of Bangladesh using hybrid locally weighted linear regression and Gaussian process regression modeling. *Theoretical and Applied Climatology*, 1-21.
- Farooque, A. A., Afzaal, H., Abbas, F., Bos, M., Maqsood, J., Wang, X., & Hussain, N. (2022). Forecasting daily evapotranspiration using artificial neural networks for sustainable irrigation scheduling. *Irrigation Science*, 40(1), 55-69.
- Gocić, M., Motamedi, S., Shamshirband, S., Petković, D., Ch, S., Hashim, R., & Arif, M. (2015). Soft computing approaches for forecasting reference

- evapotranspiration. *Computers and Electronics in Agriculture*, 113, 164-173.
- Ibrahim, Z., Tulay, P., & Abdullahi, J. (2022). Multi-region machine learning-based novel ensemble approaches for predicting COVID-19 pandemic in Africa. *Environmental Science and Pollution Research*, 1-23.
- Maqsood, J., Farooque, A. A., Abbas, F., Esau, T., Wang, X., Acharya, B., & Afzaal, H. (2022). Application of artificial neural networks to project reference evapotranspiration under climate change scenarios. *Water Resources Management*, 36(3), 835-851.
- Sobh, M. T., Nashwan, M. S., & Amer, N. (2022). High Resolution Reference Evapotranspiration for Arid Egypt: comparative analysis and evaluation of empirical and artificial intelligence models. *International Journal of Climatology*.



## 5<sup>th</sup> Intercontinental Geoinformation Days

igd.mersin.edu.tr



### Utilizing GIS to select potential sites for biomass-utilizing mills in Louisiana USA

Cornelis F. de Hoop<sup>\*1</sup>, Anil Raj Kizha<sup>2</sup>, Arif Oguz Altunel<sup>3</sup>

<sup>1</sup>Louisiana State University Agricultural Center, School of Renewable Natural Resources, Baton Rouge, LA, USA

<sup>2</sup>University of Maine, School of Forest Resources, Orono, ME, USA

<sup>3</sup>Kastamonu University, Faculty of Forestry, Kastamonu, Türkiye

#### Keywords

GIS  
Biomass  
Site Selection  
Economic Development  
Energy

#### Abstract

Louisiana has a well-developed oil & gas network and is rich in agricultural production, including a thriving forest industry. Situated at the mouth of the Mississippi River, it is a natural location for a biomass energy industry, yet biomass energy is clearly lacking. At the Louisiana State University Agricultural Center, researchers have been working with industry to quantify potential energy demand and supply. These activities led to identifying potential sites for mills utilizing wood and other forms of biomass. While the earliest efforts focused on creating databases of biomass users and suppliers, GIS became a critical tool in conducting analyses efficiently. Tracking biomass proved to be a constantly moving target. As GIS developed from an obscure database on someone's computer to an online, publicly accessible database, each iteration of updates mandated that we improve the way this information is distributed.

#### 1. Introduction

Tracking complicated data has always been a challenge in all aspects of forest management and in related operations, such as logging and fire management. Even at the primary products level (pulp, lumber, plywood, etc.), selection of the proper site for mills will determine raw material cost for the life of each mill. This paper explores how Geographic Information Systems (GIS) has influenced these activities in Louisiana. Louisiana is a coastal state (largest city is New Orleans) located where the Mississippi River enters the Gulf of Mexico in an area often referred to as the Mid-South. The climate is mild and wet, so forests grow prolifically. Since the 1980s, the Mid-South and Southeastern states have been considered the "wood basket" of the country, producing more wood products than other regions. The most common commercial species are southern pine (*Pinus spp.*) and oak (*Quercus spp.*). Pine is used primarily for construction lumber and panels (primarily domestic market), while oak is used primarily in furniture and furnishings (domestic and export markets). Southern pine forests are natively fire-dependent ecosystems.

#### 2. Forest products applications

From about the period 2005 to 2015, we were contacted twice per month by a new party that had an idea for a bio-based mill, and they were searching for a suitable site to locate and build the mill. Common requirements were a sustainable input of 500,000 to 1 million tons of biomass, dry weight basis. This is a tall order that competes with the size of major pulp/paper mills and sawmills in the region.

While they all envision utilizing sawdust, bark, rice straw, rice husks, sugarcane bagasse and other agricultural/forestry wastes, they quickly realized that these materials already have a market in which they would have to compete. Transportation costs of the waste material usually equals or exceeds the current value of the waste material, nullifying those input sources. Also, while most say they can use any kind of biomass, eventually economic realities force them to settle on one or two input products.

Since waste materials are very limited in supply, the only realistic raw material available is pine timber of pulpwood size (standing timber 12-23 cm diameter).

#### \* Corresponding Author

(cdehoop@lsu.edu) ORCID ID 0000 - 0002 - 0348 - 1693  
(anil.kizha@maine.edu) ORCID ID 0000-0002-5274-2255  
(aoaltunel@kastamonu.edu.tr) ORCID ID 0000-0003-2597-5587

#### Cite this study

de Hoop C., Kizha A. & Altunel A. (2022). Utilizing GIS to select potential sites for biomass-utilizing mills in Louisiana USA. 5<sup>th</sup> Intercontinental Geoinformation Days (IGD), 18-21, Netra, India

This means they have to compete directly with the pulp/paper industry for low-value standing trees. Fortunately, there is an excess supply of these trees throughout the Mid-South and Southeast. The trick is to locate a new mill as far away as practicable from existing pulp/paper mills.

The pulp/paper industry has been trending toward consolidation. In the last 30 years, 6 pulp/paper mills closed permanently in Louisiana alone. Four of them belonged to International Paper (IP). In the meantime, other mills increased their capacity – in this area, most notably IP near Texarkana, Texas, and IP in Mansfield, Louisiana. This leaves potential “holes” in the wood procurement “basket” for new mills. In other words, site your new mill where a paper mill moved out (Fig. 1).

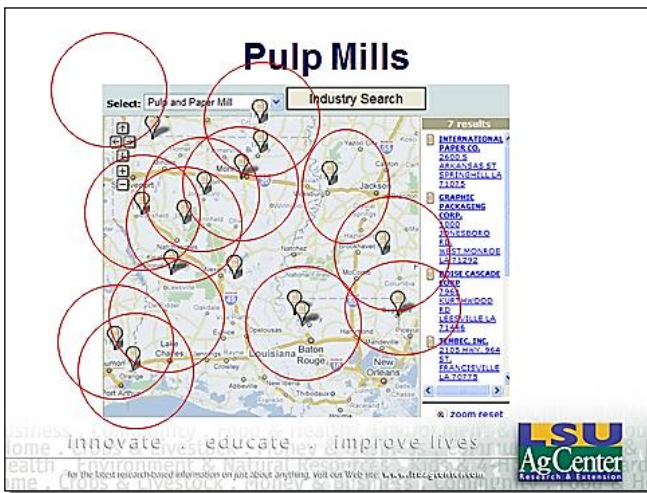


**Figure 1.** Site selection for a new wood-utilizing facility begins with looking at the current pulp/paper industry and searching for voids between their wood procurement areas.

Our research of the 1990s determined that the primary forest industry sites are rural – located near their natural resource supply to minimize transportation costs (Fig. 2, 3 & 4). The secondary industry (furniture, doors, windows, etc.) is located in urban areas, where there is better access to labor and markets (Fig. 5) (de Hoop et al. 1997; Kleit et al. 1994).

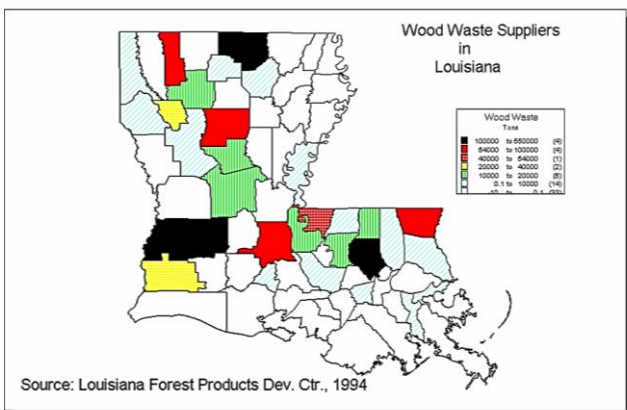


**Figure 2.** The primary forest products industry is located in rural areas close to the natural resource base.

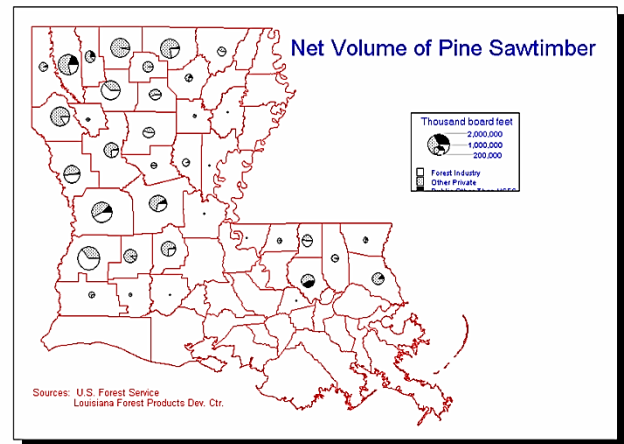


**Figure 3.** GIS using MapInfo to query where the usable pine timber is located. Data source is US Forest Service.

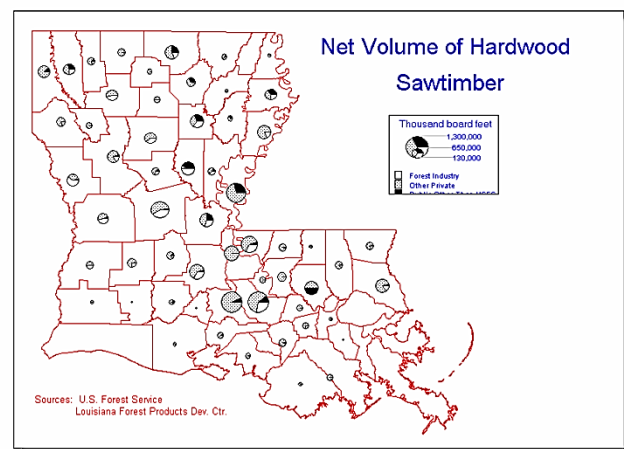


**Figure 4.** Usable hardwood timber and biomass supply is along the major rivers and can be sourced up to 800 km if water access is feasible.

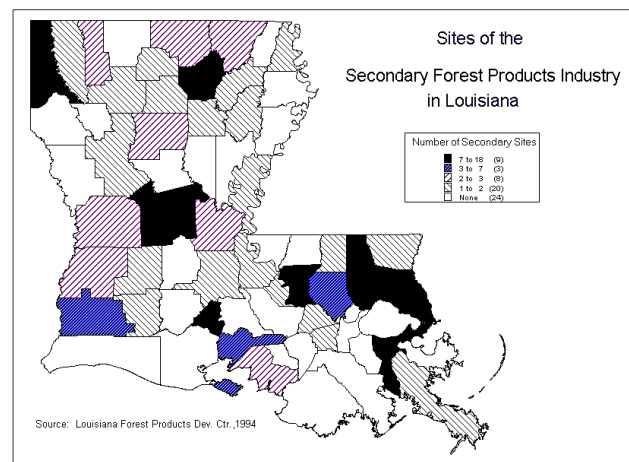


**Figure 5.** The secondary wood industry (e.g., furniture) is located in urban areas.

The Louisiana Department of Natural Resources was interested in developing/improving the utilization of biomass, as were several local economic development agencies. Our team developed a publicly-accessible database of potential biomass supply. Using data from the US Forest Service’s Forest Inventory & Analysis

program, we were able to overlay this with areas where timber growth exceeded drain (de Hoop et al. 2007).

Transportation access is another obvious concern. While road access is generally good throughout the country, rail and water access are obviously more limited. Through conversations with industry personnel, we determined that trucking is the cheapest mode of transportation if the haul distance is under about 150 km. Between 150 and 300 km, rail is the cheapest. Between 300 and 800 km, water (barge) is the cheapest. Of course, that is assuming that rail and water are available. Louisiana is well-situated with rail and water networks.

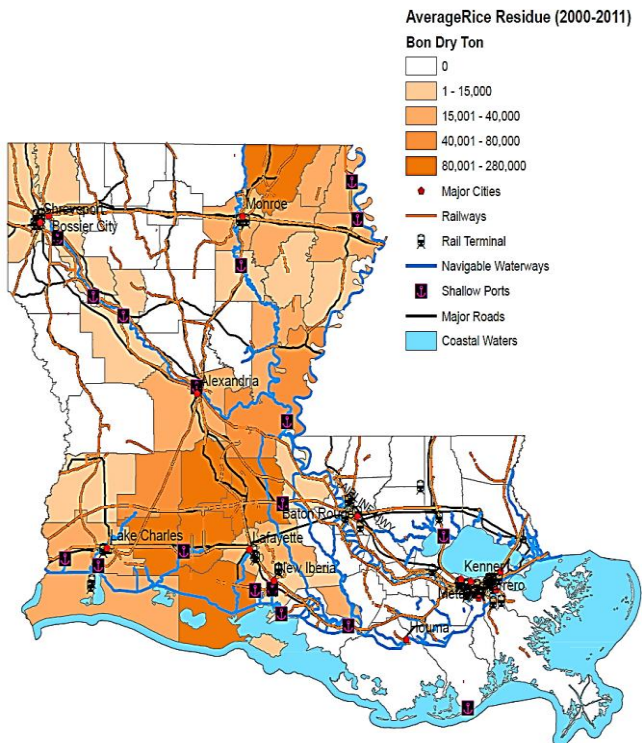


**Figure 6.** Port, rail and major highway network in the state. This map happens to be an overlay with potential rice crop residue production (Kizhakkepurakkal, 2012).

The final product was an online public database with a geographic component (Fig. 6). Through this, one could quickly collect the following information:

1. Where in Louisiana are the “holes” in the wood procurement areas of the current industry?
2. What is the volume of timber available in the parishes (counties) of interest?
3. What are the timber growth/drain ratios in the parishes of interest?
4. What is the potential volume of wood waste or agricultural waste (Fig. 7) in the parishes of interest?

This product is intended for people who are taking a “first look” at the state to help them focus quickly on a few potential sites. After this point, they typically hire a consultant to conduct a more detailed investigation.

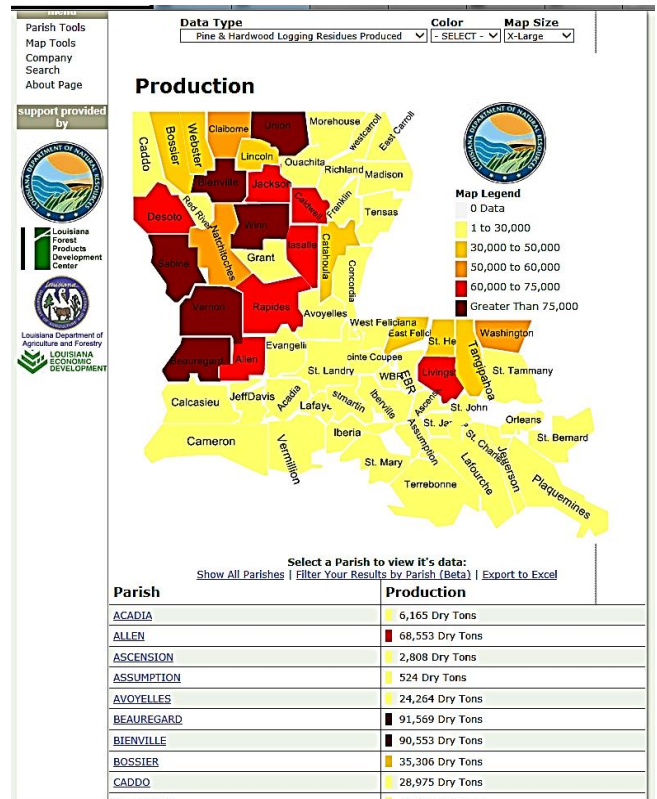


**Figure 6.** An online query result showing potential logging residues (tops, limbs) availability. Wood mill residues are 97% utilized, while very little of logging residues are currently utilized, although they do have nutrient value in the forest.

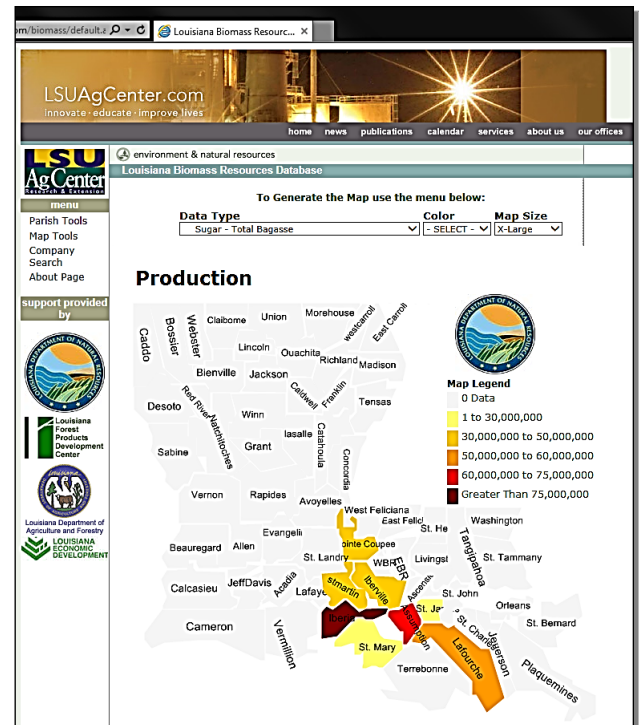


**Figure 7.** Query of sugar mill bagasse production, which has the potential as a biomass feedstock for other products.

### 3. Discussion

The development of a biomass supply database has been an iterative process. Our data collection in the 1990s started with the assumption that much wood mill residue was unutilized. By contacting the mills directly, we learned that practically all wood waste generated by the primary wood-utilizing industry was already utilized and bore an intrinsic value. While some of it was used for energy (especially the bark), much of it was used to make other products, such as particleboard. The amount of wood waste produced by the secondary industry was so small that it was economically infeasible to collect and transport. In addition, it contained many contaminants such as melamine and nails.

In the 2000s and 2010s, the attention turned from bioenergy to bio-based products, with their greater potential for economic growth. Thus, more attention was given to proximity to raw materials and to transportation networks. There were several success stories, such as a succinic acid plant and a biofuels plant. All the larger facilities were located on the Mississippi River network. The most notable success story is Drax LLC siting several wood pellets manufacturing facilities and exporting pellets out of the Port of Baton Rouge (also on the Mississippi River). The pellets are utilized in the UK to generate electricity.

### 4. Conclusion

The initial motivation to quantify wood and agronomic residues was two-fold: the federal government was interested in developing energy sources that were an alternative to coal, oil and natural gas, while the state government was interested in anything that improved economic development. Because products are usually more valuable than fuels, the search for bioenergy sources always turned into a search for potential bioproducts sites.

Biomass databases are quickly outdated. At the same time, GIS products evolve rapidly. Thus, there is

constant quest to update data while presenting it in a more accessible and user-friendly format.

Today, perhaps the major disadvantage of a publicly accessible database is that we obtain less natural feedback about how valuable this information is and how it is utilized.

### Acknowledgement

This work has been supported over the years by several programs then-sponsored by the US Dept. of Energy, and through several state entities, including the Louisiana Dept. of Agriculture & Forestry, Louisiana Dept. of Natural Resources, Louisiana Economic Development, and several local economic development organizations. Consistent backup support was provided by the National Institute of Food and Agriculture, U.S. Department of Agriculture, currently McIntire Stennis project # LAB94417.

### References

- de Hoop, C. F., Kleit, S. R., Chang, S. R., Gazo, R. & Buchart, M. (1997). Survey and Mapping of Wood Residue Users and Producers in Louisiana. *Forest Products Journal* 47(3):31-37.
- de Hoop, C.F., Chang, S. J., Hanumappa-Reddy, A. & Kizhakkepurakkal, A. (2007). Developing biomass utilization in Louisiana, USA: educating policy-makers, assessing supply and demand, and integrating with forest management. *Austro2007 Conference, Institute of Forest Engineering, Vienna, Austria*. 8pp.
- Kizhakkepurakkal, A. (2012). *Biomass Energy Production in Louisiana: A GIS Study on the Supply Chain*. Doctoral Thesis, Louisiana State University.
- Kleit, S., de Hoop, C. and Chang, J. (1994). An Overview of Agriforestry Waste Production and Use in Louisiana. In: *Biomass Energy, Bioenergy '94, Sixth National Bioenergy Conference, Conference Proceedings, Volume 2*. pp. 573-580.



## 5<sup>th</sup> Intercontinental Geoinformation Days

igd.mersin.edu.tr



### Identification of landslide susceptible zones in Idukki district (Southern Western Ghats) employing the REPTree model and geospatial techniques

Rajendran Shobha Ajin<sup>1</sup>, Hamza Vijith<sup>1</sup>, Mohan Akshaya<sup>2</sup>, Jayan Bindu Jibitha<sup>3</sup>, Kunnummal Agina Chandran<sup>4</sup>, Romulus Costache<sup>5,6,7</sup>

<sup>1</sup>Kerala State Emergency Operations Centre (KSEOC), Kerala State Disaster Management Authority (KSDMA), Thiruvananthapuram, India

<sup>2</sup>University College, Department of Geology, Thiruvananthapuram, Kerala, India

<sup>3</sup>University of Kerala, Department of Environmental Sciences, Thiruvananthapuram, Kerala, India

<sup>4</sup>Kannur University, Department of Environmental Studies, Kannur, Kerala, India

<sup>5</sup>National Institute of Hydrology and Water Management, Bucharest, Romania

<sup>6</sup>Department of Civil Engineering, Transilvania University of Brasov, Brasov, Romania

<sup>7</sup>Danube Delta National Institute for Research and Development, Tulcea, Romania

#### Keywords

2018 Kerala floods  
Idukki district  
Landslides  
REPTree  
Western Ghats

#### Abstract

Landslides, being the most frequent natural catastrophe in the Western Ghats of India, need immediate attention and further research to minimize their impacts. This research aimed at identifying landslide susceptible zones in Idukki district, situated in the Southern Western Ghats, one of the most impacted districts. For the analysis, a machine learning ensemble model called REPTree (Reduced Error Pruning Tree) has been employed, and the map has been created using geospatial techniques. The conditioning factors selected for the analysis include slope, distance from the road, soil texture, curvature, lineament density, aspect, topographic position index (TPI), lithology, land use/land cover (LULC), stream power index (SPI), elevation, and rainfall. According to this modeling, 13.30% of the district is very highly susceptible; 17.00% is highly susceptible to sliding. The validation of the created map employing the ROC curve techniques proved that the map has good predictive capacity. This ascertained the efficacy of the REPTree model in identifying susceptible zones, which therefore can be successfully applied in other regions of similar geomorphological and climatic settings.

#### 1. Introduction

Landslides are common in the Western Ghats region of Kerala (Akshaya et al. 2021), especially due to severe rainfall. In addition to this, land use practices and development activities increase the frequency of landslides (Abraham et al. 2021; Ajin et al. 2022b; Thomas et al. 2021). The recent landslides with significant death tolls are: the Koottickal disaster with a total death of 10 people (Ajin et al. 2022a), the Kokkayar disaster with 7 deaths (Ajin et al. 2022a), the Pettimudi disaster with 70 deaths (Achu et al. 2021), the Kavalappara disaster with 59 deaths (Ajin et al. 2022a), and the Puthumala disaster with 17 deaths (Ajin et al. 2022a).

The 2018 monsoon devastated the state of Kerala due to the flooding and landslides, which caused severe loss

of property and numerous lives. According to Hao et al. (2020), a total of 4728 landslides have been reported in Kerala in the year 2018, with a total of 48 casualties (Ajin et al. 2022a). Most of the landslides have been recorded in the Idukki district. A total of 2219 landslides have been reported in Idukki district during the 2018 monsoon season (Hao et al. 2020). Hence, there needs to be a validated susceptibility map that helps planners and policymakers take steps to reduce the effects of landslides in this district and that can be used as a model for other areas with similar geological and environmental conditions.

The objectives of this analysis are to identify the area susceptible to landslides by applying the REPTree model and geospatial techniques, and to assess the predictive accuracy of the created susceptibility map. Twelve

#### \* Corresponding Author

<sup>\*</sup>(ajinares@ieee.org) ORCID ID 0000-0003-3073-4390  
(vijithh@gmail.com) ORCID ID 0000-0002-1064-2088  
(akshayamohan0329@gmail.com) ORCID ID 0000-0002-7746-5100  
(jibithajb@gmail.com) ORCID ID 0000-0001-9748-300X  
(aginachinnu06@gmail.com) ORCID ID 0000-0003-4469-203X  
(romuluscostache2000@yahoo.com) ORCID ID 0000-0002-6876-8572

#### Cite this study

Ajin RS, Vijith H, Akshaya M, Jibitha JB, Chandran KA, & Costache R (2022). Identification of landslide susceptible zones in Idukki district (Southern Western Ghats) employing the REPTree model and geospatial techniques. 5<sup>th</sup>Intercontinental Geoinformation Days (IGD), 22-25, Netra, India

landslide conditioning factors such as slope, distance from the road, soil texture, curvature, lineament density, aspect, topographic position index (TPI), lithology, land use/land cover (LULC), stream power index (SPI), elevation, and rainfall have been employed for this modeling.

## 2. Materials and methods

### 2.1. Study Area

The Idukki district is comprised of rugged mountains and forests, with fourteen mountain peaks exceeding 2000 metres (Jones et al. 2021). This undulating topography and land use modifications as a part of development and recreational activities weaken the stability of the district, resulting in frequent landslides (Jones et al. 2021). The major rivers flowing through this district are Periyar, Muthirappuzhayar, Thodupuzhayar, and Thalayar, and the district spans an area of around 4358 km<sup>2</sup> (Thomas et al. 2021). The location of the Idukki district is depicted in Figure 1.

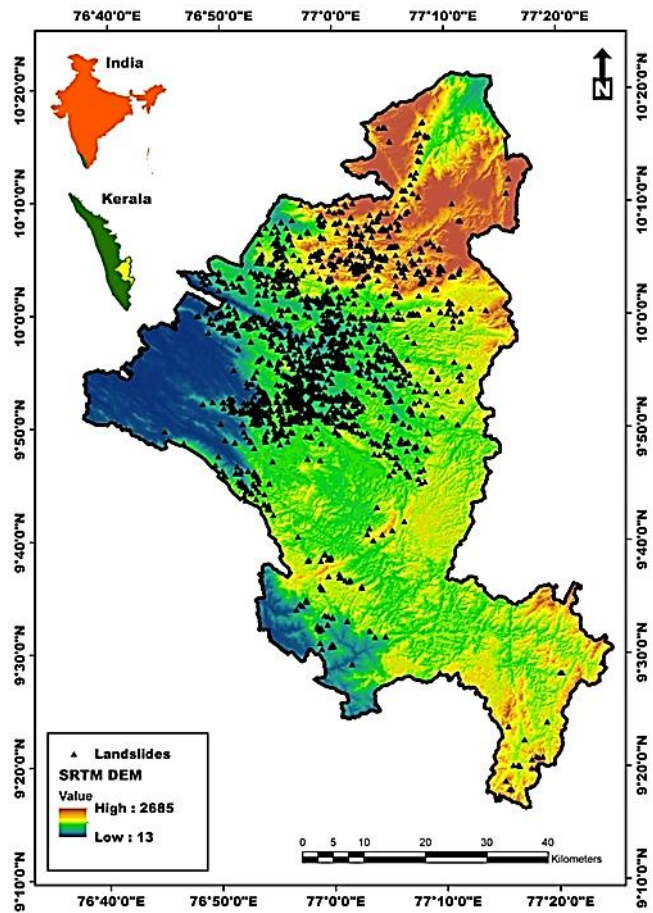


Figure 1. Location of the study area with landslide incidences

### 2.2. Creation of landslide inventory

A training dataset (80%) and a validation dataset (20%) were created (Muhammad et al. 2021) from the landslide incidence data obtained from the study of Hao et al. (2020). In the training dataset, there are 1775 slides, and in the validation dataset, there are 444 slides.

### 2.3. Derivation of conditioning factors

Using the ArcGIS 10.4 spatial analyst tools, the parameters like slope, aspect, and elevation were extracted from the SRTM DEM. Using raster calculator and spatial analyst tools, the curvature, SPI, and TPI were generated from the DEM. The lithology and lineaments were derived from the map produced by the Geological Survey of India, whilst the soil types were derived from the map published by the National Bureau of Soil Survey and Land Use Planning (NBSS&LUP). The lineament density was computed using ArcGIS's line density tool. Using the ERDAS Imagine 9.3 software, the LULC types were identified from the Landsat 8 OLI images. The topographic map and Google Earth were used to extract the road networks, and the Euclidean distance tool in ArcGIS was used to generate the distance from the road layer. The rainfall was extracted from the World Climate Report portal, which is available at <https://www.worldclim.org/>. The REPTree model weights were determined using the R 4.2.1 software. The landslide susceptibility of the study area has been categorized into five zones by applying the Natural Breaks method (Senan et al. 2022).

### 2.4. REPTree model

The REPTree is an ensemble model that leverages information gain or variance to build a decision tree using reduce-error pruning and back overfitting, and C4.5 will use an embedded technique to fill in the missing values (Nhu et al. 2020; Vishwakarma et al. 2022). Equation 1 and the entropy (E) function were applied to estimate the IGR values (Bui et al. 2020).

$$IGR(x, S) = \frac{E(S) - \sum_{i=1}^n \frac{E(S_i)|S_i|}{|S|}}{-\sum_{i=1}^n \frac{|S_i|}{|S|} \log_2 \frac{|S_i|}{|S|}} \quad (1)$$

Where S = training dataset, S<sub>i</sub> = subset (i = 1, 2, 3, ..., n), E = entropy function

### 2.5. Validation of the created map

For binary classification problems, predictive accuracy has been extensively measured using the area under the ROC curve (AUC) technique (Wu et al. 2007). The validation is considered excellent for AUC scores between 0.9 and 1.0, good for scores between 0.8 and 0.9, and fair for AUC scores between 0.7 and 0.8 (El Khouli et al. 2009). IBM SPSS Statistics 23.0 was employed for creating the ROC curve and computing the AUC scores.

## 3. Results

From the analysis, it is confirmed that the central part of the district is very-highly susceptible to landslides. In the created map, susceptibility is represented by five different zones (Figure 2). The validation of the created map confirmed good accuracy with an AUC score of 0.801 (80.1%). The ROC curve is depicted in Figure 3. The percentage of area of each zone is mentioned in Table 1.

**Table 1.** Percentage of landslide susceptible zones

Susceptible zones	Percentage of susceptible zones
Very low	28.31
Low	18.08
Moderate	23.31
High	17.00
Very high	13.30
<b>Total</b>	<b>100</b>

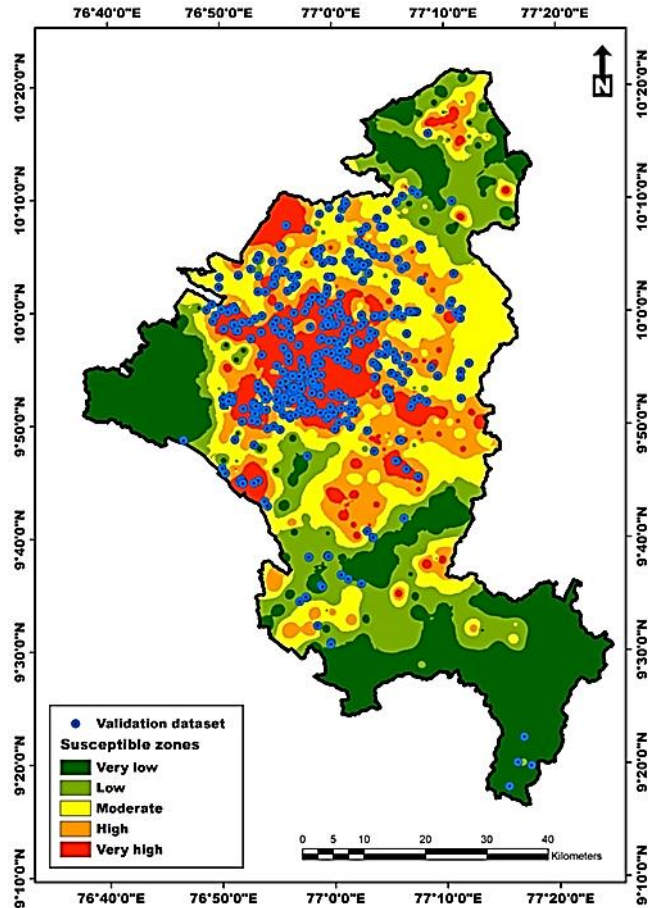


**Figure 2.** Landslide susceptibility map

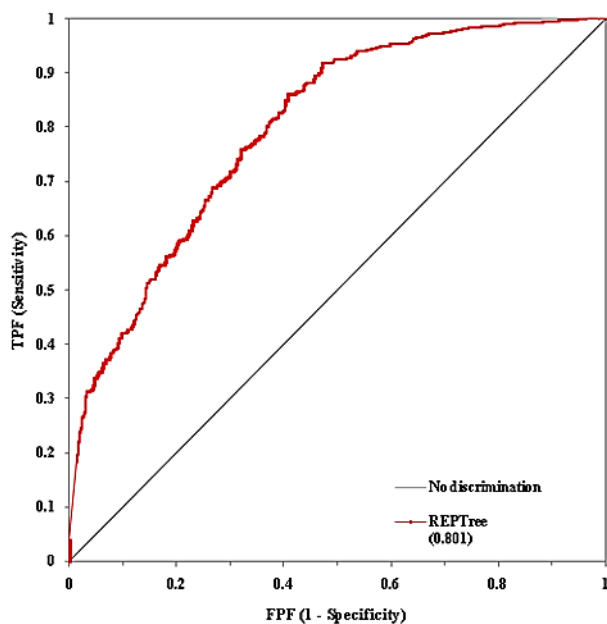


**Figure 3.** The ROC curves

**4. Conclusion**

The susceptibility map created employing the REPTree model identified 13.30% of the district as very highly landslide susceptible. A susceptible map of good predictive capacity will be of the utmost useful for decision makers in identifying suitable mitigation strategies, including zoning regulations. This map will also help identify roads and other infrastructure in critical zones so that an effective plan for evacuation can be prepared.

**References**

Abraham, M. T., Satyam, N., Jain, P., Pradhan, B., & Alamri, A. (2021). Effect of spatial resolution and data splitting on landslide susceptibility mapping using different machine learning algorithms. *Geomatics, Natural Hazards and Risk*12(1),3381-3408. <https://doi.org/10.1080/19475705.2021.2011791>

Achu, A. L., Joseph, S., Aju, C. D., & Mathai, J. (2021). Preliminary analysis of a catastrophic landslide event on 6 August 2020 at Pettimudi, Kerala State, India. *Landslides*18, 1459–1463. <https://doi.org/10.1007/s10346-020-01598-x>

Ajin, R. S., Nandakumar, D., Rajaneesh, A., Oommen T., Ali, Y. P., & Sajinkumar, K. S. (2022a). The tale of three landslides in the Western Ghats, India: lessons to be learnt. *Geoenvironmental Disasters*9. <https://doi.org/10.1186/s40677-022-00218-1>

Ajin, R. S., Saha, S., Saha, A., Biju, A., Costache, R., & Kuriakose, S. L. (2022b). Enhancing the accuracy of the REPTree by integrating the hybrid ensemble meta-classifiers for modelling the landslide susceptibility of Idukki district, South-western India. *Journal of the Indian Society of Remote Sensing* 50, 2245-2265. <https://doi.org/10.1007/s12524-022-01599-4>

Akshaya, M., Danumah, J. H., Saha, S., Ajin, R. S., & Kuriakose, S. L. (2021). Landslide susceptibility zonation of the Western Ghats region in Thiruvananthapuram district (Kerala) using geospatial tools: A comparison of the AHP and Fuzzy-AHP methods. *Safety in Extreme Environments* 3, 181–202. <https://doi.org/10.1007/s42797-021-00042-0>

Bui, D. T., Shirzadi, A., Amini, A., Shahabi, H., Al-Ansari, N., Hamidi, S., Singh, S. K., Thai Pham, B., Ahmad, B. B., & Ghazvinei, P. T. (2020). A hybrid intelligence approach to enhance the prediction accuracy of local scour depth at complex bridge piers. *Sustainability*, 12(3). <https://doi.org/10.3390/su12031063>

El Khouli, R. H., Macura, K. J., Barker, P. B., Habba, M. R., Jacobs, M. A., & Bluemke, D.A. (2009). Relationship of temporal resolution to diagnostic performance for dynamic contrast enhanced MRI of the breast. *Journal of Magnetic Resonance Imaging*, 30, 999-1004. <https://doi.org/10.1002/jmri.21947>

Hao, L., Rajaneesh A., van Westen, C., Sajinkumar K. S., Martha, T. R., Jaiswal, P., & McAdoo, B. G. (2020). Constructing a complete landslide inventory dataset for the 2018 monsoon disaster in Kerala, India, for

- land use change analysis. *Earth System Science Data* 12, 2899–2918. <https://doi.org/10.5194/essd-12-2899-2020>
- Jones, S., Kasthurba, A. K., Bhagyanathan, A., & Binoy, B. V. (2021). Landslide susceptibility investigation for Idukki district of Kerala using regression analysis and machine learning. *Arabian Journal of Geosciences* 14. <https://doi.org/10.1007/s12517-021-07156-6>
- Muhammad, A. R., Aguiar, A., & Mendes-Moreira, J (2021). Transportation Mode Detection from GPS data: A Data Science Benchmark study. 2021 IEEE International Intelligent Transportation Systems Conference (ITSC), pp. 3726-3731. <https://doi.org/10.1109/ITSC48978.2021.9564659>
- Nhu, V. H., Janizadeh, S., Avand, M., Chen, W., Farzin, M., Omidvar, E., Shirzadi, A., Shahabi, H., Clague, J. J., Jaafari, A., Mansoorypoor, F., Thai Pham, B., Ahmad, B. B., & Lee, S. (2020). GIS-based gully erosion susceptibility mapping: A comparison of computational ensemble data mining models. *Applied Sciences*, 2020, 10(6). <https://doi.org/10.3390/app10062039>
- Senan, C. P. C., Ajin, R. S., Danumah, J. H., Costache, R., Arabameri, A., Rajaneesh, A., Sajinkumar, K. S., & Kuriakose, S. L. (2022). Flood vulnerability of a few areas in the foothills of the Western Ghats: a comparison of AHP and F-AHP models. *Stochastic Environmental Research and Risk Assessment*. <https://doi.org/10.1007/s00477-022-02267-2>
- Thomas, A. V., Saha, S., Danumah, J.H., Raveendran, S., Prasad, M. K., Ajin, R. S., & Kuriakose, S. L. (2021). Landslide susceptibility zonation of Idukki district using GIS in the aftermath of 2018 Kerala floods and landslides: a comparison of AHP and frequency ratio methods. *Journal of Geovisualization and Spatial Analysis* 5. <https://doi.org/10.1007/s41651-021-00090-x>
- Vishwakarma, D. K., Ali, R., Bhat, S. A., Elbeltagi, A., Kushwaha, N., Kumar R., Rajput J., Heddham, S., & Kuriqi, A. (2022). Pre- and post-dam river water temperature alteration prediction using advanced machine learning models. *Environmental Science and Pollution Research*. <https://doi.org/10.1007/s11356-022-21596-x>
- Wu, S., Flach, P., Ferri, C. (2007). An improved model selection heuristic for AUC. In: Kok, J. N., Koronacki, J., Mantaras, R. L. d., Matwin, S., Mladenič, D., & Skowron, A. (Eds) *Machine Learning: ECML 2007*. ECML 2007. Lecture Notes in Computer Science, vol 4701. Springer, Berlin, Heidelberg. [https://doi.org/10.1007/978-3-540-74958-5\\_44](https://doi.org/10.1007/978-3-540-74958-5_44)



## 5<sup>th</sup> Intercontinental Geoinformation Days

igd.mersin.edu.tr



### Landslide susceptibility assessment employing machine learning ensemble models: a study in the most severely battered district of the Southern Western Ghats

Rajendran Shobha Ajin<sup>\*1</sup>, Hamza Vijith<sup>1</sup>, Megha Krishna Prasad<sup>2</sup>, Jayan Bindu Jibitha<sup>3</sup>, Romulus Costache<sup>4,5,6</sup>

<sup>1</sup>Kerala State Emergency Operations Centre (KSEOC), Kerala State Disaster Management Authority (KSDMA), Thiruvananthapuram, Kerala, India

<sup>2</sup>Bharathidasan University, Department of Remote Sensing, Tiruchirappalli, Tamil Nadu, India

<sup>3</sup>University of Kerala, Department of Environmental Sciences, Thiruvananthapuram, Kerala, India

<sup>4</sup>National Institute of Hydrology and Water Management, Bucharest, Romania

<sup>5</sup>Department of Civil Engineering, Transilvania University of Brasov, Brasov, Romania

<sup>6</sup>Danube Delta National Institute for Research and Development, Tulcea, Romania

#### Keywords

GIS  
Idukki  
Landslides  
Machine learning  
REPTree  
Western Ghats

#### Abstract

Landslides are one of the natural catastrophes which are frequently reported in the Western Ghats region and result in severe loss. This modelling intends to demarcate susceptible zones in one of the most impacted districts in the southern Western Ghats. Idukki, being the worst affected district, reported more than 2000 landslides in the year 2018. Two machine learning ensemble models and geoinformation techniques have been employed to identify the susceptibility. Twelve landslide conditioning factors have been utilized for this study. The ROC curve-based validation technique ascertained good and fair prediction capability for the created maps, with AUC scores of 0.821 and 0.776 for the MB-REPTree and AB-REPTree models, respectively. From the validation scores, it is found that the MB-REPTree model is more efficient and of good operational use. The study found 7.81% of the district as very highly susceptible and 16.06% as highly susceptible. So, this study suggests that the MB-REPTree model is the best model to demarcate susceptible zones, not just in the Western Ghats but also in other places with similar climatic and terrain conditions.

#### 1. Introduction

The Western Ghats region of Kerala has been severely battered by landslides, especially during the 2018 monsoon season (Ajina et al. 2022a; Ajina et al. 2022b; Hao et al. 2020; Thomas et al. 2021). A total of 4728 landslides have been reported in Kerala in the year 2018 alone (Hao et al. 2020). The Pettimudi disaster, which resulted in the deaths of 70 people (Achu et al. 2021), was the most disastrous, with the highest death toll reported in Kerala, followed by the Kavalappara disaster with 59 deaths (Ajina et al. 2022a). According to the landslide incidence data collected from the Bhukosh portal (<https://bhukosh.gsi.gov.in/Bhukosh/Public>) of the Geological Survey of India (GSI), Idukki district witnessed 1304 landslides during the 2018 monsoon (Ajina et al. 2022b; Thomas et al. 2021). Recent studies revealed that apart from heavy downpour, development

activities and unplanned modification of hill slopes were the major causes of landslides in Idukki district (Abraham et al. 2019, 2021; Ajina et al. 2022b). This underlines the need for a susceptibility map that is validated by employing efficient statistical methods and verified incidence data.

This research is an attempt to identify landslide susceptible zones in Idukki district employing two machine learning (ML) ensemble models such as AdaBoost Reduced-Error Pruning Tree (AB-REPTree) and MultiBoost Reduced-Error Pruning Tree (MB-REPTree) and to assess the efficacy of these models to identify the best model among these two. The analysis used twelve conditioning factors that can induce landslides, including slope, distance from the road, curvature, lineament density, topographic position index (TPI), soil types, lithology, land use/land cover (LULC), stream power index (SPI), aspect, elevation, and rainfall.

#### \* Corresponding Author

(ajinares@ieee.org) ORCID ID 0000-0003-3073-4390  
(vijithh@gmail.com) ORCID ID 0000-0002-1064-2088  
(meghakprasad99@gmail.com) ORCID ID 0000-0002-9890-1207  
(jibithajb@gmail.com) ORCID ID 0000-0001-9748-300X  
(romuluscostache2000@yahoo.com) ORCID ID 0000-0002-6876-8572

#### Cite this study

Ajina RS, Vijith H, Prasad MK, Jibitha JB, & Costache R (2022). Landslide susceptibility assessment employing machine learning ensemble models: a study in the most severely battered district of the Southern Western Ghats. 5<sup>th</sup> Intercontinental Geoinformation Days (IGD), 26-29, Netra, India

## 2. Method

### 2.1. Study Area

Idukki, Kerala's second-largest district, is covered by forests on more than half of its land (Abraham et al. 2019). This hilly district is located in the Western Ghats region and has a total area of 4358 km<sup>2</sup> (Abraham et al. 2021). The main landforms are structural and denudational hills, as well as some mountains that are higher than 2000 metres (Abraham et al. 2021). Figure 1 depicts the location of the study area.

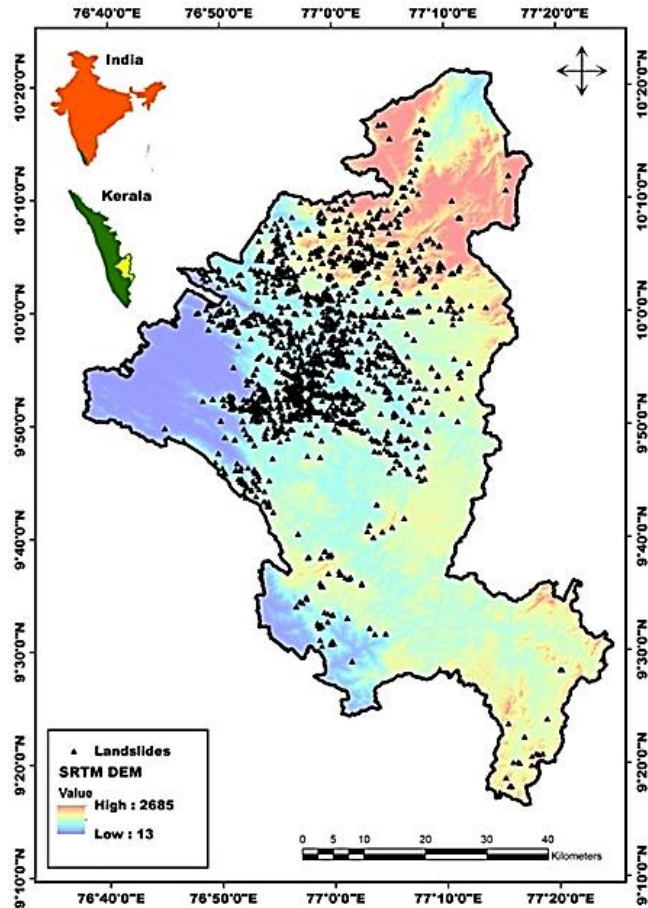


Figure 1. Location of the study area

### 2.2. Construction of landslide inventory

This study has utilized the landslide inventory created by Hao et al. (2020), which comprises 2219 landslides. The data has been split into training (80%) and validation (20%) datasets (Gautam et al. 2021). The training dataset comprises 1775 landslide locations and the validation dataset comprises 444 landslide locations, respectively.

### 2.3. Derivation of factors

The factors such as slope, aspect, and elevation were derived from the SRTM DEM utilizing the ArcGIS 10.4 spatial analyst tools. The curvature, SPI, and TPI were derived from the DEM by employing spatial analyst and raster calculator tools. The soil types were extracted from the map published by the National Bureau of Soil Survey and Land Use Planning (NBSS&LUP), whereas the

lithology and lineaments were derived from the map published by the GSI. The line density tool in ArcGIS was used to compute the lineament density. The LULC types were extracted from the Landsat 8 OLI images using ERDAS Imagine 9.1 software. The road networks were extracted from the topographic map and Google Earth, and the Euclidean distance tool was used to derive the distance from the road layer. The rainfall distribution was extracted from the World Climate Report portal (<https://www.worldclim.org/>). The R 4.2.1 software was utilized for computing the weights. The landslide susceptibility of the district is categorized into five zones employing the Natural Breaks method (Babitha et al. 2022).

### 2.4. REPTree model

The reduced-error pruning tree (REPTree) is an ensemble model of the decision tree (DT) and reduced error pruning (REP) techniques that is used to generate a DT model by reducing the variance and can successfully manage missing data (Bui et al. 2020; Vishwakarma et al. 2022). It utilizes information gain ratio (IGR) values to construct a regression/decision tree and employs reduced-error pruning to prune the tree (Al Snousy et al. 2011). The IGR values were computed by applying Equation 1 and the entropy (E) function (Bui et al. 2020).

$$IGR(x, S) = \frac{E(S) - \sum_{i=1}^n \frac{E(S_i) |S_i|}{|S|}}{-\sum_{i=1}^n \frac{|S_i|}{|S|} \log_2 \frac{|S_i|}{|S|}} \quad (1)$$

Where S = training dataset,  $S_i$  = subset ( $i = 1, 2, 3, \dots, n$ ), E = entropy function

### 2.5. AB-REPTree model

AdaBoost (AB) is an ensemble approach that performs boosting, which integrates weak classifiers in series to produce a strong classifier, and trains and deploys trees in series (Misra and Li 2020). AB reduces variance and bias (Jukic et al. 2020), but it performs poorly in noisy environments and takes longer to train (Misra and Li 2020). The weights were computed by applying Equation 2 (Wang et al. 2021).

$$F_n(x) = F_{m-1}(x) + \underset{i=1}{\operatorname{argmin}_h} \sum_{i=1}^n L(y_i | F_{m-1}(x_i) + h(x_i)) \quad (2)$$

where  $F_n(x)$  is the overall model,  $F_{n-1}(x)$  is the overall obtained in the previous round,  $y_i$  is the prediction result of the  $i$ -th tree, and  $h(x_i)$  is the newly added tree (Wang et al. 2021).

### 2.6. MB-REPTree model

MultiBoost (MB) is an ensemble model of AdaBoost and Bagging, and can reduce both bias and variance, thereby reducing the errors to a greater extent (Webb 2000, 2011). The base classifier errors were computed employing Equation 3 (Shirzadi et al. 2018).

$$e = \frac{\sum_{x_j \in S', C_t(x_j) \neq y_j} \text{weight}(x_j)}{m} \quad (3)$$

where  $e$  = errors of base classifiers,  $S'$  = dataset; and  $x_j$  and  $y_j$  = elements of datasets (Shirzadi et al. 2018).

## 2.7. Validation of the models

The created maps were validated by employing the ROC curve technique (Metz 1978) and the validation dataset. The AUC scores between 0.5-0.6, 0.6-0.7, 0.7-0.8, 0.8-0.9, and 0.9-1.0 depict failure, poor, fair, good, and excellent prediction capabilities, respectively (Lüdemann et al. 2006). The IBM SPSS Statistics 23.0 software was utilized for creating the ROC curves and determining the AUC scores.

## 3. Results

The landslide susceptibility maps created employing two different ML ensemble models are depicted in Figure 2. The validation of the models revealed that the MB-REPTree model (0.821, or 82.1%) has a better prediction capability than the AB-REPTree model (0.776, or 77.6%) (Figure 3). According to the MB-REPTree model, a total of 7.81% of the district is categorized as a very high-susceptible zone. The percentage of each susceptible zone is depicted in Table 1.

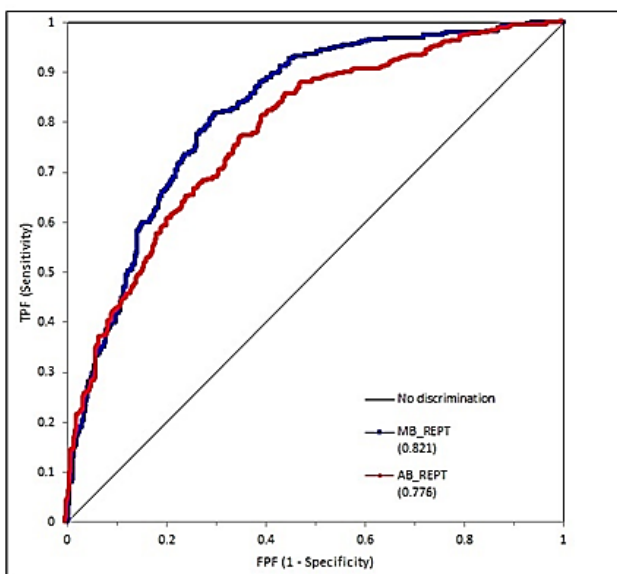


Figure 3. The ROC curves

## 4. Conclusion

This study effectively categorized the landslide susceptible zones in Idukki district utilizing ML ensemble models and identified the MB-REPTree model as the best model among these two models. The created maps will help decision makers and officials of the emergency management department implement ideal mitigation measures that will help in reducing disaster risks in the future. Also, these types of validated susceptibility maps will help find important buildings and infrastructure that are in critical zones.

Table 1. Percentage of landslide susceptible zones

Susceptible zones	Percentage of susceptible zones	
	AB-REPTree	MB-REPTree
Very low	10.08	21.49
Low	27.41	32.32
Moderate	30.76	22.32
High	21.66	16.06
Very high	10.09	7.81
<b>Total</b>	<b>100</b>	<b>100</b>

## References

- Abraham, M. T., Pothuraju, D., & Satyam, N. (2019). Rainfall thresholds for prediction of landslides in Idukki, India: An empirical approach. *Water*, 11(10). <https://doi.org/10.3390/w11102113>
- Abraham M. T., Satyam, N., Shreyas, N., Pradhan, B., Segoni, S., Maulud, K. N. A., & Alamri, A. M. (2021). Forecasting landslides using SIGMA model: a case study from Idukki, India. *Geomatics, Natural Hazards and Risk*, 12(1), 540-559. <https://doi.org/10.1080/19475705.2021.1884610>
- Achu, A. L., Joseph, S., Aju, C. D., & Mathai, J. (2021). Preliminary analysis of a catastrophic landslide event on 6 August 2020 at Pettimudi, Kerala State, India. *Landslides*, 18, 1459-1463. <https://doi.org/10.1007/s10346-020-01598-x>
- Ajin, R. S., Nandakumar, D., Rajaneesh, A., Oommen, T., Ali, Y. P., & Sajinkumar, K. S. (2022a). The tale of three landslides in the Western Ghats, India: lessons to be learnt. *Geoenvironmental Disasters*, 9. <https://doi.org/10.1186/s40677-022-00218-1>
- Ajin, R. S., Saha, S., Saha, A., Biju, A., Costache, R., & Kuriakose, S. L. (2022b). Enhancing the accuracy of the REPTree by integrating the hybrid ensemble meta-classifiers for modelling the landslide susceptibility of Idukki district, South-western India. *Journal of the Indian Society of Remote Sensing* 50, 2245-2265. <https://doi.org/10.1007/s12524-022-01599-4>
- Al Snousy M. B., El-Deeb, H. M., Badran, K., & Al Khilil, I. A. (2011). Suite of decision tree-based classification algorithms on cancer gene expression data. *Egyptian Informatics Journal*, 12(2), 73-82. <https://doi.org/10.1016/j.eij.2011.04.003>
- Babitha, B. G., Danumah, J. H., Pradeep, G. S., Costache, R., Patel, N., Prasad, M. K., Rajaneesh, A., Mammen, P. C., Ajin, R. S., & Kuriakose, S. L. (2022). A framework employing the AHP and FR methods to assess the landslide susceptibility of the Western Ghats region in Kollam district. *Safety in Extreme Environments* 4, 171-191. <https://doi.org/10.1007/s42797-022-00061-5>
- Bui, D. T., Shirzadi, A., Amini, A., Shahabi, H., Al-Ansari, N., Hamidi, S., Singh, S. K., Pham, B. T., Ahmad, B. B., & Ghazvinei, P. T. (2020) A hybrid intelligence approach to enhance the prediction accuracy of local scour depth at complex bridge piers. *Sustainability*, 12(3). <https://doi.org/10.3390/su12031063>

- Gautam, P., Kubota, T., Sapkota, L. M., & Shinohara, Y. (2021). Landslide susceptibility mapping with GIS in high mountain area of Nepal: a comparison of four methods. *Environmental Earth Sciences* 80. <https://doi.org/10.1007/s12665-021-09650-2>
- Hao, L., Rajaneesh A., van Westen, C., Sajinkumar K. S., Martha, T. R., Jaiswal, P., & McAdoo, B. G. (2020). Constructing a complete landslide inventory dataset for the 2018 monsoon disaster in Kerala, India, for land use change analysis, *Earth System Science Data*, 12, 2899–2918. <https://doi.org/10.5194/essd-12-2899-2020>
- Jukic, S., Saracevic, M., Subasi, A., & Kevric, J. (2020). Comparison of ensemble machine learning methods for automated classification of focal and non-focal epileptic EEG signals. *Mathematics*, 8(9). <https://doi.org/10.3390/math8091481>
- Lüdemann, L., Grieger, W., Wurm, R., Wust, P., & Zimmer, C. (2006). Glioma assessment using quantitative blood volume maps generated by T1-weighted dynamic contrast-enhanced magnetic resonance imaging: a receiver operating characteristic study. *Acta Radiologica*, 47(3), 303-310. <https://doi.org/10.1080/0284185050053>
- Metz, C. E. (1978). Basic principles of ROC analysis. *Seminars in Nuclear Medicine*, 8(4), 283-298. [https://doi.org/10.1016/S0001-2998\(78\)80014-2](https://doi.org/10.1016/S0001-2998(78)80014-2)
- Misra, S., & Li, H. (2020). Chapter 9 - Noninvasive fracture characterization based on the classification of sonic wave travel times, In: Misra, S., Li, H., He, J. (Eds) *Machine Learning for Subsurface Characterization*, Gulf Professional Publishing, pp. 243-287. <https://doi.org/10.1016/B978-0-12-817736-5.00009-0>
- Shirzadi, A., Soliamani, K., Habibnejhad, M., Kavian, A., Chapi, K., Shahabi, H., Chen, W., Khosravi, K., Pham, B. T., Pradhan, B., Ahmad, A., Ahmad, B. B., & Bui, D. T. (2018). Novel GIS based machine learning algorithms for shallow landslide susceptibility mapping. *Sensors*, 18(11). <https://doi.org/10.3390/s18113777>
- Thomas, A. V., Saha, S., Danumah, J. H., Raveendran, S., Prasad, M. K., Ajin, R. S., & Kuriakose, S. L. (2021). Landslide susceptibility zonation of Idukki district using GIS in the aftermath of 2018 Kerala floods and landslides: a comparison of AHP and frequency ratio methods. *Journal of Geovisualization and Spatial Analysis* 5. <https://doi.org/10.1007/s41651-021-00090-x>
- Vishwakarma, D. K., Ali, R., Bhat, S. A., Elbeltagi, A., Kushwaha, N. L., Kumar, R., Rajput, J., Heddarn, S. & Kuriqi, A. (2022). Pre- and post-dam river water temperature alteration prediction using advanced machine learning models. *Environmental Science and Pollution Research*. <https://doi.org/10.1007/s11356-022-21596-x>
- Wang, C., Xu, S., & Yang, J. (2021). Adaboost algorithm in artificial intelligence for optimizing the IRI prediction accuracy of asphalt concrete pavement. *Sensors*, 21(17). <https://doi.org/10.3390/s21175682>
- Webb, G. I. (2000). MultiBoosting: A technique for combining boosting and wagging. *Machine Learning* 40, 159–196. <https://doi.org/10.1023/A:1007659514849>
- Webb, G. I. (2011). MultiBoosting. In: Sammut, C., Webb, G. I. (Eds) *Encyclopedia of Machine Learning*. Springer, Boston, MA. [https://doi.org/10.1007/978-0-387-30164-8\\_567](https://doi.org/10.1007/978-0-387-30164-8_567)

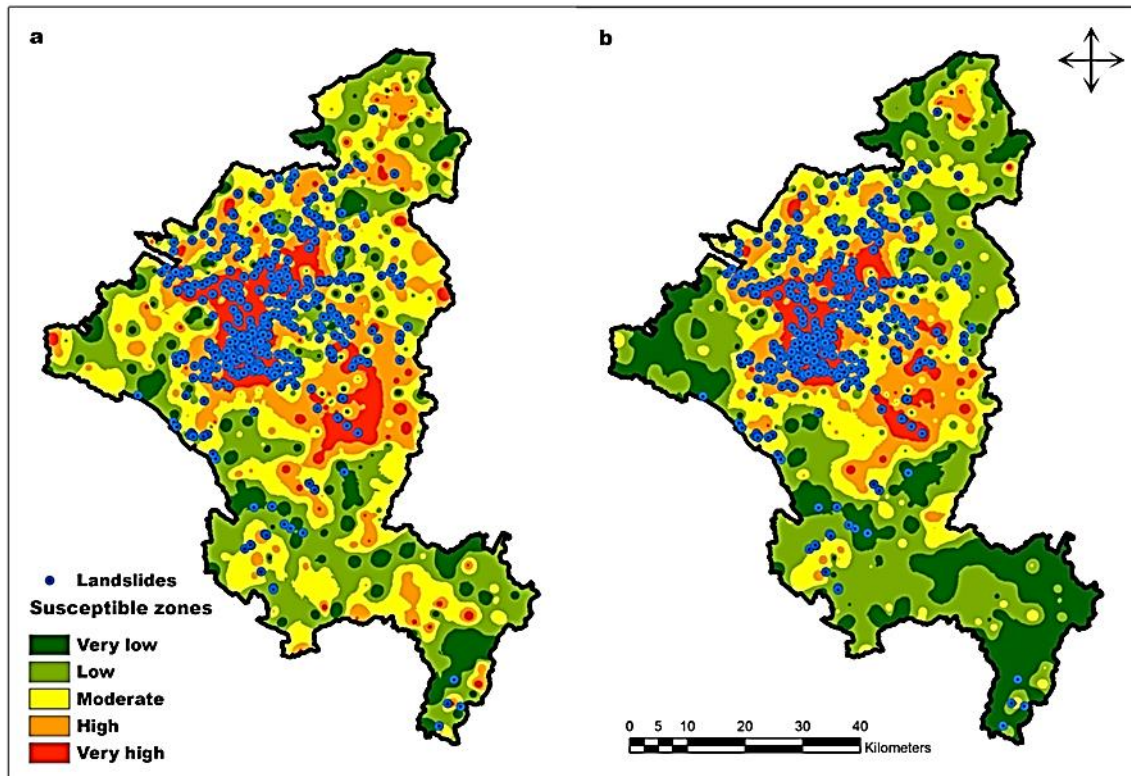


**Figure 2.** Landslide susceptible zones **a.** AB-REPTree model **b.** MB-REPTree model



## 5<sup>th</sup> Intercontinental Geoinformation Days

igd.mersin.edu.tr



### Assessment of variation in water table of Quetta valley of 2010 & 2020

Liaqat Ali \*<sup>1</sup>

<sup>1</sup>Government Post Graduate College, Quetta, Balochistan, Pakistan

#### Keywords

Aquifers  
Groundwater  
ArcGIS

#### Abstract

Groundwater has always been and continues to be an essential source of drinking water in Balochistan. Which is extracted from tube wells. Since the 1970s, the number of tube wells has increased from 5,000 to 40,000. The rapid increase in the number of drillings has caused the water table to drop hundreds of feet deep. So, Assessment of water level variability of aquifers is an important step to explore the appropriate groundwater management. Therefore, this study is designed to assess the variation in water table of Quetta valley of 2010 & 20. This research is done on the basis of statistical analysis using computer based software (ArcGIS and Microsoft office) to detect the change in groundwater level. An overall characterization method has been used on the water table of Quetta valley. The analysis was conducted using groundwater level data from 132 tubewell monitoring sites in Quetta valley of 2010 & 2020. The average water level of tube wells in 2010 was 281 feet while in 2020 it was 372 feet. Both mean values are included in the standard deviation. Where, it turns out that the difference between the two data sets is 64 feet. Maps and graphs were also evaluated by comparing the observed values of groundwater levels of 2010 & 2020. This analysis demonstrates the water table variation of Quetta valley of 2010 & 2020.

#### 1. Introduction

The subsurface border between the soil surface and the region where groundwater (water found in an aquifer) saturates spaces between cracks and sediments in the rock is known as the water table (also known as the water level). At this limit, the water pressure and air pressure are equal. The unsaturated sector of the soil is the area above the water table where water and oxygen enter the spaces between the sediments. Due to the oxygen content of the soil, the unsaturated zone is also known as the area of aeration (the phase of land above the water table, holding air between particles). The saturated area, when water fills all spaces between sediments, is located under the water table. The land surface that is above it has an impact on the height and form of the water table, which rises beneath hills and descends beneath valleys. Even within one location, there might be differences in the water table level. Precipitation variations and excessive groundwater pumping are the main causes of water table instability. (National Geographic Society, 2019).

#### 2. Study Area

At an average elevation of 1680 meters above sea level, the Koi-i-Murdar, Koi-i-Chaltan, and Zarghun mountains encircle the Quetta Valley (figure 2). Due to constant population increase and the influx of Afghan migrants, Quetta is currently experiencing several socio-financial problems. Along with other problems, a major issue in Quetta has been the lack of water, and times of low rainfall would make the situation worse (Zainuddin Kakar, 2018).

#### 3. Method

The research is a “descriptive” type of research, during research several departments of were visited for data collection. Then data was arranged, analyzed and interpreted. The data was collected as secondary and statistical tools were applied for arranging, analyzing and interpreting.

The variation of water table is analyzed statistically, using mean, variance and standard deviation. Further, GIS (Geographic Information System) and excel were used to generate maps, graphs and tables.

\* Corresponding Author

(liaqatali66677@gmail.com) ORCID ID 0000-0001-5955-3302

Cite this study

Ali L, (2022). Assessment of variation in water table of Quetta valley of 2010 & 2020. 5<sup>th</sup> Intercontinental Geoinformation Days (IGD), 30-32, Netra, India

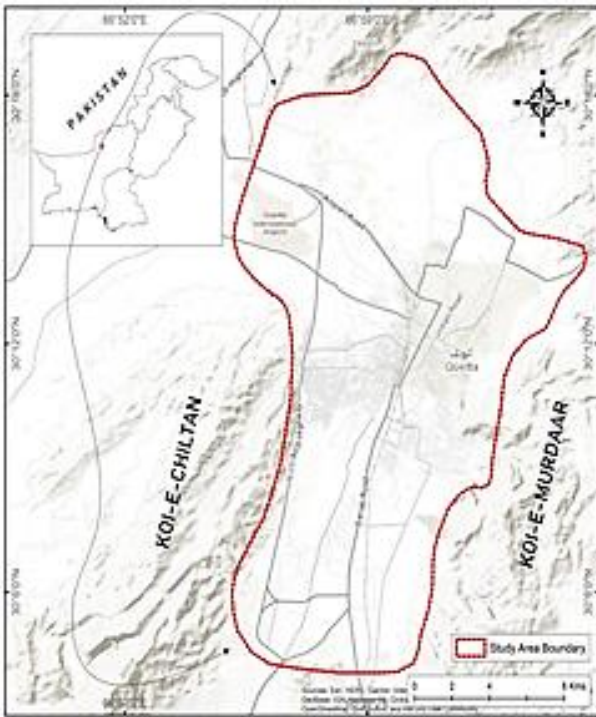


Figure 1. Study area

#### 4. Results

This research titled "Assessment of variation in water table of Quetta valley of 2010 & 2020 " is a descriptive type of research in which data has been collected from WASA, PHE and Irrigation Departments. The data were analyzed and interpreted using statistical methods. Over all 66 tube wells' data in the study area from 2010 to 2020 were analyzed. The average water level of tube wells in 2010 was 281 feet while in 2020 it was 372 feet. Both mean values are included in the standard deviation (in statistics, the standard deviation is a measure of the amount of variation of a set of values). Where, it turns out that the difference between the two data sets is 64.11 feet. The results are also shown on graphs as well as on maps which depict the variations in the water level of the given time period (2010-20).

The results of the study are shown in the Figure 2 and 3.

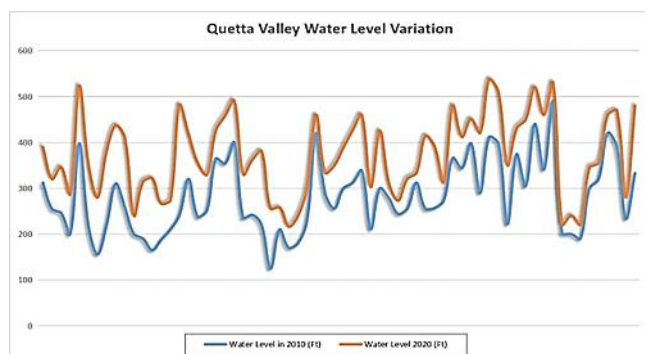


Figure 2. The Line chart showing the variation of water level of Quetta valley from 2010 to 2020 in two separate lines, where the left corner is showing the depth of tube-wells in feet

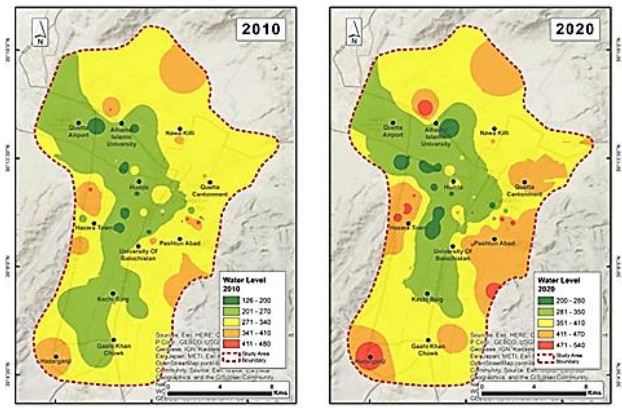


Figure 3. Showing the variation in water level of Quetta valley of 2010 & 2020

#### 5. Conclusion

This research (Assessment of variation in Water Table/Level of Quetta Valley of 2010 & 2020) is completed on the basis of statistical analysis and computer based softwares to achieve the objective set for the study. The analysis was conducted using groundwater level data from 66 tube-well monitoring sites in Quetta Valley from 2010 to 2020. The statistical calculation such as Standard Deviation, Variance and Mean have been used to detect the variation of water level, also some maps and graphs were drawn using ArcGIS and Excel by comparing the observed values of groundwater levels from 2010 to 2020. This analysis demonstrated the water table variation of Quetta Valley from 2010 to 2020. And finally, came to result by using the Mean values of 2010 data set and 2020 data set, and putting the values in standard deviation, which gave the result of 64. Thus, the variation in water table/level of Quetta valley from 2010 to 2020 is 64 feet.

#### Acknowledgement

First and foremost, we would like to praise Allah the Almighty, the Most Gracious, and the Most Merciful for His blessing given to me and my group-mates during my study and in completing this thesis. May Allah's blessing goes to His final Prophet Muhammad (peace be up on him), his family and his companions.

We wish to express hearty gratitude to our supervisor Prof Bashir Ahmed Sumelani for his continuous encouragement, guidance and supervision throughout this study. Also, thanks to all the professors of the staff of Geography Department Prof Tariq Baloch, Prof Muhammad Iqbal, Prof Ismail Jamote, Prof Rahat Ullah and Prof Muhammad Rafiq Ahmed who have taught us in the BS program and helped us step by step due to which we were able to complete the BS program.

#### References

Aftab, S. M., Siddiqui, R. H., & Farooqui, M. A. (2018, September). Strategies to Manage Aquifer Recharge in Balochistan, Pakistan: An Overview. In *IOP Conference Series: Materials Science and*

- Engineering* (Vol. 414, No. 1, p. 012023). IOP Publishing.
- Ashraf, M. (2020). Groundwater Management in Balochistan, Pakistan.
- Damkjaer, S., & Taylor, R. (2017). The measurement of water scarcity: Defining a meaningful indicator. *Ambio*, 46(5), 513-531.
- Lenzen, M., Moran, D., Bhaduri, A., Kanemoto, K., Bekchanov, M., Geschke, A., & Foran, B. (2013). International trade of scarce water. *Ecological Economics*, 94, 78-85.
- Majeed, A. (2000). Natural and artificial recharge techniques for Baluchistan. *IUCN Balochistan programme, water programme document series* [http://www. waterinfor. net. pk/pdf/nartb. pdf](http://www.waterinfor.net.pk/pdf/nartb.pdf).
- Nieuwoudt, W. L., Backeberg, G. R., & Du Plessis, H. M. (2004). The value of water in the South African economy: Some implications. *Agrekon*, 43(2), 162-183.
- Shatanawi, M., & Naber, S. (2011). Valuing water from social, economic and environmental perspective. *Dialogues on Mediterranean Water Challenges: Rational Water Use, Water Price Versus Value and Lessons Learned from The European Water Framework Directive*.
- Van Steenberg, F., Kaisarani, A. B., Khan, N. U., & Gohar, M. S. (2015). A case of groundwater depletion in Balochistan, Pakistan: Enter into the void. *Journal of Hydrology: Regional Studies*, 4, 36-47.
- Veldkamp, T. I., Wada, Y., de Moel, H., Kummu, M., Eisner, S., Aerts, J. C., & Ward, P. J. (2015). Changing mechanism of global water scarcity events: Impacts of socioeconomic changes and inter-annual hydro-climatic variability. *Global Environmental Change*, 32, 18-29.
- Walter, T., Kloos, J., & Tsegai, D. W. (2010). Improving water use efficiency under worsening scarcity: Evidence from the Middle Olifants sub-basin in South Africa.
- Yin, Y., Tang, Q., Liu, X., & Zhang, X. (2017). Water scarcity under various socio- economic pathways and its potential effects on food production in the Yellow River basin. *Hydrology and Earth System Sciences*, 21(2), 791-804.



## 5<sup>th</sup> Intercontinental Geoinformation Days

igd.mersin.edu.tr



### Content analysis of real estate valuation courses taught in the relevant departments of vocational schools in Turkey

Nuri Erdem\*<sup>1</sup>

<sup>1</sup>Osmaniye Korkut Ata University, Engineering Faculty, Department of Geomatics, Osmaniye, Türkiye

#### Keywords

Vocational Schools  
Real Estate Valuation  
Course  
Course Content Analysis

#### Abstract

The value of real estate is used directly or indirectly in many applications. These practices are primarily taxation, expropriation, management of immovables, establishment of rights and similar practices. These practices are carried out by institutions based on the methods defined in the relevant legislation. Real estate valuation is a field that constantly renews itself depending on technical and legal developments. Therefore, more competent valuation experts are needed in the sector. At this point, the importance of the real estate valuation course taught in vocational colleges of universities in order to improve the quality and scope of real estate appraisal education is increasing. Meeting the needs in the sector and training new real estate appraisers depend on the quality of the training provided. In this study; The content analysis of the real estate valuation courses taught in the relevant programs of vocational schools is made, the importance of being up-to-date on the topics covered is revealed, and the place and importance of the education in the field of real estate valuation is emphasized.

#### 1. Introduction

The Turkish Language Association (TDK) defines the concept of real estate as “house, field, etc. immovable property, real estate” (TDK, 2022). According to another definition, real estate; it is the name given as a whole with the land and the buildings on it (FIG, 1995). It is the general name of immovable property, property, land, field, house, garden. Real estate in the International Valuation Standards (IVS) Book published by the International Valuation Standards Committee (IVSC); Land and everything that is a natural part of the land such as trees, mines, as well as anything made by humans such as buildings and improvement works are defined as the land itself, which is a physical entity, or as artificial structures built on this land. It also defines real estate as anything tangible that can be seen or touched, with all its additions above or below the ground (IVSC, 2005). Real estate valuation in general; It can be defined as the estimation of the probable value of a real estate, real estate project or the rights and benefits attached to the real estate on the valuation day, based on independent, impartial and objective criteria (Açlar and Çağdaş, 2008). Real estate valuation is a multidimensional process that requires examining many factors together. This situation requires the expert to analyze and interpret a complex structure from a technical and legal perspective. The

business known as real estate valuation and real estate valuation in the 1980s, today comes to the fore more with the name of real estate valuation. While most of the companies that make real estate valuation work under the name of real estate valuation and consultancy, some of them work under the name of real estate valuation and consultancy. It is necessary to strengthen the technical and legal infrastructure for real estate valuation expertise. For this, universities have important duties (Erdem, 2018).

In this study, a general evaluation of the courses on real estate valuation taught in different departments of universities in vocational schools was made and the course contents were analyzed. As a result of the analysis, solution suggestions were presented to increase the quality of education.

The study was conducted in an analysis style within the scope of the curriculum, application methods and criteria of real estate valuation courses taught in different departments of vocational schools. With this study, it is aimed to contribute to the business life after graduation and transitions between universities by renewing the application infrastructure and course curricula in vocational schools of universities providing real estate valuation education in accordance with the real estate valuation sector. It is also important in terms

\* Corresponding Author

<sup>\*</sup>(nurierdem@osmaniye.edu.tr) ORCID ID 0000-0002-1850-4616

Cite this study

Erdem N (2022). Content analysis of real estate valuation courses taught in the relevant departments of vocational schools in Turkey. 5<sup>th</sup> Intercontinental Geoinformation Days (IGD), 33-36, Netra, India.

of training valuation personnel suitable for the needs of the sector.

## 2. Method

First of all, from the guide booklet published by the Higher Education Institution (YÖK) every year, it was researched which university and vocational school had departments such as Map and Cadastre, Land Registry and Cadastre, Real Estate and Real Estate Management. Then, by entering the web pages of the relevant vocational schools, it was checked whether there were courses related to real estate valuation from the course information package pools of the programs. The following tables contain the names of the courses and related vocational schools (Tables 1, 2, 3).

**Table 1. Map and Cadastre Program**

University Name	Vocational School Name	Course Name*
Adıyaman	Kahta	Real Estate Valuation
Kocatepe	Uzaktan Eğit.	"
Afyon Kocatepe	Emirdağ	"
Amasya	Teknik Bilimler	"
Hacettepe	Başkent OSB Teknik Biliml.	"
Akdeniz	Teknik Bilimler	"
Çoruh	Artvin	"
Balıkesir	Bigadiç	"
Mehmet Akif Ersoy	Göhlisar	"
Uludağ	Gemlik Asım K.	"
Bursa Uludağ	İznic	"
Elâzığ Fırat	Sivrice	"
Binalı Yıldırım	MYO	"
Giresun	Teknik Bilimler	"
Isparta Uygulamalı Bilimler	Teknik Bilimler	"
Isparta Uygulamalı Bilimler	Uluborlu	"
İstanbul Okan	Selahattin Karasoy	"
İzmir Dokuz Eylül	MYO	"
Sütçü İmam	İzmir	"
Kayseri	Göksun	"
Ahi Evran	Tomarza	"
Selçuk	Mustafa Akıncioğlu	"
Selçuk	Kaman	"
Selçuk	Kadınhanı Faik İçil	"
Selçuk	Taşkent	"
Selçuk	Hadim	"
Teknik	Güneysınır	"
Turgut Özal	Teknik Bilimler	"
Celal Bayar	Darende Bekir İlicak	"
Celal Bayar	Sarıgöl	"
Artuklu	Köprübaşı	"
Mersin	Savur	"
Sitki Koçman	Teknik Bilimler	"
Samsun	Yatağan	"
Siirt	Kavak	"
Korkut Ata	Eruh	"
Avrasya	Osmaniye	"
Sinop	MYO	"
Bülent Ecevit	Boyabat	"
Karamanoğlu	Zonguldak	"
Mehmet Bey	Teknik Bilimler	"
Hakkâri	Çömerik	"

**Table 2. Land Registry and Cadastre Program**

University Name	School Name	Course Name*
Ankara Hacı Bayram Veli	Polatlı	Real Estate Financing and Valuation
Niğde Ömer Halis Demir	Bor	Real Estate Valuation I
Aydın Adnan Menderes	Atça	Real Estate Valuation
Manisa Celal Bayar	Sarıgöl	Real Estate Valuation
Mehmet Akif Ersoy	Göhlisar	Real Estate Valuation
Pamukkale	Çayeli	Real Estate Valuation
Gaziosmanpaşa	Zile	Real Estate Valuation
Bartın	Ulus	Real Estate Valuation
Niğde Ömer Halis Demir	Bor	Real Estate Valuation II
Çorum Hitit	Osmancık Ömer Derindere	Real Estate Valuation
Bitlis Eren	Teknik Bilimler	Real Estate Valuation
Yozgat Bozok	Şefaati	Real Estate Valuation
Uşak	Sivaslı	Real Estate Valuation
Elâzığ Fırat	Karakoçan	Real Estate Valuation
Dumlupınar	Hisarcık	Real Estate Valuation
Artvin Çoruh	Ardanuç	Real Estate Valuation

**Table 3. Real Estate and Real Estate Management Program**

University Name	School Name	Course Name*
İstanbul	Sosyal Bilimler	Real Estate Valuation Methods
Cerrahpaşa	Bilimler	Real Estate Valuation Methods
Kocaeli	Ali Rıza Veziroğlu	Real Estate Valuation Techniques
Adana	Adana	Real Estate Valuation Techniques
Çukurova	Adana	Real Estate Valuation Techniques
Aydın Adnan Menderes	Yenipazar	Real Estate Valuation Principles
Sakarya	Geyve	Real Estate Valuation Principles
Uygulamalı Bilimler		Real Estate Valuation Principles
Samsun 19 Mayıs	Havza	Real Estate Valuation Techniques
Denizli	Çivril Atasay	Real Estate Valuation Techniques
Pamukkale	Kamer	Real Estate Valuation Techniques

In the Tables 4, 5 6, the ECTS credits and course type information of the Map and Cadastre, Land Registry and Cadastre, Real Estate and Property Management programs in the vocational schools of the universities are given. The necessary information was obtained from the current course information package pool of the universities and by e-mails sent to vocational schools or by contacting vocational schools directly.

**Table 4.** Map and Cadastre Program ECTS Credits and Course Type Information

University Name	School Name	C	E	T	U	Z	S
		R	C	H			
		E	T	E			
		D	S	O			
		I		R			
		T		Y			
Adıyaman	Kahta	2	3	2	1	-	+
Kocatepe	Uzaktan Eğit.	2	4	2	0	-	+
Afyon Kocatepe	Emirdağ	2	4	2	0	-	+
Amasya	Tekn. Biliml.	2	4	2	0	-	+
Hacettepe	Başkent OSB	2	3	2	0	-	+
Akdeniz	Tek. Bilimler	2	3	2	0	-	+
Çoruh	Artvin	2	2	2	0	+	-
Balikesir	Bigadiç	2	3	2	0	-	+
Mehmet Akif	Göhlisar	2	4	2	0	+	-
Uludağ	Gem. Asım K.	3	3	3	0	+	-
Bursa Uludağ	İznik	2	3	2	2	+	-
Elâzığ Fırat	Sivrice	2	3	2	2	+	-
Binali Yıldırım	MYO	3	3	3	0	-	+
Giresun	Teknik Bilimler	2	4	2	0	-	+
Isparta	Teknik Bilimler	4	3	4	0	-	+
Isparta	Uluborlu	2	3	2	1	-	+
Okan	MYO	2	3	2	1	-	+
Dokuz Eylül	İzmir	3	6	3	0	+	-
Sütçü İmam	Göksun	3	4	3	0	-	+
Kayseri	Tomarza	3	3	3	0	-	+
Ahi Evran	Kaman	2	2	2	0	-	+
Selçuk	Kadınhanı Faik	3	3	3	0	-	+
Selçuk	Taşkent	4	4	4	0	-	+
Selçuk	Hadim	4	4	4	0	-	+
Selçuk	Güneysınır	4	4	4	0	-	+
Teknik	Teknik Bilimler	4	4	4	0	-	+
Turgut Özal	Darende Bekir	4	4	4	0	-	-
Celal Bayar	Sarıgöl	2	3	2	0	-	+
Celal Bayar	Köprübaşı	2	2	2	0	-	+
Artuklu	Savur	2	2	2	0	-	+
Mersin	Teknik Bilimler	3	3	3	0	+	-
Sitki Koçman	Yatağan	2	2	2	0	-	+
Samsun	Kavak	2	3	2	0	-	+
Siirt	Eruh	3	4	3	0	+	-
Korkut Ata	Osmaniye	2	4	2	0	+	-
Avrasya	MYO	3	3	2	1	-	+
Sinop	Boyabat	3	3	3	0	-	+
Bülent Ecevit	Zonguldak	2	4	2	0	-	+
Karamanoğlu	Teknik Bilimler	3	3	3	0	-	+
Mehmet Bey		3	3	3	0	-	+
Hakkâri	Çömerik	3	3	2	0	-	+

### 3. Results

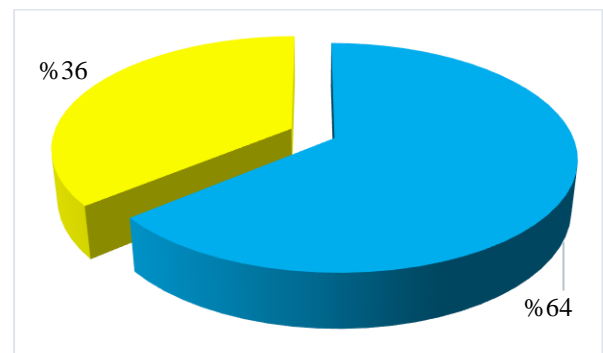
Real estate valuation courses show a similarity of 64%. In this context, it can be said that the 36% difference in the course contents is due to the wide scope of the real estate valuation and the course being given within the framework of different purposes (Figure 1). In addition, it can be said that the application methods in universities are different and the course is tried to be shaped according to today's conditions. While creating the graph, the subjects in the content part of the course were obtained as a percentage based on vocational schools.

**Table 5.** Land Registry and Cadastre Program ECTS Credits and Course Type Information

University Name	School Name	C	E	T	U	Z	S
Ankara Hacı Bayram Veli	Polatlı	2	2	2	0	-	+
Adnan Menderes	Atça	3	3	2	1	-	+
Ömer Halis Demir	Bor	2	2	2	0	+	-
Ömer Halis Demir	Bor	2	2	2	0	+	-
Celal Bayar	Sarıgöl	3	4	3	0	+	-
Mehmet Akif Ersoy	Göhlisar	2	3	2	0	+	-
Pamukkale	Çayeli	2	4	2	0	-	+
Gaziosmanpaşa	Zile	3	3	3	0	-	+
Bartın	Ulus	2	2	2	0	-	+
Çorum Hitit	Osmancık Ömer	2	3	2	0	-	+
Bitlis Eren	Derindere Teknik Bilimler	3	3	3	0	-	+
Yozgat Bozok	Şefaati	3	3	3	0	-	+
Uşak	Sivash	2	3	2	0	+	-
Elâzığ Fırat	Karakoçan	2	3	2	0	+	-
Artvin Çoruh	Ardanuç	3	3	3	0	+	-
Kütahya Dumlupınar	Hisarcık	3	4	3	0	-	+

**Table 6.** Real Estate and Real Estate Management Program ECTS Credits and Course Type Information

University Name	School Name	C	E	T	U	Z	S
İstanbul	Sosyal	3	3	3	0	+	-
Cerrahpaşa	Bilimler						
Adana	Adana	3	5	3	1	+	-
Çukurova							
Kocaeli	Ali Rıza Veziroğlu	3	3	2	1	+	-
Aydın Adnan Menderes	Yenipazar	3	3	2	1	+	-
Sakarya	Geyve	3	3	2	0	+	-
Uygulamalı Bilimler							
Denizli	Çivril Atasay	4	4	4	0	+	-
Pamukkale	Kamer						
Samsun 19 Mayıs	Havza	4	7	3	1	+	-

**Figure 1.** Content of the Course Similarity Difference Graph

While creating the similarity graph for the purpose of teaching the course, the percentage ratio was calculated by numbering according to the universities. When the aim of the lesson was examined, it was observed that there was a similarity of about 66% and a difference of 34%. Educational planning of universities is the leading factor in the formation of this difference. As a result of the

examinations, it can be said that the aim of the course and its content differ due to the same reasons (Figure 2).

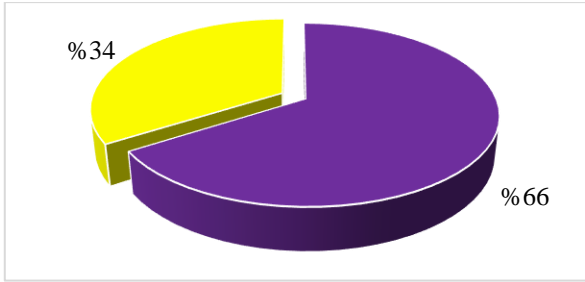


**Figure 2.** Course Objective Similarity Difference Graph

In Figure 3, the graph created as a result of the percentage ratio of the references used by vocational schools in real estate valuation training is given. When the graph is examined, the most preferred reference in vocational schools is "Açlar A., Çağdaş V, Immovable (Real Estate) Valuation for Engineers, Architects and Experts, TMMOB, HKMO Publications". 34% of Vocational Schools use this reference. It can be said that this reference has an important place in real estate valuation education. Apart from this reference, 13% of the lecturers of the related lecturer or the Valuation of Real Estate, Prof. Dr. Erol Kokturk, Dr. Erdal Köktürk uses its reference, and 40% uses other references (Figure 3).

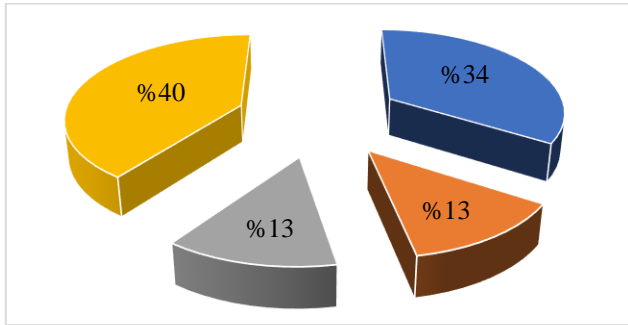


**Figure 3.** Graph of Utilized Resources

#### 4. Conclusion

Real estate valuation process, rural area regulation, GIS, advanced mathematics, real estate law, etc. It is a multi-disciplinary study. For this reason, the training provided should be comprehensive. For example, real estate valuation courses should be given especially in the last semester and the infrastructure should be strengthened in this way. In addition, real estate valuation issues are in compliance with the CMB Licensing Exam. In addition to theoretical education, practical education should be given and various projects, seminars, report samples and assignments should be

organized in the field of application. Students should be encouraged and informed during training and internships in vocational schools. Real estate valuation is not a field that can only be explained with the theoretical education given at the university, so a better understanding of the course can be achieved with the field work to be done in the applied education given at the schools. The real estate appraisal course is mostly an elective course in vocational schools. In this context, considering the importance of the course, it should be given as a compulsory course. In addition, in terms of the resources used, the course should be updated in terms of resources. By adding new current resources to the curriculum, the situation in the sector can be understood. Considering the current sector situation, the areas where students can get more information and do research should be increased.

In the field of real estate valuation, there are sample applications from the world and Turkey, how the real estate valuation is made, the relevant process, legal regulations, etc. A website that can be accessed open to everyone, including how the work is done, its definition, purpose and scope, can be used in and outside the classroom. In addition, a platform to be created between universities and a common resource pool can be created and real estate valuation can be discussed here with all its aspects.

#### References

- Açlar A & Çağdaş V (2008). Real estate valuation, Ankara: Union of Chambers of Turkish Engineers and Architects, Chamber of Surveyors and Cadastre Engineers Publication, ISBN: 975-395-551-0, 500 pages.
- AI Appraisal Institute (2013). The appraisal of real estate. 14th ed. Chicago. ISBN: 978-1-935328-38-4.
- Erdem, N. (2018). Türkiye Taşınmaz Değerleme Sisteminin Yeniden Yapılandırılmasına Yönelik Bilimsel Çalışma ve Öneriler Üzerine Bir Değerlendirme. Niğde Ömer Halisdemir Üniversitesi Mühendislik Bilimleri Dergisi 7.1 (2018): 159-170.
- FIG, (1995). FIG Statement on Cadastre, Publication, No. 11, Fédération Internationale des Géomètres. Information, Department of Geomatics the University of Melbourne.
- TDK, (2022). Güncel Türkçe Sözlük, Türk Dil Kurumu Resmi İnternet Sitesi, <http://www.tdk.gov.tr>
- IVSC, 2005. <https://www.iasplus.com/en/news/2005/February/news2009>



## 5<sup>th</sup> Intercontinental Geoinformation Days

igd.mersin.edu.tr



### Evaluating kernel functions of support vector machines for supervised classification of land use classes

Sinan Bulut\*<sup>1</sup>

<sup>1</sup>Çankırı Karatekin University, Faculty of Forestry, Department of Forest Management, Çankırı, Türkiye

#### Keywords

Support vector machine  
Kernel functions  
Land use  
Sentinel-2  
Supervised classification

#### Abstract

The aim of the study is to compare the accuracy of the kernel functions of the SVM method in terms of land use classification. The study was conducted in Abant Planning Unit within the north-west of Turkey. Supervised classification was performed using Sentinel-2 satellite image. Classification was made according to land use, and kernel functions of support vector machines method such as linear, polynomial, radial and sigmoid were used. According to the findings, the classification accuracies of the kernel functions were similar to each other. However, the sigmoid kernel function showed the highest classification success (kappa coefficient=0.775). When the confusion matrix was examined, the most accurately classified land classes were broadleaf forest, mixed forest, and other areas. Kernel functions were insufficient in classifying coniferous and degraded forests.

#### 1. Introduction

Developing technology, satellite systems and new techniques that have been put into practice are developing and diversifying over time. Remote sensing has also been at the center of these developments and is used in many different study subjects. It has an intensive use area, especially in the field of forestry. Classification of satellite images and estimation of stand parameters are applications that have been extensively studied in forestry. There are many different remote sensing data that can be used in these studies and different techniques that can be used for these data. Especially in supervised and unsupervised classification, different satellite images and algorithms are frequently used. In studies on supervised classification, satellite images such as Landsat 8, Sentinel-2, IKONOS, Quickbird are used extensively. Supervised classification methods such as maximum likelihood, minimum distance, mahalanobis distance, support vector machine (SVM), neural net and decision trees are also used with these satellite images (Kavzoğlu and Çölkesen 2010; Otukey and Blaschke 2010; Srivastava et al. 2012; Taati et al. 2014; Üstüner et al. 2015; Kulkarni and Lowe 2016).

This study is comparative analysis between kernel functions of SVM technique. The aim of this study is to

classify land use classes using different kernel functions of the SVM method based on Sentinel-2 satellite image and to determine the most appropriate approach.

#### 2. Method

In this study, the Sentinel-2 satellite image and the stand map produced as a result of the forest management inventory were used as material. Kernel functions of the SVM method were used for land use classification.

##### 2.1. Study area

The study was carried out at the Abant Planning Unit within the Bolu Forest Regional Directorate. The area is located in the north-west of Turkey (Fig. 1). The study area is totally 6319.1 ha. Approximately 82 percent of the study area is covered by forests (5179.9 ha). Areas of coniferous forest (CF), broadleaf forest (BF), mixed forest (MF), degraded forest (DF), and other areas (OA) are 981.5, 1011.2, 3090.3, 96.9 and 1139.2 ha, respectively (Fig. 2). Most of the study area consists of mixed stands (48.9%). The smallest areal distribution belongs to the stands with degraded structure (1.5%). The areal distribution of coniferous stands, broadleaf stands and other areas is close to each other.

\* Corresponding Author

(sbulut@karatekin.edu.tr) ORCID ID 0000-0001-6149-0910

Cite this study

Bulut S (2022). Evaluating kernel functions of support vector machines for supervised classification of land use classes. 5<sup>th</sup> Intercontinental Geoinformation Days (IGD), 37-40, Netra, India



Figure 1. Location of the study area

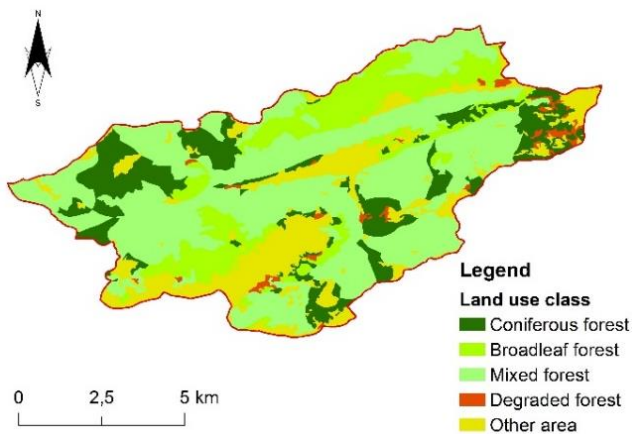


Figure 2. Land use map of the study area

### 2.2. Sentinel-2 satellite image

Sentinel-2 satellite image acquired 29 August 2015 was obtained free of charge from the USGS Earth Explorer data portal. A total of 10 bands from Sentinel-2 were used for classification. Bands 2, 3, 4 and 8 with a spatial resolution of 10 m, and bands 5, 6, 7, 8A, 11 and 12 with a spatial resolution of 20 m were combined and made ready for classification.

### 2.3. Support vector machine

The SVM, which is one of the supervised classification algorithms, is based on the structural risk minimization principle and statistical learning theory. SVM was designed for the classification of two-class linear data, then it was developed to solve the classification problem

of multi-class and non-linear data. The aim in SVM is to obtain the optimal hyperplane that can separate the two classes. Different kernel functions such as linear, polynomial, radial and sigmoid can be used in a classification process using SVM.

### 2.4. Supervised classification of the Sentinel-2 satellite image

In this study, linear, polynomial, radial and sigmoid kernel functions of SVM were used to perform supervised classification. Stand map was used as reference data for the study area. The land uses of the study area were divided into five classes by using the stand map. These classes were CF, BF, MF, DF, and OA. Ten training fields were taken from Sentinel-2 satellite image for each land use classes. The same training fields were used in all classification processes to ensure equivalence in the comparison of applied linear, polynomial, radial and sigmoid kernel functions. ENVI 5.2 software was used for the processes carried out for the supervised classification.

### 3. Results

Overall accuracy and kappa coefficient were presented for linear, polynomial, radial and sigmoid kernel functions (Table 1). Overall accuracies were obtained between 82.82 and 83.80%. Kappa statistics were found from 0.765 to 0.775. Classification successes were similar among to kernel functions. But the highest kappa statistics was found for sigmoid kernel function (0.775).

Table 1. Classification performance of the kernel functions

Kernel function type	Overall accuracy	Kappa coefficient
Linear	83.46%	0.769
Polynomial	82.82%	0.768
Radial	83.25%	0.765
Sigmoid	83.80%	0.775

Confusion matrices for linear, polynomial, radial and sigmoid kernel functions were showed in Table 2-5. When the matrices were examined, it was seen that the kernel functions classified the CF class incorrectly. Kernel functions have classified the CF class mostly as MF class. The CF class was best classified by the polynomial function. BF class was distinguished by all kernel functions and classified with high accuracy. BF class was distinguished and classified with high accuracy. All kernel functions for the BF class showed similar success. The best classification for the MF class was made by the radial function, and the worst classification was by the polynomial function. Kernel functions were not successful in distinguishing the DF class. DF class was misclassified by the kernel functions and assigned to BF and MF classes. The classification success rate was high for the OA class. The most successful kernel function in classification for OA was linear. The most unsuccessful function was the sigmoid.

**Table 2.** Results of the confusion matrix for linear function

Class	CF	BF	MF	DF	OA	Total
CF	75	0	51	0	0	126
BF	3	1919	7	74	8	2011
MF	1051	5	2549	109	4	3718
DF	0	1	2	6	5	14
OA	2	3	1	11	2199	2216
Total	1131	1928	2610	200	2216	8085

**Table 3.** Results of the confusion matrix for polynomial function

Class	CF	BF	MF	DF	OA	Total
CF	580	0	601	30	0	1211
BF	3	1919	7	74	9	2012
MF	547	5	1998	81	8	2639
DF	0	1	2	3	3	9
OA	1	3	2	12	2196	2214
Total	1131	1928	2610	200	2216	8085

**Table 4.** Results of the confusion matrix for radial function

Class	CF	BF	MF	DF	OA	Total
CF	27	0	11	0	0	38
BF	3	1919	7	74	11	2014
MF	1100	5	2589	113	8	3815
DF	0	1	2	2	3	8
OA	1	3	1	11	2194	2210
Total	1131	1928	2610	200	2216	8085

**Table 5.** Results of the confusion matrix for sigmoid function

Class	CF	BF	MF	DF	OA	Total
CF	182	0	109	3	0	294
BF	4	1920	7	75	16	2022
MF	945	5	2491	114	16	3571
DF	0	2	2	2	4	10
OA	0	1	1	6	2180	2188
Total	1131	1928	2610	200	2216	8085

The classified land use maps obtained by the kernel functions were presented in the Fig. 3. When the maps were examined visually, it was seen that the DF class with limited area cannot be classified well. It has been seen that the CF class was assigned to more areas than it should be with the polynomial function. In linear and radial function maps, the CF class was classified independently and very dispersedly. The most stable map for the CF class was obtained with the sigmoid function. OA class was mapped similarly by all kernel functions.

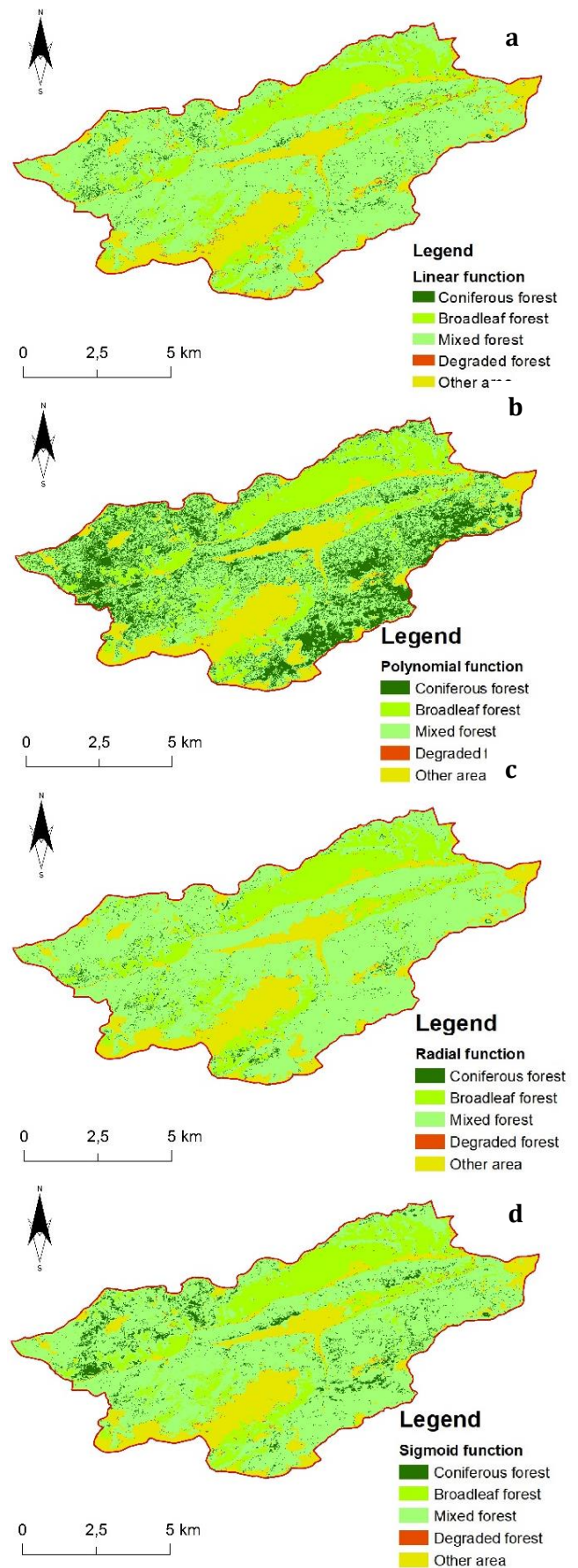


**Figure 3.** Classified land use maps by linear (a), polynomial (b), radial (c) and sigmoid (d) functions

#### 4. Discussion

In the study, controlled classification of Sentinel-2 satellite image was made for land use classes. Linear, polynomial, radial and sigmoid kernel functions of SVM were used as classifier, and forest management stand map as referenced. Kappa statistics values ranged between 0.765 and 0.775. Highest success was achieved with the sigmoid function in terms of overall accuracy and kappa statistics. In this study, land use classification with success of 80 percent or higher could not be made. There are many studies in the literature on land use classification. Deilmai et al. (2014) generated land use and land cover maps using maximum likelihood (ML) and SVM method. They reported that the SVM method was better than ML method. Kappa statistics were 0.65 and 0.86 for ML and SVM method, respectively. Huang et al. (2002) classified to land cover classes with MODIS satellite imagery using SVM, maximum likelihood, artificial neural networks, and decision trees methods. The highest success was obtained with the SVM method, and the overall classification success was 75.62%. Kesikoğlu et al. (2019) used three different classifier method such as ML, ANN and SVM technique and land cover types were classified for 2005 and 2012. The highest success was found for ANN and SVM methods.

In the study, classification successes for CF and DF were quite low. Since the spatial resolution of the satellite image used was medium, coniferous areas in mixed stands can be distinguished. Therefore, the CF class was mostly classified as MF. The DF class had very limited area in the region. Because of this, kernel functions had a hard time separating these small areas from the others. The resolution characteristics of the satellite image such as spatial, radiometric, and spectral used affect the classification to a high degree. Especially when the spatial resolution of the satellite image is high, smaller details can be distinguished and classification can be made more sensitive. Lower resolution images can be used when the scale of the object to be classified is coarse. Therefore, it is important to select the appropriate satellite image according to the details of the classification in terms of classification success (Günlü 2012; Bulut and Günlü 2016; Abbas and Jaber 2020; Jamali and Karas 2022).

#### 5. Conclusion

Kernel functions of the SVM method were used for land use classification. Classification success of all kernel functions was close to each other, and they were not especially successful in classifying forest types. Therefore, the dissemination of such studies, the use of satellite images with different resolutions and classification techniques will provide more accurate information for the selection of appropriate techniques and materials.

#### Acknowledgement

I would like to thank the Turkish General Directorate of Forestry for providing data.

#### References

- Abbas, Z., & Jaber, H. S. (2020). Accuracy assessment of supervised classification methods for extraction land use maps using remote sensing and GIS techniques. In IOP Conference Series: Materials Science and Engineering (Vol. 745, No. 1, p. 012166). IOP Publishing.
- Bulut, S., & Günlü, A. (2016). Arazi kullanım sınıfları için farklı kontrollü sınıflandırma algoritmalarının karşılaştırılması. *Kastamonu University Journal of Forestry Faculty*, 16(2), 528-535.
- Deilmai, B. R., Ahmad, B. B., & Zabihi, H. (2014). Comparison of two classification methods (MLC and SVM) to extract land use and land cover in Johor Malaysia. In IOP conference series: Earth and environmental science (Vol. 20, No. 1, p. 012052). IOP Publishing.
- Günlü, A. (2012). Landsat TM uydu görüntüsü yardımıyla bazı meşcere parametreleri (gelişim çağı ve kapalılık) ve arazi kullanım sınıflarının belirlenmesi. *Kastamonu University Journal of Forestry Faculty*, 12(1), 71-79.
- Huang, C., Davis, L. S., & Townshend, J. R. G. (2002). An assessment of support vector machines for land cover classification. *International Journal of Remote Sensing*, 23(4), 725-749.
- Jamali, A., & Karas, İ. R. (2022). Land Use Land Cover Mapping in Support of Land Degradation Mapping Using Tree-Based Classifiers. In *Environmental Degradation in Asia* (pp. 3-16). Springer, Cham.
- Kavzoğlu, T., & Çölkesen, İ. (2010). Destek vektör makineleri ile uydu görüntülerinin sınıflandırılmasında kernel fonksiyonlarının etkilerinin incelenmesi. *Harita Dergisi*, Temmuz 2010, 144:73-82.
- Kesikoglu, M. H., Atasever, U. H., Dadaser-Celik, F., & Ozkan, C. (2019). Performance of ANN, SVM and MLH techniques for land use/cover change detection at Sultan Marshes wetland, Turkey. *Water Science and Technology*, 80(3), 466-477.
- Kulkarni, A. D., & Lowe, B. (2016). Random forest algorithm for land cover classification. *Computer Science Faculty Publications and Presentations*. Paper 1. <http://hdl.handle.net/10950/341>.
- Otukei, J., & Blaschke, T. (2010). Land cover change assessment using decision trees, support vector machines and maximum likelihood classification algorithms. *Int J Appl Earth Obs Geoinf* 12: 27–S31.
- Srivastava, P. K., Han, D., Rico-Ramirez, M. A., Bray, M., & Islam, T. (2012). Selection of classification techniques for land use/land cover change investigation. *Adv Space Res* 50(9):1250–1265.
- Taati, A., Sarmadian, F., Mousavi, A., Pour, C. T. H., & Shahir, A. H. E. (2014). Land use classification using support vector machine and maximum likelihood algorithms by Landsat 5 TM images. *Walailak Journal of Science and Technology*, 12(8): 681-687.
- Üstüner, M., Şanlı, F. B., & Dixon, B. (2015). Application of support vector machines for landuse classification using high-resolution RapidEye images: a sensitivity analysis. *European Journal of Remote Sensing*, 48: 403-422.



## 5<sup>th</sup> Intercontinental Geoinformation Days

igd.mersin.edu.tr



### A Mass Valuation Model Proposal for Residential Property Taxation in Türkiye

Ecem Sirkeci\*<sup>1</sup>, Reha Metin Alkan <sup>1</sup>, Muhammed Oğuzhan Mete <sup>1</sup>

<sup>1</sup>Istanbul Technical University, Faculty of Civil Engineering, Department of Geomatics Engineering, Istanbul, Türkiye

#### Keywords

Real Estate Valuation  
Mass Valuation  
Nominal Valuation  
Property Tax Regulation  
Taxation

#### Abstract

Real estate valuation, which is an important part of land management functions, is encountered in many applications. One of these application areas is property taxation. In Türkiye, property tax for lands, minimum unit values on street basis are determined by municipalities, and minimum tax value is determined for residential properties. Since spatial, physical and socio-economic characteristics of the properties are not analyzed adequately in the practical studies for taxation purposes, a significant income loss occurs in tax amounts on behalf of the public. In order to ensure fair property taxation in Türkiye, it is clear that the value of each property should be appraised as stated in the property tax regulations, instead of making a generalized valuation on the basis of streets. However, considering the vast amount of properties, it is not practical to carry out the valuation using classical methods. In this study, a mass valuation model based on Nominal Valuation method, which takes into account the criteria expressed in the "Regulation on the Appreciation of Tax Values to be Subject to Property Tax" was developed. The performance of the developed model was tested with 1,000 residential properties whose tax values and current market values are known by the municipality in Gaziosmanpaşa district of Istanbul. According to the results, it has been observed that there is an approximate 6 to 7 times difference between the value of the taxable real estate applied by the Municipality and the market values. On the other hand, several performance metrics of the regression analysis showed that prediction accuracy was high enough. It is evaluated that the developed model will give more accurate results with the increase of data density and the use of real market values instead of property listing data.

#### 1. Introduction

Real estate includes everything that is a natural part of the land, trees and mines, as well as additions made by people to the land like buildings and improvements (Açlar and Çağdaş, 2008). Thus, real estate represents all additions above or below the ground.

Valuation is an activity that aims to determine the monetary amount of an asset or liability. It can also be considered a valuation process. Real estate valuation, on the other hand, is the process of determining the value of a property by evaluating the affecting factors. At the same time, real estate valuation is the independent and impartial valuation of the probable value of a real estate, real estate project or rights and benefits attached to a real estate at a certain date (SPK, 2008).

Many factors such as zoning status, location, ground and construction structure, income earned from the property, accessibility (proximity to public transport,

etc.), infrastructure status, parcel shape / size / width / slope should be taken into consideration on the valuation day. For the built environment, when determining the building tax value, the cost of unit m<sup>2</sup> according to the type, class, and usage style of the construction, the external surface area of the building (if there is a share, the area corresponding to the share), the value of the building calculated according to the normal construction cost in square meters, the heating difference, if any, Factors such as elevator difference, depreciation rate, tax-exempt amount are taken into consideration.

In Türkiye, property tax legislation is based on Property Tax Law no. 1319 (Official Gazette, 1970) and application details are expressed in " Regulation on the Appreciation of Tax Values to be Subject to Property Tax" (Official Gazette, 1972). In practice, municipalities calculate the tax value of a residential property as a summation of minimum unit land value on the street

#### \* Corresponding Author

(sirkeci16@itu.edu.tr) ORCID ID 0000-0003-3182-0047  
(alkanr@itu.edu.tr) ORCID ID 0000-0002-1981-9783  
(metemu@itu.edu.tr) ORCID ID 0000-0002-9312-1965

#### Cite this study

Sirkeci E, Alkan R.M, & Mete M.O. (2022). A Mass Valuation Model Proposal for Residential Property Taxation in Türkiye. 5<sup>th</sup> Intercontinental Geoinformation Days (IGD), 41-44, Netra, India

basis and roughly calculated minimum tax value of the improvement. Besides, spatial, physical and socio-economic characteristics of the properties are not analyzed adequately in the practical studies for taxation purposes. Thus, a significant income loss occurs in tax amounts on behalf of the public. In order to ensure fair property taxation in Türkiye, it is clear that the value of each property should be appraised as stated in the property tax regulations, instead of making a generalized valuation on the basis of streets. In this study, by using GIS-supported Nominal Valuation Method, the taxation process was applied to 1,000 residential properties located in Gaziosmanpaşa district in İstanbul, Türkiye according to the criteria included in the property tax regulation. Thus, it is aimed to prevent real estate tax losses and to make fair taxation by carrying out the valuation on a building basis instead of applying street-based taxation.

## 2. Method

Within the scope of the study, it was preferred to use the Nominal Valuation Method, which is one of the most widely used methods among mass real estate valuation methods. It is a stochastic method based on the weighted sum of the factors affecting the property value at different levels (Yomralioglu, 1993). By assigning scores on a certain scale (for example, in the range of 0-100) to each criterion affecting the value, the values of both land and buildings can be determined parametrically with this objective approach (Mete, 2022). Nominal criterion scores are multiplied by the weight of each property to obtain unit nominal values. As a result of multiplying the nominal unit value with the area, the total nominal values of the properties can be calculated (1). With this method, it is possible to calculate the tax values of the properties according to the property tax regulation.

$$V_i = S_i * \sum_{j=1}^k (f_{ji} * w_j) \quad (1)$$

- V: Total nominal value
- S: Parcel or pixel area
- f: Factor value (Score)
- w: Factor weight
- k: Total number of factors

### 2.1. Best-Worst Method (BWM)

The Best-Worst Method is a method which covers the application of a weighting process for each criterion. When carrying out pairwise comparisons, the best (most important) criteria are chosen, and the criteria scores are decreased according to the order of importance. Likewise, for the worst criterion, the highest score is given to the criterion with low importance, and the criterion score is decreased as the order of importance is increased. Criteria weights are calculated as a result of solving this process. In this method, the sum of the weights of the criteria is 1.

### 2.2. Study Area

Turkey has an important position in the world since it is located on the intersection of the continents of Asia and Europe. Connecting these two continents, İstanbul, Turkey's most populous city, is located in the northwest of the Marmara region. Gaziosmanpaşa is an important district with a population of 493,096 and an area of 11.67 km<sup>2</sup>, located in the city center of İstanbul. The region has a vibrant real estate market due to urban transformation projects. For these reasons, Gaziosmanpaşa district of İstanbul was chosen as the study area (Figure 1).

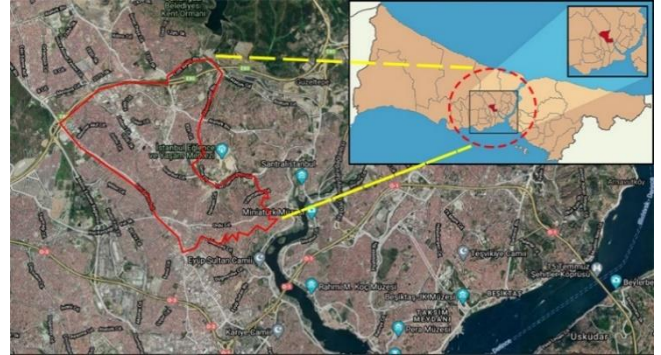


Figure 1. Gaziosmanpaşa District, İstanbul, Türkiye

Within the scope of the study, property tax values are calculated for Gaziosmanpaşa district by using the necessary factors (Table 1) according to the issues specified in the “Regulation on the Appreciation of Tax Values to be Subject to Property Tax”. The issues specified in the regulation and considered appropriate to be used as a factor are selected from 1,000 residential property; type of use, type of construction, building class, number of rooms, number of halls, water-electricity-gas, front-rear facade situation, presence of elevator, heating, air conditioner, extension, proximity to fire stations, proximity to universities, other education centers (primary school-secondary school-high school), proximity to hospitals, other health centers (health care centers, medical centers, etc.), proximity to metro stations, proximity to police stations, proximity to shopping malls and proximity to hazardous areas. Considering those criteria, nominal factor scores are calculated. For proximity criteria, GIS-based Network Analysis is carried out and the proximity of residential properties to these centers are evaluated by considering road network instead of Euclidean distance.

Table 1. Factors affecting property value

#	Criteria	#	Criteria
1	Type of Use	11	Proximity to Fire Stations
2	Type of Construction	12	Proximity to Education Centers
3	Building Class	13	Proximity to Health Centers
4	Number of Rooms	14	Proximity to Universities
5	Number of Halls	15	Proximity to Hospitals
6	View Quality	16	Proximity to Subway Stations
7	Water, Electricity, Gas	17	Proximity to Police Stations
8	Front - Rear Facade	18	Proximity to Shopping Malls
9	Elevator, Heating, Air Conditioning	19	Proximity To Hazardous Areas
10	Extension		

### 2.3. Network-Based Proximity Analysis

Network Analysis is used for decision-making with geographic data showing line characteristics and performed with vector-based geographic data (Yomralioğlu, 2000). There are several GIS-based network analysis applications like service area, location-allocation, and shortest path. In this study, Network-Based Proximity Analysis is carried out by using building and road data obtained for the study area, and proximity criteria of the selected properties are analyzed in 7 distance thresholds (Figure 2).

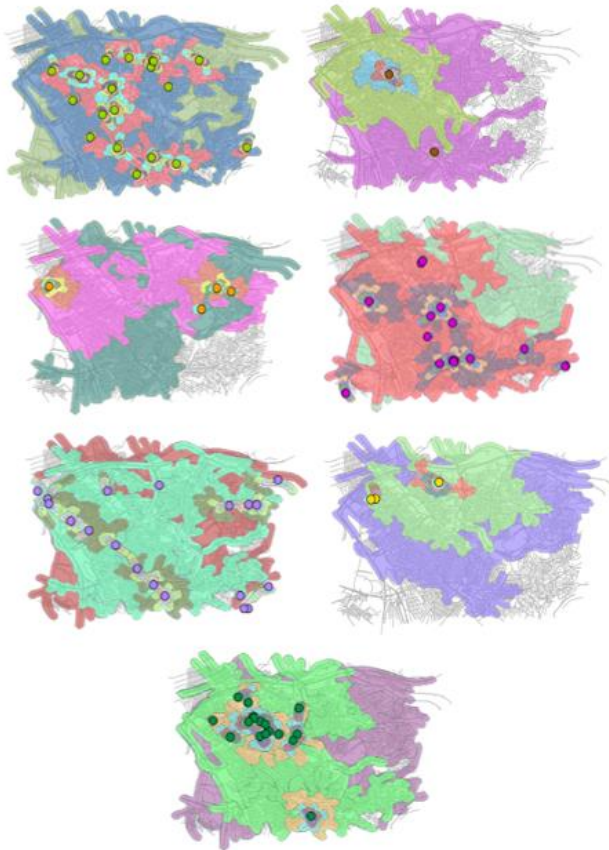


Figure 2. Network Analysis

In the literature, it has been observed that the ranges of distances vary according to the purpose and field of study. For this reason, it was deemed appropriate to select classes as 0-100, 101-200, 201-300, 301-500, 501-1000, 1001-3000, and 3001-5000 in order to have good distinguishability and to easily identify class differences by processing more than one class. Nominal Valuation Method was used to normalize the criteria and calculate the total values after the analysis, and each factor was scored between 0-100 (Table 2). After scoring the criteria, pairwise comparisons were made using the Best-Worst Method to calculate the factor weights, and the weight value of each criterion was calculated with a high consistency ratio (Figure 3).

By using the criteria points and weights, the total nominal values of the buildings have been calculated considering the Property Tax Regulation.

Table 2. Classification of criteria and nominal scores

Proximity Status	Score
0 - 100	100
101 - 200	90
201 - 300	80
301 - 500	70
501 - 1000	60
1001 - 3000	40
3001 - 5000	20
5000 - ↑	0
View Quality	Score
15 - 20	100
10 - 15	75
5 - 10	50
0 - 5	25
0 ↓	0
Building Class	Score
Luxury	100
1.Class	75
2.Class	50
3.Class	25
Simple	0
Number of Rooms	Score
10 - ↑	100
9	90
8	80
7	70
6	60
5	50
4	40
3	30
2	20
1	10
Number of Halls	Score
5 - ↑	100
4	80
3	60
2	40
1	20
0	0

In order to express the nominal values in Turkish Lira so that they can be used for taxation purposes, the sales value of the 1,000 residential property selected in the study area using a real estate listing web page. In this context, 80% of the sales values were selected randomly as training data and 20% as test data set, and a mass valuation model is developed by performing regression analysis (Figure 4). Thus, property tax values calculated according to 19 criteria in the study area.

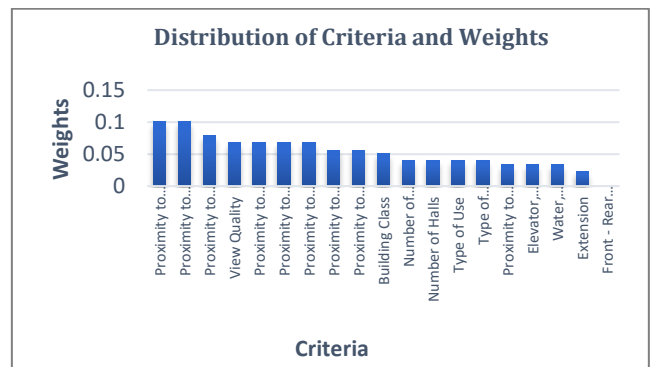


Figure 3. Distribution of Criteria and Weights

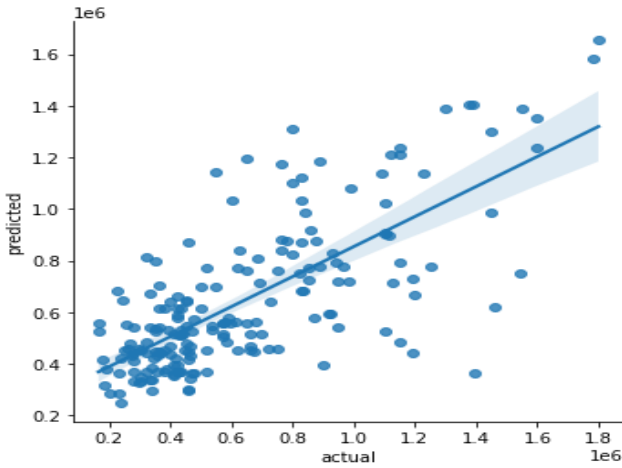


Figure 4. Actual and predicted property values

### 3. Results & Conclusion

As a result of the study, the tax values for residential properties (%02) calculated with GIS-based Nominal Valuation Method based on “Regulation on the Appreciation of Tax Values to be Subject to Property Tax” with 0.5244  $R^2$ , 0.3428 Mean Absolute Percentage Error (MAPE), and 248,039 Root Mean Square Error (RMSE). The results of the proposed method were compared with the tax values levied by the municipality and it was observed that there was a difference of approximately 6-7 times. Suggestions to overcome this problem can be listed as follows:

- A GIS-based property valuation system can be created by using real estate listing pages and property attributes can be automatically entered and updated in the created database.
- Up-to-date data about features such as "Building Class, Number of Floors, Location" can be gathered from Google Street View imagery.
- With the HGM Atlas Application, information such as "Building Class, Number of Floors, Location in the Street" can be accessed.
- With the 3D Cadastre and 3D City Modeling project carried out by the General Directory of Land Registry and Cadastre (GDLRC), some information can be accessed from the computer environment and related features can be valued more easily.
- By establishing a dynamic, GIS-based, Property Information System, it will be possible to prevent tax loss as a result of the more equitable determination of the property tax.
- Tax values of lands are updated every four years and the revaluation rates do not reflect the real value increase/decrease rates of the properties. In order to avoid such problems, it will be useful to determine the current value of properties every year or every two years. (Organ and Çiftçi,2015).

### Acknowledgement

This study was carried out as part of the master's thesis prepared by Ecem Sirkeci at Istanbul Technical University, Graduate School.

We sincerely thank Gaziosmanpaşa Municipality for providing the "Gaziosmanpaşa District Land and Land Values in 2021" and other data that we used in the determination of the accuracy of the models developed within the scope of this study.

### References

- Açlar, A. ve Çağdaş, V. (2008). Taşınmaz (Gayrimenkul) Değerlemesi, TMMOB Harita ve Kadastro Mühendisleri Odası, ISBN 975-395-551-0, Ankara, 500 s.
- Mete, M.O. (2022). Development of Mass Property Valuation Model Based on Geographic Information Systems Integrated Machine Learning Methods, PhD Thesis, Istanbul Technical University (In Turkish).
- Official Gazette. (1970). Emlak Vergisi Kanunu (1319).
- Official Gazette. (1972). Emlak Vergisine Matrah Olacak Vergi Değerinin Takdirine İlişkin Tüzük.
- Organ İ., Çiftçi T.E.(2015). Türkiye’de Emlak Vergisi Uygulamasından Kaynaklanan Sorunlar Ve Çözüm Önerileri, Niğde Üniversitesi İktisadi ve İdari Bilimler Fakültesi Dergisi. 8 (4), 127-147.
- SPK. (2008). Capital Markets Authority. Real Estate Valuation and Other Real Estate Valuation Activities in the Capital Market [retrieved from: <https://www.spk.gov.tr/kurumlar/gayrimenkul-degerleme-kuruluslari/tanitim-rehberi>].
- Yomralıoğlu, T., (1993). A Nominal Asset Value-Based Approach for Land Readjustment and Its Implementation Using Geographical Information Systems, PhD Thesis, University of Newcastle upon Tyne, UK.
- Yomralıoğlu, T. (2000). Geographic Information Systems Basic Concepts and Applications. Istanbul: Seçil Offset.



## 5<sup>th</sup> Intercontinental Geoinformation Days

igd.mersin.edu.tr



### The role of geomatics engineering discipline on nearly zero energy building concept for Türkiye

Büşra Kartal\*<sup>1</sup>, Reha Metin Alkan <sup>1</sup>, Mehmet İşiler <sup>1</sup>

<sup>1</sup>Istanbul Technical University, Civil Engineering Faculty, Geomatics Engineering Department, İstanbul, Türkiye

#### Keywords

Energy Efficiency  
CO<sub>2</sub> Footprint  
nZEB  
BIM

#### Abstract

In order to cope with the climate crisis and achieve the carbon neutrality target for the year of 2030 and the year of 2050, the factors that cause carbon footprint should be investigated, and required actions to reduce the effects of greenhouse gases should be determined. It is a fact that the building sector causes about 40% of carbon dioxide emissions from energy consumption, especially in European countries. In this context, several actions on energy efficiency for buildings have been applied in the European Union (EU) in the last two decades. In parallel with EU policies on energy efficiency for buildings, some legal regulations have also been enacted, and some strategic action plans have been introduced in Türkiye. These efforts should be carried out based on the land management paradigm. Accurate, up-to-date, and well-organized location-based data is required to achieve the aims of related legal regulations and action plans. This study aims to reveal the main study areas to be carried out by the Geomatics Engineering discipline to reduce the carbon footprint and to reach the carbon-neutral target by planning carbon sink areas.

#### 1. Introduction

According to NASA, global warming has been caused by increasing the levels of heat-trapping greenhouse gases in the Earth's atmosphere due to human activities and the burning of fossil fuels (URL 1). One of the significant reasons for global warming is the amount of carbon dioxide (CO<sub>2</sub>) emitted into the atmosphere. The increasing use of fossil fuels due to population growth in the world stimulates the amount of carbon dioxide, the most abundant primary greenhouse gas in the atmosphere. The most significant negative impact of greenhouse gas emissions is climate change. Instead of using fossil fuels, alternative renewable energy sources that do not emit carbon dioxide, such as biofuels, wind, solar, geothermal, nuclear, and hydraulic energy, should be used to eliminate the damages of global warming (Güllü & Bayraç, 2017).

Unlike fossil fuels, renewable energy sources can be considered as sustainable and clean energy sources. In accordance with Law No. 6094 on Electricity Energy of Renewable Energy Sources published in 2010, Renewable Energy Sources (RES) are defined as non-

fossil energy such as hydraulic, wind, solar, geothermal, biomass, gas derived from biomass (including landfill gas), wave, current energy and tidal energy (URL 2).

Climate change has become an important issue that is urgently required to deal for all countries. Türkiye is one of the countries with a primary risk of being affected by climate change due to its geographical location, climate regime, industrial development, and density population on the coast sides (Bozoğlu, 2018). According to the United Nations Environment Program (UNEP), Türkiye, which accounts for 1.17% of global emissions, is one of the countries producing the most greenhouse gases (URL 3). According to the results of the greenhouse gas inventory in Türkiye, the total greenhouse gas emission in 2020 increased by 3.1% compared to the previous year. It was calculated as 523.9 million tons (Mt) CO<sub>2</sub> equivalent (eq.). CO<sub>2</sub> eq. in total greenhouse gas emissions in 2020. Energy-related emissions have the largest share at 70.2%, followed by agriculture at 14%, industrial processes and product use at 12.7%, and the waste sector at 3.1% (TUIK, 2022). Figure 1 shows the ratios of greenhouse gas emissions by sectors:

#### \* Corresponding Author

(durmusbu@itu.edu.tr) ORCID ID 0000-0003-1217-7527  
(alkanr@itu.edu.tr) ORCID ID 0000-0002-1981-9783  
(isiler@itu.edu.tr) ORCID ID 0000-0003-0543-0029

#### Cite this study

Kartal B, Alkan R M & İşiler M (2022). The Role of Geomatics Engineering Discipline on Nearly Zero Energy Building Concept for Türkiye. 5<sup>th</sup> Intercontinental Geoinformation Days (IGD), 45-47, Netra, India

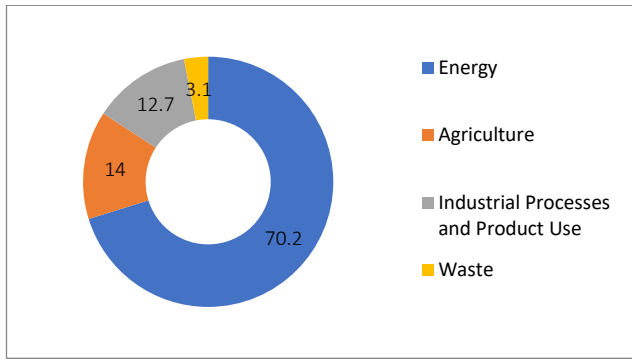


**Figure 1.** Ratios of greenhouse gas emissions by sectors (TUİK, 2022)

According to the Regulatory Indicators for Sustainable Energy (RISE) report published by the World Bank in 2019, Türkiye ranked 69th out of 111 countries in the "World Sustainable Energy" ranking with a total of 82 points, scoring 80 points in renewable energy, 100 points in energy access and 66 points in energy efficiency. In the renewable energy category, it ranked 28th worldwide with 71 points (URL 4).

Although our country has become a party of international conventions later because of its various drawbacks on some climate change steps, it has continued to carry out its own national studies about decreasing greenhouse gas emissions (Ecer et al., 2021). The national legal frame is given in Table 1.

**Table 1.** The National Legal Frame

Release Date	Legal Documents
2007	Energy Efficiency Law
2008	Building Energy Performance Regulation
2010	National Climate Change Strategical Document (2010-2023)
2010	Climate Change Action Plan (2011-2023)
2010	Tenth Development Plan (2014-2018)
2013	ENR Strategic Plan (2015-2019)
2014	National Energy Efficiency Action Plan (2017-2023)
2018	ENR Strategic Plan (2019-2023)
2019	Eleventh Development Plan (2019-2023)
2019	Regulation on the Amendment of Energy Performance in Buildings Regulation
2022	

The European Green Deal, announced by the European Union in 2019 and adopted by Türkiye in 2021, aims to reduce carbon emissions by fifty percent by 2030 and to be carbon neutral by 2050. This agreement has set targets for climate neutrality and a greener and more sustainable world.

In 2021, Türkiye became a party to the Paris Agreement, the first legally binding international agreement on climate change. The agreement's purpose is for each country party to contribute to global climate activities in line with their means and to report their national contribution declarations every five years. Another goal of the 2030 agreement is to keep global warming below 2°C at the international level by reducing greenhouse gas emissions that cause global warming to pre-industrial levels (URL 5). In addition to energy efficiency and renewable energy activities in our

country, Türkiye has declared that its activities in this direction will continue and that it is open to joint initiatives in this field with the acceptance of the Paris Agreement (İsiler et al., 2022).

In this context, one of the essential studies in the "Regulation on the Amendment of the Regulation on Energy Performance in Buildings" is the obligation to design buildings as nZEB (Nearly Zero Energy Building) by 2025, that is, to meet 5% of its primary energy needs from renewable energy sources.

Electricity, water, and natural gas consumption in residential buildings directly cause carbon emissions. Buildings have the largest share in final energy consumption, with approximately 34% in Türkiye and 40% worldwide. This situation reveals the importance of energy efficiency studies for buildings (Ministry of Environment, Urbanization and Climate Change, 2020).

## 2. The Role of Geomatics Engineering Discipline in the Realization of Türkiye's Alternative/Clean Energy Policies

According to the International Federation of Surveyors (FIG), Geomatics Engineers have a wide range of skills and tools that can be used to adapt to and mitigate climate change (FIG, 2014). Some of the studies that the Geomatics Engineering discipline can do to prevent the climate crisis are as follows:

- GIS-based tracking of the carbon footprint as a time series
- Determining the solar energy potential of the roofs of existing buildings by establishing a Building Information System
- Creating 3D Models of the building stock using Unmanned Aerial Vehicles (UAV) or LIDAR systems.
- Energy analysis of new buildings and existing buildings whose digital twins are created with the help of UAV or LIDAR systems through Building Information Management.
- Monitoring the amount of energy produced and consumed by nZEB buildings.
- Determining the carbon tax criteria for nZEB buildings that cannot produce their energy share.
- Integration of consumed energy amount for independent sections in the nZEB buildings into the real estate evaluation process (Doldur, 2022).
- Studies about resident density analysis, estimating shadows created by urban features, etc.
- Creation of surface temperature maps using satellite images for preliminary studies on geothermal energy field research and access to clean energy (Cambazoğlu et al., 2015).
- Geographical Information System (GIS) to determine the most suitable location for a wind power plant (Aitzhanov, 2016) and to utilize wind energy.
- Evaluation of location criteria for nuclear power plants with GIS (Başkurt and Aydın, 2020).
- Preparation of emergency action plans in case of a leakage in a nuclear power plant and determination of the regions to be affected according to the hazard level.

- Establishment of 3D City Models Management Information System and monitoring and querying building stock updates.

### 3. Conclusion

This study reveals the importance of energy efficiency nationally and internationally. In this sense, it is seen that the Geomatics Engineering discipline can take part in a wide variety of fields of study in line with carbon-neutral targets. This discipline plays a very crucial role in energy efficiency since they are professionals who ensure the collection, storage, processing, analysis, querying, and visualization of spatial data. Decision makers and end users can access up-to-date, reliable, location-based energy data with sufficient accuracy with the contributions of the Geomatics Engineering discipline. In this context, it is seen that a new subject of study has emerged for our profession.

### Acknowledgment

This study was carried out as part of the PhD Thesis prepared by Büşra KARTAL at Istanbul Technical University, Graduate School.

### References

- Aitzhanov C. (2016), "Site Selection Technique for Wind Turbine Power Plants Utilizing Geographical Information Systems (Gis) and Analytical Hierarchy Process (AHP)", M.Sc. THESIS Chingis Department of Civil Engineering Construction Management Program Thesis, May 2016, Istanbul.
- Başkurt, Z. & Aydın, C. C. (2020). Nükleer Santraller için Yer Belirleme Kriterlerinin Coğrafi Bilgi Sistemleri ile Değerlendirilmesi. *Türkiye Coğrafi Bilgi Sistemleri Dergisi*, 2 (1), 37-48. Retrieved from <https://dergipark.org.tr/en/pub/tucbis/issue/52936/655064>.
- Bozoğlu B. (2018), "Paris İklim Anlaşması Kapsamında Türkiye'nin Erken Uyarı Sistemine Dair Yapması Gerekenler", Ankara Üniversitesi Sosyal Bilimler Enstitüsü, Doktora Tezi, Ankara.
- Cambazoğlu S., Yal G. P., Eker A. M., Koçkar M. K., Şen O., and Akgün H., "Jeotermal Arama Çalışmaları Kapsamında ASTER Uydu Görüntüleri ile Yüze Sıcaklığı Haritalaması ve Jeotermal Anomalilerinin Araştırılması," 68. Türkiye Jeoloji Kurultayı Bildiri Özleri Kitabı (6-10 Nisan 2015), Ankara, Türkiye, 2015,
- Ministry of Environment, Urbanization and Climate Change (2020), "Guide to Energy Efficient Renovation of Public Buildings", October 2020, Ankara.
- Doldur M. (2022), "Enerji Verimliliği Odaklı Yapı Yönlendirmesi İçin BİM Tabanlı Bir Model Önerisi: Kentsel Dönüşüm Örneği", Yüksek Lisans Tezi, İstanbul.
- Ecer K., Güner O., Çetin M. (2021), "Avrupa Yeşil Mutabakatı Ve Türkiye Ekonomisinin Uyum Politikaları", İşletme Ve İktisat Çalışmaları Dergisi, Yıl: 2021, Cilt: 9, Sayı: 2, S. 125-144.
- FIG (2014), "The Surveyor's Role in Monitoring, Mitigating, and Adapting to Climate Change".
- Güllü M. ve Bayraç H.N. (2017), "Biyoyakıt Üretimi, Karbon Emisyonu ve Ekonomik Büyüme İlişkisi: Amerika, Brezilya Ve Almanya Örnekleri", Akademik Bakış Dergisi Sayı: 64, Uluslararası Hakemli Sosyal Bilimler E-Dergisi.
- İşiler, M., Yanalak, M. & Selbesoğlu, M. O. (2022). Arazi Yönetimi Paradigması Çerçevesinde Türkiye'de Binalar İçin Enerji Kimlik Belgesi Uygulamasının Değerlendirilmesi. *Niğde Ömer Halisdemir Üniversitesi Mühendislik Bilimleri Dergisi*, 11 (3), 689-705. DOI: 10.28948/ngumuh.1054333
- TUİK 2022, Sera Gazı – Emisyon Gazı İstatistikleri: <https://data.tuik.gov.tr/Bulten/Index?p=Sera-Gazi-Emisyon-Istatistikleri-1990-2020-45862>.
- URL1: <https://climate.nasa.gov/resources/global-warming-vs-climate-change/#:~:text=Global%20warming%20is%20the%20long,gas%20levels%20in%20Earth's%20atmosphere>. Last accessed: November 30, 2022.
- URL2: <https://www.resmigazete.gov.tr/eskiler/2011/01/20110108-3.htm> Last accessed: November 30, 2022
- URL3: [https://www.unep.org/explore-topics/climate-action/what-we-do/climate-action-note/state-of-climate.html?gclid=CjwKCAjwwL6aBhBlEiwADycBIAASOXcNqzQY4Jf9eyEqImRovGGITjsrVhOGPWHS9rQ1-mPVfe8CRoCp4cQAvD\\_BwE](https://www.unep.org/explore-topics/climate-action/what-we-do/climate-action-note/state-of-climate.html?gclid=CjwKCAjwwL6aBhBlEiwADycBIAASOXcNqzQY4Jf9eyEqImRovGGITjsrVhOGPWHS9rQ1-mPVfe8CRoCp4cQAvD_BwE). Last accessed: November 30, 2022
- URL4: [https://rise.esmap.org/data/files/reports/rise\\_2020\\_country\\_profiles.pdf](https://rise.esmap.org/data/files/reports/rise_2020_country_profiles.pdf). Last accessed: November 30, 2022
- URL5: <https://unfccc.int/process-and-meetings/the-paris-agreement/the-paris-agreement> November 30, 2022.



## 5<sup>th</sup> Intercontinental Geoinformation Days

igd.mersin.edu.tr



### A preliminary research on methodology for establishing legal infrastructure regarding public law restrictions cadastre in Türkiye

Mehmet İşiler\*<sup>1</sup> , Mustafa Yanalak <sup>1</sup> 

<sup>1</sup>Istanbul Technical University, Civil Engineering Faculty, Department of Geomatics Engineering, İstanbul, Türkiye

#### Keywords

Public Law Restrictions  
PLR Cadastre  
Turkish Cadastral System

#### Abstract

*Cadastre* is a parcel-based information system that determines and records real estate's legal status and geometric features. Throughout the world, the production, storage, and sharing of land tenure, land value, and land use information are generally managed within the scope of cadastral activities. Today, the cadastre has begun to transform into a multi-purpose structure that includes other data related to the land. The land property consists of three main components: rights, restrictions, and responsibilities. The property right is limited. Private ownership of the property is restricted by law to protect public interests. For instance, zoning, coastal, forest, and expropriation laws include several articles that can directly limit property rights. The report titled "Cadastre 2014 – A Vision for the Future Cadastral System," published by FIG in 1998, can be shown as among the essential studies guiding cadastral activities worldwide. Statement 1 of Cadastre 2014 aims to register the entire legal status of the land, including public restrictions. With the effects of Cadastre 2014, some studies named PLR Cadastre have been carried out to include public law restrictions into its cadastral system in Switzerland. With PLR – Cadastre, legal restrictions on land are visible and accessible. This study aims to determine a methodology for establishing legal infrastructure regarding PLR cadastre activities in Türkiye.

#### 1. Introduction

Today, the land is considered a limited resource that should be managed within the sustainable development principles [İsiler et al., 2022]. As stated in Brutland Report published in 1987 by the "World Commission on Environment and Development," sustainable development can be described as meeting the needs of the present without compromising the needs of the future generation. Using land with a sustainable development approach is only possible with an effective land administration and management system (Yomralıoğlu, 2011). Land administration systems record, maintain and share land tenure, land use, and land value data required in the land management process (UNECE, 1996). Cadastre, real estate valuation, mapping, and planning activities are the main parts of the land administration system (Yomralıoğlu, 2011).

The cadastre's primary purpose is to ensure property rights' security. Cadastre is a parcel-based system that

determines and records real estate's legal status and geometric features. With the technological development in recent years, cadastral systems have increased their abilities and have become a central part of the land information system. The cadastral system can be integrated with other data sets to provide effective and efficient land policies in a holistic approach. The cadastre, which is aimed at registering property under the guarantee of the state in our country, contains the necessary data for many public and private institutions (Balcıoğlu, 2016). The importance of the cadastre has been increasing in recent years since it has become a financial tool for immovables and has become the central element of planning and real estate markets (Balcıoğlu, 2016).

Today, property rights are considered finite and limited. In this context, since the beginning of the 20th century, property rights have been seen as a social right that imposes some duties for the benefit of society, such as decisions on zoning plans and tax payment obligations

\* Corresponding Author

(isiler@itu.edu.tr) ORCID ID 0000-0003-0543-0029  
(yanalak@itu.edu.tr) ORCID ID 0000-0001-6805-8768

Cite this study

İsiler M, Yanalak M (2022). A Preliminary Research on Methodology for Establishing Legal Infrastructure about Public Law Restrictions Cadastre in Türkiye, 5<sup>th</sup> Intercontinental Geoinformation Days (IGD), 48-51, Netra, India

(Ülger, 2016). Private property rights can be limited by various laws to protect public interests. Accessing land use decisions on real estate, which is one of the essential investment tools, is crucial to determine the investment method and analyzing the possible future risks (Çağlar et al., 2016). In addition, public institutions need information about existing projects and applications in related areas before implementing their projects (İl, 2019). All of these restrictions are not recorded through land registration systems.

With Cadastre 2014, the cadastral parcel has become a land object defined by related legal regulations. A land object has the same homogeneous status within its boundaries (Cadastre 2014). Private ownership parcels, administration boundaries, and land use zones can be given as examples of land objects (Cadastre 2014). Many rights, restrictions, and responsibilities defined as an object can be overlapped within the framework of the principle of legal independence by using their geographical coordinates. With the contribution of this approach, several restrictions on property rights can be visible, recordable, and accessible.

Statement 1 of Cadastre 2014 aims to show the entire legal status of the land, including public restrictions. With the parallel of Statement 1 stated in Cadastre 2014, Switzerland has begun to carry out some PLR Cadastre studies to integrate public law restrictions into its cadastral system. Legal legislation in Switzerland introduced at the beginning of 2008 has a straightforward structure. Laws related to land administration have been combined with a new regulation called the “Geoinformation Act” (İl, 2019). This law's primary purpose is to ensure geodata's availability for general use to the public authorities and private sectors within a standard legal frame. One of the most critical sections stated in this law is the “Cadastre of Public Law Restrictions on Landownership.” (Geoinformation Act, 2009).

A PLR cadastre contains a plan that shows the area where PLR applies and legal regulations that define the related PLRs (Nicodet, 2014). In the preliminary studies, 150 possible restrictions were determined, and the project was limited to 17 PLRs from 8 sectors. (PLR Cadastre Brochure, 2015). Users can access their property information, maps of restrictions, and public rules regarding restrictions through a portal.

## 2. The Concept of Cadastre 2034

After Cadastre 2014, Australia and New Zealand published their cadastral 2034 strategy reports for the next 20 years. The report titled as “Cadastre 2034- A 10-20 Year Strategy for Developing The Cadastral System – Knowing the “Where” of Land-related Rights,” published by Land Information New Zealand, emphasizes that the existing cadastral systems should be expanded in a way that shows the entire legal status of the land, including public rights and restrictions with its spatial characteristics. The report can be summarized as follows,

- Expanding cadastral systems to show all rights, restrictions, and responsibilities on real estate

- Providing a spatial representation of the rights, restrictions and responsibilities on the landownership.
- The spatial accuracy of the RRRs should be able to meet the needs.
- The ability of cadastral systems to obtain data from reliable sources effectively.
- Providing citizens with access to cadastral data integrated with different data sets.

According to the report, a cadastral system should be able to answer some questions within a location-based framework. The main questions are summarized in Table 1.

**Table 1.** a location-based framework for RRRs

No	Query Elements	Explanation
1	RRRs	What are the rights, restrictions, and responsibilities on real estate specified in the laws?
2	Responsible Institutions	Which institution holds these RRRs?
3	When and in which case	In which case and when do the RRRs affect related real estate?
4	Boundaries of RRRs	Where do these RRRs affect/apply the real estate?

After determining RRRs in the public laws related to land management, the following questions should be answered. The crucial questions about spatial characteristics that are emphasized in the related report are summarized in Table 2.

**Table 2.** spatial characteristics for RRRs

N	Query Elements	Explanation
0		
1	The ability of spatial representation for defined RRRs	Is the spatial representation of RRRs possible?
2	Suitable Methods for representing RRR boundaries	Static - dynamic - fuzzy logic
3	Update requirement	How can RRRs be updated, and in what conditions and when can the relevant RRRs change spatially?
4	Spatial Accuracy of RRRs	What is the required geometrical accuracy in representing RRRs?
5	Data Acquisition Method	Which data collection method will be used? GNSS-remote sensing-LIDAR etc.
6	Dimension of RRRs	2D / 3D

Cadastre 2034-Powering Land and Real Property – Cadastral Reform and Innovation for Australia – A National Strategy is the other published Cadastre 2034 Document. This report presents five main goals for its strategic framework.

- Goal-1: a cadastral system that is the central part of land ownership.
- Goal-2: an easily accessible and readily understandable cadastral system
- Goal-3: a cadastral system integrated with broader legal and social interests on land
- Goal-4: a 3- dimensional and dynamic digital cadastre
- Goal-5: a federated cadastral system under common standards.

### 3. A methodology for establishing legal framework of PLR Cadastre in Türkiye

In Türkiye, establishing the land registry system defined by the Turkish Civil Code is conducted under the General Directorate of Land Registry and Cadastre (TKGM in Turkish). Cadastral activities are carried out in accordance with Cadastre Law No. 3402. Firstly, it is necessary to determine land ownership's legal and geometrical status through the cadastral works before registration (İl, 2019). Turkish cadastral system is based on the registration of 2-dimensional parcels.

Due to increased land use with different functions and many restrictive regulations introduced regarding using property rights for public benefit, the three-dimensional cadastre has become a crucial topic in recent years. (İşiler et.al, 2022). Vertically defined rights in existing cadastral systems cannot be registered sufficiently. Furthermore, it is known that rules limiting ownership rights are not directly accessible for private and public organizations/institutions or individuals. It is evident that some innovations in access to essential restrictions on private property should be performed in the Turkish cadastral system. The first step towards achieving PLR cadastre goals is to create a solid legal infrastructure. In this context, this study aims to define a methodology to establish PLR Cadastre System in Türkiye.

According to researchers, legal infrastructure related to land management issues have fragmented and repetitive structures. Therefore, legal regulations related to land should be reorganized in a holistic approach (İşiler, 2012).

- Legal regulations regarding ownership, land use, and land valuation in our country have an extremely complex structure.
- A separate law should be prepared for land valuation activities.
- A legal regulation called “Land Law” should be implemented to create a solid frame. This law should be in a structure that constitutes the primary principles of land management issues (İşiler, 2012).
- This proposed “Land Law” should include land tenure, cadastre, mapping and surveying, real estate valuation, national spatial data infrastructure, urban and rural development, and environmental protection sub-titles.
- After the preparation of land law, criteria should be set for which restrictions will be included in the current cadastral system.

- Restrictions that can be applied politically and technically should be determined. For our country, restrictions originating from zoning plans and environmental protection policies should be prioritized.
- There will be a transformation from a parcel-based registration approach to an object-based registration approach. Therefore, this transformation should be considered while preparing the PLR cadastre’s legal frame.
- Proposed PLR Cadastre should be able to answer some questions within a location-based framework as stated in Cadastre 2034 Vision documents.

### 4. Conclusion

It is understood that the PLR cadastre is needed to increase the land markets’ efficiency, ensure the legal security of investments, and provide an opportunity to follow projects implemented by different public institutions. The primary requirement for establishing a reliable and efficient PLR cadastral system is preparing and implementing a solid legal framework. At the preparation stage, the land object approach, legal independence principle, and common coordinate infrastructure concepts defined in Cadastre 2014 should be used. Also, the crucial questions about spatial characteristics that are emphasized in the related Cadastre 2034 reports should be answered for selected RRRs. In addition, it is easily seen that the roles and effects of our profession in the real market will be increased with the PLR cadastre integration.

### Acknowledgment

This study was carried out as part of the PhD Thesis prepared by Mehmet İŞİLER at Istanbul Technical University, Graduate School.

### References

- Balcıoğlu, C. (2016), Arazi nesnesi bağlamında mülkiyeti etkileyen sınırlayıcı hükümler. Yüksek Lisans Tezi, Aksaray Üniversitesi, Fen Bilimleri Enstitüsü
- Cadastre 2034 – A 10-20 Year Strategy for Developing The Cadastral System - Knowing the “Where” of Land-related Rights. Land Information New Zealand.
- Cadastre 2034 – Powering Land and Real Property – Cadastral Reform and Innovation for Australia- A National Strategy. ICSM – Anzlic Committee on Surveying and Mapping
- Çağlar T., Uzun, B., Demir, O., Nişancı R., Yıldırım V. (2017). Gayrimenkul yatırımında hukuki güvenlik, Adalet Yayınevi, Ankara, 1.Baskı, ISBN: 978-605-300-093-8.
- İl, Ş. (2019). Kamu hukuku kısıtlamaları kadastrounun uygulanmasına yönelik yaklaşımın belirlenmesi, YL Tezi, Gebze Teknik Üniversitesi, Fen Bilimleri Enstitüsü.
- İşiler, M., (2012). Arazi yönetimine dair mevzuat analizi”, YL Tezi, İstanbul Teknik Üniversitesi, Fen Bilimleri Enstitüsü.

- İsiler, M., Yanalak, M., Selbesoglu, M.O. (2022). Arazi yönetimi paradigması çerçevesinde Türkiye’de binalar için enerji kimlik belgesi uygulamasının değerlendirilmesi, Niğde Ömer Halisdemir Üniversitesi Mühendislik Bilimleri Dergisi, 11(3), 689-705.  
<https://doi.org/10.28948/ngumuh.1054333>
- Kaufmann, J. ve Steudler, D. (1998). Cadastre 2014 – A Vision for a Future Cadastral System, FIG Publication.
- Nicodet, M. (2014). “The cadastre of public law restriction of land ownership in Switzerland”, CLGE 21 March 2014.
- Ortak Geleğimiz Brundtland Raporu (1987), Brundtland Komisyonu, Birleşmiş Milletler.
- Swiss Federal Office of Topography (2015). Brochure: The Cadastre of Public-law Restrictions on Landownership (PLR Cadastre).
- UNECE (1996) Land administration guidelines, United Nations Publication, UNECE, New York and Geneva
- Ülger, N.E. (2016). Arazi yönetimi. Yem Yayınları, 1.Baskı, İstanbul, ISBN: 978-605-4793-64-8.
- Yomralıoğlu, T. (2011). Dünya’da arazi yönetimi, Türkiye’de Sürdürülebilir Arazi Yönetimi Çalıştayı, 26-27 Mayıs 2011, Okan Üniversitesi, İstanbul.

5<sup>th</sup> Intercontinental Geoinformation Days

igd.mersin.edu.tr



## Estimation of the ground surface temperature using Sebal method and the decision tree from ETM+ (Case study: Maraqeh Town)

Khalil Valizadeh Kamran <sup>\*1</sup>

<sup>1</sup>University of Tabriz, Faculty of Planning and Environmental Sciences, Department of Remote sensing and GIS, Tabriz, Iran

### Keywords

SEBAL  
Decision tree  
Maraqeh  
Thermal  
Remote sensing  
GIS

### Abstract

Land surface temperature is highly used in various kinds of studies, eg. Climatology, hydrology, Ecology, geology, design and improvement of the transport networks places. According to the stability of the land surface temperature in some limited number of climatology stations, and the need of the spatial surface temperature distribution in a vast area and simultaneously, the surface temperature was estimated. In order to access the surface temperature, the SEBAL (surface Balance Algorithms for Land) and the decision tree were used. The images used for SEBAL, were the ETM images taken on the 31st of August 2000, which were preprocessed by the Envi4.8 and ArcGIS9.3. In the study, the differences between the 12 years data of the surface temperature measured at the atmospheric stations (1993-2005), were compared with the data estimated by the SEBAL and there is in significant difference. So, the remote sensing can be recommended to be applied in the earth science and Environmental studies.

## 1. Introduction

Temperature of the surface of land, including Soil, Water, snow and plant covering, is one of the variables which is highly used in the earth science and environmental studies and a wide spatial view is usually needed, the RS technology, helps the studies of the variable be done in a vast area and temporal series of images, forms a continual spatial-temporal body of the variable. Such a continual body is used in the most modelling of the energy balance, like what is necessary in the evaporation estimation of an area, or optimization of the use and distribution of energy or the atmospheric pollutants (Danesh Kar & et al., 2004). According to the point measurements of the land surface temperature at a limited number of climatology stations, and the need of the spatial distribution of the surface temperature in a vast width at a same time, the temperature of the surface was estimated. Considering the advanced technology of the thermal RS, the Land Surface Temperature (LST) of a vast area, is obtained accurately. But the LST estimation is along with some error, because of being unknown the surface radiation (Runing, 1994).

In order to estimate the surface temperature of the land by the SEBAL algorithm, the ETM+ images taken the 31st of August 2000 and the atmospheric data of the

Maraqeh station of eastern Azerbaijan Province, were used.

The decision tree in the Envi4.8 and ArcGIS9.3 were used for preprocess and the algorithm of SEBAL process and the classification. The calibration and estimation of the land data were done by the SPSS 16 and Excel 2007. The levels of the task are shown in Figure 1.

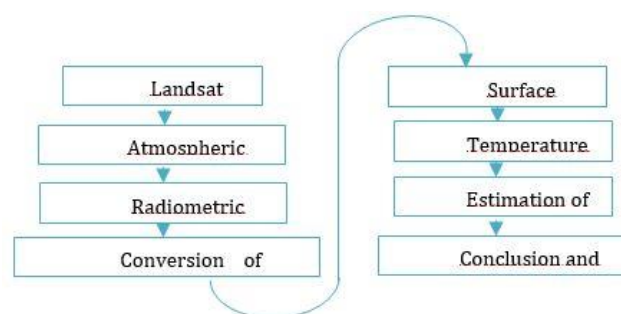


Figure 1. The chart of study process

## 2. Method

### 2.1. Study Area

The study area is located at 37 degree and 23 minutes of the north Latitude, and 46 degree and 16 minutes of the eastern longitude, on the southern side of

\* Corresponding Author

<sup>\*</sup>(e-mail) ORCID ID xxxx – xxxx – xxxx – xxxx

Cite this study

Kamran, K. V., (2022). Estimation of the ground surface temperature using Sebal method and the decision tree from ETM+ (Case study: Maraqeh Town). 5<sup>th</sup> Intercontinental Geoinformation Days (IGD), 52-56, Netra, India

Sahand Mountain. It reaches to the Uromia lake from west and Hashtroud from the east and to the Miandoab plain. The area of the city is 20 square kilometers. The climate is temperate and ranges between -20 to 35 ° C. the rainfall is 300 mm/year. The city is 135 kilometers far from Tabriz.

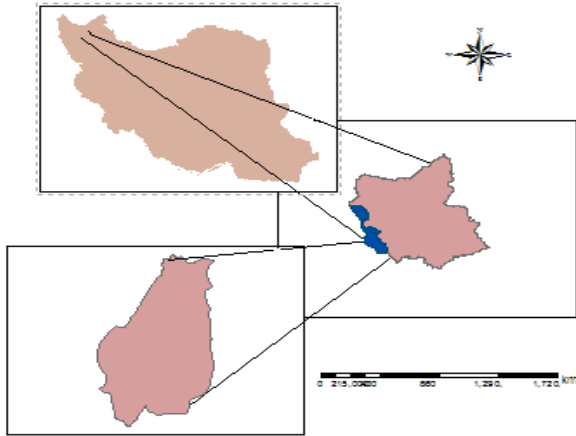


Figure 2. The study area

The SEBAL method, ETM+ images of 31st of August, was used to estimate the land surface temperature by the mono thermal band. The process was done as follows:

## 2.2. Preprocessing

The preprocessing includes the radiometric, atmospheric and geometric correction. The radiometric correction is the calculation of the spectral radiance. The atmospheric correction is the bulk correction of the reflection bands with the option of the dark subtract. The Envi4.7 and the thermal atm correction option were used to do the atmospheric correction.

- SEBAL method for calculation of the surface temperature:

The method estimates the surface temperature by the corrected thermal radiance (Allen et al., 2002). In order to calculate the corrected thermal radiance, the emissivity in the thermal band is needed. To calculate the thermal band emissivity needs the spectral radiance ( $L\lambda$ ), reflectivity in each band ( $\rho\lambda$ ) and the surface Albedo, respectively.

- spectral radiance ( $L\lambda$ ):

The spectral radiance is the radiance energy at the top of atmosphere which is detected by the sensors. The spectral radiance for each band is calculated by the following formula (Allen et al., 2002):

$$L\lambda = \frac{L_{max} - L_{min}}{255} * DN + L_{min}$$

The DN is the grey degree of the pixels and the  $L_{max}$  and  $L_{min}$  are the calibration constants of the sensor and the  $L\lambda$  is in ( $W / m^2 / sr / \mu m$ ). The  $L_{max}$  and  $L_{min}$  (Maximum and minimum of the spectral radiance in ( $W$

$/ m^2 / sr / \mu m$ ) detectable for each band by the sensor) for the ETM+ sensor is brought in the Table 1.

Table 1. The  $L_{max}$  and  $L_{min}$  for ETM+

Band	$L_{min}$	$L_{max}$
1	-6.200	293.700
2	-6.400	300.900
3	-5.000	234.400
4	-5.100	241.100
5	-1.000	47.570
61	0.000	17.040
7	-0.350	16.540
8	-4.700	243.100

In case of having the gain and offset values in the header file, the radiance can be estimated by the following formula (Landsat project science office, 2002)

$$L\lambda = gain * DN + offset$$

- Reflectivity of hemisphere ( $\rho\lambda$ ):

The surface reflectivity is the ratio of the reflected energy to the amount of energy striking the surface. The amount of the reflections is calculated in each band by the following formula (Allen et al, 2002)

$$\rho\lambda = \frac{\pi L\lambda}{ESUN\lambda * \cos\theta * dr}$$

The  $\rho\lambda$  is the sperectal reflectivity for each band,  $ESUN\lambda$  is the average of the striking radiation of the sun at the top of the atmosphere for each band in ( $W / m^2 / \mu m$ ). The  $ESUN\lambda$  values for the ETM+ sensor are shown in the table below (Allen et al, 2002).

Table 2. The  $ESUN\lambda$  values for the ETM+

Band	6	5	4	3	2	1	7
$ESUN\lambda$	-	225.7	1044	1551	1840	1969	1368

$\theta$  is the striking angle of the sun which is obtained as follows:

$$\theta = 90 - \beta$$

In which the  $\beta$  is the sun elevation which is obtained from Header file. In the study image, the sun elevation is 54.3277460.

$d_2$  is the reverse of the square distance between the earth and the sun, which is calculated by the Beckman and Duffie formula (Allen et al.,2002).

$$dr = 1 + 0.033 \cos\left(DOY \frac{2\pi}{365}\right)$$

The DOY is the sequential day the amount of which is obtained according to the image date in the 243 paper (Ahmadian Marj, 2004)

- The surface albedo ( $\alpha$ ):

The Albedo is the ratio of the reflected electromagnetic radiation from the soil and plant surface to the striking radiation from the sun. The amount of the surface albedo is calculated by the following formula (Allen et al., 2002).

$$\alpha = \frac{\alpha_{toa} - \alpha_{path} - radiance}{\tau^2_{sw}}$$

The  $\alpha_{toa}$  is the top of the atmosphere albedo,  $\alpha_{path}$ -radiance is the albedo caused by the effective radiance and the  $\tau^2_{sw}$  is the atmospheric transitivity.  $\alpha_{path}$ -radiance is the average of some of the striking radiance which is transmitted by the atmosphere and shows the absorption and dispersion events happened in the atmosphere. Since the effect is available for the both striking and reflected radiance, the surface albedo is the square of the atmosphere transmission.  $\tau_{sw}$ , regarded a fair sky and dry weather, is obtained by the following formula:

$$\tau_{sw} = 0.75 + 2 \cdot 10^{-5} \cdot z$$

In which the Z is the elevation from the sea in meter. The elevation should indicate the region elevation, like the climatology station elevation of the region (Allen et al., 2002). The station of Maraqeh is 147707 m.

$\alpha_{toa}$  is the top of the atmosphere albedo which is obtained by the formula below (Allen et al., 2002)

$$\alpha_{toa} = \sum (\omega_{\lambda} * \rho_{\lambda})$$

That  $\rho_{\lambda}$  spectral reflectivity for each band and  $\omega_{\lambda}$  is scaled coefficients for non-thermal bands.  $\omega_{\lambda}$  is calculated by the following function:

$$\omega_{\lambda} = \frac{ESUN_{\lambda}}{\sum ESUN_{\lambda}}$$

For non-thermal bands of ETM+,  $\omega_{\lambda}$  values is in the Table 3.

**Table 3.** The values of  $\omega_{\lambda}$

Band	5	4	3	2	1	7
$\omega_{\lambda}$	0.028	0.131	0.194	0.23	0.246	0.171

Surface radiation is the ratio of the emitted thermal energy from surface to the emitted thermal energy from black body in same temperature. In SEBAL method two surface radiation is used. The first referred surface behavior for emitted thermal in thermal band that shown by  $\epsilon_{NB}$  (10.4 to 12.5 micron). The second referred thermal wide range (6 to 14 micron) that shown by  $\epsilon_0$ . for calculate surface temperature ( $T_s$ ),  $\epsilon_{NB}$  is used. surface radiations is calculated by followed experimental functions:

When NDVI>0 we have:

a) For LAI<3

$$\begin{aligned} \epsilon_{NB} &= 0.97 + 0.0033 * LAI \\ \epsilon_0 &= 0.95 + 0.01 * LAI \end{aligned}$$

b) For LAI>3

$$\epsilon_{NB} = 0.98, \epsilon_0 = 0.98$$

In water and snow for  $\epsilon_{NB}$  and  $\epsilon_0$  filter is used.

Water:

$$NDVI < 0, \alpha < 0.47 \rightarrow \epsilon_{NB} = 0.99, \epsilon_0 = 0.985$$

Snow:

$$NDVI < 0, \alpha \geq 0.47 \rightarrow \epsilon_{NB} = 0.99, \epsilon_0 = 0.985$$

In top function NDVI is The Normalized Difference Vegetation index, LAI is leaf surface index and  $\alpha$  is surface albedo.

$$NDVI = \frac{B_4 - B_3}{B_4 + B_3}$$

$$LAI = 0.57 \cdot \exp(2.33 \cdot NDVI)$$

LAI function is depending to production type and geographical position and manufactured on the basis of NDVI-LAI relation mean in Czech Republic of America (Tewari et al., 2003).

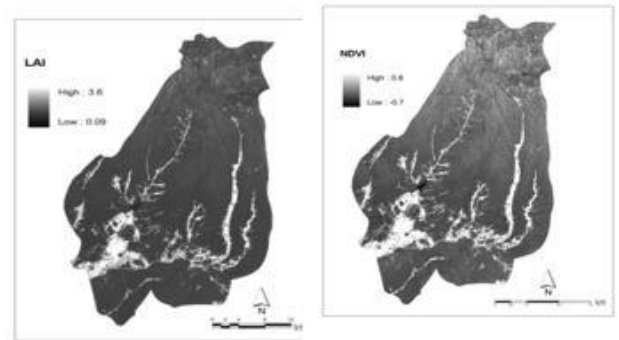


**Figure 3.** The map of NDVI and LAI of study area

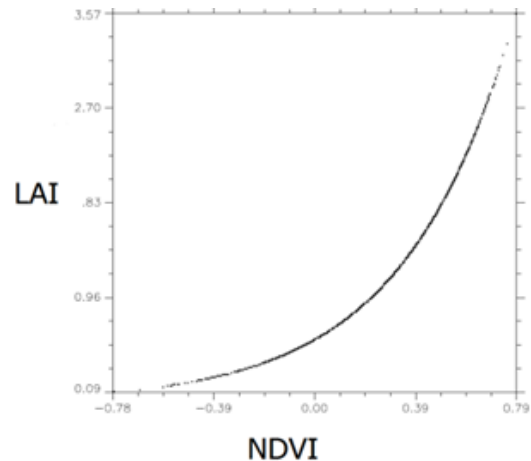


**Figure 4.** Relation between LAI and NDVI

Due to present of conditions and threshold levels for estimating surface radiation, decision tree method for classifying is used. With definition of threshold levels, desired bands, LAI, NDVI and ( $\alpha$ ), decision tree option from ENVI software environment is used to running function. The following classification can be seen in Figure 5.

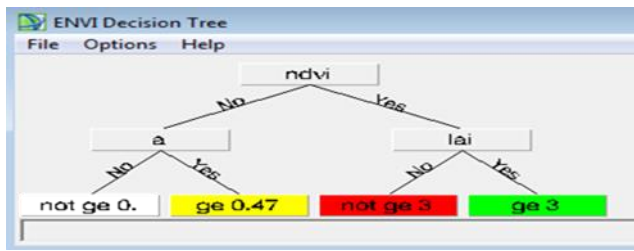


Figure 5. The decision tree in ENVI

Desired image from classifying convert to vector and then compiled to ArcGIS 9.3. After the process of dissolving, converting to raster and reclassifying, the value of each class saved in separated image as a Boolean function (Assigned value 1 to the class and zero to other). With importing these files to ENVI 4.7 surface radiation values calculated in each class. Finally with aggregating of three files, the value of surface radiation is assessed on total.

**Corrected thermal radiance (Rc)**

R<sub>c</sub> is actual emitted radiance that is corrected for atmospheric effects. The following relation is offered by Wukeli & etal for correcting emitted thermal radiance (Allen et al., 2002).

$$R_c = \frac{L_{NB} - R_P}{\tau_{NB}} - (1 - \epsilon_{NB})R_{sky}$$

L<sub>NB</sub> is radiance of thermal band, R<sub>P</sub> is course radiance of thermal band, R<sub>sky</sub> is radiance of clear sky in thermal band, and τ<sub>NB</sub> is atmospheric transition capability in thermal band. R<sub>sky</sub> can calculate by following experimental formula that offered by Idso-Jackson. T<sub>a</sub> is air temperature near surface (k) in pass moment. τ<sub>NB</sub> and R<sub>P</sub> values respectively was placed 1 and 0. (Ahmadian, 2006). Due to unequal pixel size of thermal band and other band resize data option were used.

$$R_{sky} = (1.807 \times 10 - 10)Ta^4[1 - 0.26 * \exp(-7.77 * 10 - 4[273.15 - Ta]^2)]$$

T<sub>a</sub> is air temperature near surface (k) in pass moment. τ<sub>NB</sub> and R<sub>P</sub> values respectively was placed 1 and 0. (Ahmadian, 2006). Due to unequal pixel size of thermal band and other band resize data option were used.

**Surface temperature:**

Using the following formula is calculated.

$$T_s = \frac{k_2}{Ln(\frac{\epsilon_{NB} * K_1}{R_c} + 1)}$$

Values of k<sub>1</sub> and k<sub>2</sub> are respectively 666.09 and 1282.71. All stages for calculating surface temperature except decision tree part was used Band Math option from Envi4.7. Final stages were done in Arc GIS 9.3.

**3. Results**

With respect to the lack of ground data of surface temperature on 10:09 am and need to estimate

temperature in ...(10:09 am) single variable regression method were used. Using 12 years measured data from August in different hours (1993 to 2005), regression equation is prepared. For estimation of single-variable regression, Excel2007 and SPSS 16 was used.

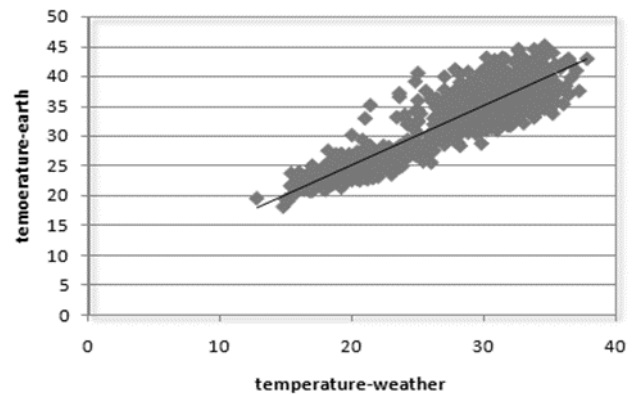


Figure 6. Diagram of estimated land data

Table 4. Computation of “R<sup>2</sup>”

R	R Square	Adjusted R Square	Std. Error of the Estimate
.914	.836	.836	2.43828

Table 5. Computation of F”

Model	Sum of Squares	df	Mean Square	F
Regression	36140.598	1	36140.598	6.079E3
Residual	7092.651	1193	5.945	
Total	43233.249	1194		

$$y = 0.994x + 5.159$$

In this equation x is air temperature and y are ground temperature at 5 cm depth. With knowledge of air temperature in 31 August 2000, ground temperature at the 5 cm depth in meteorological station of Maraqhe have estimated.

Obviously, the temperature difference between soil temperature at 5 cm depth and surface is variable during day. Research by Vazquez & et al., (1997) in the region of spain was that the temperature difference between surface and depth of soil is variable during the day. As in the early morning hours, the difference is negligible and then surface temperature increased than the temperature at 5 cm depth. From 12 to 14 pm surface temperature is about 10 degrees higher than the temperature at 5 cm depth. During sunset the temperatures of surface and depth are equal. At the night temperature in depth of soil will increase. As a result, at the desired time of this paper, surface temperature more than 5cm soil depth temperature and is less than 10 degrees centigrade. Due to the lack of exact amount of difference, temperature difference between estimated through remote sensing processing and 5cm depth of soil are considered. But we know the difference will be less.

Errors related to mismatch of thermal band resolution and other bands, geometric correction, atmospheric correction, lack of calibrated parameters in the study area, uncertainty of accuracy used meteorological data (Mobasheri & et. al., 2005) and the lack of measured data of ground surface at a desired time

in meteorological stations. These are example of errors in the process of current research.

#### 4. Conclusion

Estimation of ground surface temperature in several studies is required continuously. The following table can be said using SEBAL method, difference between actual and estimated surface temperature of satellite image less than 5.57 degree in meteorological station of maraqeh. If more accurate atmospheric data at time of imagine is available and more accurate atmospheric corrections, surface temperature estimation accuracy can be improved.

#### References

- Ahmadian Marj. A, (2007). Offering a suitable algorithm to determine areas with potential malaria outbreaks using satellite image, *M.sc. thesis, Khaje Nasir Toosi University, Department of remote sensing*
- Alavipanah. K, (2003). Application of remote sensing in geology (Earth science), *Tehran University, p 264-280*
- Alavipanah. S. K., Saradjian. M., Savaghebi. Gh. R., Komaki.Ch. B., Moghimi. E. and Karimpour Reyhan. M., (2007). Land Surface Temperature in the Yardang egion of Lut Desert (Iran) Based on Field Measurements and Landsat Thermal Data, *J. Agric. Sci. Technol, Vol. 9:pp. 287-303.*
- Allen. Richard, Tasumi. Masahiro, Trezza. Ricardo, Wim Bastiaanssen, August 2002, SEBAL: Surface Energy Balance Algorithms for Land, Version 1.0, *Funded by a NASA EOSDIS/Synergy grant from the Raytheon Company through The Idaho Department of Water Resources.*
- Daneshkar. P, Tajrishi. M, saghafian. B, (2005). Determination surface temperature using remote sensing technology in Sistan province, *journal of Water and Watershed, 4(1), p 20-29*
- Landsat Project Science Of.ce, 2002. *Landsat 7 Science Data User's Handbook. Goddard Space Flight Center, Greenbelt, MD.*
- Li, Z. L., and Becker, F. (1993). Feasibility of Land Surface Temperature and Emissivity Determination from AVHRR Data. *Remote Sens. Envir, 43: pp. 67-85.*
- Mobasheri. M, Khavrian. H, Ziaeyan. P, Kamali. G, (2005), Estimation of actual evapotranspiration using modis images and the algorithm of sebal, *Geomatic conference, surveying organization, Tehran, Iran*
- Running, S.W., Justice, C., Salomonson, V., et al., (1994). Terrestrial remote sensing science and algorithms planned for EOS/MODIS. *International Journal of Remote Sensing 15 (17), pp. 2620-3587.*
- Tewari. S., Kulhavy. J., Rock. B. N., Hadas. P., (2003). Remote monitoring of forest response to changed soil moisture regime due to river regulation, *JOURNAL OF FOREST SCIENCE, 49, pp.429-438.*
- Vázquez D. P., F. J. O., Reyes and L. A., Arboledas. (1997). A comparative study of algorithms for estimating land surface temperature from AVHRR Data. *Remote Sensing of Environment, 62(3): pp.215-222.*



## 5<sup>th</sup> Intercontinental Geoinformation Days

igd.mersin.edu.tr



### Determination of evapotranspiration on Dicle Basin

Abdullah Karatoprak <sup>1</sup>, Nizar Polat <sup>2</sup>

<sup>1</sup>General Directorate of Mining and Petroleum Affairs (Mapeg), Ankara, Türkiye

<sup>2</sup>Harran University, Engineering Faculty, Geomatics Engineering Department, Şanlıurfa, Türkiye

#### Keywords

Remote sensing  
UAV  
SEBAL  
DEM  
IRRIGATION

#### Abstract

The use of water in agriculture is a necessity for plant production, and it is necessary to determine the water consumption of the plant to meet the water needs of the plant in a sufficient and efficient way. Water consumption by plants varies not only with weather conditions, but also with plant variety. The use of suitable methods for calculating the water consumption of plants in the planning of irrigation systems at the basin level facilitates operations. Today, as a result of population growth, industrialization and especially climate change, the importance of water has increased as a result of global warming, use efficiency and performance criteria have gained importance. In this study, we intend to determine important parameters such as water consumption and plant biomass in large areas with satellite technology, which is one of the most important application areas of remote sensing. Evapotranspiration; It is the transfer of water from the soil to the atmosphere by evaporation and from plants to the atmosphere by transpiration. For this purpose, the SEBAL model was used, which is the Surface Energy Balance Algorithm for Land, which is one of the most preferred methods in the literature for mapping true evapotranspiration. With the execution of the model, data on reference evapotranspiration, plant coefficient, true evapotranspiration, indices of plant vegetation and biomass production were obtained. These values were compared with climatic data and results obtained at field level. It is thought that remote sensing techniques, which produce much faster and less expensive results than climate data and calculation methods, will be used more in the near future.

#### 1. Introduction

In recent years, the importance of water has increased due to the increasing impact of climate change. Evaporation-transpiration is an important parameter affecting the water balance in the water cycle. Accurate determination of the evaporation-transpiration amount is also important in determining the plant water requirement.

In our country, unconscious or wrong irrigation is applied in more than one agricultural area. The aim of this project is to know and calculate the actual plant water consumption (ET<sub>o</sub>), which is the amount of water needed by plants in order to increase the product obtained in an irrigation system and to achieve maximum efficiency.

Effective water management and planning is very important in important agricultural lands such as the Dicle Basin. Evapotranspiration calculations and measurements, which were made as point until recently,

can be calculated more quickly and accurately as a result of the developments in the discipline of remote sensing and optical satellite systems.

Evapotranspiration; Remote sensing-based evaporation-transpiration methods rely on surface energy balance and often provide accurate evaporation-sweat predictions (Allen et al.2011).

Due to the increase in water consumption, effective use of water has become a much more important process than in the past. For this reason, it is very important to calculate the water budget as accurately as possible and to make water management effectively (Goyal et al.2013).

Water loss from evapotranspiration is one of the most important components of a region's water budget. Evapotranspiration means the sum of water loss from evaporation and perspiration (Allen et al.2011).

Geographical information system (GIS) and Remote Sensing techniques, which are used in many areas today and can be combined with earth data, are very effective

#### Corresponding Author

(abdullah-karatoprak@hotmail.com) ORCID ID: 0000-0001-8124-221X  
(nizarpolat@harran.edu.tr) ORCID ID: 0000-0002-6061-7796

#### Cite this study

Karatoprak, A., & Polat, N. (2022). Determination of evapotranspiration On Dicle Basin. 5<sup>th</sup> Intercontinental Geoinformation Days (IGD), 57-59, Netra, India

tools in evaluating ET<sub>p</sub> and ET<sub>o</sub> in large-scale irrigated areas.

In the literature review, it was seen that this study was carried out in important water areas in the world. Although most of the studies have been used with satellite images such as Landsat 5, Landsat 7, Aster, MODIS, AVHRR, it has not been used with Landsat 8 (LDCM). Therefore, with this method, which will be applied for the first time in the Diyarbakir Basin, a current and high-accuracy study has been revealed.

## 2. Method

The study area is the Devegeçidi Irrigation Area connected to the Dicle-Fırat Basin (Figure 1).

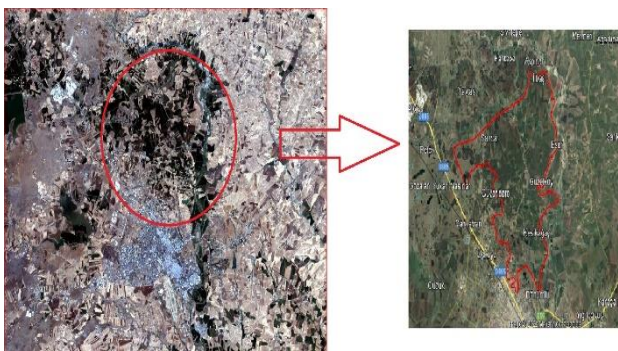


**Figure 1.** Study Area

It is located between 38°05'-38°57' North parallels and 40°13'-40°12' East meridians in the Upper Mesopotamian region. It was opened for irrigation in 1972 and later included in the Southeastern Anatolia irrigation project. In the Devegeçidi irrigation basin, an irrigation system has been established on an area of 5800 hectares.

The continental climate of the Diyarbakir basin is dominated by a desert-like air current, which is mostly tropical in origin and enters the region through the Arabian Peninsula. Winters are cold and rainy; summers are very hot and dry. Winters are cold and rainy; summers are very hot and dry. Annual precipitation is 473.6 mm, annual evaporation is 1775 mm, evaporation amount in summer is 1036 mm, annual average temperature is 15.6 °C.

### 2.1. Evapotranspiration Calculation with CROPWAT

CROPWAT 8.0 software developed by FAO Water Resources Development and Management Service (int.link1) was used. The climate data required for the Cropwat ET calculation were obtained with the Climwat plugin, which includes long-term data. Climate data was entered into the cropwat screen, and ET<sub>o</sub> values were calculated according to the Penman-Monteith method.

### 2.2. SEBAL (Surface Energy Balance Algorithm For Land) Model

Multi-channel satellite images are used in the SEBAL technique. In this study, data from Landsat-8 (OLI/TIRS)

satellite with 11 bands were used. The meteorological data required to run the model were obtained from the Kayapınar/Devegeçidi station operating in the research area. ET<sub>o</sub> calculations to be obtained with climate data were made using Cropwat software (FAO Penman Technique).

The model is able to estimate plant water parameters from the surface energy balance by using satellite images, digital elevation model (DEM), soil moisture properties, instant-daily average air temperature, wind speed, relative humidity and solar radiation climate data.

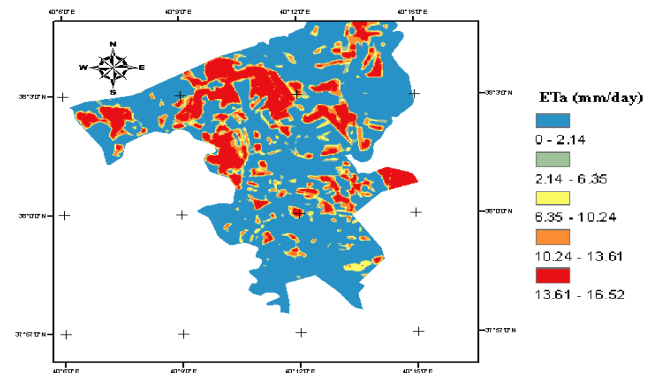


**Figure 2.** ETo map obtained from sebal bu using satellite image dated 21 July 2020

The SEBAL model, which is used to determine plant water consumption, and open source QGIS software and GRASS GIS plug-in were used. The Eto maps obtained with the SEBAL model were analyzed in QGIS software and compared with the Eto values obtained from the Cropwat program.

## 3. Results

Evapotranspiration values were calculated using the Penman-Monteith method with the data obtained from the Meteorology Observation Stations of the Diyarbakir Regional Directorate of Meteorology. Pixels belonging to the study area were selected from the thematic maps obtained with the SEBAL model and their controls were provided.

**Table 1.** CropWat program camelgate station penman-monteith ET<sub>o</sub> values

Month	Humidity %	Wind Speed km/day	Eto mm/day
January	82	216	1.78
March	77	185	3.5
May	60	135	8.32
July	28	190	15.08
September	30	154	10.78
November	59	254	5.12

SEBAL Model can process more than one type and number of data sets at the same time in its Findings. The outputs are in.ovr extension and can be taken in the desired format in GrassGIS program.

As output data, pixel-based selection can be made as ET<sub>o</sub>, NVDI (Normalized Difference Vegetation Index), SAVI (Soil Adjusted Vegetation Index), RGB, PHOT, PCOLD and the values are reported. In the calculation

made with CropWat (Penman-Monteith) for the day the satellite image was taken on July 21, 2020, the ETo for the month of July was found as 15.08 mm/day (Table 1).

The values obtained with the SEBAL model are between 13.61 – 16.52 mm/day (Figure 2).

#### 4. Discussion

ET, irrigation time planning in crop production; In other words, it is considered as the most important input in determining when and how much water will be applied to the area to be irrigated. Calculations made with climate data include some assumptions compared to the net result, and spatial differences are ignored.

ET calculations made by sampling in the fields, on the other hand, involve some assumptions since the sample amount remains within a certain limit, although it takes time and expense. However, with the SEBAL methods, an example of which was carried out in this study, a more precise and accurate calculation, as well as a cost-free calculation with a number of operational processes, was carried out in a short time.

Due to these benefits, the agricultural use of Remote Sensing has become a subject that needs to be researched in a way that cannot be ignored.

#### 5. Conclusion

One of the most important components of water management is true evapotranspiration. This parameter, which has been calculated as a point in many scientific studies or projects carried out in our country so far; It can be calculated as a fully spatial thematic map with the help of satellite images.

SEBAL is one of the most preferred methods for calculating true evapotranspiration. In this study, real evapotranspiration mapping was applied in the important agricultural area of Diyarbakır using the SEBAL technique.

In this way, the applicability of the said technique within the borders of Diyarbakır with the Landsat 8 satellite was examined and demonstrated. The obtained areal ETo map can be used in water management studies on a basin basis. These maps can be prepared on a weekly, 15-day, monthly or quarterly basis and can be made available to decision makers.

#### References

- Allen, R., Irmak, A., Trezza, R., Hendrickx, J.M.H., Bastiaanssen, W., Kjaersgaard, J., (2011). Satellite-based.
- Allen, R., Irmak, A., Trezza, R., Hendrickx, J.M.H., Bastiaanssen, W., Kjaersgaard, J., (2011). ET estimation in agriculture using SEBAL and METRIC. Hydrological Processes.
- Allen, R.G., Tasumi, M., Trezza, R., (2007). Satellite-based energy balance for mapping evapotranspiration with internalized calibration (METRIC)- Model.
- Bastiaanssen, W.G.M., Thiruvengadachari, S., Sakthivadivel, R. and Molden. D.J., (1999). Satellite Remote Sensing for Estimating Productivities of Land and Water.
- GOYAL, Megh R.; HARMSEN, Eric W., (2013) Evapotranspiration: principles and practices for water management.
- Monteith, J.L. (1965). Evaporation and environment. Symp. Soc. Exp. Biol. 19: 205–234.
- Penman, H.L. (1948). "Natural evaporation from open water, bare soil and grass." Proc.Roy. Soc. London, A193, 120-146.
- URL: <https://www.fao.org/land-water/databases-and%20software/cropwat/en/>



## 5<sup>th</sup> Intercontinental Geoinformation Days

igd.mersin.edu.tr



### Implementation of supervised SID algorithm in preparation of map of geological units

Parviz Zeaiean Firouzabadi <sup>1</sup>, Parisa Safarbeyranvand <sup>\*1</sup>, Ali Hosingholizade <sup>1</sup>

<sup>1</sup>Kharazmi University, Geography, Remote sensing and GIS, Tehran, Iran

#### Keywords

Remote sensing  
UAV  
Photogrammetry  
DEM  
SID

#### Abstract

Using remote sensing technology and satellite data often reduces the expenses and increases the speed and accuracy. Providing the map of geological units has improved so that detection and classification of geological units. In this research, it was done by hyperspectral image, related to Khoramabad zone, Lorestan, and also by applying the SID (Spectral Information Divergence) supervised classification algorithm for detection and separation of geological units. After the necessary pre-processes, the MNF conversion and the PPI algorithm were used for reducing data and extracting the pure pixels on the image. Then extracted for each member by the overlay of pure pixels with geological units and ground data, these pure members were used as input for the mentioned algorithm and the image was classified. Finally, the classification accuracy of this method (66/71) was obtained.

#### 1. Introduction

Preparing a map of geological units, while identifying valuable mineral deposits, creates a suitable and integrated vision of the study area for managers and decision makers (Sousa and Sousa. 2020). In the past, maps of geological units were usually prepared by traditional methods, including visual inspection with laboratory sampling (Lorenz et al. 2021) It is while these days, the use of remote sensing images, especially hyperspectral images, due to the use of many spectral bands and in a very narrow range of the electromagnetic spectrum, reduces costs and increases accuracy and speed (Qasim et al. 2022). On the other hand, the vastness of the regions makes it necessary to use precise and piracy methods that are able to process and extract valuable information from this mass data (Douglas et al. 2022). The use of remote sensing technology as one of the most important tools for collecting information has been the focus of many experts and specialists in various sciences, especially geology, mining, environment, meteorology and agriculture (Schodlok et al. 2022). Compared to multispectral images, hyperspectral images provide data with higher spectral resolution and identify land features more accurately (Stuart et al. 2022). In hyperspectral remote sensing, even the reflection of

earth surface phenomena can be measured in very narrow bands with a spectral width of 0.01 micrometers in the spectral range of 0.4 to 2.5 (Johnson et al. 2019). Narrow and wide spectral bands of hyperspectral images provide the possibility of

Geological research and identification of geological units of the region with better results (Ramanaidou et al. 2012). In this research, it has been tried to use the capabilities of remote sensing technology to prepare these maps.

Remote sensing technology images provide efficient data that requires processing on the image to extract the necessary information (Barton et al. 2021). Among the different methods of remote sensing, the classification technique has a special place in the analysis, separation and recognition of different geological units. Image classification is one of the main components of the subject information extraction process, which is done by examining the relationship between the spectral effect and different classes or classifications (Fonteneau et al. 2019). The algorithm used in this research is supervised. Examining the supervised algorithm with full pixels and the results of these algorithms will help us to improve the classification and detection of the desired targets (Johnson et al. 2019). That is, which algorithms are more efficient in preparing maps of geological units. In this research, an attempt has been made to increase

#### \* Corresponding Author

(p.zeaiean@gmail.com) ORCID ID 0000-0001-8407-5605  
\*(pbeyranvandgis@gmail.com) ORCID ID 0000 - 0002 - 7860 - 2621  
(a.hosingholizade@ut.ac.ir) ORCID ID 0000 - 0001 - 5286 - 1361

#### Cite this study

Zeaiean Firouzabadi P, Safarbeyranvand P & Hosingholizade A (2022). Plying to SID supervised algorithm in providing the map of geological units. 5<sup>th</sup> Intercontinental Geoinformation Days (IGD), 60-63, Netra, India

the accuracy of the created maps by classification and diagnosis based on the obtained spectra, and to identify geological units with the help of Hyperion satellite images and separation.

**2. Method**

**2.1. Study area**

The studied area is located in the west of Iran, Lorestan province, Khorramabad city. Khorramabad is geographically located in the range of 33 degrees, 29 minutes north latitude and 48 degrees, 21 minutes east longitude. Examining the structural-sedimentary situation of the province shows that its different parts have acquired different geological features over time and have been differentiated from each other, therefore according to the tectonic activities and construction style of the different age units or sedimentary basins and the type of sediments related to them Also, the magmatic and metamorphic activities of Lorestan province are highly diverse based on geological and structural units (Noroozi et al. 2015).

**2.2. Satellite image of Hyperion sensor EO-1**

The image used in this research was taken on September 14, 2019. The coordinates of the center of the zone and image are 31°N3700.09" and 47°E53'19.11". Spectral curve effect correction is one of the necessary corrections for Hyperion data, performed by pushbroom 1 imaging technology, and is present in all Hyperion data. Also, error correction was done by adjusting the average in the luminance space.1. Visible-near infrared

**2.3. Band Selection**

Among the 242 spectral bands of the Hyperion sensor used in this research, 196 bands are calibrated and unique, and 155 bands were entered into the processing stage by removing the bands that absorb water or have a lot of noise. Table 1 shows the range of acceptable electromagnetic wavelengths for entering the processing stage.

**Table 1.** Acceptable bands which enter processing

Spectral range	Acceptable bands
VNIR range	8-57
	79
	83-119
SWIR range	133-164
	183-184
	188-122

**2.4. Minimum Noise Fraction**

Transform (MNF) reduces data dimensionality and noise when using hyperspectral data. The MNF transform is considered as a noise reduction transform. It is a linear transformation that is used to determine the original dimensions and volume of the image, separate

noise from other information and reduce the degree of processing in the next step. In this conversion, the image is first converted to noise and noise-free, then the noise-free part is considered as the main part and the noise is removed.

**2.5. Implementation of the image purity index (PPI)**

PPI algorithm is used in hyperspectral images to find pure pixels (final pixels). For this purpose, the ten output bands obtained from the MNF transformation, which are noise-free, are given as input to the PPI algorithm. The output of this algorithm is an image that specifies pure pixels.

**2.6. Endmember spectrum extraction and Endmember extraction through pure pixel identification**

Many classification algorithms in hyperspectral images need to enter the spectral characteristics of the members (any class or complex that is classified or revealed in the hyperspectral image is called a member) to start processing.

Pure members were extracted from areas where the type of geological unit was identified. With 4 stages of surveying and field surveying and recording the coordinates of geological units using a high-precision GPS device and using the sampled points that corresponded to the pure pixels extracted from the PPI algorithm, the average reference spectrum of the units was extracted from the image itself and this reference spectrum It was used as an input for the classification algorithm (Figure 1).

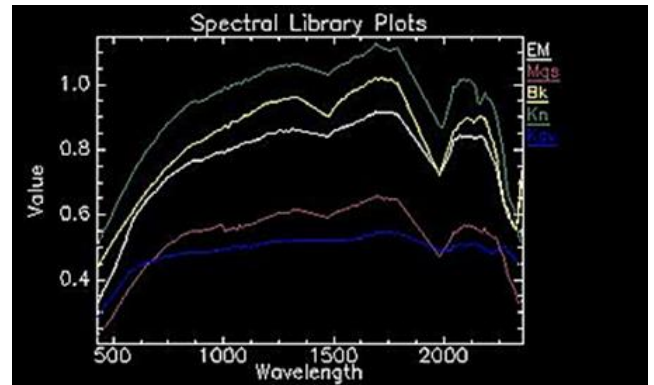


**Figure 1.** The electromagnetic spectrum extracted from the image related to the geological units of the region

**2.7. Spectral Information Divergence**

The spectral similarity between two pixels vectors was measured based on the probability distribution difference obtained from their spectral signatures (1).

$$SID = \sum_{l=1}^L p_l \log(p_l / q_l) + \sum_{l=1}^L q_l \log(q_l / p_l)$$

$$p_l = s_{jl} / \sum_{k=1}^L s_{lk}$$

$$q_1 = s_{j1} / \sum_{k=1}^L s_{jk}$$

Where p1 and q1 are spectral component probability of Si1 and Sj1 of two-pixel vectors of and rj respectively and L is the vector dimension. In the above method, the obtained value should be normal to have a picture in the range of 0 to 1.

**Table 2.** Stations of study area Guide Sarvkad

Guide	Sarvkad
Casestudy: Khoramabad	Bakhtiari
Used algorithm: SID	Kashkan
	Asmari -Shahbazan
	Gachsaran
	Other Residential area

Table 2 and Figure 2 show the studied station and SID Area map.

### 3. Results

After processing, the map of the geological formations of the studied area was obtained, divided into seven classes including Sarvak, Bakhtiari, Kashkan, Asmari-Shahbazan, Gachsaran, Residential area and other (Figure 2).

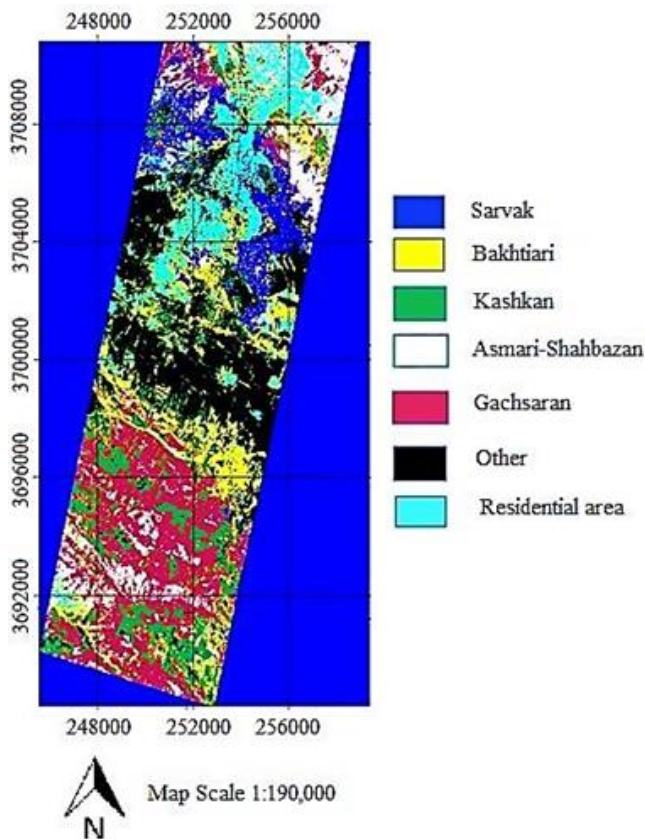


**Figure 2.** SID Area map

Table 3 shows the area of each of the seven classifications in hectares and Table 4 show Error matrix parameters.

**Table 3.** Area of geological units using the algorithm

Formation	SID (Hectare)
Sarvak	15334.65
Gachsaran	3696.93
Asmari - Shahbazan	2006.46
Kashkan	2425.59
Bakhtiari	2374.47

**Table 4.** Error matrix, general accuracy, and kappa coefficients for the results of the SID algorithm

class	Ground data (experimental pixels)						
	residential	Bakhtiari	Kashkan	Asmari	Gachsaran	Sarvak	Full pixels
Not classified	0.42	0.84	0.00	0.00	0.02	0.09	0.07
Sarvak	0.42	0.17	0.19	0.00	0.1	62.97	22.61
Gachsaran	0.42	13.34	4.46	20.92	68.05	4.76	35.98
Asmaran	0.42	19.43	8.33	75.02	28.94	17.60	28.31
Kashkan	0.00	2.53	48.06	0.08	0.87	1.02	1.9
Bakhtiari	1.69	55.57	8.91	3.35	1.96	3.89	4.26
Residential	96.62	3.72	5.04	0.63	0.06	6.02	3.39
others	0	4.39	25	0	0	3.64	3.54
Full pixels	100.00	100.00	100.00	100.00	100.00	100.00	100.00
Total accuracy: 66.71					Kappa coefficient: 0.53		

### 4. Discussion

The evaluation of the results of this research shows that the comparison of the map of geological units, which was obtained using the SID algorithm, with the maps previously prepared by the Geological Organization of Lorestan province and the Geological Organization of the country, shows the fact that the algorithm SID has a high accuracy with an overall accuracy of 66.71 percent and a kappa coefficient of 0.53 percent. Also, the results show that the SID algorithm is an efficient method for classifying the region based on existing geological units, in the research of preparing geological maps, taking into account the conditions of the region. Due to the high capability of hyperspectral images in the resolution of phenomena, it shows that the identification and separation of geological units using these images is easier and more accurate than other methods such as the use of multi-band images.

### 5. Conclusion

Preparation of maps of geological units over many years as well as conducting extensive studies and researches has now reached a point where instead of being in the area and doing fieldwork and spending a lot of time and money, with the help of remote sensing and the use of hyperspectral images in It can be done in a short time and with high accuracy. In this research, the SID algorithm was evaluated for the identification of geological units. The results of this study show that SID can help in preparing geological maps for areas where some information on the types of geological units is currently available. According to the results of calculating the area of different formations in the study area as shown in Table (4), Saruk Formation has the largest area calculated in the SID classification method. Therefore, it is suggested that in future research, sensors with a higher spatial resolution than Hyperion (with a pixel size of 30 meters) should be used to identify

valuable geological units in order to produce maps with higher accuracy.

### Acknowledgement

The authors of the research are grateful to the General Department of Industries and Mines of Lorestan province and Mr. Alireza Beyranvand.

### References

- Barton I. F, Gabriel M. J, Lyons-Baral J, Barton M. D, Duplessis L & Roberts C (2021). Extending geometallurgy to the mine scale with hyperspectral imaging: A pilot study using drone-and ground-based scanning. *Mining, Metallurgy & Exploration*, 38(2), 799-818.
- Douglas A, Kereszturi G, Schaefer L. N & Kennedy B (2022). Rock alteration mapping in and around a fossil shallow intrusion at Mt. Ruapehu New Zealand with laboratory and aerial hyperspectral imaging. *Journal of Volcanology and Geothermal Research*, 107700.
- Fonteneau L C, Martini B & Elsenheimer D (2019). Hyperspectral imaging of sedimentary iron ores–beyond borders. *ASEG Extended Abstracts*, 2019(1), 1-5.
- Johnson C. L, Browning D. A & Pendock N. E (2019). Hyperspectral imaging applications to geometallurgy: Utilizing blast hole mineralogy to predict Au-Cu recovery and throughput at the Phoenix mine, Nevada. *Economic Geology*, 114(8), 1481-1494.
- Johnson C. L, Browning D. A & Pendock N. E (2019). Hyperspectral imaging applications to geometallurgy: Utilizing blast hole mineralogy to predict Au-Cu recovery and throughput at the Phoenix mine, Nevada. *Economic Geology*, 114(8), 1481-1494.
- Lorenz S, Ghamisi P, Kirsch M, Jackisch R, Rasti B, & Gloaguen R (2021). Feature extraction for hyperspectral mineral domain mapping: A test of conventional and innovative methods. *Remote Sensing of Environment*, 252, 112129.
- Noroozi M, Kakaie R & Jalali S. E (2015). 3D Geometrical-Stochastic modeling of rock mass joint networks: case study of the right bank of Rudbar Lorestan Dam plant. *Journal of Geology and Mining Research*, 7(1), 1-10.
- Qasim M, Khan S. D & Haider R (2022). Integration of multispectral and hyperspectral remote sensing data for lithological mapping in Zhob Ophiolite, Western Pakistan. *Arabian Journal of Geosciences*, 15(7), 1-19.
- Ramanaidou E. R & Wells M. A (2012). Hyperspectral imaging of iron ores. In *Proceedings of the 10th International Congress for Applied Mineralogy (ICAM)* (pp. 575-580). Springer, Berlin, Heidelberg.
- Schodlok M. C, Frei M & Segl K (2022). Implications of new hyperspectral satellites for raw materials exploration. *Mineral Economics*, 35(3), 495-502.
- Sousa, F J, & Sousa D. J (2022). Hyperspectral Reconnaissance: Joint Characterization of the Spectral Mixture Residual Delineates Geologic Unit Boundaries in the White Mountains, CA. *Remote Sensing*, 14(19), 4914.
- Stuart M. B, Davies M, Hobbs M. J, Pering T. D, McGonigle A. J & Willmott J. R (2022). High-resolution hyperspectral imaging using low-cost components: Application within environmental monitoring scenarios. *Sensors*, 22(12), 4652.



## 5<sup>th</sup> Intercontinental Geoinformation Days

igd.mersin.edu.tr



### A quantitative and qualitative assessment from official statistics to spatial statistics: Agricultural greenhouses detection over time integrating of remote sensing and transfer learning-based machine learning approach

Fuat Kaya\*<sup>1</sup>, Gordana Kaplan<sup>2</sup>, Levent Başayığıt<sup>1</sup>

<sup>1</sup>Isparta University of Applied Sciences, Faculty of Agriculture, Department of Soil Science and Plant Nutrition, Isparta, Türkiye

<sup>2</sup>Eskisehir Technical University, Institute of Earth and Space Sciences, Eskişehir, Türkiye

#### Keywords

Remote sensing  
Greenhouse mapping  
Spatial statistics  
PlanetScope  
Sentinel 2A  
Spatiotemporal dynamics

#### Abstract

The availability of medium-resolution satellite data such as the open-access Sentinel-2 as well as high-resolution commercial satellite imagery from PlanetScope presents significant opportunities for the agricultural sector and allows us to gain insight into the land surface, land use, and their management. Agricultural Greenhouses (AGs) are the fastest-growing food or commercial ornamental production approach around cities, driven by different factors. The current study is aimed to conduct temporal greenhouse maps in the covered upland greenhouse region (Isparta-Deregümü region, Southwestern Türkiye) from 2016 to 2021 using open-access Sentinel 2 and PlanetScope imagery and machine learning algorithm in a high-performance computing environment (R Core Environment). As a result of the qualitative evaluation of satellite imagery with two different spatial and spectral resolutions, PlanetScope, which has a higher spatial resolution, was determined to be useful in the detection of AGs. Temporal greenhouse maps were generated using random forest algorithm at two-time periods, and the overall accuracy of the predictions was around 90%. While the total greenhouse area in the current area increased by 47% from 2016 to 2021 in official statistics, the methodology allowing to obtain spatial statistics detected this increase by 76%. The current study significantly improves the link between spatial statistics and official statistics.

#### 1. Introduction

Sustainable agricultural production constantly needs up-to-date spatial data that is key to various land management decisions (İbrahim ve Gobin 2021). Agricultural Greenhouses (AGs), one of the pioneers of controlled agriculture, have been expanding uncontrollably in different geographies in recent years (Li et al., 2020). The significant increase in greenhouses in certain urban areas not only changes the shape of the seasonal food supply but also can completely change the landscape of farmland in expanding regions (Ou et al., 2019).

In this context, to relieve the pressure of agricultural production on other sectors and to maintain the balance between food production and the environment, scientists in different disciplines use up-to-date technologies to make definitive decisions about the extent of greenhouse expansion. Thus, it may be necessary to better understand the temporal-spatial dynamics of a city in a short time on a regional scale. Spatial effective monitoring of greenhouses can only be done most

accurately by integrating Geographic Information System (GIS) and Remote Sensing (RS) data with advanced statistical learning methods (Kurucu and Erden 2015).

In monitoring greenhouses from satellite images (Aguilar et al., 2020), current studies tend to offer many different methods that integrate machine learning to improve classification accuracy and determine their dynamics in the long term (Koc-San 2013). Open-access Sentinel and Landsat series satellite images have been the subject of studies with medium spatial resolutions (Aguilar et al., 2020; İbrahim and Gobin 2021).

This study aims to i) present a qualitative assessment using PlanetScope and Sentinel series satellite images for temporal greenhouse mapping in an area where typical highland greenhouse cultivation is active (Buyurgan et al., 2019); ii) identify greenhouse areas and present a quantitative assessment with machine learning and transfer of the learned model, iii) determine the distribution of greenhouses between 2016

#### \* Corresponding Author

(fuatkaya@isparta.edu.tr) ORCID ID 0000-0003-0011-9020  
(kaplangorde@gmail.com) ORCID ID 0000-0001-7522-9924  
(leventbasayigit@isparta.edu.tr) ORCID ID 0000-0003-2431-5763

#### Cite this study

Kaya F, Gordana K & Başayığıt L (2022). A quantitative and qualitative assessment from official statistics to spatial statistics: Agricultural greenhouses detection over time integrating of remote sensing and machine learning algorithm. 5<sup>th</sup> Intercontinental Geoinformation Days (IGD), 64-68, Netra, India

and 2021 by integrating spatial statistics information with official statistics.

## 2. Method

### 2.1. Study area

The current study area is located in the central part of Isparta Province, Türkiye (279504 - 285538 E, 4183775 - 4188045 N - WGS 1984 UTM North Zone 35) (Figure 1).

The study area has a typical Mediterranean climate, characterized by a rainy spring, a hot summer, and a cold and wet winter. Since it is close to the province of Antalya, which has a high vegetable-fruit export potential, production in the plateau starts in this region when the production on the Mediterranean coast ends in the greenhouses. The exporter can continue this export throughout the year (Buyurgan et al., 2019).

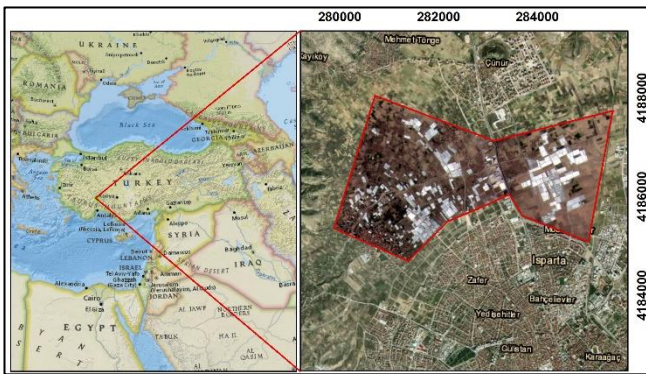


**Figure 1.** Location of the study area and distribution of AGs in PlanetScope satellite image (September 2021) with natural colours band combination

### 2.2. Data Acquisition for official statistics and remote sensing imagery

According to TURKSTAT (2022), while the greenhouse area in the center district of Isparta was 1715 decares in 2016, in 2021, it was recorded as 2520 decares (Figure 2). Considering the most recent data, the majority of the greenhouse areas (about 80%) are located in the central district of Deregümü, Çünür and Yakaören villages of Isparta district (Anonymous, 2022).

An increase of approximately 34% in the field of greenhouse agriculture was recorded in 2017 compared to 2016.

September 2016, 2017, and 2021 images of the open-access Sentinel 2A, which contains the short-wave infrared band sensitive to anthropogenic structures, and the PlanetScope satellite, which includes the visible and near-infrared band with higher spatial resolution, were provided (ESA 2022; Planet Team 2022).

### 2.3. Qualitative evaluation

An evaluation was presented considering both satellite images' spectral and spatial differences. A composite image was produced using the B12-8A-B4 (SWIR, NIR narrow, Red) band combination of the Sentinel 2 satellite. This process was performed on metafile satellite images taken at 20 meters resolution.

Planet Scope satellite images were obtained at 3 m spatial resolution. From the Planet Scope satellite imagery, natural color band combination was created.

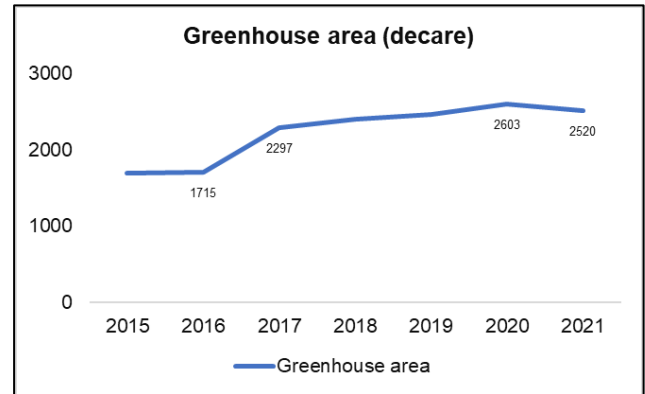


**Figure 2.** Agricultural greenhouses area amounts in Isparta Central District.

### 2.4. Quantitative evaluation

Supervised machine learning algorithms use data samples or experience to train classification results to optimize. In this study, random forest classifier was used for modeling. The "Greenhouse absence-presence" model, learned from the observations in 2021, was transferred to the 2016 images.

#### 2.4.1. Dataset for training samples and modelling process

Control data were collected by photo-interpretation of "historical images" in Google Earth® in September 2021. 122 points were labelled as "non-greenhouse", and 128 points were labelled as "Greenhouse". To solve this binary classification problem, we used the "randomForest" package R (Breiman 2001; R Core Team 2022). The model was established by randomly choosing 70% of the observations as training points, while the rest of 30% were randomly selected as validation points to evaluate the accuracy of the classification results in 2021. Different criteria were used to evaluate the produced greenhouse maps for 2021 year in this study, including overall accuracy, kappa coefficient, producer's accuracy, and user's accuracy (Congalton, 1991).

#### 2.4.2. Area Changes Analysis

Pixels identified as "Greenhouse" in 2016 and 2021 were vectorized using the "ArcGIS - ArcToolbox-Conversion Toolbox-Raster to Polygon" tool and area calculations were converted in "decares". The obtained results were compared with TURKSTAT (2022) statistics. The methodological flow chart was presented in Fig. 3.

## 3. Results

### 3.1. Temporal greenhouse maps and their qualitative evaluation

After the generated multi-time band combination maps, evaluations are presented for 2 different satellites

to explore the scene composition change of the greenhouses.

The results showed that there is a greenhouse increase in the area north of the study area, as it can be seen at Figure 4. This increase can be clearly distinguished qualitatively by the SWIR band combination of the Sentinel 2A satellite. Also in 2021, greenhouse areas increased significantly in the eastern region of the study area.

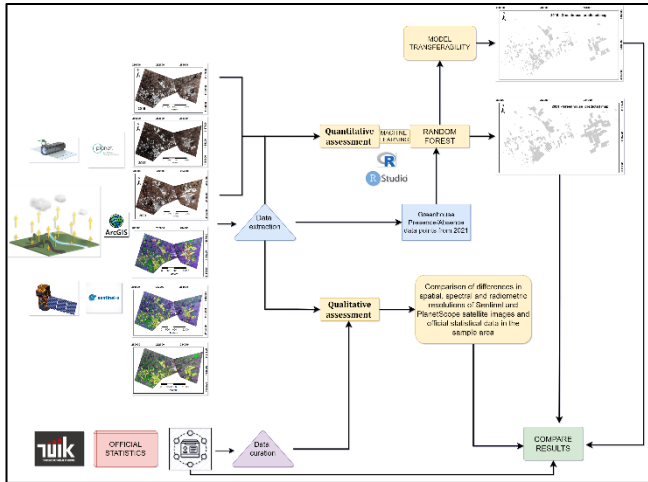


**Figure 3.** Flow chart of the methodological conducted for AGs detection and comparison with official statistics

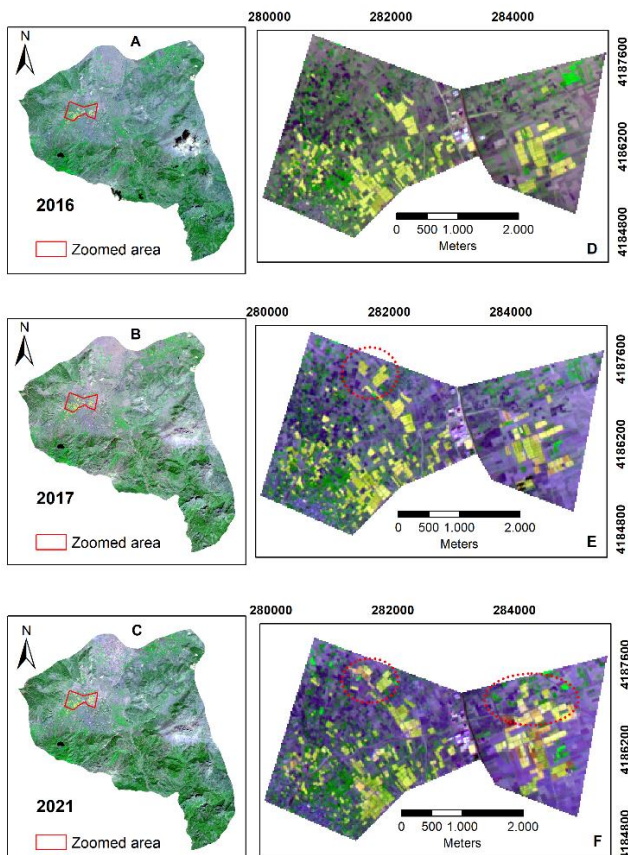


**Figure 4.** Qualitative evaluation of AGs over the years using the SWIR band combination of the Sentinel 2A-MSI satellite.

While Sentinel-2's band combination containing the shortwave infrared bands was useful for the photo-

interpretation, it was noteworthy that the Planet Scope satellite could better reflect the boundaries of greenhouses (Figure 5). This is expected as PlanetScope has significantly better spatial resolution than Sentinel-2.

Especially the time series (Figure 4) of Sentinel 2A satellite with SWIR band was not preferred for quantitative evaluation. Because it is seen that these images are very affected by the building material used in the greenhouses. Greenhouses with fine plastic materials can be mixed with bare soil in these images (Figure 4-E, F).

### 3.2. Greenhouse Maps and Their Quantitative evaluation and Area Change of Greenhouses during 2016–2021

Temporal greenhouse maps were produced using RF classifier for 2016 and 2021 (Figure 6). The overall accuracy of the RF model, which was also transferred to 2016, in 2021 is more than 90% and the user's accuracy of the greenhouse class is over 95%, representing map accuracy (Table 1). The performance metrics of classification process shown in Table 1 showed that the mapping results of the greenhouses could meet the needs for measuring their spatio-temporal dynamics in this study. It can be stated that classification errors occur in plate roofs of buildings and greenhouses where soil is seen a lot under the cover.

Looking at the official statistics (Table 1), 805 da increase in greenhouse area from 2016 to 2021 was determined while 895 da because of the Planet scope satellite being classified with the RF model (Table 1). This finding is an indication that the increase in greenhouse areas in the area of interest (AOI) we focus on is higher than in the district in general. Here, relatively, the presence of sheet roof structures may trigger an excessive increase. Because in our AOI via quantitative approach, a greenhouse area estimates of more than 80% of the official statistical value (Table 1) was made.

**Table 1.** Accuracy assessment of greenhouse maps (2021) and the total area of the greenhouses by comparing dates (O: Overall, A: Accuracy, P: Producer's, U: User's)

Accuracy assessment greenhouse map					
Model	Class	PA	UA	OA	Kappa
RF	Non-Greenhouse	95.54%	87.70%	90.18	0.80
	Greenhouse	89.13%	96.09%	%	
The total area changes of greenhouses					
		Official statistics		Spatial statistics	
Years	2016	2021	2016	2021	
AGs (da)	1715	2520	1170	2065	

### 3.3. Importance levels of satellite bands

The Blue band of the Planet Scope satellite was the most important variable in distinguishing plastic greenhouses planned for planting different plants, which had significantly higher “digital number” values (Figure 7-c) compared to non-greenhouse areas.

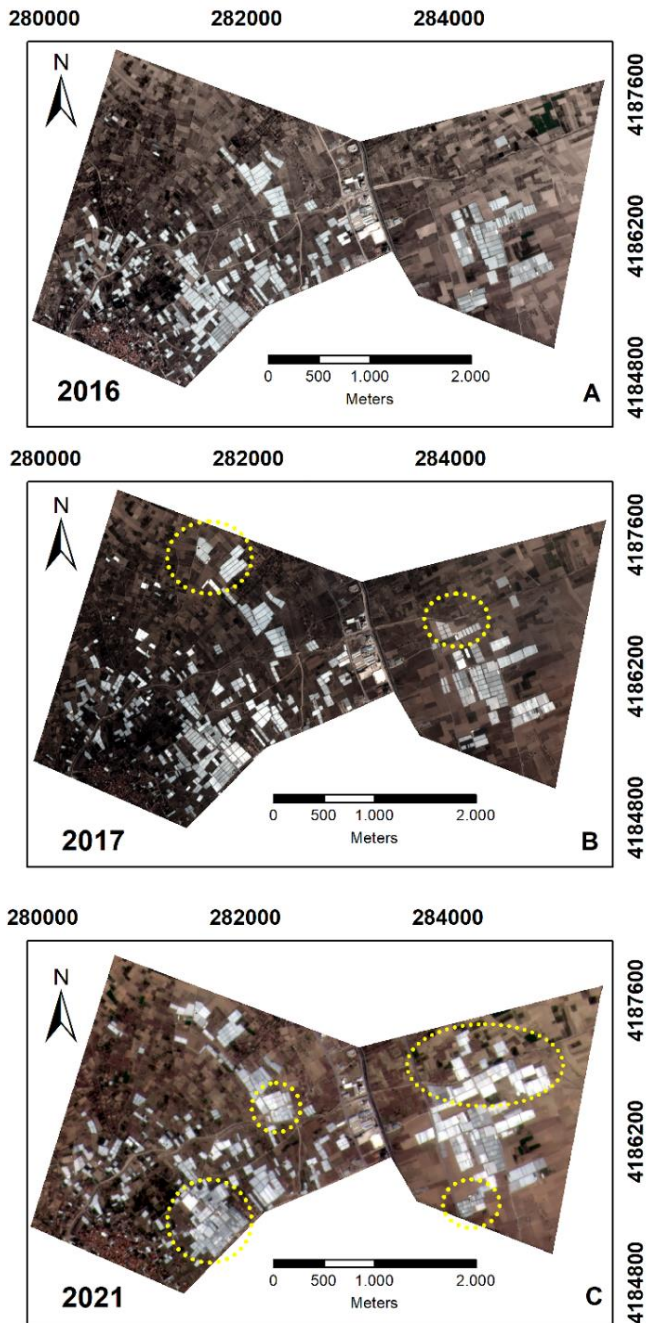


**Figure 5.** Qualitative evaluation of AGs over the years using the natural band combination of the PlanetScope satellite.

#### 4. Discussion

Greenhouse mapping as time series and analysis of related dynamics are important for agronomists and different disciplines to understand and evaluate the sustainable development of protected agriculture.

The proposed multi-temporal greenhouse mapping and comparison with official statistics method used open access medium and high-resolution satellite images and RF supervised classification algorithm.

Greenhouse areas in 2017, where there was a sharp increase (about 34%) in official statistics, were qualitatively more noticeable with the Planet Scope satellite.

Quantitative calculations based on remote sensing in our study area, which includes the borders of 3 villages

where production is intensified in the central district of Isparta, is expected to be below the official statistics (Table 1). The next goal here is to focus on more quantitative methods for the entire district center.

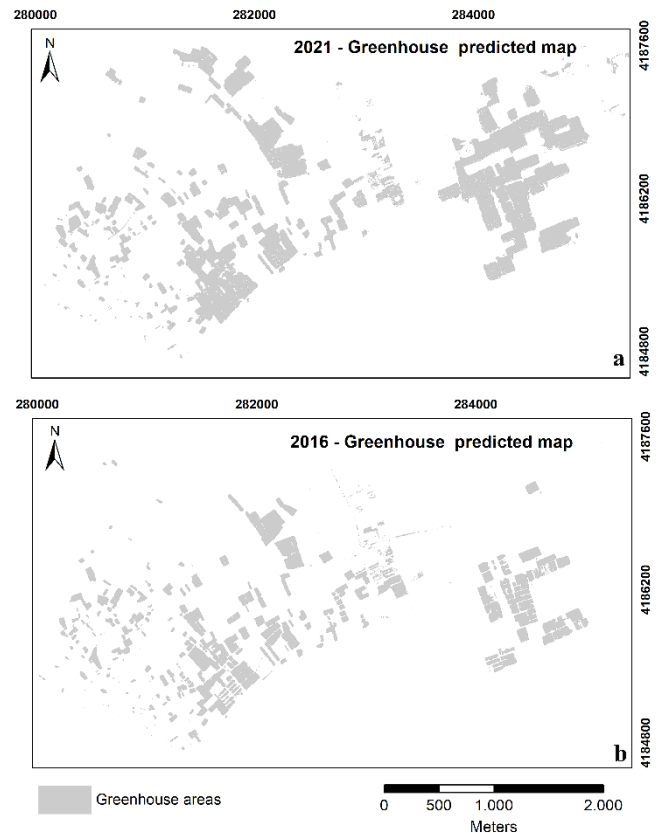


**Figure 6.** Temporal density of agricultural greenhouses expansion (a:2021, b:2016).

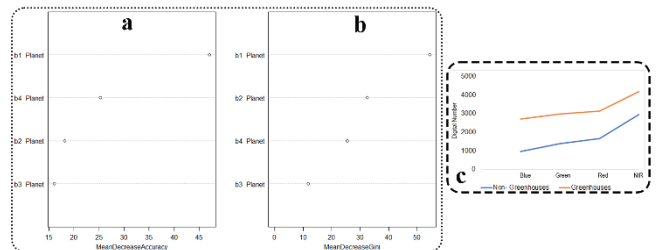


**Figure 7.** Importance levels of the PlanetScope bands used to predict the agricultural greenhouses using the RF algorithms (a-b). Digital number profile of agricultural greenhouse status (c).

#### 5. Conclusion

In this study, we first made maps of the development of highland greenhouse cultivation in Isparta from 2016 to 2021. Compared to greenhouse detection studies that traditionally involve accuracy assessment, our study significantly advances the link between spatial distribution and official statistics. Furthermore, compared to studies based on official statistical data such as agricultural extension, our study includes spatial statistics of temporal remote sensing data and may contribute a more intuitive approach for future studies.

## Acknowledgement

We acknowledge the usage of modified Copernicus Sentinel 2A Level 2A data and PlanetScope Ortho Scene Level 3B Product data.

## References

- Aguilar, M. Á., Jiménez-Lao, R., Nemmaoui, A., Aguilar, F. J., Koc-San, D., Tarantino, E., & Chourak, M. (2020). Evaluation of the Consistency of Simultaneously Acquired Sentinel-2 and Landsat 8 Imagery on Plastic Covered Greenhouses. *Remote Sensing*, 12, 2015. <https://doi.org/10.3390/rs12122015>
- Anonymous. (2022). Yayla Şartlarında Örtüaltı Yetiştiriciliğinde Hasat Başladı. Accessed on <https://isparta.tarimorman.gov.tr/Haber/478/Yayla-Sartlarinda-Ortualti-Yetistiriciliginde-Hasat-Basladi>
- Breiman, L. (2001). Random forests. *Machine Learning*, 45, 5–32.
- Buyurgan, K., Altunbaş, S. & Gözükara, G. (2019). Farklı fizyografya ünitelerinde gelişen yayla seracılığının zamansal ve mekansal değişiminin uzaktan algılama ve CBS teknikleri ile belirlenmesi: Elmalı/Antalya örneği. *Derim*, 36, 217-227. <https://doi.org/10.16882/derim.2019.614303>
- Congalton R, (1991). A review of assessing the accuracy of classifications of remotely sensed data. *Remote Sensing of Environment*, 37, 35–4
- ESA (2022). European Space Agency. Copernicus Open Access Hub.
- Ibrahim, E., & Gobin, A. (2021). Sentinel-2 Recognition of Uncovered and Plastic Covered Agricultural Soil. *Remote Sensing*, 13, 4195. <https://doi.org/10.3390/rs13214195>
- Koc-San, D. (2013). Evaluation of different classification techniques for the detection of glass and plastic greenhouses from WorldView-2 satellite imagery. *Journal of Applied Remote Sensing*, 7, 073553. <https://doi.org/10.1117/1.JRS.7.073553>
- Kurucu, Y., & Erden, H. (2015). Control of farmer statements integrated in national farmer register system by remote sensing data. 2015 Fourth International Conference on Agro-Geoinformatics (Agro-geoinformatics), 97–100. Istanbul, Türkiye. <https://doi.org/10.1109/AgroGeoinformatics.2015.7248144>
- Ou, C., Yang, J., Du, Z., Liu, Y., Feng, Q., & Zhu, D. (2020). Long-Term Mapping of a Greenhouse in a Typical Protected Agricultural Region Using Landsat Imagery and the Google Earth Engine. *Remote Sensing*, 12, 55. <https://doi.org/10.3390/rs12010055>
- Planet Team (2022) Planet Explorer.
- R Core Team. (2022) R: A Language and Environment for Statistical Computing; R Foundation for Statistical Computing: Vienna, Austria.
- Turkstat. (2022). Turkish Statistical Institute, Agriculture database. Date of access: 17.10.2022, website: <https://biruni.tuik.gov.tr/medas/?locale=tr>



## 5<sup>th</sup> Intercontinental Geoinformation Days

igd.mersin.edu.tr



# Approximation of COVID-19 effect on land surface temperature using MODIS data over YSR district, India

Jagadish Kumar Mogaraju \*<sup>1</sup>

<sup>1</sup>Lovely Professional University, Research Scholar, Department of Geography, Phagwara, India

### Keywords

Remote sensing  
LST  
MODIS  
COVID-19  
GIS

### Abstract

This work involved using satellite-derived data to know the disparities in Land Surface Temperatures (LST) due to the COVID-19 pandemic. To know the effect of this pandemic on LST, MODIS data from three years before the pandemic (2017-2019) was procured and compared with post-pandemic data (2020-2022). It was observed that there is a decreasing trend in the LST, ranging from 17.13 to 15.76 in terms of average LST difference. The northern portion of the study area has pronounced LST variation than the southern portion. It was observed that post COVID LST has a strong positive correlation with pre COVID LST. The LST of 2022 has a positive correlation with the LST of 2017 and a slight correlation with the LST from 2018 to 2021. LST time series plots were presented in this study along with the GIS maps. This work supports the notion that COVID-19 has lowered LST relatively.

## 1. Introduction

Land surface temperature (LST) is an important parameter as it affects the population directly and needs to be checked regularly (Zhang, et al., 2019). The urban landscape change has changed the surface temperature patterns, especially in developed areas (Dutta, et al., 2019; Mukherjee & Singh, 2020). Land Use Land Cover changes have altered LST in many regions, and satellite-derived data was used to understand the LST dynamics (Guha & Govil, 2022; Ullah et al., 2019). Several studies have focused on investigating the effect of COVID-19 on LST using satellite products (Abir, et al., 2021; Bera, Chatterjee, et al., 2022; Ghosh, et al., 2022; Hidalgo García & Arco Díaz, 2022; Parida, et al., 2021; Teufel et al., 2021; Xiao, et al., 2021; Xin et. al., 2022). This work focuses on understanding the LST changes during preCOVID (2017-2019) and postCOVID (2020-2022) periods. YSR district of Andhra Pradesh state of India is chosen as a study area for this research.

## 2. Method

MODIS data was procured for the years starting from 2017 through 2022. The data was classified as preCOVID (2017-2019) and postCOVID (2020-2022). MOD11A2

products were used as they provide LST of 8 days average per pixel. They have a 1200 x 1200 km grid with a spatial resolution of one kilometer. LST images of daytime have a 0.02 scale factor with a 16-bit unsigned integer data type. The GIS maps were prepared using the composite images generated from all months for the years starting from 2017 to 2022. Time series plots of LST for these years are provided. The methodology used in this work is shown in Figure 1.

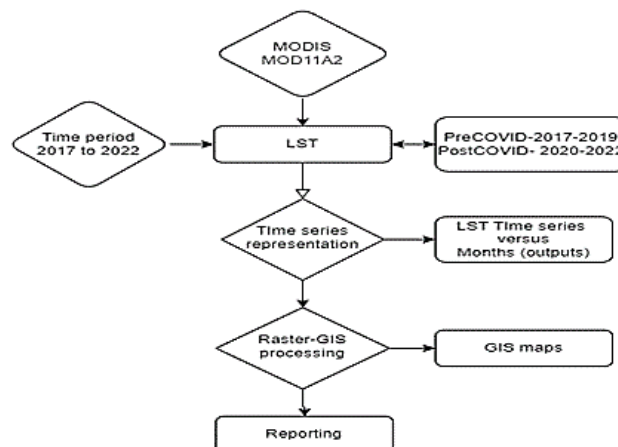


Figure 1. Methodology

\* Corresponding Author

<sup>\*</sup>(e-mail) ORCID ID xxxx - xxxx - xxxx - xxxx

Cite this study

Mogaraju J. K. (2022). Approximation of COVID-19 effect on land surface temperature using MODIS data over YSR district, India. 5<sup>th</sup> Intercontinental Geoinformation Days (IGD), 69-73, Netra, India

### 3. Results

The LST maps obtained in this study are given in figures 2 through 7. The LST map of 2017 showed that this region has a low temperature of 26.1°C and a high temperature of 43.5°C. The LST map of 2018 reflects that this region has a low temperature of 26.3°C and a high temperature of 43.8°C. The LST map of 2019 showed that this area experienced a low temperature of 27.2°C and a high temperature of 43.8°C. The LST map of 2020 explains that this area experienced a low temperature of 26.8°C and a high temperature of 43.2°C. The LST map of 2021 reflects that this area experienced a low temperature of 26.1°C and a high temperature of 41.7°C. The LST map of 2022 (without Dec) reflects that this area has a low temperature of 25.7°C and a high temperature of 41°C. The LST change is more evident in the north portion of the study area than south. This can be attributed to the natural geomorphological setup of the region. There are several high elevated areas in the south portion than the north.

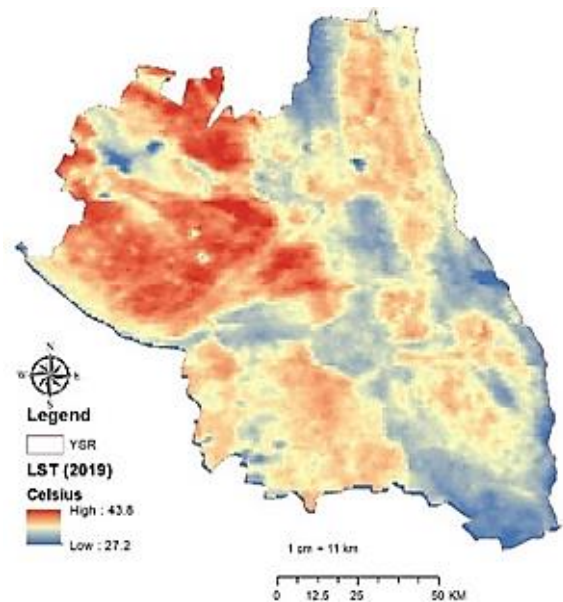


Figure 4. Land surface temperature (2019)

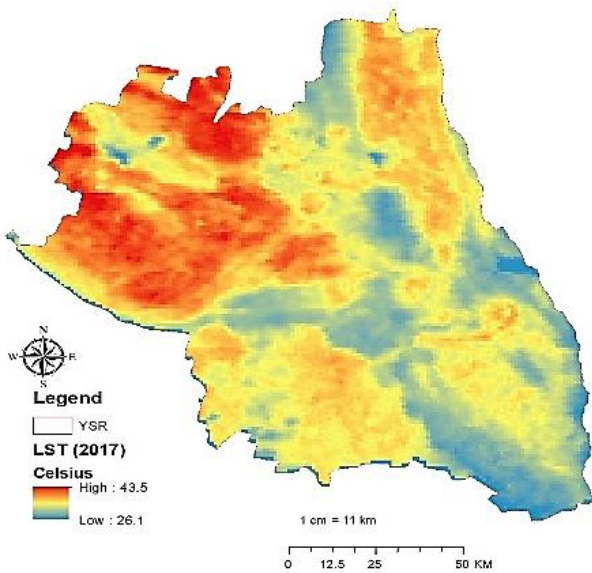


Figure 2. Land surface temperature (2017)

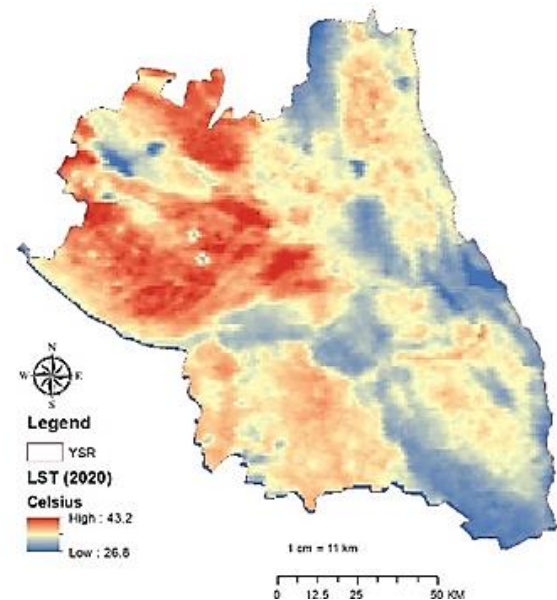


Figure 5. Land surface temperature (2020)

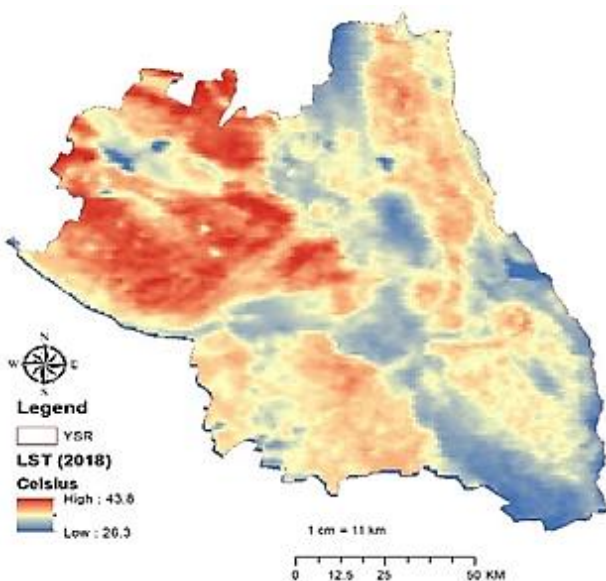


Figure 3. Land surface temperature (2018)

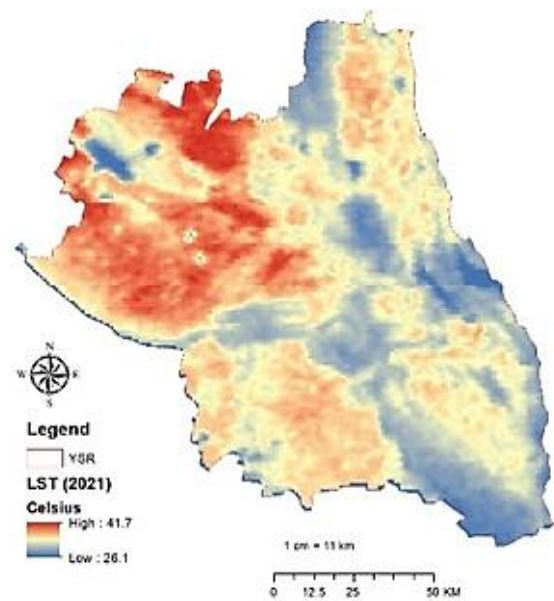


Figure 6. Land surface temperature (2021)

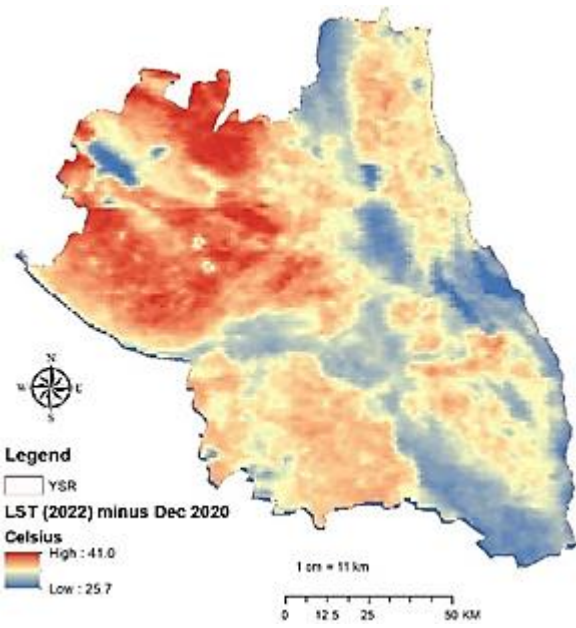


Figure 7. Land surface temperature (2022)

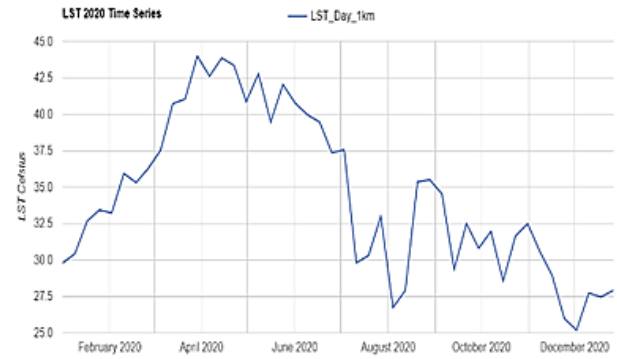


Figure 11. LST time series plot (2020)

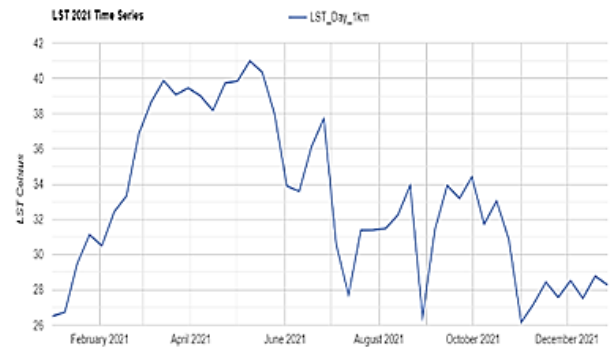


Figure 12. LST time series plot (2021)



Figure 8. LST time series plot (2017)



Figure 13. LST time series plot (2022)



Figure 9. LST time series plot (2018)



Figure 10. LST time series plot (2019)

	2017	2018	2019	2020	2021	2022
2017	1					
2018	0.748983	1				
2019	0.816605	0.694646	1			
2020	0.867334	0.811889	0.842392	1		
2021	0.823853	0.772584	0.78577	0.801296	1	
2022	0.745609	0.585115	0.656755	0.678405	0.597222	1

Figure 14. Correlation plot

The LST time series plots (LST-TS) obtained in this study are given in figures 8 through 13. The LST-TS of 2017 showed that there were high temperatures (>35°C) from February to August 2017 (slight dip in July) than the rest of the months. The LST-TS of 2018 reflects that there are high temperatures (>34°C) from February to October 2018 (slight dip in August) than the rest of the months. The LST-TS of 2019 showed that there were high temperatures (>35°C) from February to September 2019 (slight dip in August) than the rest of the months. The

LST-TS of 2020 showed that there are high temperatures (>35°C) from February to September 2020 (slight dip in August) than the rest of the months. The LST-TS of 2021 showed that there are high temperatures (>35°C) from February to July 2021 (slight dip in June) than the rest of the months. The LST-TS of 2022 showed that there are high temperatures (>35°C) from March to June 2022 (slight dip in may) than the rest of the months.

The post COVID (2020-2021(without 2022)) LST has a strong positive correlation with pre COVID (2017-2019) LST, and this is represented in figure 14 as a correlation plot. The LST of 2022 has a positive correlation with the LST of 2017 and a slight correlation with the LST from 2018 to 2021.

#### 4. Discussion

This work was based on the hypothesis that there will be a hugely positive effect of the COVID-19 pandemic on LST. Through this work, it is evident that there is a slight decrease in the LST. This can be attributed to several factors, and lockdown is one of them. The decrease in air pollution has also contributed to a decrease in surface temperatures. The low and high temperatures recorded during pre-pandemic periods were 26.2/43.5°C, 26.3/43.8 °C, and 27.2/43.8°C respectively. The low and high temperatures recorded during post-pandemic periods were 26.8/43.2°C, 26.1/41.7°C, and 25.7/41°C, respectively. The temperature difference obtained was 17.3, 17.5, and 16.6 during the pre-pandemic period. The temperature difference obtained were 16.4, 15.6, and 15.3 during the post-pandemic period. There is a decreasing trend in the LST ranging from 17.13 (pre) (Averaged difference) to 15.76 (post) (Averaged difference).

#### 5. Conclusion

This work supports the notion that the COVID-19 pandemic has a positive effect on LST owing to several other factors like lockdown, decreased pollution, etc. It is concluded that satellite-derived products (MODIS) with GIS processing can be used in understanding Land Surface Temperatures.

#### Acknowledgement

This work is a self-funded project undertaken as a part of Ph.D. work. The authors are grateful to Lovely Professional University for allowing this work to be presented at this conference.

#### References

- Abir, F. A., Ahmmed, S., Sarker, S. H., & Fahim, A. U. (2021). Thermal and ecological assessment based on land surface temperature and quantifying multivariate controlling factors in Bogura, Bangladesh. *Heliyon*, 7(9), e08012. <https://doi.org/10.1016/j.heliyon.2021.e08012>
- Bera, D., Chatterjee, N. D., Ghosh, S., Dinda, S., & Bera, S. (2022). Recent trends of land surface temperature in relation to the influencing factors using Google Earth Engine platform and time series products in megacities of India. *Journal of Cleaner Production*, 379, 134735. <https://doi.org/10.1016/j.jclepro.2022.134735>
- Dutta, D., Rahman, A., Paul, S. K., & Kundu, A. (2019). Changing pattern of urban landscape and its effect on land surface temperature in and around Delhi. *Environmental Monitoring and Assessment*, 191(9), 551. <https://doi.org/10.1007/s10661-019-7645-3>
- Ghosh, S., Kumar, D., & Kumari, R. (2022). Assessing spatiotemporal dynamics of land surface temperature and satellite-derived indices for new town development and suburbanization planning. *Urban Governance*. <https://doi.org/10.1016/j.ugj.2022.05.001>
- Guha, S., & Govil, H. (2022). Seasonal impact on the relationship between land surface temperature and normalized difference vegetation index in an urban landscape. *Geocarto International*, 37(8), 2252-2272. <https://doi.org/10.1080/10106049.2020.1815867>
- Hidalgo García, D., & Arco Díaz, J. (2022). Impacts of the COVID-19 confinement on air quality, the Land Surface Temperature and the urban heat island in eight cities of Andalusia (Spain). *Remote Sensing Applications: Society and Environment*, 25, 100667. <https://doi.org/10.1016/j.rsase.2021.100667>
- Mukherjee, F., & Singh, D. (2020). Assessing Land Use-Land Cover Change and Its Impact on Land Surface Temperature Using LANDSAT Data: A Comparison of Two Urban Areas in India. *Earth Systems and Environment*, 4(2), 385-407. <https://doi.org/10.1007/s41748-020-00155-9>
- Parida, B. R., Bar, S., Kaskaoutis, D., Pandey, A. C., Polade, S. D., & Goswami, S. (2021). Impact of COVID-19 induced lockdown on land surface temperature, aerosol, and urban heat in Europe and North America. *Sustainable Cities and Society*, 75, 103336. <https://doi.org/10.1016/j.scs.2021.103336>
- Parida, B. R., Bar, S., Roberts, G., Mandal, S. P., Pandey, A. C., Kumar, M., & Dash, J. (2021). Improvement in air quality and its impact on land surface temperature in major urban areas across India during the first lockdown of the pandemic. *Environmental Research*, 199, 111280. <https://doi.org/10.1016/j.envres.2021.111280>
- Teufel, B., Sushama, L., Poitras, V., Dukhan, T., Bélair, S., Miranda-Moreno, L., ... Bitsuamlak, G. (2021). Impact of COVID-19-Related Traffic Slowdown on Urban Heat Characteristics. *Atmosphere*, 12(2), 243. <https://doi.org/10.3390/atmos12020243>
- Ullah, S., Tahir, A. A., Akbar, T. A., Hassan, Q. K., Dewan, A., Khan, A. J., & Khan, M. (2019). Remote Sensing-Based Quantification of the Relationships between Land Use Land Cover Changes and Surface Temperature over the Lower Himalayan Region. *Sustainability*, 11(19), 5492. <https://doi.org/10.3390/su11195492>
- Xiao, Y., Zhao, W., Ma, M., & He, K. (2021). Gap-Free LST Generation for MODIS/Terra LST Product Using a Random Forest-Based Reconstruction Method. *Remote Sensing*, 13(14), 2828. <https://doi.org/10.3390/rs13142828>
- Xin, J., Yang, J., Sun, D., Han, T., Song, C., & Shi, Z. (2022). Seasonal Differences in Land Surface Temperature under Different Land Use/Land Cover Types from the

- Perspective of Different Climate Zones. *Land*, 11(8), 1122. <https://doi.org/10.3390/land11081122>
- Zhang, Y., Middel, A., & Turner, B. L. (2019). Evaluating the effect of 3D urban form on neighborhood land surface temperature using Google Street View and geographically weighted regression. *Landscape Ecology*, 34(3), 681–697. <https://doi.org/10.1007/s10980-019-00794-y>



## 5<sup>th</sup> Intercontinental Geoinformation Days

igd.mersin.edu.tr



### Evaluation of the TEC prediction performance of NeQuick2 model

Salih Alcay<sup>1</sup>, Sermet Ogutcu<sup>1</sup>, Gurkan Oztan<sup>\*2</sup>, Behlul Numan Ozdemir<sup>3</sup>

<sup>1</sup>Necmettin Erbakan University, Engineering Faculty, Department of Geomatics Engineering, Konya, Türkiye

<sup>2</sup>Nige Omer Halisdemir University, Bor Vocational School, Department of Land Registry and Cadastre, Nigde, Türkiye

<sup>3</sup>Konya Technical University, Engineering and Natural Science Faculty, Department of Geomatics Engineering, Konya, Türkiye

#### Keywords

GPS  
NeQuick2  
RMSE  
TEC

#### Abstract

This paper examines the performance of the NeQuick2 model, an empirical three-dimensional ionospheric electron density model, in terms of TEC prediction. The investigation was carried out for three months period in 2022 (January-March), which includes geomagnetic active, solar active, and calm days. In order to evaluate the accuracy of the model, NeQuick2-VTEC values were compared with the TEC data from four GPS stations in different regions. The results show that the differences between the VTEC values obtained from the NeQuick2 and IGS are less on calm days and at stations in high latitude regions. However, discrepancies increase on geomagnetic and solar active days.

#### 1. Introduction

The ionosphere is a part of Earth's upper atmosphere that contains free ions and electrons, affecting the transmission of electromagnetic signals. The density of free electrons and ions in the ionosphere is not constant, and changes depending on various factors such as geomagnetic activity, solar activity, and natural disasters. Thus, regularly monitoring the changes in the ionosphere and modeling the layer is of great importance. In order to describe the ionosphere, physical models, mathematical models, and empirical models are generally used (Wang et al 2022). Among them, empirical models are widely used. The main parameter used to examine the changes in the ionosphere is Total Electron Content (TEC) which is defined as the total number of electrons along a ray path of 1 m<sup>2</sup> cross-section. In recent years GNSS is widely used for the study of the ionosphere and verification of the empirical models.

Among the empirical models, the International Reference Ionosphere (IRI) model and the NeQuick model are widely used. Both models are regularly improved and updated. Recent versions of these models are IRI-2020 and NeQuick2. Many studies have been conducted on the analysis of both models from different aspects (Pietrella et al. 2017; Alcay et al. 2017; Atıcı et

al. 2021; Guo et al 2021; Alcay 2021; Liu et al. 2022; Iluore et al. 2022; Wang et al. 2022; Poudel et al. 2022).

In this study, TEC prediction performance of NeQuick2 model was evaluated over four IGS stations in different regions.

#### 2. Method

In this study, quarterly GPS-VTEC values of MDVJ, ZECK, GUUG, and CHPI IGS stations were used for validation of the NeQuick2 model. The locations of the stations are given in "Fig. 1".

In order to examine whether there is any activity on the experimental days, the kp, Dst, and F10.7 indices, which indicate the level of geomagnetic storm, geomagnetic activity, and solar activity, respectively, were taken into consideration "Fig. 2". The dashed lines in "Fig. 2" represent threshold values for the presence of activity.

GPS-VTEC values were obtained using ionolabtecv1.35 software (<http://www.ionolab.org/index.php?page=index&language=tr>). Details of the software are provided in Arikan et al. (2003), (2004), Nayir et al. (2007), and Sezen et al. (2013). NeQuick2 VTEC values were obtained using the web interface of the model available at <https://t-ict4d.ictp.it/nequick2/nequick-2-web-model>.

#### \* Corresponding Author

(salcay@erbakan.edu.tr) ORCID ID 0000-0001-5669-7247  
(sermetogutcu@erbakan.edu.tr) ORCID ID 0000-0002-2680-1856  
(oztangurkan@ohu.edu.tr) ORCID ID 0000-0002-7629-4629  
(bnozdemir@ktun.edu.tr) ORCID ID 0000-0001-7351-1870

#### Cite this study

Alcay S, Ogutcu S, Oztan G & Ozdemir B N (2022). Evaluation of the TEC Prediction Performance of NeQuick2 Model. 5<sup>th</sup> Intercontinental Geoinformation Days (IGD), 74-77, Netra, India



Figure 1. Location of the IGS stations used

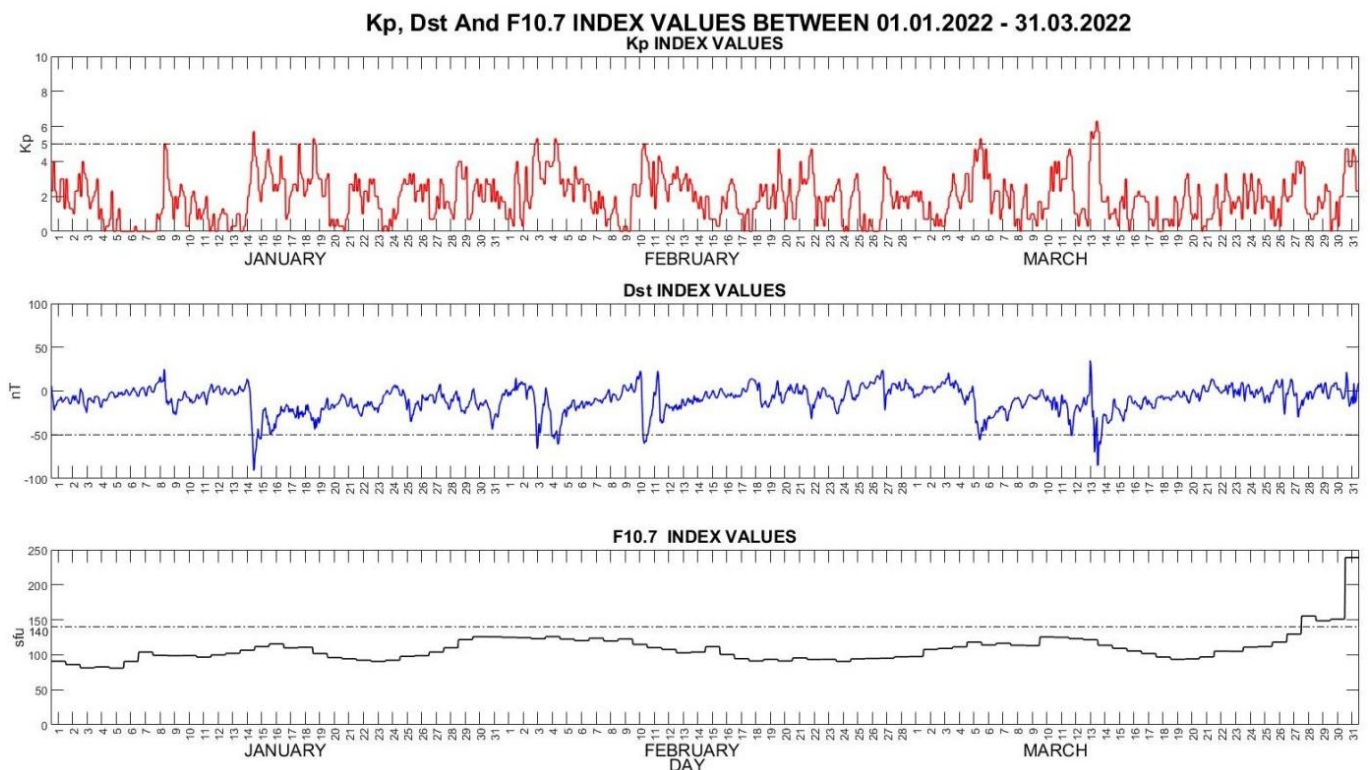


Figure 2. kp, Dst and F10.7 index values

### 3. Results and Analysis

The differences between obtained hourly GPS-VTEC and NeQuick2 VTEC values between 01.01.2022 and 31.03.2022 are given in “Fig. 3”. “Fig. 3” shows that VTEC differences are larger in February and March compared to January, particularly at GUUG and CHPI stations. The differences in the calm day range between 0.06-23.87 TECU, 2.01-29.24 TECU, 0.02-61.48 TECU, and 3.69-66.61 TECU for MDVJ, ZECK, GUUG, and CHPI

stations, respectively. Since the differences are large, the effects of solar and geomagnetic activities are not clearly observed. According to the threshold values, active and calm days were chosen and corresponding mean and RMS values were computed “Table 2”. As given in “Table 2”, the VTEC differences are larger on active days, and the mean and RMS values of the GUUG and CHPI stations located in the equatorial region are relatively large.

**GPS-VTEC AND NEQUICK 2-VTEC DIFFERENCES BETWEEN 01.01.2022 - 31.03.2022**

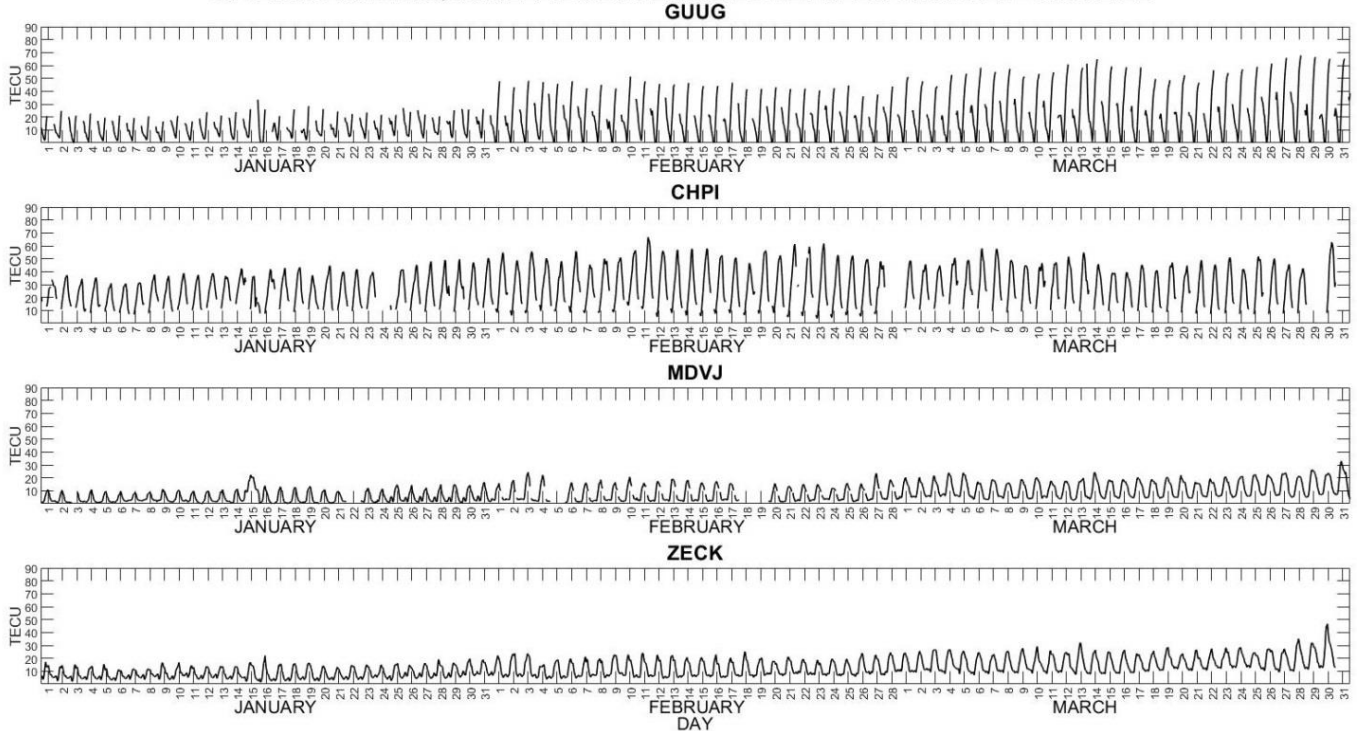


**Figure 3.** Differences between GPS-VTEC and NeQuick2 VTEC values

**Table 1.** Mean and RMS of differences corresponding to stations

Differences between GPS-VTEC and NeQuick2-VTEC		Mean	RMS
Active Days	GUUG	20.52	27.12
	CHPI	30.01	32.67
	MDVJ	9.87	12.46
	ZECK	13.88	16.23
Calm Days	GUUG	17.46	22.22
	CHPI	28.32	31.43
	MDVJ	7.68	9.54
	ZECK	11.88	13.30

**4. Conclusion**

In this study, the TEC prediction performance of the NeQuick2 model was evaluated with a comparative approach with GPS TEC values. For this purpose, hourly data of 4 IGS stations between January 1, 2022 and March 31, 2022 were taken into account. According to the results, the differences are higher on geomagnetic and solar active days. In addition, the differences of the two stations located in the equatorial region are higher than the other stations.

**Acknowledgement**

The authors would like to thank the Telecommunications/ICT for Development (T/ICT4D) Laboratory of the Abdus Salam International Centre for Theoretical Physics for the NeQuick2 model and the Ionospheric Research Laboratory (IONOLAB) for the ionolabtecv1.35 software. We also thank the

International GNSS Service (IGS) for providing GPS observation data.

**References**

Alcay, S., Oztan, G., & Selvi, H.Z. (2017). Comparison of IRI\_PLAS and IRI\_2012 model predictions with GPS-TEC measurements in different latitude regions, *Annals of Geophysics*, 6a0(5), 0549. <https://doi.org/10.4401/ag-7311>

Alcay, S. (2021). Analysis of the TEC prediction performance of IRI-2016 model in the mid-latitude region, *Geomagnetism and Aeronomy*, 61, 600–618. <https://doi.org/10.1134/S0016793221040149>

Arikan, F., Erol, C.B., & Arikan, O. (2003). Regularized estimation of vertical total electron content from Global Positioning System data, *Journal of Geophysical Research*, 108 (A12), 1469. <https://doi.org/10.1029/2002JA009605>

Arikan, F., Erol, C.B., & Arikan, O. (2004). Regularized estimation of VTEC from GPS data for a desired time period, *Radio Science*, 39, RS6012. <https://doi.org/10.1029/2004RS003061>

Atıcı, R., Sağır, S., Emelyanov, L.Y., & Lyashenko, M. (2021). Investigation of ionospheric electron density change during two partial solar eclipses and its comparison with predictions of NeQuick 2 and IRI-2016 Models, *Wireless Personal Communications*, 118, 2239–2251. <https://doi.org/10.1007/s11277-021-08122-x>

Guo, Z., Yao, Y., Kong, J., Chen, G., Zhou, C., Zhang, Q., Shan, L., & Liu, C. (2021). Accuracy analysis of international reference ionosphere 2016 and NeQuick2 in the Antarctic, *Sensors*, 21, 1551. <https://doi.org/10.3390/s21041551>

- Iluore, K., Lu, J., Okeke, F., & Keyston, O. (2022). Performance of NeQuick-2 and IRI-Plas 2017 Models during solar maximum years in 2013–2014 over equatorial and low latitude regions, *Universe*, 8, 125. <https://doi.org/10.3390/uni-verse8020125>
- Liu, J., Jia, X., Zhu, Y., Xu, J., Fu, J., Zhang, R., & He, Y. (2022). Comparing GNSS TEC data from the African continent with IRI-2016, IRI-Plas, and NeQuick predictions, *Advances in Space Research*, 69, 7, 2852-2864. <https://doi.org/10.1016/j.asr.2022.01.008>
- Nayir, H., Arikan, F., Arikan, O., & Erol, C.B. (2007). Total electron content estimation with Reg-Est, *Journal of Geophysical Research*, 112, A11313. <https://doi.org/10.1029/2007JA012459>
- Pietrella, M., Nava, B., Pezzopane, M., Migoya, O. Y., Ippolito, A., & Scotto, C. (2017). NeQuick2 and IRI2012 models applied to mid and high latitudes, and the Antarctic ionosphere, *Antarctic Science*, 29(3), 265-276. <https://doi.org/10.1017/S0954102016000602>
- Poudel, P., Silwal, A., Ghimire, B.D., Gautam, S.P., Karki, M., Chapagain, N.P., Adhikari, P., Pandit, D., & Amory-Mazaudier, C. (2022). A study of vTEC above Nepal exploring different calibration techniques, including a comparison with the NeQuick-2 model, *Astrophysics and Space Science*, 367, 41. <https://doi.org/10.1007/s10509-022-04041-w>
- Sezen, U., Arikan, F., Arikan, O., Ugurlu, O., & Sadeghimorad, A. (2013). Online, automatic, near-real time estimation of GPS-TEC: IONOLAB-TEC, *Space Weather*, 11, 297–305. <https://doi.org/10.1002/swe.20054>
- Wang, L., Wei, E., Xiong, S., Zhang, T., Shen, & Z. (2022). Evaluation of NeQuick2 model over mid-latitudes of northern hemisphere, *Remote Sensing*, 14, 4124. <https://doi.org/10.3390/rs14164124>



## 5<sup>th</sup> Intercontinental Geoinformation Days

igd.mersin.edu.tr



### Zenith Tropospheric Delay Estimation Using a Low-Cost GNSS

Ceren Konukseven<sup>\*1</sup>, Sermet Ogutcu<sup>1</sup>, Salih Alçay<sup>1</sup>

<sup>1</sup>Necmettin Erbakan University, Faculty of Engineering, Department of Geomatics Engineering, Konya, Türkiye

#### Keywords

CSRS-PPP  
GNSS  
GPS  
Low-cost  
ZTD

#### Abstract

Global Navigation Satellite Systems (GNSS) are widely used in many fields such as surveying, navigation, meteorological studies, and other geomatic applications. Although high-performance GNSS receivers are widely used for GNSS applications, interest in low-cost GNSS receivers has increased in recent years and has become a research point. Many studies are realized to investigate the usability and performance of GNSS receivers with these properties. One of the topics to be investigated due to the ubiquity of low-cost receivers is the Zenith Tropospheric Delay (ZTD). This paper aims to test whether low-cost GNSS receivers can provide tropospheric parameters with close accuracy to high-performance GNSS receivers. For this reason, dual-frequency low-cost u-blox F9P GNSS receivers and CHC P5 geodetic GNSS receivers were chosen in the study. RINEX observation files of 4 days with a data recording interval of 30 seconds were obtained with chosen receivers. These observation files were processed with CSRS-PPP, one of the internet-based PPP services, and tropospheric parameters were estimated for the relevant days. ZTD values obtained from u-blox F9P GNSS receiver and geodetic receiver were examined with a comparative approach.

#### 1. Introduction

Global Navigation Satellite Systems (GNSS) are widely used in many fields such as surveying, navigation, precision agriculture, and meteorological forecasts with relative and absolute positioning methods. These applications are usually carried out using high-precision GNSS receivers to obtain accurate results. However, applications may be limited due to the high cost. Low-cost receivers have several advantages compared to high-cost receivers. These are low power consumption, small size, portability, etc. (Lu et al. 2019).

Low-cost GNSS devices are produced as double-frequency shortly after they start to be produced as single-frequency. Various studies have been conducted to test the ongoing improvements and performance of low-cost GNSS receivers (Hamza et al. 2021; Odolinski and Teunissen 2019; Gill et al. 2017). Especially the positioning and navigation with low-cost receivers (Nie et al. 2020; Yi et al. 2021; Odolinski and Teunissen 2020; Uradziński and Bakula 2020), structural health monitoring (Xue et al. 2022; Manzini et al. 2022),

landslide monitoring (Zuliani et al. 2022), crustal deformation monitoring (Tunini et al. 2022), coastal sea levels measuring (Knight et al. 2020) and many others.

Another parameter that can be used for testing low-cost GNSS receivers is tropospheric zenith delays (ZTD). ZTD is the basic tropospheric parameter used in GNSS data processing. ZTD is composed of two parts: Zenith Hydrostatic Delay (ZHD) and Zenith Wet Delay (ZWD). ZHD is modeled using meteorological data such as surface pressure and temperature. ZHD constitutes 90% of the total delay. ZWD relates to water vapor, which is difficult to model. Therefore, it can change rapidly temporally and spatially. Several studies have been conducted to test the performance of the low-cost GNSS receiver in terms of ZTD. Krietemeyer et al. 2020 evaluated ZTD estimates using precise point positioning (PPP) using a low-cost dual-frequency receiver and antennas of different quality. With their experiments, they concluded that the limiting factor in the low-cost receiver is the quality of the receiving antenna, and it gives high-quality results. Koohzadi et al. 2019, developed several models for the tropospheric delay.

#### \* Corresponding Author

(cerenkonk@gmail.com) ORCID ID 0000 – 0001 – 6598 – 9479  
(sermetogutcu@erbakan.edu.tr) ORCID ID 0000 – 0002 – 2680 – 1856  
(salcay@erbakan.edu.tr) ORCID ID 0000 – 0001 – 5669 – 7274

#### Cite this study

Konukseven C, Ogutcu, S., & Alçay, S. (2022). Zenith Tropospheric Delay Estimation Using a Low-Cost GNSS. 5<sup>th</sup> Intercontinental Geoinformation Days (IGD), 78-81, Netra, India

They tested whether the models were sufficient for low-cost real-time positioning. Stepniak and Paziewski 2022 tested whether low-cost GNSS receivers would provide tropospheric parameters with near accuracy to high-order receivers. They concluded that the difference is about 1.6mm and the two receivers are of comparable accuracy.

Although there have been a few studies on low-cost GNSS and zenith delays, low-cost GNSS is still of great interest for meteorological and atmospheric research. In this study, four days of data were recorded using a dual frequency u-blox F9P GNSS receiver and a geodetic GNSS receiver. We tested whether tropospheric zenith delays obtained with low-cost GNSS receivers provide accuracy and reliability close to tropospheric zenith delays obtained with geodetic GNSS receivers. The results were evaluated in terms of accuracy.

**2. Method**

Different GNSS receivers were chosen to evaluate the ZTD performance of the low-cost GNSS receiver compared to the high-cost receiver. Thus, u-blox F9P was chosen as low cost and the CHC P5 geodetic GNSS receiver was chosen as high cost. As a low-cost GNSS receiver, the u-blox F9P high-precision GNSS module was used, which provides cm-level accuracy. U-blox F9P is 118-channel multi-band GNSS receiver and capable of monitoring GPS(L1C/A, L2C), GLONASS(L1,L2OF), Galileo (E1B/C, E5b) and BeiDou (B1,B2) signals. The u-blox F9P receiver and the geodetic receiver were placed on an apparatus from the roof of the Engineering Faculty of Necmettin Erbakan University, in Konya. The status of the receivers during data recording is shown in Fig. 1.



**Figure 1.** Low-cost and geodetic receivers

For both receivers, 4-day (26.08.2022-29.08.2022) and 24-hour observation data were collected. Observation data were collected in clear sky conditions with a sufficient number of satellites and at 10 degrees cut-off angle. GPS+GLONASS (GR) combination was used for the geodetic receiver and u-blox.

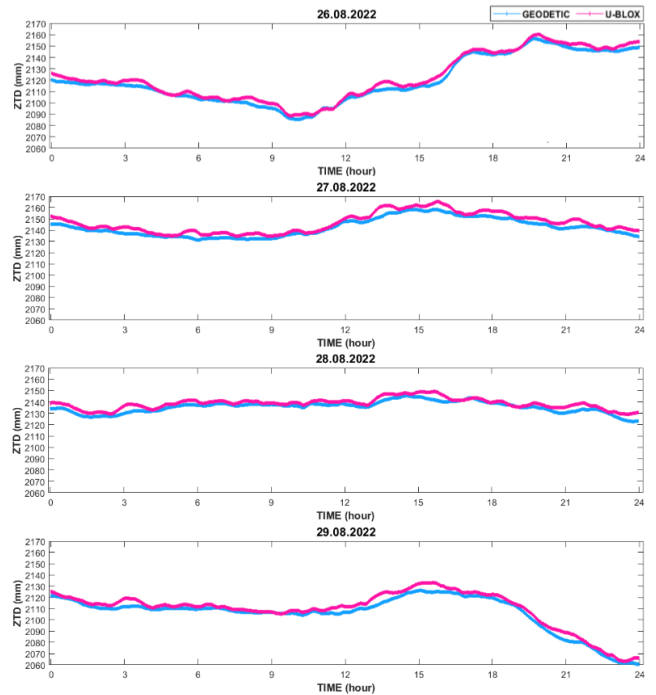
**3. Results**

The 4 days of observation data obtained from 26 August 2022 to 29 August 2022 with u-blox F9P and the geodetic receiver were converted into RINEX format. Then, RINEX data were processed with the online GNSS data processing service CSRS-PPP. The troposphere file, one of the CSRS-PPP outputs contains zenith hydrostatic delay, zenith wet delay, and tropospheric gradient data in 30-sec data record intervals. Using this file, the tropospheric zenith delays obtained at each epoch for both receivers and four days were calculated. Tropospheric zenith delays were obtained from zenith wet delay and zenith hydrostatic delay values. The calculated tropospheric zenith delays are shown in Fig. 2.

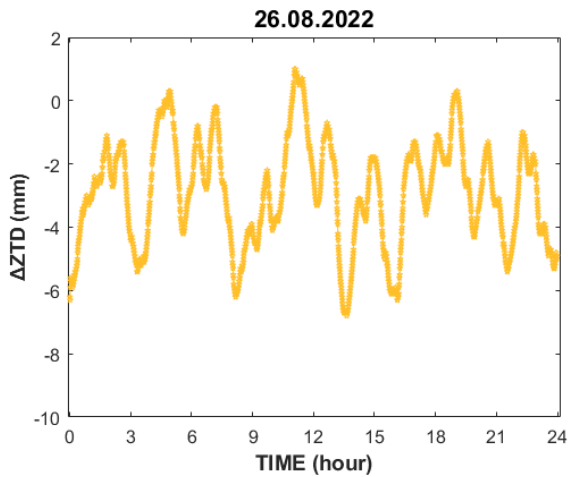
The accuracy assessment of the ZTD values obtained with the u-blox F9P receiver was applied by comparing them with the results of the geodetic receiver.

Fig. 3-6 show graphs of ZTD differences between u-blox and geodetic receiver. According to the figures, ZTD differences between the two receivers range from -6.8/1.0 mm, -9.1/-0.5 mm, -7.6/0.8 mm, and -8.8/0.3 mm respectively.

Furthermore, root mean square error (RMSe), absolute maximum and mean values were calculated. The basic statistical values of the differences between the two receivers are given in Table 1.



**Figure 2.** ZTD values of u-blox F9P and geodetic receiver



**Figure 3.** ZTD differences between u-blox F9P and geodetic receiver.

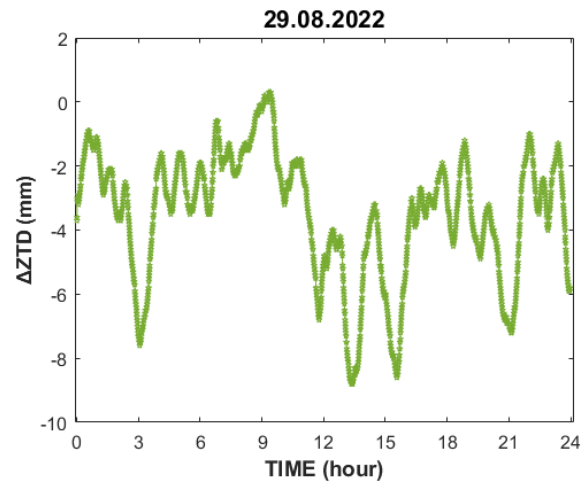


**Figure 6.** ZTD differences between u-blox F9P and geodetic receiver.

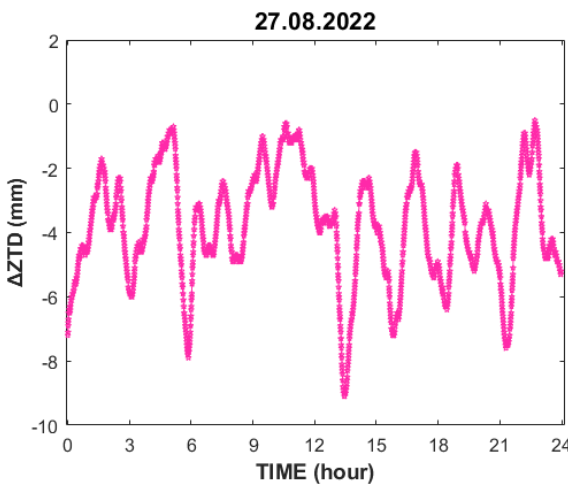


**Figure 4.** ZTD differences between u-blox F9P and geodetic receiver.

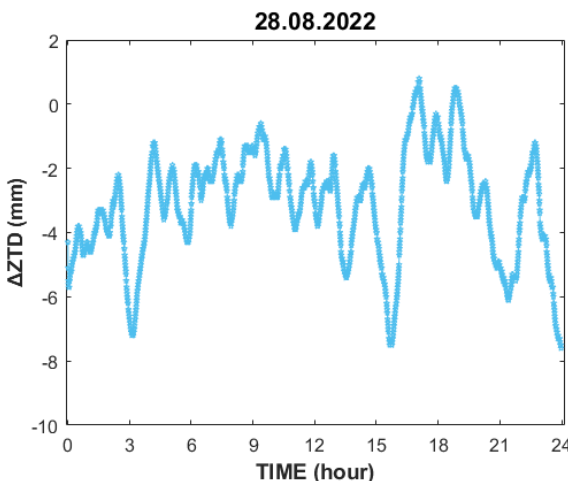


**Figure 5.** ZTD differences between u-blox F9P and geodetic receiver.

**Table 1.** The statistical values for ZTD differences between the geodetic and u-blox F9P receiver solutions

Days	RMS <sub>e</sub> (mm)	Max (abs) (mm)	Mean (mm)
26 Aug 2022	3.34	6.80	-2.88
27 Aug 2022	4.15	9.10	-3.76
28 Aug 2022	3.54	7.60	-3.10
29 Aug 2022	4.00	8.80	-3.47

As seen in Table 1, the absolute maximum values of ZTD differences between the two receivers range from 6.80 mm to 9.10 mm. When mean values are analyzed, it is seen that similar findings are obtained. In addition, the lowest RMS<sub>e</sub> value is 3.34 mm, while the highest RMS<sub>e</sub> value is 4.15 mm.

#### 4. Conclusion

In this study, the performance of a low-cost GNSS receiver in terms of ZTD prediction was tested by comparing it with a geodetic GNSS receiver. For this purpose, 4-day RINEX observation data with u-blox F9P and geodetic receivers were used. The results showed that the biggest absolute difference between the two receivers is 9.10mm. When the average difference of the four days is examined, it is seen that it varies from -2.88mm to -3.76mm.

By examining all these outcomes, we concluded that the tropospheric parameters derived from the low-cost GNSS receiver can compete with the high-cost GNSS receivers in terms of accuracy.

#### Acknowledgement

We thank to Natural Resources Canada (NRCan) for the web-based online CSRS-PPP used for data processing.

#### References

- Gill, M., Bisnath, S., Aggrey, J., & Seepersad, G. (2017, September). Precise point positioning (PPP) using low-cost and ultra-low-cost GNSS receivers. In Proceedings of the 30th International Technical Meeting of The Satellite Division of The Institute of Navigation (ION GNSS+ 2017) (pp. 226-236).
- Hamza, V., Stopar, B., & Sterle, O. (2021). Testing the performance of multi-frequency low-cost GNSS receivers and antennas. *Sensors*, 21(6), 2029.
- Knight, P. J., Bird, C. O., Sinclair, A., & Plater, A. J. (2020). A low-cost GNSS buoy platform for measuring coastal sea levels. *Ocean Engineering*, 203, 107198.
- Krietemeyer, A., van der Marel, H., van de Giesen, N., & ten Veldhuis, M. C. (2020). High quality zenith tropospheric delay estimation using a low-cost dual-

- frequency receiver and relative antenna calibration. *Remote Sensing*, 12(9), 1393.
- Koohzadi, M., Ebadollahi, S., Vahidnia, R., & Dian, F. J. (2019, October). Implementation and comparison of different tropospheric models to reduce error Low-cost Real-time GPS positioning. In *2019 IEEE 10th Annual Information Technology, Electronics and Mobile Communication Conference (IEMCON)* (pp. 0082-0086). IEEE.
- Lu, L., Ma, L., Wu, T., & Chen, X. (2019). Performance analysis of positioning solution using low-cost single-frequency u-blox receiver based on baseline length constraint. *Sensors*, 19(19), 4352.
- Manzini, N., Orcesi, A., Thom, C., Brossault, M. A., Botton, S., Ortiz, M., & Dumoulin, J. (2022). Performance analysis of low-cost GNSS stations for structural health monitoring of civil engineering structures. *Structure and Infrastructure Engineering*, 18(5), 595-611.
- Nie, Z., Liu, F., & Gao, Y. (2020). Real-time precise point positioning with a low-cost dual-frequency GNSS device. *Gps Solutions*, 24(1), 1-11.
- Odolinski, R., & Teunissen, P. J. (2019). An assessment of smartphone and low-cost multi-GNSS single-frequency RTK positioning for low, medium and high ionospheric disturbance periods. *Journal of Geodesy*, 93(5), 701-722.
- Odolinski, R., & Teunissen, P. J. (2020). Best integer equivariant estimation: Performance analysis using real data collected by low-cost, single-and dual-frequency, multi-GNSS receivers for short-to long-baseline RTK positioning. *Journal of Geodesy*, 94(9), 1-17.
- Ogaja, C. A. (2022). *Introduction to GNSS Geodesy: Foundations of Precise Positioning Using Global Navigation Satellite Systems*. Springer Nature.
- Stepniak, K., & Paziewski, J. (2022). On the quality of tropospheric estimates from low-cost GNSS receiver data processing. *Measurement*, 111350.
- Tunini, L., Zuliani, D., & Magrin, A. (2022). Applicability of Cost-Effective GNSS Sensors for Crustal Deformation Studies. *Sensörse*, 22(1), 350.
- Uradziński, M., & Bakuła, M. (2020). Assessment of static positioning accuracy using low-cost smartphone GPS devices for geodetic survey points' determination and monitoring. *Applied Sciences*, 10(15), 5308.
- Xue, C., Psimoulis, P. A., & Meng, X. (2022). Feasibility analysis of the performance of low-cost GNSS receivers in monitoring dynamic motion. *Measurement*, 111819.
- Yi, D., Bisnath, S., Naciri, N., & Vana, S. (2021). Effects of ionospheric constraints in Precise Point Positioning processing of geodetic, low-cost and smartphone GNSS measurements. *Measurement*, 183, 109887.
- Zuliani, D., Tunini, L., Di Traglia, F., Chersich, M., & Curone, D. (2022). Cost-effective, single-frequency GPS network as a tool for landslide monitoring. *Sensors*, 22(9), 3526.



## 5<sup>th</sup> Intercontinental Geoinformation Days

igd.mersin.edu.tr



### Near-Real-Time Precise Point Positioning Technique with Single-Frequency Raw GNSS Observations on Android Smartphones

Hüseyin Pehlivan<sup>\*1</sup>, Barış Karadeniz<sup>1</sup>, Barışcan Arı<sup>1</sup>

<sup>1</sup>Gebze Technical University, Department of Geomatics Engineering, Kocaeli, Türkiye

#### Keywords

Smartphone  
Single-Frequency  
GNSS  
N-RT-PPP

#### Abstract

In this study, positioning performance was evaluated by making single-frequency GNSS (Global Navigation Satellite System) observations under real-time conditions with a smartphone. In experiments, GNSS observations were recorded with the Xiaomi Redmi Note 8 Pro via the Geo++ Logger application. Measurements were made with the geodetic-grade CHC I80 GNSS receiver to evaluate the performance of the smartphone. In addition to the collected raw observation data set, solutions were realized with the Near-Real-Time Precise Point Positioning (N-RT-PPP) technique by using satellite orbit and clock correction products produced under real-time conditions from the CNES (Centre National D'Etudes Spatiales) archive. When all the observations with the epoch difference are examined, it is observed that the root mean square error (RMSE) values of the GPS/GLONASS observations give better results than the only-GPS solutions. In addition, in the epoch differenced time series produced from the smartphone, an improvement between 92% and 98% was observed for the part below 1 cm horizontally and 2 cm vertically after the fluctuation.

#### 1. Introduction

Recently, with the development of satellite constellations and modernized signals in global satellite systems, and innovations in satellite-based positioning theory and algorithm, studies on geodetic-grade GNSS receiver/antenna(s) as well as low-cost GNSS receiver/antenna(s) and even smartphones have increased (Banville and Diggelen 2016; GSA 2017). Smartphones initially provided position information with a single-frequency, single constellation of satellites. In the beginning, smartphones produced single-frequency, single-satellite constellation and position information without open access to GNSS raw data. However, based on the raw GNSS observations from the satellite, Google announced at the "I/O 2016" conference in 2016 that with the Android N (Nougat=Version 7) version, raw GNSS data will be made available to the user on Android-based smartphones (Banville and Diggelen 2016; Gül et al. 2021). This statement has been a milestone for many studies on positioning on smartphones. Smartphones, which are widely used by most people in the global community for their needs and have a large mass market

in the mobile smart device market, have now become a subject that is researched in precise positioning studies for different applications in the GNSS market. The first GNSS data evaluation study by Banville and Diggelen (2016) recorded raw multi-GNSS code, carrier-phase and Doppler observations at L1 frequency with a Samsung Galaxy S7 smartphone. However, single-frequency only-GPS raw data quality was studied. According to the results, they stated that the main problems of smartphones for precise positioning are GNSS antenna quality and cycle slip. A similar study evaluated the quality of the raw measurements and the obtained position accuracy with the linear polarized antenna and external GNSS antenna in order to evaluate the antenna quality with the Huawei Mate 9 smartphone with the GNSS chip (Broadcom 4774) of the same model (Siddakatte et al. 2017). While positioning, navigation and timing applications with smartphones were made through single-frequency GNSS observations until 2018, Xiaomi produced and marketed Mi8 model smartphone that can collect dual-frequency GNSS raw observation data for the first time in May (Chen et al. 2019). This event has been a start that will lead to the evaluation of precise positioning performance using different

\* Corresponding Author

(b.karadeniz@gtu.edu.tr) ORCID ID 0000 - 0002 - 5093 - 5467  
(hpehlivan@gtu.edu.tr) ORCID ID 0000 - 0002 - 0018 - 6912  
(b.ari2021@gtu.edu.tr) ORCID ID 0000 - 0001 - 6646 - 0315

Cite this study

Pehlivan H, Karadeniz B & Ari B (2022). Title of the study. 5<sup>th</sup> Intercontinental Geoinformation Days (IGD), 82-85, Netra, India

positioning techniques (Real-Time Kinematic, Precise Point Positioning, etc.) and many studies in engineering applications on smartphones (Chen et al. 2019; Liu et al. 2021; Odolinski and Teunissen 2019; Robustelli et al. 2019; Wu et al. 2019). In the literature, the positioning performance of smartphones has been evaluated by using geodetic-grade receivers as a reference to relative positioning or differential positioning technique, or by using a smartphone as a reference station (Gao et al. 2019; Geng and Li 2019; Paziewski et al. 2021). Although the positioning studies with smartphones are low cost, due to the GNSS antenna/chip feature used, the signals reflected from the objects in the environment are sensitive to the multipath effect, which causes the collection of low quality GNSS measurements. GNSS receiver/antenna(s), which are high cost and designed to minimize the multipath effect, have advantages over the antenna/chip(s) used in smartphones. In addition, many positioning applications use carrier-phase observations for high positioning accuracy. However, due to the GNSS antenna/chip structure used in carrier phase observations on smartphones, it causes interruptions in phase observations (Paziewski et al. 2019; Zangenehjad and Gao 2021).

In Nowadays, with a single GNSS receiver, position determination studies with PPP technique under real-time conditions have gained great momentum. In this context, it has eliminated the need for a simultaneous reference receiver, a network or an infrastructure compared to previous methods. Along with the dual-frequency raw GNSS data collection of smartphones, PPP-based point positioning performance in both static and kinematic mode has been evaluated in many studies. In the studies, it was stated that the position accuracy can be determined at the decimeter level in static mode and with an accuracy of a few meters in kinematic mode (Aggrey et al. 2019; Elmezayen and El-Rabbany 2019; Kulikov et al. 2019). In this study, single-frequency GNSS raw observations were collected using both smartphone and CHC I80 GNSS receiver/antenna, and evaluation was carried out with the N-RT-PPP method.

## 2. Method

This study includes the N-RT-PPP technique based on multi-GNSS code and phase observations. In this context, the equations can be written as:

$$P_r^s = \rho_r^s + c \cdot \delta t_r - c \cdot \delta t^s + T_r^s + I_r^s + m_r^s + \varepsilon_{r,p}^s \quad (1)$$

$$\Phi_{r,j}^s = \rho_r^s + c \cdot \delta t_r - c \cdot \delta t^s + \lambda N_r^s + T_r^s - I_r^s + m_r^s + \varepsilon_{r,\phi}^s \quad (2)$$

In these equations, the subscript  $r$  represents the receiver, while the superscript  $s$  represents the satellite; The pseudorange and carrier-phase measurements of the receiver relative to the satellite in  $P$  and  $\Phi$  length units, respectively;  $\rho$  is the geometric distance between the receiver and the satellite;  $c$  is the speed of light in vacuum,  $\delta t_r$  and  $\delta t^s$  are receiver and satellite clock corrections, respectively;  $T_r^s$  indicates tropospheric delay along the path between receiver and satellite;  $I_r^s$  is

the ionospheric delay along the path from the satellite to the receiver;  $\lambda$  is the carrier-phase wavelength;  $N_r^s$  is the initial phase ambiguity;  $m_r^s$  and  $\varepsilon_r^s$  represent the multipath and noise of the code and phase observations, respectively.

## 3. Results and Discussion

In this section, information and observation data sets of GNSS receiver/antenna used in the experiments are introduced. In addition, the observations collected on GNSS receiver/antenna(s) are demonstrated by the N-RT-PPP method. Finally, the results of the positioning performance of N-RT-PPP solutions obtained from the data collected from different GNSS receivers/antenna(s) are presented.

### 3.1. Experiment design and data processing

Within the scope of this study, observations were made with a total of 2 GNSS receiver/antenna(s) at a sampling range of 1 Hz using CHC I80 GNSS receivers and Xiaomi Redmi Note 8 Pro model smartphone. Experiments were carried out in Gebze Technical University campus in the Department of Geomatics Engineering in November 2022 and lasted for about 1.5 hours. During the experiment, GPS and GLONASS satellite observations were collected with 2 GNSS receiver/antenna(s). With the IGS (International GNSS Service)-RTS (Real-Time Service) service project initiated by IGS, RTS products can be broadcast over the internet in RTCM/SSR (Radio Technical Commission for Maritime Services/ State Space Representation) data format with NTRIP (Networked Transport of RTCM via Internet Protocol) data transmission protocol, and real-time satellite orbit and clock correction information can be obtained (Elsobeiey and Al-Harbi 2016). In a similar role to IGS-RTS, satellite orbit and clock correction products for GPS and GLONASS are routinely provided by the CNES. N-RT-PPP solution was realized by using satellite orbit and clock correction information generated under real-time conditions from the CNES archive. In this study, a solution was made with the rtkpost application module of the RTKLIB software to the point positioning and to monitor it in real time using the N-RT-PPP method.

### 3.2. Positioning performance with RT-PPP method

In this section, the raw GPS/GLONASS observations obtained from the Xiaomi Redmi Note 8 smartphone are processed with the N-RT-PPP technique in static mode, together with the satellite orbit and clock information produced under real-time conditions. Single-frequency GPS and GPS/GLONASS solutions were evaluated in the study. In this context, N-RT-PPP solution was made in static mode using a single GNSS receiver (CHC I80) to fairly evaluate the positioning performance of smartphones with single-frequency GNSS observations. In Fig. 1, the epoch differenced time series of the solutions generated from both the geodetic-grade GNSS receiver and the smartphone during the whole experiment are shown. In addition, statistical histograms of the epoch differenced obtained from the

smartphone are given by taking the solutions obtained with the geodetic-grade GNSS receiver as reference. In the first row of the figure, the epoch differenced time series of the north, east and up components, respectively, based on GPS-only observations are shown.

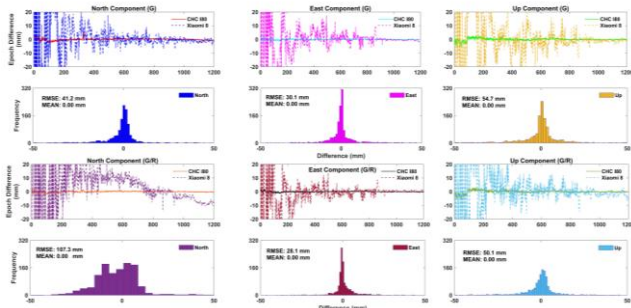


**Figure 1.** The epoch differenced time series and histogram distributions throughout the experiment.

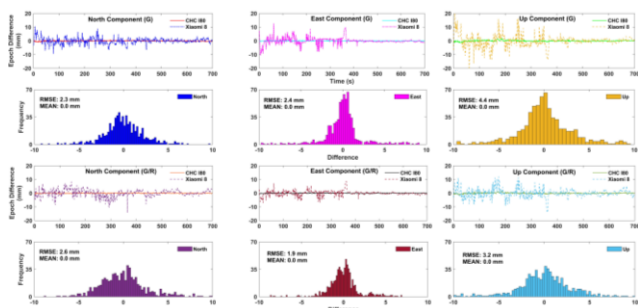


**Figure 2.** The epoch differenced time series and histogram distributions after fluctuation.

In the second row of the figure, with reference to the epoch differences obtained from the CHC 180 GNSS receiver, RMSE values and histogram distributions of the three different components of the epoch differenced produced from the Xiaomi 8 smartphone are given. In the 3rd row of the figure, unlike the first row, the time series of the epoch differences obtained using GPS/GLONASS observations, and the statistical values of the observations obtained from the smartphone are presented in the 4th row. According to the results, there were clearly fluctuations in the solutions obtained from the smartphone. Despite being a static solution, these fluctuations persisted between approximately 600 (s) and 800 (s) epochs, although different for the three components. Therefore, from the instant that the fluctuations fall below 1 cm in the horizontal component and below 2 cm in the vertical component, the epoch differenced time series and statistical histograms are shown as seen in Fig. 2. According to the results, it was observed that the RMSE values of GPS and GPS/GLONASS solutions, whose epoch differenced were taken after fluctuation, were improved according to the results throughout the whole experiment. In Table 1, the RMSE values of the epoch differenced measurements of the GPS and GPS/GLONASS solutions during the all experiment (A) and after fluctuations (B) are given.

**Table 1.** RMSE values of North, East and Up components for Xiaomi 8 smartphone

	GPS			GPS/GLONASS		
	North (mm)	East (mm)	Up (mm)	North (mm)	East (mm)	Up (mm)
A	41.2	30.1	54.7	107.3	28.1	50.1
B	2.3	2.4	4.4	2.6	1.9	3.2

#### 4. Conclusion

In this study, near-real-time positioning performance of GNSS observations collected statically with a smartphone was evaluated. In the experiment, the data set collected with the Xiaomi Redmi Note 8 smartphone was solved with a single-frequency combination of both GPS and GPS/GLONASS satellites. In order to evaluate the results fairly, observations were also made with a single geodetic-grade GNSS receiver. It has been observed that the results obtained with the combination of GPS/GLONASS satellites give better results than the only-GPS observations. Considering at the epoch differenced time series after fluctuation, 94.4%, 92.0% and 92.0% improvements were shown in the north, east and up components, respectively, in the solutions realized by only-GPS observations. This assessment showed an improvement of 97.6%, 93.2% and 93.6% in the GPS/GLONASS satellite combination, respectively. In this context, it is clear that the addition of GLONASS satellite to single-frequency GPS satellite observations collected in static mode with smartphones improves real-time positioning performance. It has also been observed that the smartphone's static positioning accuracy improves significantly under real-time conditions after approximately 600 (s) to 800 (s) epochs. In addition to this study, it is considered to evaluate the positioning performance of smartphones capable of dual-frequency multi-GNSS observations with current technological developments in different satellite combinations in real-time.

#### References

Aggrey, J., Bisnath, S., Naciri, N., Shinghal, G., & Yang, S. (2019). Use of PPP processing for next-generation smartphone GNSS chips: key benefits and challenges. Proceedings of the 32nd International Technical Meeting of the Satellite Division of The Institute of Navigation (ION GNSS+ 2019), 3862-3878.

Banville, S., & Diggelen, F. (2016). Precise GNSS for everyone: precise positioning using raw GPS measurements from Android smartphones. GPS World, 27(1), 43-48.

Chen, B., Gao, C., Liu, Y., & Sun, P. (2019). Real-Time Precise Point Positioning with a Xiaomi MI 8 Android Smartphone. Sensors, 19, 2835.

Elmezayen, A., & El-Rabbany, A. (2019). Precise point positioning using world's first dual-frequency GPS/GALILEO smartphone. Sensors, 19(11), 2593.

- Elsobeiey, M., & Al-Harbi S. (2016). Performance of real-time Precise Point Positioning using IGS real-time service. *GPS Solutions*, 20(3), 565–571.
- Gao, R., Xu, L., Zhang, B., & Liu, T. (2021). Raw GNSS observations from Android smartphones: Characteristics and short-baseline RTK positioning performance. *Measurement Science and Technology*, 32(8), 084012.
- Geng, J., & Li, G. (2019). On the feasibility of resolving Android GNSS carrier-phase ambiguities. *Journal of Geodesy*, 93(12), 2621-2635.
- GSA, European GNSS Agency (GSA) GNSS Raw Measurements Task Force 2017, Using GNSS raw measurements on Android devices (white paper) (<http://doi.org/10.2878/449581>).
- Gül, C., Doğan, A. H., & Öcalan, T. (2021). Investigation of PPP performance with dual frequency raw GNSS observations obtained from smartphones. *Journal of Geodesy and Geoinformation*, 8(2), 120-130.
- Hadas, T., & Bosy, J. (2015). IGS RTS precise orbits and clocks verification and quality degradation over time. *GPS Solutions*, 19(1), 93–105.
- Kulikov, R., Chugunov, A., & Zamolodchikov, V. (2019). Investigation of collision warning possibilities by means of GNSS receivers of Android smartphones. *IOP Conference Series: Materials Science and Engineering*, 695(1), 12013.
- Liu, Q., Gao, C., Peng, Z., Zhang, R., & Shang, R. (2021). Smartphone positioning and accuracy analysis based on real-time regional ionospheric correction model. *Sensors*, 21(11), 3879. <https://doi.org/10.3390/s21113879>.
- Odolinski, R., & Teunissen, P. (2019). An assessment of smartphone and low-cost multi-GNSS singlefrequency RTK positioning for low, medium and high ionospheric disturbance periods. *Journal of Geodesy*, 93(5), 701-722. <https://doi.org/10.1007/s00190-018-1192-5>.
- Paziewski, J., Sieradzki, R., & Baryla, R. (2019). Signal characterization and assessment of code GNSS positioning with low-power consumption smartphones. *GPS Solutions*, 23(4), 1-12. <https://doi.org/10.1007/s10291-019-0892-5>.
- Paziewski, J., Fortunato, M., Mazzoni, A., & Odolinski, R. (2021). An analysis of multi-GNSS observations tracked by recent Android smartphones and smartphone-only relative positioning results. *Measurement*, 175, 109162.
- Robustelli, U., Baiocchi, V., & Pugliano, G. (2019). Assessment of dual frequency GNSS observations from a Xiaomi Mi 8 Android smartphone and positioning performance analysis. *Electronics*, 8(1), 91.
- Siddakatte, R., Broumandan, A., & Lachapelle, G. (2017). Performance evaluation of smartphone GNSS measurements with different antenna configurations. *Proceedings of the International Navigation Conference, Brighton, 27-30 November 2017*.
- Wu, Q., Sun, M., Zhou, C., & Zhang, P. (2019). Precise point positioning using dual-frequency GNSS observations on smartphone. *Sensors*, 19(9), 2189.
- Zangenehnejad, F., & Gao, Y. (2021). GNSS smartphones positioning: Advances, challenges, opportunities, and future perspectives. *Satellite Navigation*, 2(1), 1-23.



## 5<sup>th</sup> Intercontinental Geoinformation Days

igd.mersin.edu.tr



### Using the particle swarm optimization for geoid determination

Ulku Kirici Yildirim<sup>\*1</sup>, Yasemin Sisman<sup>1</sup>

<sup>1</sup>Ondokuz Mayıs University, Engineering Faculty, Department of Geomatics Engineering, Samsun, Türkiye

#### Keywords

Geoid determination  
LS Method  
Metaheuristic Algorithm  
Particle Swarm  
Optimization

#### Abstract

Geoid determination is the modelling that enables us to determine the height of a point whose position is known. Geoid determination has made important problem of Geodesy with GPS technologies. One of the important points when determining the geoid is to select the outlier points in the data set. These points named as outlier measurements. These points are determined by the outlier measurements test. There are many different methods used in the literature to determine outlier measurements. The most widely used of these is The Least Square Method (LS). Also nowadays, very complex problems can be solved with methods such as the rapidly developing Artificial Intelligence and Machine Learning Technologies with Metaheuristic Algorithm for obtaining a close to optimum solution. One of these algorithms is Particle Swarm Optimization. In this study, the usability of the particle swarm optimization was tested to determine the outlier measurement in the geoid determination process.

#### 1. Introduction

Metaheuristic algorithms have become popular in finding the best in recent years and are still used in many optimization problems (Canayaz, 2015). Its use in Geomatics studies has just begun.

The geoid is a gravity equipotential surface to which the elevation of a point can be conveniently referred. The computation of the geoid is based on the solution of the field equation of gravitation which describes gravitation in the small and in which the rotating frame of reference is time independent to a first order approximation (Zhang, 1997). The solution is adjustment to increase the accuracy in geoid determination. In the problem, the measurements, which is much than the required number cause discrepancy between measurements and in this case, the solution is not unique. An objective function is made for the unique solution. It is seen that usually the objective functions are formed by minimization of corrections or a function of corrections and the two methods come forward (Sisman, 2010). The most used methods are The Least Square Method (LS) and The Least Absolute Value Method (LAV).

In this study a data set consisting of 312 points concern to a section of the land at Ondokuz Mayıs University in Samsun was used. Firstly, the outlier measurements in the data set were removed. Then

the same data set was tested on one of the metaheuristic algorithms, Particle Swarm Optimization (PSO). The results of both methods were examined and compared.

#### 2. Method

##### 2.1. Metaheuristic algorithm

Metaheuristic algorithms appear as comprehensive algorithms that are above heuristics and decide which method to use in solving problems. Metaheuristics have developed dramatically. (Osman & Kelly, 1997). In order for Metaheuristic algorithms to be usable, they must meet certain criteria. At the beginning of these criteria are the closeness of the solutions they found to the optimum value and the time they spent in obtaining these solutions. The fact that the algorithms are coded in a way that can be understood by everyone and provides ease of analysis is also an important factor in the selection of algorithms (Canayaz, 2015). There are many different metaheuristic algorithms in the literature. These are; Firefly Algorithm, Genetic Algorithm (Banzhaf, Nordin, Keller, & Francone, 1998), Shuffled Frog Leaping Algorithm (Eusuff, Lansey, & Pasha, 2006), Particle Swarm optimization (Lazinica, 2009), Ant Colony Optimization (Maniezzo, Gambardella, & Luigi, 2004) etc.

#### \* Corresponding Author

(ulku.kirici@omu.edu.tr) ORCID ID 0000 – 0002 – 3569 – 4482  
(yysisman@omu.edu.tr) ORCID ID 0000 – 0002 – 6600 – 0623

#### Cite this study

Kirici Yildirim U & Sisman Y (2022). Using the particle swarm optimization for geoid determination. 5<sup>th</sup> Intercontinental Geoinformation Days (IGD), 86-89, Netra, India

### 2.1.1. Particle swarm optimization

Particle swarm optimization (PSO) algorithm is a stochastic optimization technique based on swarm, which was a proposed by Eberhart and Kennedy (Eberhart & Kennedy, 1995). PSO algorithm simulates animal's social behavior, including insects, herds, birds and fishes. These swarms conform a cooperative way to find food and each member in the swarms keeps changing the search pattern according to the learning experiences of its own and other members (Wang, Tan, & Liu, 2018).

Each individual in the particle swarm is composed of three D-dimensional vectors, where D is the dimensionality of the search space. These are the current position  $x_i$ , the previous best position  $p_i$ , and the velocity  $v_i$ .

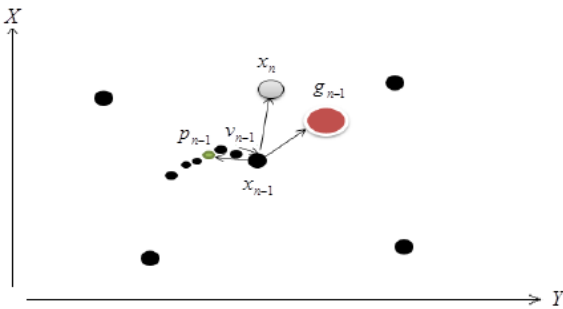


Figure 1. PSO mechanism (Gökçe, Durusu, & Ridvan, 2022)

The current position  $x_i$  can be considered as a set of coordinates describing a point in space. On each iteration of the algorithm, the current position is evaluated as a problem solution. If that position is better than any that has been found so far, then the coordinates are stored in the second vector,  $p_i$ . The value of the best function result so far is stored in a variable that can be called  $pbest_i$  (for “previous best”), for comparison on later iterations. The objective, of course, is to keep finding better positions and updating  $p_i$  and  $pbest_i$ . New points are chosen by adding  $v_i$  coordinates to  $x_i$ , and the algorithm operates by adjusting  $v_i$ , which can effectively be seen as a step size.

The particle swarm is more than just a collection of particles. A particle by itself has almost no power to solve any problem; progress occurs only when the particles interact (Poli, Kennedy, & Blackwell, 2007).

Suppose there are n particles consisting of D parameters. So, population particle matrix equation is;

$$X = \begin{bmatrix} x_{11} & x_{12} & \dots & x_{1D} \\ x_{21} & x_{22} & \dots & x_{2D} \\ \dots & \dots & \dots & \dots \\ x_{n1} & x_{n2} & \dots & x_{nD} \end{bmatrix}$$

The position ( $pbest_i$ ) of the  $i$ 'th particle the best fitness value;

$$pbest_i = [P_{i1}, P_{i2}, \dots, P_{iD}]$$

The other best value is the coordinates that provide the best solution obtained by all particles in the population so far ( $gbest_i$ ).

$$gbest_i = [P_1, P_2, \dots, P_D]$$

$i$ .th particle correction;

$$v_i = [v_{i1}, v_{i2}, \dots, v_{iD}]$$

After finding the two best values, particle velocities and positions are updated according to the equations given below (ÇEVİK & KOÇER, 2013).

$$v_i^{k+1} = v_i^k + c_1 * rand_1^k (pbest_i^k - x_i^k) + c_2 * rand_2^k (gbest_i^k - x_i^{k+1})$$

$$x_i^{k+1} = x_i^k + v_i^{k+1}$$

### 2.2. Geoid determination and GNSS levelling

The geoid is a complex surface and formed by the combination of the points have got zero potential value. The geoid determination is the most important problem in the earth. Because the geoid does not represent a regular shape. Local geoid determination studies aim was to determine a local geoid using the geoid determination methods for example Polynomial Interpolation Method (Akar, Konakoğlu, & Akar, 2022).

Development of geoid modelling is based on geodetic, gravimetric and astrogeodetic techniques. In order to define a high precision geoid, GNSS levelling, one of the geodetic techniques, can be employed. It involves the transformation of GNSS-derived ellipsoidal height ( $h$ ) into the orthometric height ( $H$ ). Instead of levelling, orthometric heights can be calculated by using well-defined geoid models. These geoid models enable us to compute the geoid height ( $N$ ), which is the difference between ellipsoidal and orthometric height values ( $N = h - H$ ) (Albayrak, Özlüdemir, Aref, & Halicioğlu, 2020).

The polynomial technique is based on the determination of polynomial surface. The surface used to determine the geoid is generally expressed in high degree polynomials with two variables (Kirici & Sisman, 2017). The orthogonal polynomials can be represented are as follow;

$$N(x, y) = \sum_{i=0}^m \sum_{j=0}^k a_{ij} x^i y^j$$

If the number of measures is greater than the unknown number in a problem, adjustment calculation is made for a univocal solution

(Montgomery, Peck, & Vining, 2021). Adjustment is a means of obtaining unique values for the unknown parameters to be determined when there are more observations than actually needed; statistical properties may be determined as by products (Ogundare, 2018). A few methods have been developed to adjustment calculation. One of these methods is the LS method.

### 2.2.1. The Least Square Method

The least squares method (LS) explained by Carl Friedrich Gauss in 1795 and Legendre in 1805. This method is used in many different applications (Sisman, 2014). Unknown parameters calculated with the following equation in this method.

$$\underline{X} = (\underline{A}^T \underline{Q}_{\ell\ell}^{-1} \underline{A})^{-1} \underline{A}^T \underline{Q}_{\ell\ell}^{-1} \underline{\ell}$$

Root mean square error (RMSE);

$$m_0 = \pm \sqrt{\frac{\underline{V}^T \underline{PV}}{f}} ; f = n - u$$

The measurement errors of the LS method influence the residual of other calculations. Thus, this correction value may not always be due to an error in the measurement. This situation is called the spread and storage effect of LS method. Different solution methods can be conducted for the analysis of spread and storage method.

### 2.3. Case study

In this study, a part of the land relate to Ondokuz Mayıs University in Samsun was used as the study area (Figure 2).

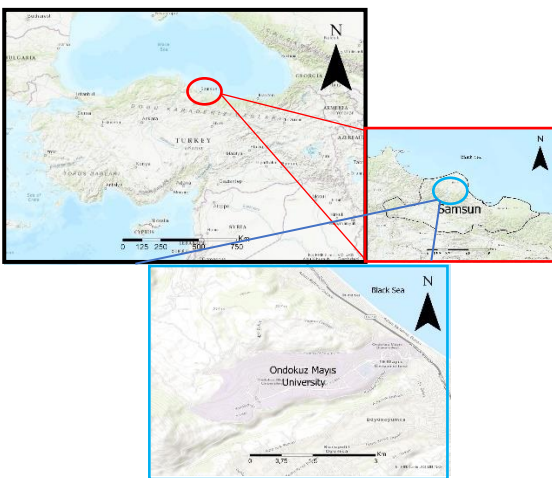


Figure 2. Study area

Data set consist of 312 points. The distribution of points with known x, y and h values is shown in Figure 3.

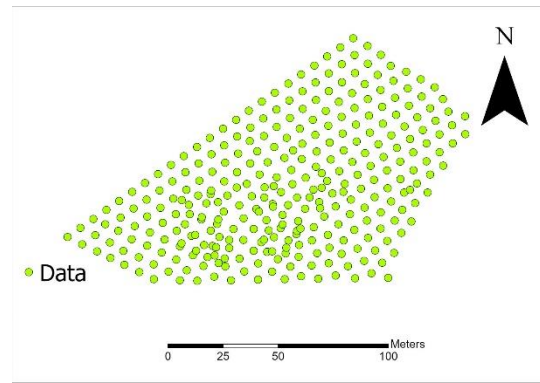


Figure 3. Data set

First, the surface model is created using the 2nd degree polynomial formula according to LS. Then, outlier points were determined depending on this method. Finally, one of the metaheuristic algorithms, PSO, was tried to determine the outlier measurement.

### 3. Results

LS method determines 51 of 312 points as an outlier. This means that the 51 points do not belong to the surface and the surface belongs 261 points. Figure 4 shows the distribution of the outliers which are found by the LS method.

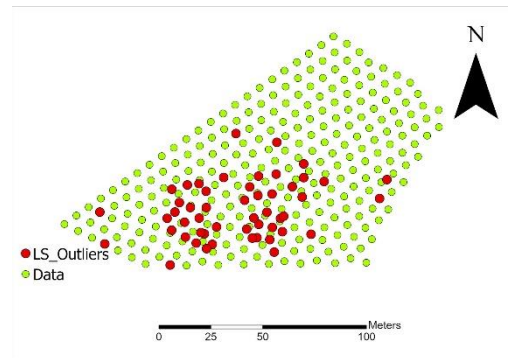


Figure 4. Outlier points of the LS Method

PSO was applied to the data set and 41 of 312 points were determined as an outlier with this method. According to the PSO, the surface consists of 271 compatible points (Figure 5).

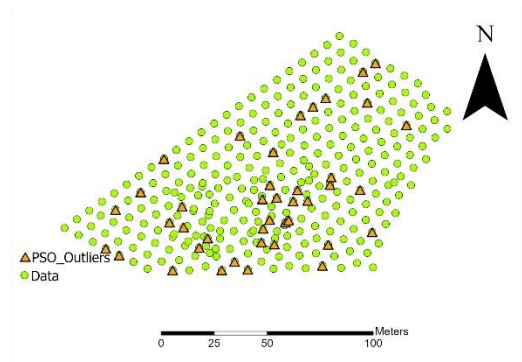


Figure 5. Outlier points of the PSO

#### 4. Discussion

LS method was determined as an outlier in 51 points. PSO determined 41 points. When the points found in common by both methods are observed, it is seen that 16 points are common. Common points found by the two methods are shown in Figure 6.

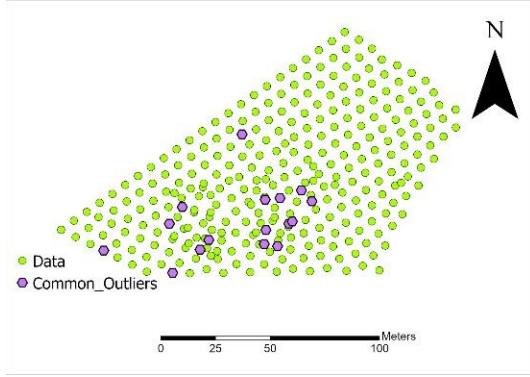


Figure 6. Common points

#### 5. Conclusion

When the intersection points are examined, it is seen that they cover each other at the rate of 32%. This rate shows us that the use of PSO in geoid detection is limited. When the points that both methods find common are examined, it is seen that there is a density in the middle parts of the study area. According to the land structure of the study area, it is seen that the middle parts are rugged and wooded. As a result, it is understood that PSO gives more accurate results, especially in rough terrain. Metaheuristic algorithms have entered our literature as an optimization method in recent years. However, its use in geomatics engineering is not common yet. In this study, the usability of the PSO in geoid determination was tested. The study can be continued by trying different metaheuristic algorithms.

#### References

Akar, A., Konakoğlu, B., & Akar, Ö. (2022). Prediction of geoid undulations: Random forest versus classic interpolation techniques. *Concurrency and Computation: Practice and Experience*, e7004.

Albayrak, M., Özlüdemir, M. T., Aref, M. M., & Halicioğlu, K. (2020). Determination of Istanbul geoid using GNSS/levelling and valley cross levelling data. *Geodesy and geodynamics*, 11(3), 163-173.

Banzhaf, W., Nordin, P., Keller, R. E., & Francone, F. D. (1998). *Genetic programming: an introduction: on the automatic evolution of computer programs and its applications*: Morgan Kaufmann Publishers Inc.

Canayaz, M. (2015). Cırcır böceği algoritması: Yeni bir meta-sezgisel yaklaşım ve uygulamaları.

Çevik, K., & Koçer, H. (2013). Parçacık sürü optimizasyonu ile yapay sinir ağları eğitime dayalı bir esnek hesaplama uygulaması. *Süleyman Demirel Üniversitesi Fen Bilimleri Enstitüsü Dergisi*, 17(2), 39-45.

Eberhart, R., & Kennedy, J. (1995). *A new optimizer using particle swarm theory*. Paper presented at the MHS'95. Proceedings of the sixth international symposium on micro machine and human science.

Eusuff, M., Lansey, K., & Pasha, F. (2006). Shuffled frog-leaping algorithm: a memetic meta-heuristic for discrete optimization. *Engineering optimization*, 38(2), 129-154.

Gökçe, C. O., Durusu, V., & Ridvan, U. (2022). Farklı Yük Çeşitleri İçin Parçacık Sürü Optimizasyonu ve Ziegler-Nichols Metodunun DC Motor Hız Kontrolü Probleminde Karşılaştırılması. *Avrupa Bilim ve Teknoloji Dergisi*(33), 88-92.

Kirici, U., & Sisman, Y. (2017). The Comparison of the Adjustment Methods in Geoid Determination Method. *FIG Working Week, Helsinki, Finland*.

Lazinica, A. (2009). *Particle swarm optimization: BoD-Books on Demand*.

Maniezzo, V., Gambardella, L. M., & Luigi, F. d. (2004). Ant colony optimization. In *New optimization techniques in engineering* (pp. 101-121): Springer.

Montgomery, D. C., Peck, E. A., & Vining, G. G. (2021). *Introduction to linear regression analysis*: John Wiley & Sons.

Ogundare, J. O. (2018). *Understanding least squares estimation and geomatics data analysis*: John Wiley & Sons.

Osman, I. H., & Kelly, J. P. (1997). Meta-heuristics theory and applications. *Journal of the Operational Research Society*, 48(6), 657-657.

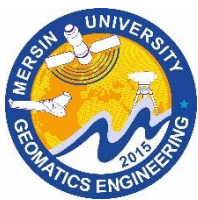
Poli, R., Kennedy, J., & Blackwell, T. (2007). Particle swarm optimization. *Swarm intelligence*, 1(1), 33-57.

Sisman, Y. (2010). Outlier measurement analysis with the robust estimation. *Scientific Research and Essays*, 5(7), 668-678.

Sisman, Y. (2014). Coordinate transformation of cadastral maps using different adjustment methods. *Journal of the Chinese Institute of Engineers*, 37(7), 869-882.

Wang, D., Tan, D., & Liu, L. (2018). Particle swarm optimization algorithm: an overview. *Soft computing*, 22(2), 387-408.

Zhang, K. (1997). *An evaluation of FFT geoid determination techniques and their application to height determination using GPS in Australia*. Curtin University,



## 5<sup>th</sup> Intercontinental Geoinformation Days

igd.mersin.edu.tr



### MCDM: A new Quantum GIS Plug-In for multi criteria decision making analysis

Emre Yılmaz\*<sup>1</sup>, Süleyman Sefa Bilgilioğlu <sup>1</sup>

<sup>1</sup>Aksaray University, Faculty of Engineering, Department of Geomatics Engineering, Aksaray, Türkiye

#### Keywords

Geographic Information System  
Python  
QGIS  
Plugin

#### Abstract

Today, open-source software is free and reliable, and its use has increased. The fact that closed-source software is designed for commercial purposes and its reliability is debatable has encouraged free software developers worldwide to develop alternative software. The number and users of GIS (Geographic Information System) software written in open-source code worldwide and our country is increasing daily. QGIS software is a GIS software developed by free software developers, which is growing in popularity with its new versions and allows plug-in development with the python programming language. The fact that the plug-ins developed with QGIS software can be shared with other users brings together users of open-source geospatial software worldwide for common goals. This study aims to create a plug-in design in which multi-criteria decision-making methods (MCDM) can be used directly and shared with other world users with a plug-in to be developed with QGIS software. For this purpose, a plugin named MCDA has been created.

#### 1. Introduction

Software known as closed source (CSS) is non-free software for which the publisher reserves certain license rights, and the user pays a fee for other people to use, modify or share the software. The expression word free is used in the sense of freedom that the word freedom carries. In this respect, open source software is defined as free software and its users as free software users (Hanbay-Tiryaki and Balaman, 2021).

The first organizational initiative for the development of free software was the establishment of the Free Software Foundation by Richard Stallman in 1985. Another foundation established for free software development is the Open Source Geography Foundation (OSGeo), established in 2006. QGIS is a user-friendly open-source Geographic Information System (GIS) software distributed under the GNU General Public License. QGIS is the official project of the Open Source Geography Foundation. It runs on Linux, Unix, Mac OSX, Windows, and Android and supports many vector, raster, and database formats and functions (Kuka ve Bushati, 2014).

The general purpose of Multi-Criteria Decision Making (MCDM) is to assist the decision maker in choosing the "best" option among the many possible

options in the presence of multiple selection criteria and different criteria priorities. A site selection decision is made in 4 steps. These steps are; determining the criteria to be used in evaluating site selection alternatives, defining critical and practical criteria, developing site selection alternatives, evaluating the alternatives, and making the site selection decision (Erden and Coşkun, 2011).

Although developers worldwide have developed plug-ins for many different purposes, there are a limited number of plug-in studies in the field of MCDM that will help decision-makers make decisions about space. Today, it has become common to make spatial analyzes using MCDM methods in public and private institutions. However, it is still a problem for users to perform these operations after a complex series of processes in the GIS software. Although the number of theses, articles, and publications using MCDM methods in our country has increased considerably in recent years, when the studies in the literature are examined, two main problems have been identified for those who do the study. First, the cost problem arose because the GIS software used in the first place was CSS. The other problem is that many tools and processes using open-source or closed-source GIS software and MCDM methods need to be clarified for the user. In this

\* Corresponding Author

(mre.yilmzz@gmail.com) ORCID ID 0000-0003-1946-4342  
(sbilgilioğlu@aksaray.edu.tr) ORCID ID 0000-0002-0881-0396

Cite this study

Yılmaz E & Bilgilioğlu S S (2022). MCDM: A New Quantum GIS Plug-In for Multi Criteria Decision Making Analysis. 5<sup>th</sup> Intercontinental Geoinformation Days (IGD), 90-93, Netra, India

context, it is aimed to develop a plug-in design where users can analyze using MCDM methods without learning the use of a GIS program.

## 2. Method

### 2.1. QT

Qt was developed in 1990 by developers Eirik Chambe-Eng and Haavard Nord to design a C++ database application for ultrasound images. Thanks to the Qt library developed over the years, Qt Designer has enabled users to design fast and effective graphical user interfaces (GUIs) without writing long codes (Rischpater, 2013).

### 2.2. Python

Python is an interpreted, object-oriented, high-level programming language with dynamic semantics. Highly built-in data structures combined with dynamic typing and dynamic linking make it very attractive for rapid application development and for use as a scripting or glue language for interconnecting existing components (URL-1).

### 2.3. PyQGIS

PyQGIS is an adapter developed by the QGIS community and required to develop a new GIS software using the Python language and the QGIS API and to make a new plug-in QGIS (Karataş & Kirbaş, 2015). By converting Qt to PyQt and QGIS to Pyqgis, the SIP tool uses Qt and QGIS libraries with the Python

programming language. When PyQt or PyQGIS classes are used with the SIP tool, the codes in C++ classes work using python.

### 2.4. PyQt

PyQt is a GUI module developed by the British company Riverbank Computing Limited, combining the Qt library and the cross-platform interpreted Python programming language. PyQt4, PyQt5, and finally, PyQt6 were released in January 2021. PyQt has many modules for developing interfaces.

### 2.5. QGIS

Free and open-source GIS software has increased its popularity as it allows the creation and customization of various spatial applications by meeting the specific needs of its users. QGIS is one of the most flexible of this software. Thanks to the use of python, where users can develop in the GIS software environment, spatial applications are allowed (Oxoli et al., 2016). QGIS also includes a "plug-in" architecture where extensions to the application's core functionality can be developed and used with existing plug-ins (Khan & Mohiuddin, 2018).

## 3. Results

The Flow Diagram, which includes the menus of the plug-in developed in QGIS software and the steps to be followed when analyzing with MCDM methods, respectively, as a geographical tool, is shown in Fig. 1.

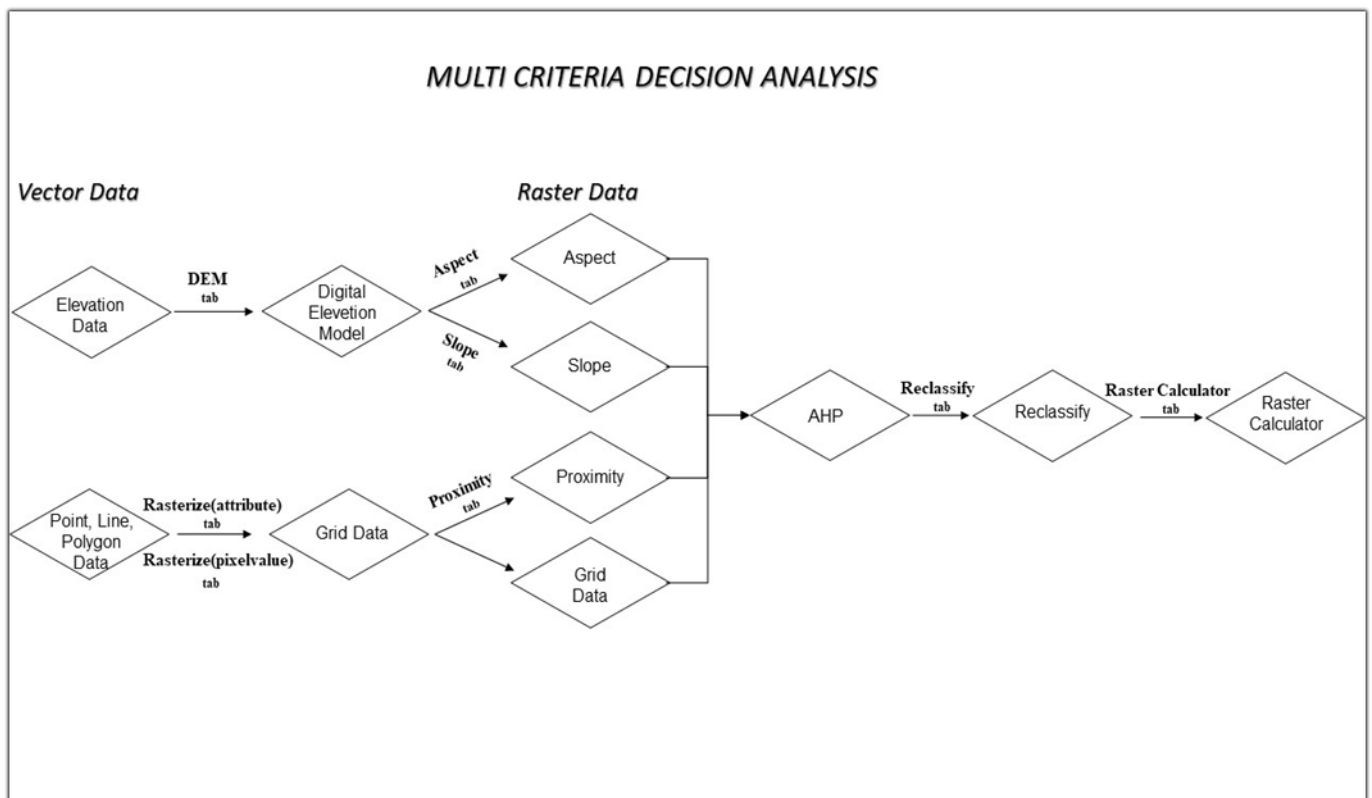


Figure 1. MCDA plugin's menu flows diagram.

Before the functions in the flow chart were coded, the functions that each function would use in common were determined, and the coding process was started. In this context, functions named `dosya_ac()`, `vector_sec()`, `raster_sec()`, `projection_check()`, `name_check()`, `progress()` were written first.

1. `dosya_ac()`: This function will create a new folder named AHP on the desktop when any function in the plug-in is run and save all the files to this folder.

2. `vector_sec()`: Written to import data in vector data format (.shp, .geojson, and .gml) into QGIS 3 software. It is coded to work when the tool buttons of Clip, Dem, Rasterize (attribute) and Rasterize (pixel value) functions are clicked.

3. `raster_sec()`: Import raster data format (.tif, .tiff) into QGIS 3 software. It is coded to run when the tool buttons of the Aspect, Slope, Proximity, Reclassify, and Raster Calculator functions are clicked. 4. `projection_check()`: It gives the information of which projection system the data used in Clip, Aspect, Slope, and RasterCalculator functions belong to, with LineEdit.

5. `name_check()`: It checks whether there is a previously saved file with the same name in the AHP folder.

6. `progress()`: Shows the time-dependent change of the ongoing process with the ProgressBar tool to the user.

7. Then, the functions of the "Grid Data Conversion" and "Weighted Sum" menus in the flow diagram; It is written in the order Clip, Dem, Aspect, Slope, Rasterize (attribute), Rasterize (pixel value), Proximity, Matrix\_Calculator(), Reclassify, Raster\_Calculator.

8. `Clip()`: Performs the split operation. It is coded to determine the working limit.

9. `Dem()`: It is coded to generate digital terrain model data in raster data format from elevation data in vector data format.

10. `Aspect()`: It is coded to generate a raster data type aspect map from the generated dem data.

11. `Slope()`: It is coded to generate a raster data type slope map from the generated brew data.

12. `Rasterize (attribute)`: It is coded to generate raster data to be created by selecting the desired attribute information from the .dbf file as the numerical value of the pixels from the line and polygon data in vector data format.

13. `Rasterize (pixel value)`: It is coded to generate raster data. The desired numerical value can be assigned as the numerical value of the pixels from the line and polygon data in vector data format.

14. `Proximity()`: Coded to generate proximity state maps.

15. `Matrix_Calculator()`: It is designed as an AHP Calculator tab. From the available comparison matrix values using Multi-Criteria decision analysis techniques, The normalized matrix was coded to calculate the random index, weight, consistency vector mean, consistency index, and consistency ratio values.

16. `Reclassify()`: The generated raster data is coded to assign new pixel values.

17. `Raster_Calculator()`: It is coded to perform mathematical operations on the pixel values of the

raster data in order to obtain a single raster data with new pixel values by multiplying and summing the consistency ratios of the criteria and sub-criteria and the pixel values.

The designed plug-in consists of two menus named Grid Veriye Dönüşüm (Grid Data Conversion) (Fig. 2) and Ağırlıklı Toplam (Weighted Sum) (Fig. 3).

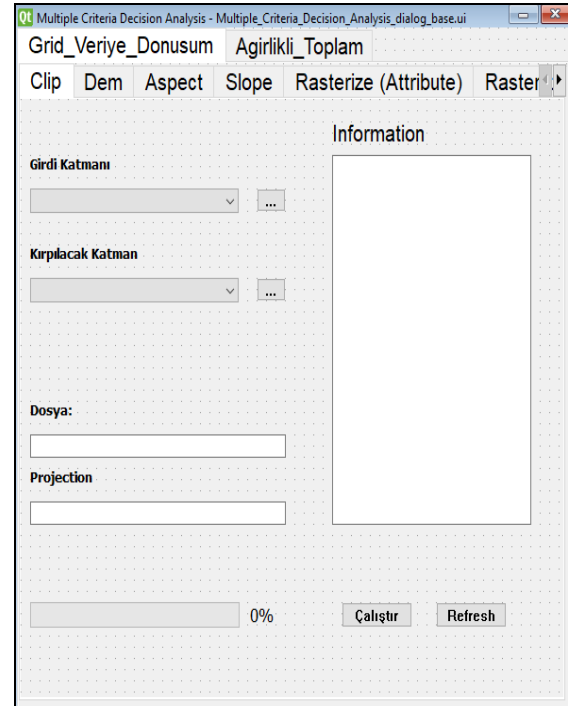


Figure 2. Grid data conversion menu.

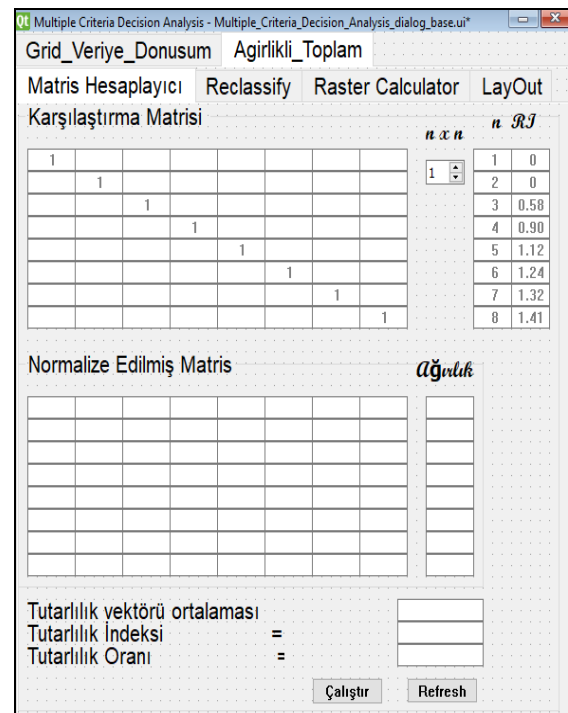


Figure 3. Weighted sum menu.

When the interface design is completed in the Qt Designer program, the functions of the geographical tools to be used for geographical analysis are coded with the help of Python and PyQGIS. After the coding of the functions is completed, it is possible to establish a

relationship between the functions and the menus in the interface design by establishing signal-slot connections. Button, Combobox, etc., in the interface design. The tools emit a signal when clicked. The connection of the broadcast signal with the function (slot) is established by coding with the python programming language. An example of function code shown in Fig. 4 and function signal-slot connection shown in Fig. 5.

```

553
554
555
556
557
558
559
560
561
562
563
564
565
566
567
568
569
570
571
572
573
574
575
576
577
578
579
580
581
582
583
584
585
586
587
588
589
590
591
592
593
594
595
596
597
598
599
600
# =====

```

Figure 4. Slope function codes.

```

1777 #Slope
1778 self.dlg.textEdit_5.setEnabled(False)
1779 self.dlg.pushButton_7.clicked.connect(self.raster_sec)
1780 self.dlg.pushButton_7.clicked.connect(self.Slope_comboBoxes)
1781 self.dlg.pushButton_7.clicked.connect(self.projection_check)
1782 self.dlg.pushButton_10.clicked.connect(self.Slope)

```

Figure 5. Slope function signal-slot connection.

#### 4. Discussion

In the literature research, it has been determined that open source GIS software is preferred over commercially licensed software in order to make spatial analyzes thanks to its advantages such as free, reliable, changeable, distributable and easily accessible in recent years. In the examinations, it is seen that the work done with the QGIS software, which is the open source GIS software, has increased in the last fifteen years. In addition, another result of the research is the increase in GIS projects using MCDM methods.

#### 5. Conclusion

The study consists of a QGIS plug-in design that will enable geographic analysis. The purpose of the application is to design an open source, free, simple to learn and use plug-in for users who will analyze using MCDM methods. Since the plug-in is designed with open-source codes, it can be further developed by its

users in the future. As a result, a GIS plug-in has been developed, and it is aimed to be presented to the user with all the design phases. The interface design of the plug-in was completed with the Qt Designer software. Geographic tools are coded using the open source python programming language and the QGIS API, and the PyQGIS adapter used in plug-in development. Geographical tools have been designed considering the interface designs of GIS software used in MCDM applications. Thus, it is aimed to be easy to understand for the user. The plug-in that has been prepared has been presented to all users of the world at the address <https://github.com/mreylmzz-hub/MCDA-Plugin>.

#### References

Erden, T. & Çoşkun, M. Z. (2011). Coğrafi Bilgi Sistemleri Ve Analitik Hiyerarşi Yöntemi Yardımıyla İtfaiye İstasyon Yer Seçimi. TMMOB Harita ve Kadastro Mühendisleri Odası, 13. Türkiye Harita Bilimsel ve Teknik Kurultayı. 18-22 Nisan 2011. Ankara.

Hanbay-Tiryaki, S. & Balaman F. (2021). Açık Kaynak Kodlu Yazılımlardan Scratch, Arduino ve Python Kullanımı Hakkında Öğrenci Görüşleri. Journal of Computer and Education Reseach, 9(18), 831-852.

Karataş, İ. & Kırbaş, İ. (2015). Özgür ve Açık Kaynak Kod Coğrafi Bilgi Sistemi Yazılımlarının Karşılaştırmalı Değerlendirmesi. Akademik Bilişim Konferansı, 68-74, Eskişehir. DOI: 10.13140/RG.2.1.3113.2241.

Khan, S. & Mohiuddin, K., (2018). Evaluating the parameters of ArcGIS and QGIS for GIS Applications, International Journal of Advance Research in Science and Engineering, 7, 582-594.

Kuka, S. & Bushati, J., (2014). On the role of GIS technology in Geospatial Education (QGIS vs ARGIS), UBT International Conference, 64.

Oxoli, D., Zurbarán, M., Shaji, S. & Muthusamy, A. K., (2016). Hotspot analysis: a first prototype Python plugin enabling exploratory spatial data analysis into QGIS. In Open Source Geospatial Research and Education Symposium (OGRS2016), PeerJ Inc. San Francisco, USA, 1-6.

Rischpater, R., (2013). Application development with Qt Creator (7-9), Packt Publishing, Birmingham.

URL-1 <https://www.python.org/doc/essays/blurb>



## 5<sup>th</sup> Intercontinental Geoinformation Days

igd.mersin.edu.tr



### Environmental risk and hazards assessment using GIS technology

Ismayilov Mirnukh <sup>1</sup>, Kazimova Latifa <sup>2</sup>

<sup>1</sup>Azerbaijan National Academy of Sciences, Institute of Geography, Baku, Azerbaijan

<sup>2</sup>Azerbaijan State Oil and Industry University, Baku, Azerbaijan

#### Keywords

Environmental  
Landslide  
Morphodynamic  
Natural disasters

#### Abstract

In modern science, different innovative methods are often used to achieve the desired results. One of these methods is GIS technology. With this technology you can achieve the right results. In order to assess the level of risk of landslides and hazards, along with the production of appropriate maps with GIS, the development of the territory will be improved and landscape planning will be properly applied. Such maps will help to minimize and eliminate losses caused by landslides that may occur in the future. The causes of landslides are classified in the above-mentioned studies. The first group of causes includes the main causes while the second group takes responsibility for the activation of landslides. The main causes of landslides are morphometric relief parameters, lithological rock composition and soil moisture index, and average constant precipitation and seismicity - activating factors. ArcGIS was used to improve the accuracy and reliability of landslide propagation.

### 1. Introduction

In recent years, mountain geosystems were under the influence of considerable anthropogenic load, driven by such factors as the rapid development of new settlements, the laying of new asphalted motorways, the construction of industrial facilities as well as the development of mining industry. In this regard, the investigation of landscape- and geomorphological processes, posing a hazard to the sustainable development of the natural-economic systems in the mountainous areas, as well as the forecasting and the prevention of this processes are regarded as topical issues. High seismicity in the south eastern part of the Greater Caucasus favourably affects the occurrence of morpho dynamic processes, including the landslides. The preliminary assessment of hazards and risks posed by landslides in the mountain areas through the application of up-date methods may prevent or reduce damage.

### 2. Study Area

The study area is situated on the 41°53' north latitude and 49°33' east longitude. The territory area makes up 1057,5 hectares. The area typically has low

relief and hilly terrains with the maximum height of 1214 m and the lowest point at 326 m (Fig. 1).



Figure 1. Location of the study area

### 3. Methodological approaches

In order to increase the extent of accuracy and reliability of the determination of level of landslide-related risk and hazard, ArcGIS/ArcMap programs and GIS were applied. Landslide risk model based on GIS (Lee,

\* Corresponding Author

(e-mail) ORCID ID xxxx - xxxx - xxxx - xxxx  
(latifa.ismaylova@gmail.com) ORCID ID 0000-0002-0254-1746

Cite this study

Mirnukh, I. & Latifa, K. (2022). Environmental risk and hazards assessment using GIS technology. 5<sup>th</sup> Intercontinental Geoinformation Days (IGD), 94-96, Netra, India

2005; Wang et al., 2009; Mora, et al., 1994; Varner, 1984; Griffiths et al., 2008) as well as related investigations (Kumtepe et al., 2011) were used in the work. The assessment and modelling of level of landslide risk and hazard along with the compiling of relevant maps will allow to increase the efficiency of mastering of territory and apply the landscape planning properly. Such maps will contribute to minimize and eliminate losses caused by landslides that may occur in the future.

The GIS-based landslide risk model of (Mora et al., 1994) was used. The reasons of occurrence of landslides are classified in the above mentioned studies. The factors were analysed through GIS in accordance with the following formula:

$$A(\text{fet})_{\text{landslide}} = (S_d \times S_{lc} \times S_{sm}) \times (T_{al} + T_{sr}) \quad (1)$$

where  $S_d$  is the degree of inclination of slopes;  $S_{lc}$  is the lithological composition of rocks;  $S_{sm}$  is soil moisture index;  $T_{al}$  is the average monthly amount of precipitation in multiyear period; and  $T_{sr}$  is the seismicity rate.

R.Kumpe et al. (Kumtepe et al., 2011) used eight indicators to assess the extent of landslide-related hazard: inclination of a slope, direction of a slope, curvature of a slope, index of plant cover, lithological composition of rocks, tectonic fracture, farness in relation to rivers and roads. Landscape- and environmental risks of landslides were identified with taking into account the specific characteristics of the studied south eastern slope of Greater Caucasus as well as such factors as anthropogenic loading, land use, relief, vertical and horizontal fragmentation, indices of landscape's ecomorphological tensity and factors of landscape- and environmental assessment. Relatedly, the following formula was used:

$$S_i = \frac{\sum S}{\sum S_{fic}} : N \quad (2)$$

where  $S_i$  is the landslide intensity index;  $S$  is the area affected by landslides;  $S_{fic}$  is the total area of factors, involved to the comparison; and  $N$  is the number of measurements.

The figures of landslide intensity index obtained due to calculations are ranked as follows: <0,1 –very weak; 0,1-0,3 – weak; 0,3-0,5 – middle; 0,6-0,8 – high; >0,8 very high. Researchers note that the correlation between the indicator of landslide intensity index and the level of landslide-related risk and hazard is available. The landslide intensity index was identified by each factor responsible for the activation of landslide. Then the gained data was analysed through GIS. The last phase of was carried out based on the following formula:

$$S_i = \frac{S_a + S_l + S_{vf} + S_i + S_e + S_{si} + S_{sd} + S_{vc} + S_{lc} + S_{fr} + S_{dr} + S_{eb}}{S_{fic}} \quad (3)$$

where  $S_a$  is the anthropogenic loading;  $S_l$  is the use of lands;  $S_{vf}$  is the vertical fragmentation of relief;  $S_e$  is the eco-geomorphological tension;  $S_{si}$  is the inclination of

slope;  $S_{sd}$  is the direction of slope;  $S_{sc}$  is the curvature of slope;  $S_{vc}$  is the vegetation cover;  $S_{lc}$  is the lithological composition of the rocks;  $S_{fr}$  is the tectonic fracture;  $S_{dr}$  is the distance from rivers;  $S_{dr}$  is the distance from roads; and  $S_{eb}$  is the environmental balance.

#### 4. Results

The use of land as one of forms of anthropogenic activity is regarded as an important factor of assessment of risk and hazard posed by landslide (Ismayilov et al., 2012). Researches show that landslides may happen at very different extent depending on agricultural activities, perennial plant-growing, gardening, pasturing, settlements' impact, the availability of roads and communications, etc. (Fig. 2).

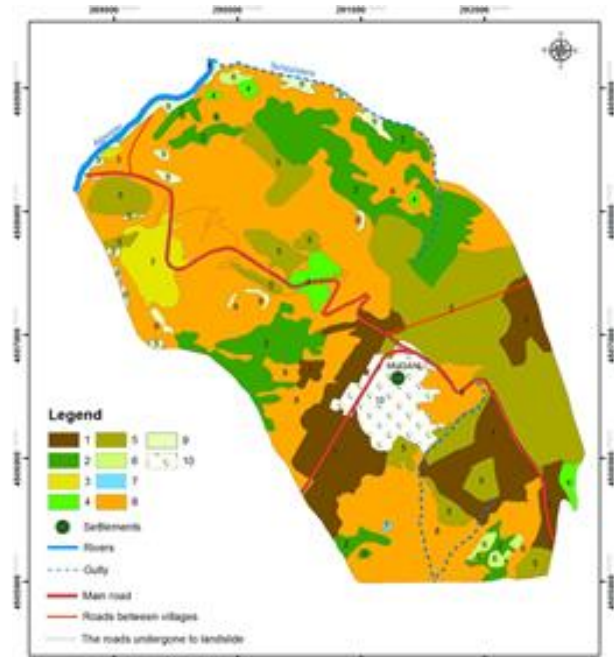


Figure 2. Impact of soil use on the landslides

The map legend reflecting the impact of soil use on the occurrence of landslides in the municipality of Mughanli and surrounding areas:

1. Plantations of perennial plant-growing – medium hazard of landslide.
2. Rare trees and shrubs used in pasturing – medium hazard of landslide.
3. Shrubberies and meadows composed of small bushes and used as pastures and hayfields – very high hazard of landslide.
4. Woodlands, partially used in pasturing and anthropogenically degraded – low hazard of landslide.
5. Arable or fallow lands of low-incline watershed areas – very weak hazard of landslide.
6. Fruit gardens, composed of perennial plants – weak hazard of landslide.
7. Artificial water reservoirs – very high hazard of landslide.
8. Pastures and hayfields on low-incline slopes – high hazard of landslide.
9. Cliffs and sandy areas, not usable in agriculture – very low hazard of landslide.
10. Rebuilt settlements, courtyards and roads – very high hazard of landslide.

In order to increase the extent of accuracy and confidence of spread of landslides, ArcGIS program was applied. Furthermore, the relations between the land use and the intensity of landslides as well as related risks and hazards were studied and given on *Table 1*. Results of

environmental risks and hazards are grouped as reflected on *Table 3*. Analysis of this table shows that 55,9% of the territory is of high and very high hazard of sliding.

**Table 1.** The relations between land use and risks, hazards and intensity of landslides in the study area

Land use form	Contours	Area, km <sup>2</sup>	Areas affected by landslide, km <sup>2</sup>	Intensity index of landslide	Risk of landslide by point
1	5	1362	409	0,3-0,5	3
2	9	1372	412	0,3-0,5	3
3	2	282	169	0,6-0,8	4
4	5	185	19	0,1-0,3	1
5	12	2155	216	0,1 and lesser	1
6	4	7139	7139	0,1 and lesser	2
7	1	4891	391	0,8 and higher	5
8	5	4455	356	0,6-0,8	5
9	17	2239	223	0,3-0,5	4
10	1	460	368	0,8 and higher	5

**Table 2.** Distribution of vegetation coverage according to risk and hazard intensity indexes of landslide areas

Number of plant group on the map	Area, km <sup>2</sup>	Intensity index of landslide	Risk of landslide by point
1	1082	0,1-0,3	2
2	2583	0,1 and lesser	1
3	46	0,1 and lesser	1
4	3964	0,6-0,8	4
5	681	0,3-0,5	3
6	998	0,6-0,8	4
7	178	0,8 and higher	5
8	151	0,8 and higher	5
9	948	0,6-0,8	4

## 5. Conclusion

1. The research model, used during this study will allow modelling and assess landscape- and environmental risks and hazards, posed by landslides in young seismic mountain areas of Azerbaijan as well as other young mountain geosystems, shaped during the Alpine folding period. The used model enables to carry out this research as well as similar works in a shorter time based on decipherment of satellite images.

2. Beside with this, the landscape- and environmental balance of the area was studied. Over related 16 factors were involved in the study. As a result of this, the extent of accuracy and reliability, as well as the possibility of application of the carried out research were increased.

3. The obtained results allow to assess risks and hazards, posed by landslides in the Greater and Lesser Caucasus, as well as Talysh Mountains and mountain areas of Nakhchivan. These results can be used in the implementation of the future regional development programs, landscape planning and also the organization of transport infrastructure in the southeastern part of the Greater Caucasus.

## References

- Gupta R.P., Joshi, B.C. (1990): Landslide hazard zoning using the GIS approach; A case study from the Ramganga Catchment, Himalayas. - *Engineering Geology* 28:119-131.
- Ismayilov M.J., Mustafayev N.M. (2012): Features of the landslide development on the southeastern slope of Greater Caucasus. - *Transactions of Azerbaijan Geographical Society*, volume. 12: 95-103.
- Lee S. (2005): Application of logistic recreation model and its validation for landslide susceptibility mapping using GIS and remote sensing data. - *International Journal of remote sensing* 26 (7): 1477-1991.
- Wang BL, Paudel B, Li HQ (2009): Retrogression characteristics of landslides in fine-grained permafrost soils, Mackenzie Valley, Canada. - *Landslides* 6(2):121-127



## 5<sup>th</sup> Intercontinental Geoinformation Days

igd.mersin.edu.tr



### Analysis of Google Point of Interest Data Based on Scoring Key Criteria for Local Restaurants

Fatemeh Rajabi<sup>1</sup>, Farhad Hosseinali<sup>1</sup>, Hamidreza Rabiei-Dastjerdi<sup>2</sup>, Mahdi Rajabi<sup>3</sup>

<sup>1</sup> Shahid Rajaee Teacher Training University (SRTTU), Faculty of Civil Engineering, Department of Surveying Engineering, Tehran, Iran

<sup>2</sup> University College Dublin (UCD), School of Architecture, Planning and Environmental Policy & CeADAR, Dublin, Ireland

<sup>3</sup> University of Tehran (UT), Faculty of Geography, Department of Remote Sensing and Geographic Information System (GIS), Tehran, Iran

#### Keywords

Food culture  
Geographical zoning  
Web data  
POI data  
Google users

#### Abstract

Food has a very important place in human daily life. The characteristics of multidisciplinary research in food culture are quite evident and from geography perspective, the relationship between the environment and humans can be emphasized in the study of food culture. With the expansion of the urbanization process and the formation of new occupations for people, geography can have a significant impact on the cooking and food culture of the people. Geographical zoning is an important way to understand and analyze the spatial structure of food production and consumption. Today, food studies have become widespread due to the availability of web data. The aim of this study is to analyze the opinions of POI data generated by Google users based on the scoring of the main criteria. The criteria considered in this article (local access, food price, food quality, customer-oriented behavior of employees, hygiene, interior space and exterior beauty of the restaurant) are in local restaurants in Tehran's 8th district. The results of this study show that people can find their desired restaurant in a shorter time according to the main criteria and based on these criteria, give more accurate points to the restaurants.

#### 1. Introduction

Food is a basic material element to meet the physiological needs of humans, studying its quality is one of the most important issues in the field of health and food preference due to the influence of the geographical environment can have significant distinguishing features. Local knowledge is underrepresented in food policy and planning (Fast et al. 2018). However, given the diverse food community operating at local scales, a collaborative approach to supporting sustainable and regenerative food systems is no small task (Fast et al. 2018). In recent years, crowd-sourced or user-generated data and web-based mapping have emerged as competitors to official data and their authoritative producers and institutions (Perkins et al. 2011). This research is designed based on the concept of city and citizen as a text (Karimzadeh et al. 2013). That is, if the city is considered as a text, citizens are authors who may translate their identity into this text and leave traces of it in the city and urban data (Rabiei-Dastjerdi et al. 2022).

Therefore, user reviews for restaurants were used in the form of Google Place of Interest (POI) data as a type of collected or user-generated data about food quality and to determine the best place, they turned into a small amount. This digital footprint can be used to describe and understand a city (Rabiei-Dastjerdi et al. 2022).

In this study, considering the fact that users, in addition to being producers of points of interest (POI) data, can also use that data. Therefore, if the rating and feedback of this data for restaurants is more accurate in the form of scoring the main criteria in the applications related to restaurants, the users can score the main criteria more accurately in a shorter time for choosing the desired place, and they can choose their favorite restaurant according to the same points. In addition, the advantage of the plan presented in this article is that it reduces the time and cost of locating the considered restaurant and increases the quality of all restaurants and discovers the strengths and weaknesses of the mentioned parameters.

#### \* Corresponding Author

\*(fatemeh.rajabi7596@gmail.com) ORCID ID 0000-0001-8113-987X  
(f.hosseinali@sru.ac.ir) ORCID ID 0000-0002-7544-8825  
(hamid.rabiei@ucd.ie) ORCID ID 0000-0003-2576-793X  
(rajabi.mahdi@ut.ac.ir) ORCID ID 0000-0001-6667-8242

#### Cite this study

Rajabi F., Hosseinali F., Rabiei-Dastjerdi H. & Rajabi M. (2022). Analysis of Google Point of Interest Data Based on Scoring Key Criteria for Local Restaurants. 5<sup>th</sup> Intercontinental Geoinformation Days (IGD), 97-100, Netra, India

## 2. Study Area

The studied area in this article is District 8 of Tehran Municipality, one of the urban areas of Tehran in Iran, which is located in the east of this city. The history of physical and spatial development of District 8 of Tehran Municipality goes back to 1320-1330 solar years. Region 8 has 3 districts and 13 council districts. Narmak, Majidieh and Tehran Pars neighbourhoods are among the old urban settlements of this region.

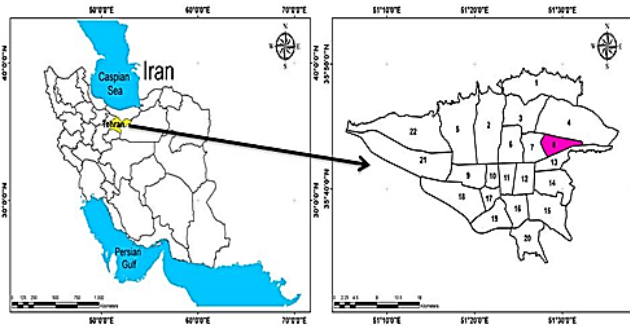


Figure 1. Location of the study area

## 3. Method

### 3.1. Data

Point of Interest (POI) data represents the location of a landmark or a building in the physical space through geographical coordinates. It has a significant role to play in connecting businesses with customers (Chaudhary 2021). The end-users use POI data to find accommodations, shopping places, transportation, and nearby emergency services. POI data equips relevant government bodies and enterprises in gleaning patterns and trends recognition, enabling them to make data-driven decisions (Chaudhary 2021). Some of the most common POI data generation methods by businesses include data extraction from open sources, user-generated data on social media platforms, extracting data from government directories, and hiring/contracting a team to manually update the company’s POI database (Chaudhary 2021). Among the above-mentioned methods, data collection and verification by a dedicated team ensures an accurate and healthy stream of POI data. This method includes the use of a smartphone and a purpose-built app in which new locations were added and the existing ones were verified in real-time. The major challenges associated with other methods mentioned include inconsistency and inaccuracy in datasets as it is highly dependent on how actively and precisely the data is being gathered and updated by companies or government bodies disseminating such information (Chaudhary 2021).

In this study, the reviews of 700 users on Google were collected for 25 local restaurants in the 8th district of Tehran by the researcher in Excel software and using these comments, the main parameters for choosing an excellent restaurant were examined and scored.

### 3.2. Main parameters

The purpose of this study is to investigate and analyse web data in the form of POI data generated by Google

users based on scoring the main criteria in local restaurants based on converting letter variables into numerical variables. In this research, six parameters affecting quality should be examined: 1. local access, 2. food price, 3. food quality, 4. customer-oriented behaviour of staff, 5. hygiene, and 6. interior and exterior beauty of the restaurant. The parameters, then, were converted to a quantitative level according to Table 1.

**Table 1.** Converting qualitative criteria into quantitative criteria

Quality Degree of Main Criteria	Quantitative Degree of Main Criteria
Very Good	5
Good	4
Medium	3
Bad	2
Very Bad	1

### 3.3. Research Methods

At first, the data was collected in Excel software, and according to Table 1, qualitative criteria were converted into quantitative criteria in the local restaurants of the study area, and they were examined in terms of quantity and ratio. Finally, all quantitative scores for a restaurant were averaged. At the level of quantitative characteristics, investigations were carried out using the optimization method in the software. Then the results were applied to the map of the studied area in Arc GIS software.

## 4. Results and Discussion

This study is useful for scoring the main criteria of local restaurants. In their opinion, users usually focus on their favorite place in choosing the main criteria in different restaurants, and the result can be determined based on choosing the best location according to the main criteria or criteria the user wants in short, the restaurant that gets the highest score among all the main criteria compared to other restaurants was known as the best restaurant.

Table 2 shows the average scores of users for six main parameters for 25 considered restaurants; finally, by averaging among these main parameters, the overall average score of the restaurant was obtained. Among the average scores, with Min operation (Equation 3), the restaurant with the lowest score and with Max operation (Equation 4), the restaurant with the highest score was obtained. [(n) in Equations (1), (2), (3) and (4) is the range of natural numbers.]

$$x, x+1, x+2, \dots, x+n \quad (1)$$

$$x < x+1 < x+2 < \dots < x+n \quad (2)$$

$$\text{Min} (x, x+1, x+2, \dots, x+n) = x \quad (3)$$

$$\text{Max} (x, x+1, x+2, \dots, x+n) = x+n \quad (4)$$

**Table 2.** Investigating the average of six main parameters for local restaurants

Name	Local Access	Food Price	Food Quality	Customer-Oriented Behaviour of Staff	Hygiene	Interior & Exterior Beauty of the Restaurant	Overall Score of the Restaurant
Sharan Food Preparation		3		2.75			2.875
Nader Restaurant	4.666667	2.615385	3.909091	3	2.75	4.769231	3.618395493
Carmado Fast Food		2.333333	3.333333	1		3	2.416666667
Sinor Restaurant			2.75	1		2	1.916666667
Soren Fast Food	4.666667	3	4	4	5	4.2	4.144444444
Walnut Cafe and Restaurant	1.5	2.25	3.538462	2.8	3.333333	4.857143	3.046489621
Khayyam Cafe and Restaurant		5	2.5	5	3.333333	4.75	4.116666667
Apple360 Pizza		1.5	3.222222	3		5	3.180555556
Mister Kentucky Fast Food		3	4.052632	4	1	5	3.410526316
Tabakhi Shakh Tala	4	1.5	3.933333	3.5	4.75	3.666667	3.558333333
Javanan Restaurant	5	2.888889	4.073529	4.034483	4	3.777778	3.962446473
Narmak Park Restaurant		3	4.666667	3	5	4.4	4.013333333
Haida		3.5	3.75	3	1	4	3.05
Bapuk Italian Restaurant		3	3.9	4	5	4.666667	4.113333333
Romana Italian Restaurant	5	2.333333	3.875	4.5			3.927083333
Babajun Fast Food		2.666667	3.166667	1	2.666667	4	2.7
Zhivan Fast Food	3	2.4	3.923077	3	4.666667	4.933333	3.653846154
Grilled Haj Abdulahi		3	4	5	1	2	3
Sibza		3	5	1			3
Khameez Burger	3	2.5	4.636364	3.5	4		3.527272727
Baguette Restaurant	2.666667	1.823529	4.02	4.035714	3.8	4.583333	3.488207283
Food Court 7 Center		3	4.5	2	3	4.8	3.46
Farhad Restaurant			4.571429	4.25		2	3.607142857
Dozli Grill	1.5	3.333333	4.153846	3	4.5	1	2.914529915
MIN	1.5	1.5	2.5	1	1	1	1.916666667
MAX	5	5	5	5	5	5	4.144444444

Meanwhile, some users are looking for a place with their desired scores. For example, a user intends to go to a place where the quality of food and the behavior of the staff in the form of customer service, and hygiene of the place are good, that is, with a score of 4 and other parameters, i.e., local accessibility, food price, and the beauty of the interior and exterior of the restaurant should be at an average level, i.e., with a score of 3. In this case, the decision-making system in locating will introduce the desired restaurant with this level of scores in the shortest time, and the user can go to his desired place.

In Fig 2, the results of the findings of Table 2 are shown on the map of the 8th district of Tehran. In the existing applications, the user can choose the restaurant he wants and go there, taking into account the general rating of other users, but in these applications, the rating of any minor parameter has not been done in detail.

The advantage of this design compared to existing applications is that users can record their opinions in the form of parameters in a more precise and accurate way and while searching for your favorite place according to these parameters, go to the restaurant you want based on the main parameters mentioned and have a good time there.

This plan reduces time and cost in locating the considered restaurant and increases the quality of all restaurants in the mentioned parameters; finally, the results obtained from this data in this paper can be used in the analysis of other types of point-of-view (POI) data.

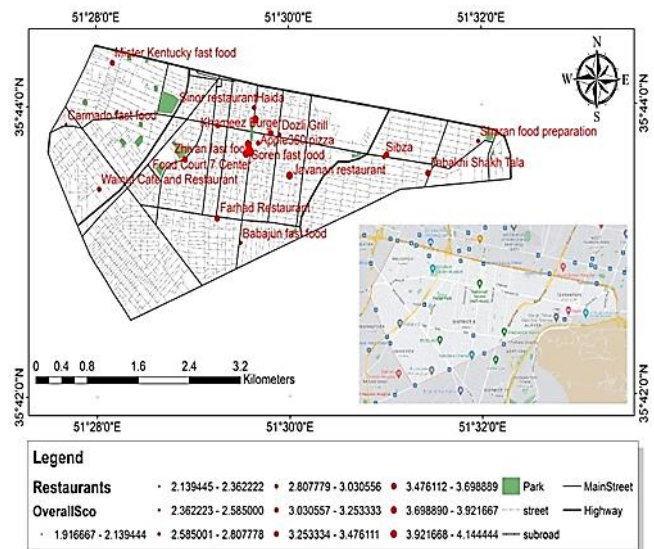


**Figure 2.** Rating map of local restaurants in district 8 of Tehran

### 3. Potential Challenges

The findings showed that using user-generated data in general and Google POI data in particular, the method and tool proposed in this research to measure and locate local restaurants have challenges due to various factors, which can be explained as follows:

- ❖ One of the main arguments in recording user opinions for local restaurants is that only giving stars without recording the opinions accurately and leaving opinions and scores without a framework and, in general, cannot record the strengths and weaknesses of a place in detail, and there is no such process in the existing applications related to this issue either but having multiple criteria for restaurant data is partially efficient for scoring, saving time and resources.
- ❖ On the other hand, the geography of each user-generated data platform and its richness depends on the socioeconomic context (e.g., population density, ethnicity, education, and income) (Ballatore et al. 2020). For example, the digital divide excludes people with less digital skills or access to digital devices from generating user-generated data (Schradie 2011). Some people do not provide reviews while using user-generated data and platforms due to their cultural values, age, and lifestyle (Wilson et al. 2012; Edelman 2013).

In this study, Google POI location data were used as partial solutions for this problem (Rabiei-Dastjerdi et al. 2022). In general, from the social, cultural and behavioural points of view in applications, users' comments should be such that their main parameters in these fields should be maintained in the accurate recording of the opinion and also the choice of the desired location.

## 5. Conclusion

The food that is consumed daily is of great importance. In addition to food, the place where people eat and the main parameters related to these two (such as the quality of raw materials for food and cooking, food hygiene, food health, environmental hygiene, food price, the behavior of people who are present in the environment, the beauty of the environment, etc.) are also very important.

The registration of points of interest (POI) is considered a kind of collaborative mapping and often, participatory mapping research is dedicated to specific communities or social groups facing local issues (indigenous-rural-community, urban, environmental-natural resources) (Fagerholm et al. 2021; de Carvalho et al. 2021).

This study developed a POI system to enable and engage customers, employees and managers of local restaurants and generate new information about regional food quality. This represents an attempt to move towards more systematic and controlled POI creation. This method describes the project, the participants, the Geo-web, and the data components needed to create the POI. This study leads to the creation of a quality data set of local POI restaurants and a map to select the best restaurant from the point of view of the main parameters proposed in order to reach the user's desired location more easily. The new data will enhance the knowledge of regional decision-makers and highlight the decision-making spatial data directly reported by Geo-web

contributors. While the scope of this study ends here, the primary recommendation for food regulatory bodies and stakeholders in this field is to develop relevant local regional food policies to be adopted by the relevant trade union and supports a community-based food decision-making system. The impact of this research on regional and urban food policy, and the development of programs and regulations that accompany it, will be determined through the continued engagement of the region's food community—both formal food policy stakeholders and all those who share their comments.

## References

- Ballatore, A., & De Sabbata, S. (2020). Los Angeles as a digital place: The geographies of user-generated content. *Transactions in GIS*, 24(4), 880-902.
- Chaudhary, P., 2021: Adapted from the book POI Data 101's ebook
- de Carvalho, C. M., Luiz Giatti, L., Fagerholm, N., Bedran-Martins, A. M., & Kytta, M. (2021). Participatory Geographic Information Systems (PGIS) to assess water, energy and food availability in a vulnerable community in Guarulhos (Brazil). *International Journal of Urban Sustainable Development*, 13(3), 516-529.
- Edelman, N. (2013). Reviewing the definitions of "lurkers" and some implications for online research. *Cyberpsychology, Behavior, and Social Networking*, 16(9), 645-649.
- Fagerholm, N., Raymond, C. M., Olafsson, A. S., Brown, G., Rinne, T., Hasanzadeh, K., ... & Kytta, M. (2021). A methodological framework for analysis of participatory mapping data in research, planning, and management. *International Journal of Geographical Information Science*, 35(9), 1848-1875.
- Fast, V., & Rinner, C. (2018). Toward a participatory VGI methodology: crowdsourcing information on regional food assets. *International Journal of Geographical Information Science*, 32(11), 2209-2224.
- Karimzadeh, A., Khosravi, A., & Dastjerdi, H. R. R. (2013). City and citizen as a text and its author: A Semiotic Reading. In *New Urban Language Conference Proceedings*.
- Perkins, C., Kitchin, R., & Dodge, M. (2011). *Cognition and Cultures of Mapping. The map reader: Theories of mapping practice and cartographic representation*, 297-303.
- Rabiei-Dastjerdi, H., McArdle, G., & Aghajani, M. A. (2022). User-Generated data in cultural mapping: Analyzing Google point of interest reviews in Dublin. *ISPRS Annals of the Photogrammetry, Remote Sensing and Spatial Information Sciences*, 107-112.
- Schradie, J. (2011). The digital production gap: The digital divide and Web 2.0 collide. *Poetics*, 39(2), 145-168.
- Wilson, A., Murphy, H., & Fierro, J. C. (2012). Hospitality and travel: The nature and implications of user-generated content. *Cornell hospitality quarterly*, 53(3), 220-228.



## 5<sup>th</sup> Intercontinental Geoinformation Days

igd.mersin.edu.tr



### Investigation of spatial change on badlands topography around Kuyulu Village (Adıyaman) with remote sensing and geographic information systems

Sezgin Abukan<sup>1</sup>, Halil İbrahim Yıldırım<sup>1</sup>, A. Serdar Aytaç<sup>2</sup>, Nizar Polat<sup>3</sup>

<sup>1</sup>Harran University, Social Sciences Institute, Geography, Sanliurfa, Türkiye

<sup>2</sup>Harran University, Faculty of Arts and Sciences, Geography, Sanliurfa, Türkiye

<sup>3</sup>Harran University, Engineering Faculty, Department of Geomatics, Sanliurfa, Türkiye

#### Keywords

Badlands Topography  
Remote sensing  
Satellite Images  
GIS

#### Abstract

The badlands topography located around Kuyulu Village (Adıyaman) to the west of Atatürk Dam, which is one of the most important erosion area in Southeastern Anatolia in Turkey. In this study, it is aimed to determine the time-dependent change in the badlands topography area around Kuyulu Village (Adıyaman) by using Remote Sensing and geographic information system techniques. As a result of the research, it was determined that there was a continuous expansion in the badlands area in the period between 1984-2020.

#### 1. Introduction

Erosion can be defined as corrosion and acquaintance of the soil with external factors and processes. Erosion examines under two headings as natural erosion (geological erosion) and ekstralated erosion. Natural erosion is the removal of soil due to natural processes throughout all geological times. Also ekstralated erosion is caused by human misuse of land. (Yılmaz, 2006).

Badlands topography is one of the important topography shapes in arid and semi-arid regions. It mostly occurs on the slopes where clayey, sandy, spindle and marly layers come in succession.

Drop erosion, which starts on slopes devoid of vegetation from time to time during heavy rains, turns into surface erosion by the flow of rain water covering the surface (Semenderoğlu et al., 2006). Later, with the progress of surface erosion, small streamlines formed on the surface and small rills occur on the slopes. Small channels that expand and deepen over time turn into grooves, slits and gullies. (Semenderoğlu ve diğ., 2006). The topography of badlands, which consists of steeply sloping slopes, is very weak in terms of vegetation, quite dense in terms of small brooks and has a high erosion rate (Erinç, 2015).

In this study, it is aimed to determine the time-dependent change in the area of badlands topography located around Kuyulu Village (Adıyaman) to the west of Atatürk Dam, using remote sensing and geographic information systems techniques.

#### 2. Study Area

The study area includes Kuyulu village and its surroundings, located within the borders of Adıyaman province in the Southeastern Anatolia Region.

The badlands topography to the west of the Atatürk Dam; It is located between the villages of Uğurca, Bebek, Akyazı and Kuyulu (Fig. 1). The study area covers an area of roughly 150 km<sup>2</sup>.

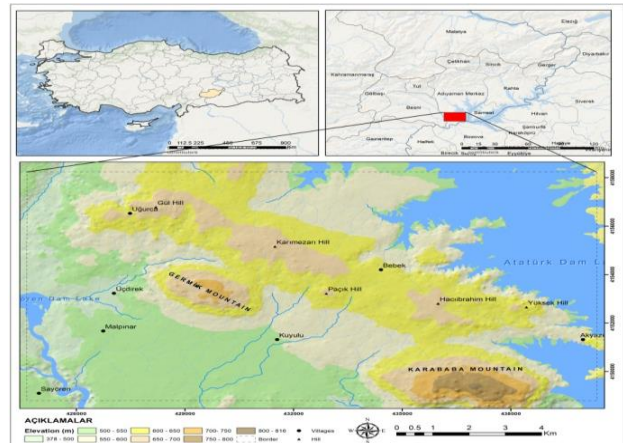


Figure 1. Location of the Study Area.

#### 2.1. Geology and Geomorphology of the Area

In the study area, the oldest units are Cretaceous limestones, clayey limestones, shales, and the youngest units are Quaternary alluviums. Badlands topography has developed on stationary clayey limestones and

#### \* Corresponding Author

(abukansezgin@gmail.com) ORCID ID 0000-0002-7017-1249  
(ibrahilyildirim@gmail.com) ORCID ID 0000-0002-8268-2521  
(aserdaraytac@harran.edu.tr) ORCID ID 0000-0001-8638-038X  
(nizarpolat@harran.edu.tr) ORCID ID 0000-0002-6061-7796

Abukan, S., Yıldırım, H. İ., Aytaç, A. S., & Polat, N. (2022). Investigation of spatial change on badlands topography around Kuyulu Village (Adıyaman) with remote sensing and geographic information systems. 5<sup>th</sup> Intercontinental Geoinformation Days (IGD), 101-104, Netra, India

ware. (Fig. 2). The highest parts of the area, which has a plateau appearance in terms of geomorphology, are Karababa Mountain Hill (816 m) and Germik Mountain Hill (732 m). The Badlands topography also developed on the slopes of the corresponding anticlines.

Atatürk Dam is located in the northeast of the study area and Sayören Dam Lake is located in the southwest.

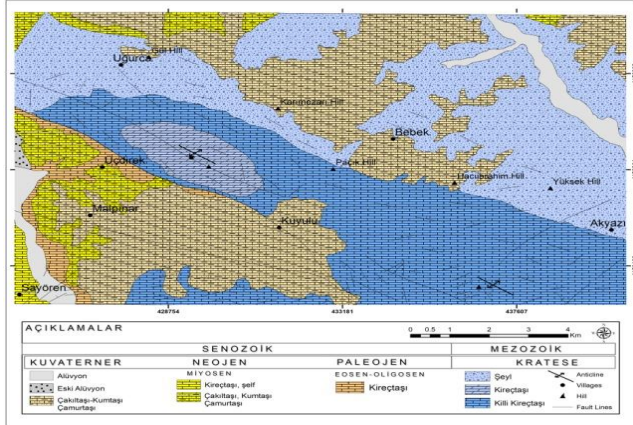


**Figure 2.** Geological of the Study Area

## 2.2. Climate features of the study area

The continental Mediterranean climate features are observed in the field, with hot and dry summers and colder winters, and the annual average temperature in the field is approximately 17 °C. Average annual precipitation in the area is around 400 mm. In the area, which has semi-arid conditions in terms of annual precipitation, the vast majority of precipitation occurs in the period between November and October. The period from June to October is quite dry. Due to its semi-arid climate characteristics, the field has very acceptable conditions for the development of badlands topography.

## 3. Material and Method

In the research, 1/100,000 scaled geology and topography maps and Landsat satellite images of the field were used. During the research, the general geological and lithological features of the area were determined. and subsequently satellite images were used to detect the spatial development of the badland's topography.

In the research, satellite images of the field from 1984 to 1990, 2000, 2010, 2020 were specified by using the Minimum Likelihood Classification method in the Controlled Classification method of the ENVI 5.3 Program, the change of the Badlands area over time has been determined (Fig. 3, Tab. 1).

Minimum Likelihood Classification method: basically, it creates a certain amount of classes by recognizing the data sets according to the number of data sets created for classification, and then compares with the average of the classes that make up the brightness value of each pixel, and selects the closest class to the pixel. (Karayol, 2012). By using this method, four classes were created to best represent the field. These classes are: Badlands, Cultivated, Uncultivated Area and the Water Area.

**Table 1.** Features of Satellite Images Used in Analysis.

	Landsat 4-5 TM C1 Level- 1	Landsat 4-5 TM C1 Level-1	Landsat 4-5 TM C1 Level-1	Landsat 4-5 TM C1 Level-1	Landsat 8 OLI- TIRS C1 Level-1
Image Properties	1984	1990	2000	2010	2020
View Date	30.08.1984	28.08.1990	23.08.2000	06.08.2010	01.08.2020
Rows/Bands	319/6	319/7	319/6	319/6	319/7
Image Cloudiness Rate	0	0	0	0	0
Image Resolution	8 bit.	8 b.	8 b.	8 b.	8 b.

The development of Badlands over the years has been revealed by digitizing on the layers and data index obtained as a result of the analysis in the ENVI 5.3 interface. Digitized Badlands layer was mapped by editing in Arcmap interface.

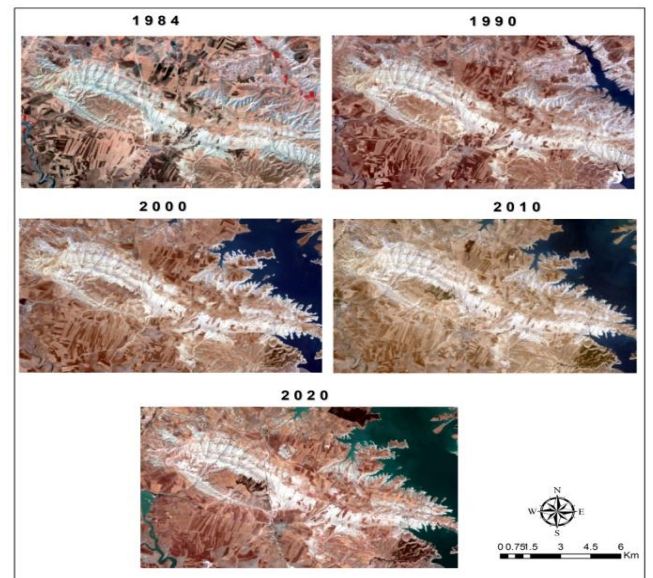


**Figure 3.** Satellite images of the study area.

## 4. Results

By using satellite images of the research area, maps of the badlands area were obtained and the spatial change of the Badlands in 10-year periods were tried to be revealed (Fig. 4-5).

As of 1984, the total area of badlands in the field is 41.35 km<sup>2</sup>. The total area of badlands in 1990 was 43.2 km<sup>2</sup>. There is an increase of about 2 km<sup>2</sup> in the area of badlands during this time period. Due to the Atatürk Dam Lake, which started to collect water in this period, some of the badland's area located under the lake.

In 2000, the total area of badlands decreased to 39.55 km<sup>2</sup>; In 2010, the total area of badlands decreased to 34.2 km<sup>2</sup>. The main reason for this situation is that some of the badland's area is flooded due to the Atatürk Dam Lake reaching its maximum level, and some areas that were not cultivated before are opened to agriculture.

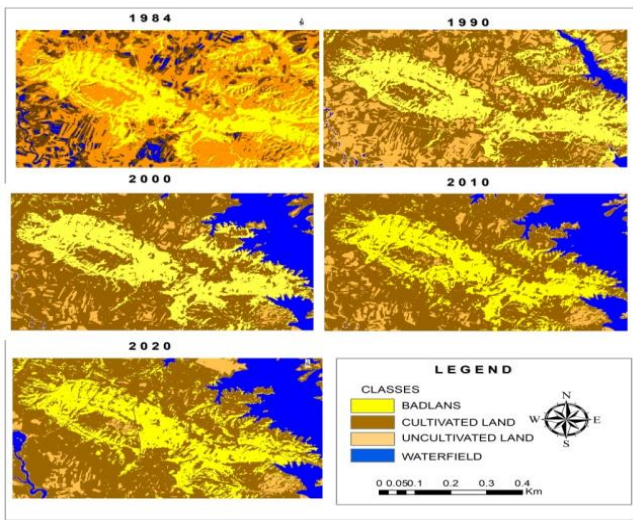


**Figure 4.** Badlands images by Maximum Likelihood Classification method.

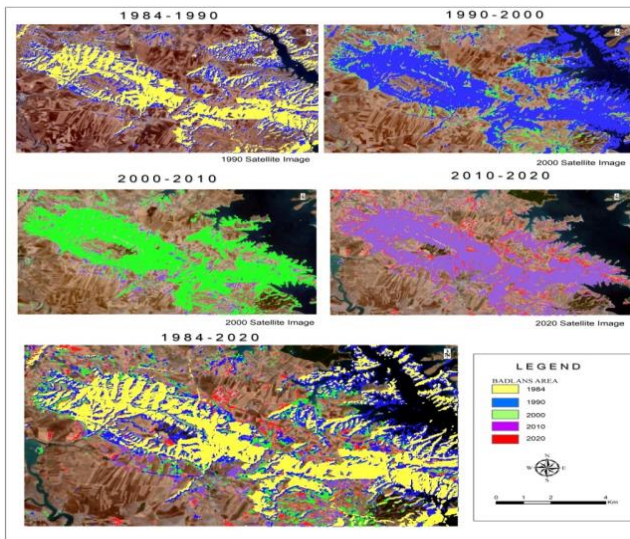


**Figure 5.** The areal changes of the Badlands land in 10-year periods

In 2020, the total area of badlands increased to 36.87 km<sup>2</sup> (Tab. 2). According to the areal changes of the badlands in 10-year periods in the between 1984-2020 increased over time; however, it is seen that it cannot be followed statistically due to the rise of the dam lake level and the opening of agricultural areas in the periods between 1990-2000 and 2000-2010.

As a matter of fact, in the areal changes of the Badlands in 10-year periods, it is clearly observed that the badlands increase regularly in the areas outside the reservoir. The amount of this increase is approximately 2 km<sup>2</sup> between 1984-1990, 0.96 km<sup>2</sup> between 1990-2000, 0.98 km<sup>2</sup> between 2000-2010, 2.9 km<sup>2</sup> between 2010-2020 (Fig. 6).

## 5. Result

According to the areal change of the Badlands in 10-year periods between 1984-2020, the badlands area has increased over time; however, it was determined that this increase could not be observed due to reasons such as the rise of the dam lake level and the farming in the periods between 1990-2000 and 2000-2010. The

combination of RS and GIS is flexible and effective tool for detecting and monitoring environmental changes.

**Table 2.** Minimum Likelihood Classification data index

1984			
Class	Pixel Count	Percent	Area km <sup>2</sup>
Summary			
Badlands	45944	27.329.237	41.35
Cultivated Area	30171	17.946.857	27.15
Uncultivated Area	5714	3.398.904	77.66
Waterfield	86284	51.325.002	5.14
1990			
Badlands	48002	28.553.413	43.2
Cultivated Area	81627	48.554.841	73.46
Uncultivated Area	4964	2.952.776	30.17
Waterfield	33520	19.938.970	4.47
2000			
Badlands	43942	26.138.371	39.55
Cultivated Area	89016	52.950.099	80.11
Uncultivated Area	23694	14.094.091	10.31
Waterfield	11461	6.817.438	21.32
2010			
Badlands	37801	22.485.471	34.02
Cultivated Area	90328	53.730.526	81.93
Uncultivated Area	26671	15.864.924	11.98
Waterfield	13313	7.919.078	24
2020			
Badlands	40970	24.370.513	36.87
Cultivated Area	89374	53.163.051	80.44
Uncultivated Area	26716	15.891.692	9.95
Waterfield	11053	6.574.744	24.05

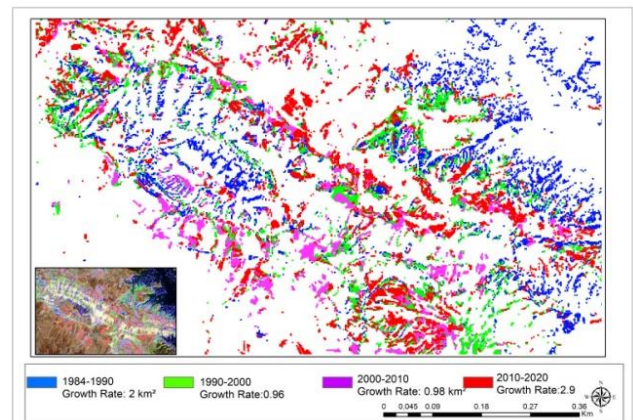


**Figure 6.** Spatial distribution of Badlands changes by years

## References

- Erinç, S., (2015) Geomorphology II, Der Publications, İstanbul.
- Semenderoğlu, A., Gülersoy, A. E., İlhan, A. (2006). Physical Land Degradation. Turkish Geography Coğrafya magazine, Number: 47, 75-98, İstanbul.
- Yılmaz, E., (2006). Erosion Problem and Risk Analysis in Çamlıdere Dam Basin. Ankara University, Social Science, Master Thesis, Ankara.
- Karayol, Ö., (2012). Determining Land Use Changes Using Remote Sensing and Geographic Information Systems: The Case of Konya. Erciyes University, Science, Master Thesis, Kayseri.



## 5<sup>th</sup> Intercontinental Geoinformation Days

igd.mersin.edu.tr



# Aircraft detection using optical remote sensing images and YOLOv7 based deep learning method

Roya Talebi \*<sup>1</sup>

<sup>1</sup>University of Tabriz, Faculty of Planning and Environmental Sciences, Department of Remote Sensing and GIS, Tabriz, Iran

### Keywords

Remote sensing image  
Aircraft detection  
YOLOv7

### Abstract

Target detection is an important application in remote sensing. Aircraft detection in remote sensing images (RSIs) has attracted widespread attention in recent years, which has been widely used in both military and civilian fields. In this study, we used YOLOv7 (You Only Look Once) model for Aircraft detection from satellite images. The results show that YOLOv7 can be well applied in the field of Aircraft detection. The YOLOv7 model with mAP, Precision, Recall, F1 score and average detection time of 95.62%, 93.27%, 93.41%, 93.34% and 0.025 s per image performed well in recognition.

## 1. Introduction

Aircraft detection in remote-sensing images is a fundamental task in civil and military applications. Deep learning techniques to achieve end-to-end object detection have attracted the attention of the Earth observation community (Lin & Chen, 2021).

Different disciplines and applications have benefited from DL methods. In the Remote Sensing (RS) domain, DL methods are also used for the detection of different geospatial objects, land cover/use segmentation, and pan-sharpening (Krizhevsky et al., 2017; Li et al., 2017; Redmon et al., 2016; Yaban et al., 2022).

YOLO is a commonly used single-stage target detection algorithm with the characteristics of fast and high accuracy (Li et al., 2022; Redmon et al., 2016). It exhibits satisfactory performance in detecting small and occluded targets in complex field environments and has better detection speed than other deep learning algorithms (Lu et al., 2019). YOLOv7 is the latest detector in YOLO series. This network is designed with trainable bag-of-freebies, which enable real-time detectors to greatly improve the accuracy without increasing the inference cost. It also involves extend and compound scaling so the target detector can effectively reduce the number of parameters and calculations, thereby greatly improving the detection speed (Wang et al., 2022; Wu et al., 2022). At present, YOLOv7, as a brand-new detector, has not been applied to Aircraft detection. Therefore, in the present work, YOLOv7 was used to detect Aircrafts.

The hardware used during computer development was to run the software. The object detection model was trained using, laptop computer with access to a Google Colab virtual machine, which offers free GPU cloud service that allows one to obtain 0.007 second inference time. That is, 140 FPS on a TESLA P100 GPU.

In this study, we aimed to automatically detect Aircrafts from very high-resolution satellite images using the DOTA dataset and a new test data set generated from satellite images of different airports and air bases obtained from the Google Earth platform.

## 2. Method

### 2.1. Data and Environment

In this study, we have used the following data:

(1) The DOTA dataset was used for training and testing purposes. It is an open-source dataset for object detection purposes from remote sensing images. The dataset includes satellite image patches obtained from the Google Earth© platform, and Jilin 1 (JL-1) and Gaofen 2 (GF-2) satellites. It contains 16 types of objects (plane, ship, storage tank, baseball diamond, tennis court, basketball court, ground track field, harbor, bridge, large vehicle, small vehicle, helicopter, roundabout, soccer ball field, swimming pool, and container crane) (Gong et al., 2022). The image sizes are in the range of 800 × 800 to 4000 × 4000. DOTA dataset was divided into 1600 training and 400 validation images.

\* Corresponding Author

<sup>\*</sup>(roya.talebi99@ms.tabrizu.ac.ir) ORCID ID 0000-0002-1553-1678

Cite this study

Talebi R., (2022). Aircraft detection using optical remote sensing images and YOLOv7 based deep learning method. 5<sup>th</sup> Intercontinental Geoinformation Days (IGD), 105-107, Netra, India

(2) In addition to this dataset, we also collected 100 images from Google Earth and used them as the independent test set.

In this study, we were the images split to the size of  $608 \times 608$  for training YOLOv7 detectors. We implemented our experiments in the Google Colab Pro development platform.

## 2.2. YOLOv7 Network Architecture

YOLOv7, a latest detector with YOLO architecture, is an object detection network that has fast detection speed, high precision and easy to train and deploy characteristics. The speed and accuracy of the network is within the range of 5–160 FPS, surpassing currently known object detectors. The network is 120% faster than YOLOv5 in the same volume (FPS). The test results on the MS COCO dataset outperform the YOLOv5 detector (Ahmad et al., 2022; Wu et al., 2022).

## 2.3. Establishment of Model

The establishment of Aircraft object detection model was divided into training and testing stages. The YOLOv7 neural network was trained using the training set, and the evaluation indicators were verified on the validation set after model weights were obtained. Finally, the model with the best performance weight was selected as the preliminary model for object detection for Aircraft. In the testing phase, the detection model was run on the test set. The workflow is illustrated in Figure 6.

## 2.4. Evaluation Indicators of Model

In this paper, Precision, Recall, Mean Average Precision (mAP) and F1 score were used to accurately and objectively evaluate the performance of the model. Precision is the most common evaluation index, and it is the number of right targets divided by the number of detected targets. In general, the higher the Precision is, the better the detection effect will be. Precision is a very intuitive evaluation index, but sometimes high Precision does not represent all. Therefore, mAP, Recall and F1 score were introduced for comprehensive evaluation. Precision (Eq.1), Recall (Eq.2), Average Precision (Eq. 3) mAP (Eq.4), and F1 score (Eq. 5) were calculated as follows:

$$P = \frac{TP}{TP + FP} \times 100\% \quad (1)$$

$$R = \frac{TP}{TP + FN} \times 100\% \quad (2)$$

$$AP = \int_0^1 P(r) dr \quad (3)$$

$$mAP = \frac{1}{n} \sum_{i=1}^n AP_i \quad (4)$$

$$F1 = 2 \times \frac{P \times R}{P + R} \quad (5)$$

where TP (True Positive) represents the number of Aircraft objects that are correctly detected; FP (False Positive) represents the number of other objects detected as Aircraft; and FN (False Negative) represents the number of Aircraft that are undetected/missed (Wu et al., 2022).

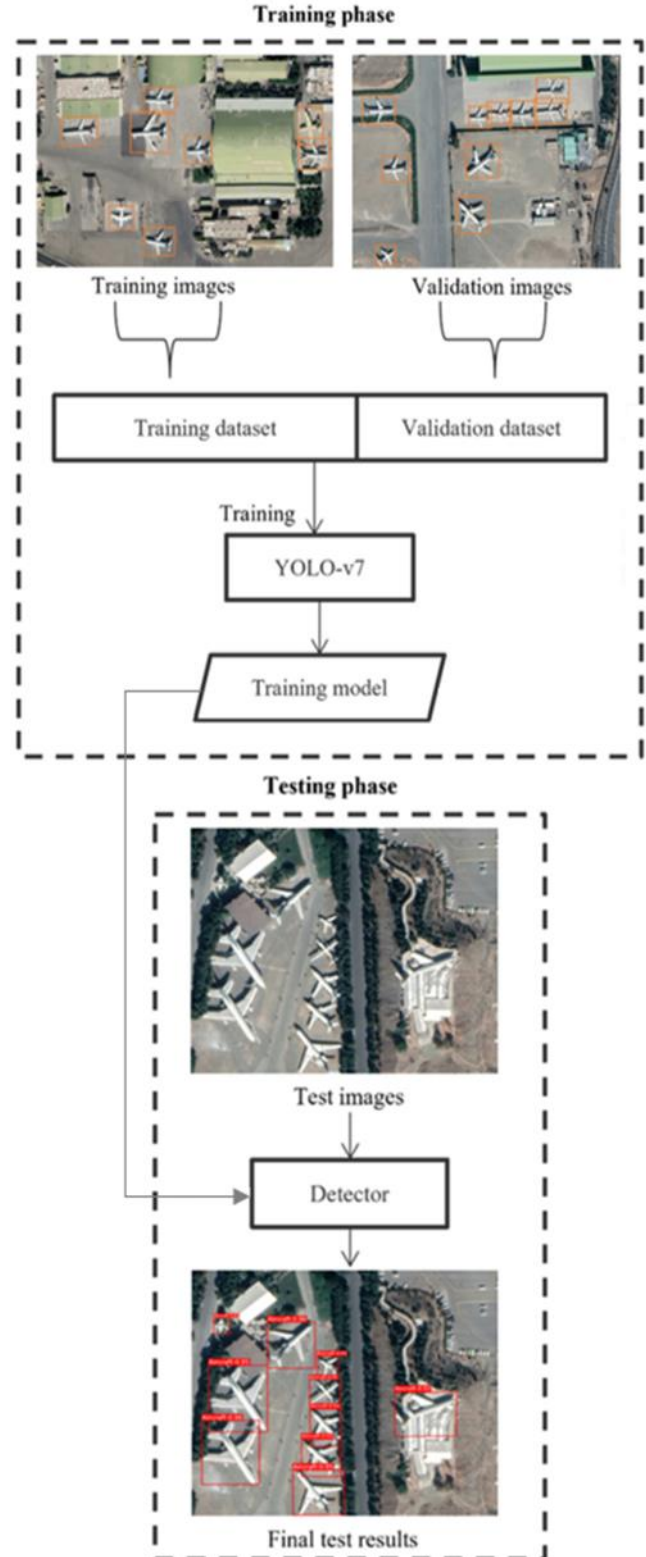


**Figure 1.** Workflow of the proposed study

## 3. Results and Discussion

The YOLOv7 model for object detection of Aircraft was established based on the original dataset and the

YOLOv7 network. This study determined that the model after 258 epochs was the suitable detection model for Aircraft.

The performance indicators of the YOLOv7 model shown in the Table 3. It can be seen that The YOLOv7 model with mAP, Precision, Recall, F1 score and average detection time of 95.62%, 93.27%, 93.41%, 93.34% and 0.025 s per image performed well in recognition.



Figure 1. Detection previews from YOLOv7 Architecture

Table 1. Evaluation indexes results

Target Detection Network	mAP (%)	Precision (%)	Recall (%)	F1 Score (%)	Average Detection Speed (s/Image)
YOLOv7	95.62	93.27	93.41	93.34	0.025

Table 2. Detection result of YOLOv7 model

Model	Detection Results	Numbers
YOLOv7	Number of detected objects	1338
	Number of right objects (TP)	1248
	Number of wrong objects (FP)	90
	Number of missed objects (FN)	88

#### 4. Conclusion

Preferring smaller scale models of YOLOv7 and using more powerful graphics cards can enable model training with higher number of batch sizes, thus may result in higher success rates indirectly. Furthermore, if the inference time is not a strong requirement, many more models can be built to create an ensemble with higher accuracy.

#### References

Ahmad, I., Yang, Y., Yue, Y., Ye, C., Hassan, M., Cheng, X., Wu, Y., & Zhang, Y. (2022). Deep Learning Based Detector YOLOv5 for Identifying Insect Pests. *Applied Sciences*, 12(19), 10167.

Gong, H., Mu, T., Li, Q., Dai, H., Li, C., He, Z., Wang, W., Han, F., Tuniyazi, A., & Li, H. (2022). Swin-Transformer-Enabled YOLOv5 with Attention Mechanism for Small Object Detection on Satellite Images. *Remote Sensing*, 14(12), 2861.

Krizhevsky, A., Sutskever, I., & Hinton, G. E. (2017). Imagenet classification with deep convolutional neural networks. *Communications of the ACM*, 60(6), 84-90.

Li, G., Suo, R., Zhao, G., Gao, C., Fu, L., Shi, F., Dhupia, J., Li, R., & Cui, Y. (2022). Real-time detection of kiwifruit flower and bud simultaneously in orchard using YOLOv4 for robotic pollination. *Computers and Electronics in Agriculture*, 193, 106641.

Li, X., Wang, S., Jiang, B., & Chan, X. (2017). Airplane detection using convolutional neural networks in a coarse-to-fine manner. 2017 IEEE 2nd Information Technology, Networking, Electronic and Automation Control Conference (ITNEC),

Lin, Y.-C., & Chen, W.-D. (2021). Automatic aircraft detection in very-high-resolution satellite imagery using a YOLOv3-based process. *Journal of Applied Remote Sensing*, 15(1), 018502.

Lu, S., Wang, B., Wang, H., Chen, L., Linjian, M., & Zhang, X. (2019). A real-time object detection algorithm for video. *Computers & Electrical Engineering*, 77, 398-408.

Redmon, J., Divvala, S., Girshick, R., & Farhadi, A. (2016). You only look once: Unified, real-time object detection. Proceedings of the IEEE conference on computer vision and pattern recognition,

Wang, C.-Y., Bochkovskiy, A., & Liao, H.-Y. M. (2022). YOLOv7: Trainable bag-of-freebies sets new state-of-the-art for real-time object detectors. *arXiv preprint arXiv:2207.02696*.

Wu, D., Jiang, S., Zhao, E., Liu, Y., Zhu, H., Wang, W., & Wang, R. (2022). Detection of Camellia oleifera Fruit in Complex Scenes by Using YOLOv7 and Data Augmentation. *Applied Sciences*, 12(22), 11318.

Yaban, B., Alganci, U., & Sertel, E. (2022). Aircraft detection in very high-resolution satellite images using YOLO-based deep learning methods. *Intercontinental Geoinformation Days*, 4, 270-273.



## 5<sup>th</sup> Intercontinental Geoinformation Days

igd.mersin.edu.tr



### Calculation of daily land surface temperature values using Google Earth Engine

Mehmet Numan Fırat<sup>\*1</sup>, Yunus Kaya<sup>1</sup>, Nizar Polat<sup>1</sup>

<sup>1</sup>Harran University, Faculty of Engineering, Department of Geomatics Engineering, Sanliurfa, Türkiye

#### Keywords

Remote sensing  
Land surface temperature  
Google Earth Engine,  
Temperature

#### Abstract

In parallel with urbanization, the temperature in dense residential areas is observed to be higher than in rural areas around the city. Urban areas being warmer than the surrounding natural areas is defined as an urban heat island. With the use of thermal bands in remote sensing platforms, the determination of Land Surface Temperatures (LST) and the spatial distribution of related parameters have begun to be represented better than the old methods. This data, obtained from the images detected by satellites, has enabled them to be used as a data source in a wide variety of applications due to its accessibility and coverage of large areas. In this study, LST maps and temperature tables within the provincial borders of Şanlıurfa were created by using the thermal band of a total of 9 Landsat 8 satellite images belonging to September of each year between 2013 and 2021. Finally, Normalized Difference Vegetation Index (NDVI) images were created from the satellite images and the correlation between them was examined.

#### 1. Introduction

In parallel with urbanization, the temperature in dense residential areas is observed to be higher than in rural areas around the city. The materials that make up the buildings, asphalt and concrete roads, roofing materials and pavements absorb more energy from the sun than other natural surfaces.

The phenomenon of urban settlements having higher temperatures than the surrounding natural areas; it is defined as an urban heat island (Oke 1982; Gerçek and Bayraktar 2014). The vertical development of cities creates urban canyons by increasing the amount of energy reaching the earth and increases the urban heat island effect. Due to these urban canyons, cities show different climatic characteristics according to their surroundings (Yılmaz 2015).

Land Surface Temperature (LST) can be defined as the temperature emitted by the earth's surface. The main source of this heat is the sun. The heat energy reaching the earth from the sun heats the objects. The materials used in urbanization and construction absorb the energy reaching the earth by not reflecting it back, thus causing an increase in LST. LST is shown as an important factor that has an impact on various kinds of events on earth. LST data is a frequently preferred data type in plant

change analysis, land use and land cover change analysis, global warming studies and meteorological studies (Parker and Warner 1973; Zhang et al. 2006; Li et al. 2013; Ndossi and Avdan 2016; Yıldız et al. 2017).

With the use of thermal images in remote sensing platforms, the determination of surface temperatures and spatial distributions of related parameters have begun to be better represented. The data obtained from the images detected by satellites has enabled them to be used as a data source in various applications due to its low cost and coverage of large areas. The Landsat 8 remote sensing platform was launched into space in 2013 by the National Aeronautics and Space Administration (NASA). It provides data to users with its nine spectral and two thermal bands.

It is of great importance that the data be used quickly and effectively in the studies carried out. Considering the importance of remote sensing and geographic information systems, the use of developing technologies is increasing. In parallel with this, geographic information system software is also developing. Advances in remote sensing and geographic information systems have enabled detailed investigations using high-resolution data. These developments also enabled the data to be obtained numerically and to reach the user quickly and to use the data effectively.

#### \* Corresponding Author

(mehmetnumanfirat@gmail.com) ORCID ID 0000-0002-7259-7008  
(yunuskaya@harran.edu.tr) ORCID ID 0000-0003-2319-4998  
(nizarpolat@harran.edu.tr) ORCID ID 0000-0002-6061-7796

#### Cite this study

Firat M N, Kaya Y & Polat N (2022). Calculation of daily land surface temperature values using Google Earth Engine. 5<sup>th</sup> Intercontinental Geoinformation Days (IGD), 108-111, Netra, India

The use of data obtained from satellites and geographic information systems provide fast, comparable, and updatable information about the changes that have occurred on the earth from past to present. In line with these developments, Google Earth Engine, which offers the opportunity to conduct research by combining large satellite images and data obtained from satellites, has provided a great advantage to users in recent years.

## 2. Method

The most widely used remote sensing platform for determining the LST is the Landsat 8 satellite, operated by NASA. The Landsat 8 platform has an altitude of 705 km, a temporal resolution of 16 days, and a sun-synchronous orbit that can orbit the earth in 98.9 minutes. The Landsat 8 platform contains two different sensor systems. The first of these is the Operational Location Imager (OLI). In addition to the bands included in previous Landsat sensors, the OLI system has 3 new bands for deep blue (Band 1) for coastal/aerosol applications, short wave infrared (Band 9) for analysis and detection of cirrus clouds, and band quality assessment. The second sensing system is the Thermal Infrared Sensor (TIRS). The TIRS system includes 100 m spatial (30 m resampling), 16-bit radiometric resolution, two bands of 10.6 – 12.51  $\mu\text{m}$  electromagnetic spectrum thermal wavelength. The Landsat 8 (OLI&TIRS) sensor has a narrower spectral bandwidth and stronger signal-to-noise characteristics than Landsat 7 ETM+ and Landsat 5 TM sensors (USGS 2019).

In order to determine the surface temperatures in large areas on the earth, the temperature values in the study area cannot be fully represented by point-based local measurements. Thanks to remote sensing satellites, it has become possible to determine high-resolution temperature data on the earth's surface and has found the opportunity to be used in study areas such as ice thickness, phytosanitary, forest fires and determination of geothermal areas. The workflow of the study are given in Figure 1.

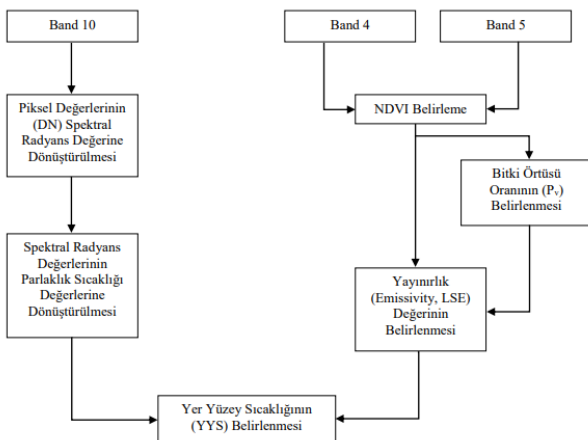


Figure 1. Workflow of the study

### 2.1. Study area

Şanlıurfa has an area of approximately 19,242 km<sup>2</sup> and is located between latitude 36,314 - 38,343 N and

longitude 37,595 - 40,458 E. It has an average altitude of 518 m above sea level. The city has an extremely hot and dry climate in summers and cool and humid winters. It is the 8th most populous city in Turkey with a population of over 2 million.

### 2.2. Google Earth Engine (GEE) system

Depending on the developing technology, UA-GIS software is also developing. With this developing technology, software can be used over the internet, access to big data is provided and this data can be processed on the internet again.

While obtaining tabular data with UA-GIS integration, presenting spatial data to the user provides convenience in data analysis. UA-GIS systems are important in terms of more conscious use of the ecosystem we are in, increasing sensitivity, conscious use of energy resources and providing opportunities for use in many areas. Google Earth Engine is a platform developed by Google for the analysis of geoscience and data. Google Earth Engine provides visualization on maps by combining large satellite images and data with analysis.

Google Earth Engine is a platform that creates resources for many analyzes with algorithms developed on satellite images. The factors used in the study were quickly obtained by time series analysis of the developed algorithms.

### 2.3. Conversion of Pixel Values (DN) to Spectral Radiance Values

Spectral radiance value transformation is applied to the thermal image band values (DN: Digital Number) that will be used to determine the LST, with the help of the parameters in the metadata file of the satellite image. Spectral radiance value is defined as the amount of energy reflected or transmitted from a certain angle and region at a certain wavelength. Equation (1) is used for this transformation;

$$L\lambda = ML * Q_{cal} + AL \quad (1)$$

where

$L\lambda$  = Calculated Radiance value ( $W/(m^2 * sr * \mu m)$ )

$ML$  = Radians multiplicative scaling factor (from Satellite metadata)

$Q_{cal}$  = Pixel value (DN) of the satellite image

$AL$  = Radians represents the additional scaling factor (from Satellite metadata).

### 2.4. Conversion of spectral radiance values to luminosity temperature values

Luminosity Temperature is the luminosity value of microwave emission traveling upwards from the highest point of the earth's atmosphere (T: Luminous Temperature). The second step is to convert the spectral radiance values obtained from the pixel values (DN) with Equation (1) to the luminance temperature (T). This transformation is calculated by equation (2).

$$T = \frac{K_2}{\ln\left(\frac{K_1}{L_\lambda} + 1\right)} - 273.15 \quad (2)$$

where

T = Luminosity temperature (C0)  
 Lλ = Calculated Radiance value (W/(m2 \* sr \* μm))  
 K1 and K2 = Defines the conversion constants for the Thermal Band found in the satellite metadata.

### 2.5 Determination of Normalized Difference Vegetation Index (NDVI)

The Normalized Difference Vegetation Index (NDVI) must be calculated in order to determine the ground surface emissivity and Vegetation Ratio. In determining the LST, NDVI values should be obtained from reflectance values, not DN values. The NDVI value is calculated by equation (3) using the reflectance values of the near infrared and red bands.

$$NDVI = \frac{NIR-Red}{NIR+Red} \quad (3)$$

On the Landsat 8 platform, the 5th band represents the near infrared and the 4th band represents the red band. The condition of the vegetation can be determined by taking the ratio of these two bands shown in Equation (3).

### 2.6 Determination of Vegetation Rate (Pv)

After the NDVI values of the study area are determined, the Vegetation Rate (Pv) is determined by using the plant and soil values of the NDVI. This ratio is determined using the maximum (NDVImax) and minimum (NDVImin) values over NDVI. Vegetation Rate (Pv); It is calculated by equation (4) (Sobrino et al. 2004). This ratio is used to calculate the earth emissivity (radiance) value (ε).

$$P_v = \left(\frac{NDVI-NDVI_{min}}{NDVI_{max}-NDVI_{min}}\right)^2 \quad (4)$$

### 2.7 Determination of Emissions Values

The emissivity (ε) value is an important parameter used in the calculation of ground surface temperatures. Many methods have been developed to determine the emissivity value. However, in this study, the method based on NDVI values was used. In this method, the NDVI values were thresholded as soil and plant values, and the emissivity values of the study area were calculated. As threshold values, the values used globally in the literature are 0.2 for soil and 0.5 for plants (Sobrino and Raissouni 2000). It is calculated by the equation ελ (5).

$$\epsilon_\lambda = \begin{cases} \epsilon_{s\lambda}, & NDVI < NDVI_s \\ \epsilon_{v\lambda} P_v + \epsilon_{s\lambda}(1 - P_v) + C, & NDVI_s \leq NDVI \leq NDVI_v \\ \epsilon_{s\lambda} + C, & NDVI > NDVI_v \end{cases} \quad (5)$$

### 2.8 Determination of Land Surface Temperature (LST) Values

After the emissivity value is determined by calculating, the last step is to determine the ground surface temperature value. For this, ground surface emissivity correction should be made to the sensor temperature value calculated in the previous steps. Equation (6) is used for this correction.

$$LST = \frac{T}{\left(1 + \left(\frac{w \cdot T}{\rho}\right) \cdot \ln(\epsilon)\right)} \quad (6)$$

Here, T represents the temperature values calculated in the previous stages, w represents the average wavelength value of the thermal band used (10.9 μm), and ε represents the emissivity value. The value of ρ is a constant value and is calculated by equation (7).

$$\rho = h * c/s = 1.438 \times 10^{-2} \text{ mK} \quad (7)$$

h: Planck's constant (6.626 \* 10<sup>-34</sup> Js),  
 s: Boltzmann constant (1.38 \* 10<sup>-23</sup> J/K),  
 c: speed of light (2.998 \* 10<sup>8</sup> m/s)

## 3. Results

The maximum, minimum and average temperature values of Şanlıurfa province calculated between 2013-2021 are given in Table 1. In addition, the changes in daily average temperature values are given in Figure 2. When Table 1 is examined, a difference of 0.8 °C is seen between the years 2017-2018. The increase in global warming and urbanization affects the sudden changes in annual average daily temperatures.

**Table 1.** Maximum, minimum and average temperatures in 2013-2021

Year	Max	Min	Average
2013	39.5	30.5	35
2014	36.5	32.3	34.4
2015	36.3	32.1	34.2
2016	36.5	34.5	35.5
2017	37.4	34	35.7
2018	36.6	36.4	36.5
2019	38.1	34.5	36.3
2020	36.95	36.35	36.65
2021	36.25	34.05	35.15

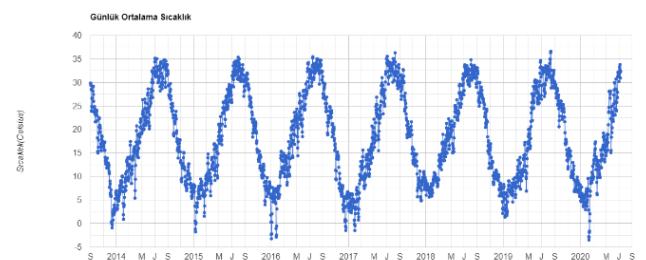


**Figure 2.** Average daily temperatures

#### 4. Conclusion

In the study, the change in the LST of Şanlıurfa province in September between 2013 and 2021 was examined by using Geographical Information Systems and Remote Sensing techniques.

Within the scope of the study, the LST from Şanlıurfa global warming was examined and the criteria that could affect these temperatures were analyzed and evaluated by means of Google Earth Engine datasets and code editor. Within the scope of the study, NDVI, land surface temperature data between 2013-2021 were calculated and graphics were revealed. The effect of NDVI, temperature independent variables on the dependent variable LST was investigated. When the regression results are examined, it is observed that the effects of global warming, temperature and population data on forest losses are high.

In the study, revealing the temporal change of LST is of great importance in terms of future planning. Along with monitoring the temporal changes of LST, the causative factors should also be investigated. It is also very important in terms of making predictions for future plans with the determinations to be made.

The rapid and effective use of the data that will form the basis for the planning to be made is possible with geographic information systems. Especially in recent years, the increasing ground surface temperature emphasizes its importance. It is of great importance to follow the increase in urban areas in the protection of the natural environment. Considering all these criteria affecting the LST in the study, it is of great importance to control these negativities for a livable nature. In the study, an increase is observed in the ground surface temperature for Şanlıurfa Province between the years 2013-2021 as the vegetation density decreases, as the evaporation caused is less. For this reason, because the amount of energy lost is low on surfaces with less vegetation and sparse vegetation, it causes warming. It was determined by the index values that the ground surface temperature was inversely proportional to the plant density and directly proportional to the urban building density. Future plans should be made with precision, taking into account the findings revealed in the light of all the data used.

#### References

Altınlı, İ. E. (1966) Geology of eastern and southeastern Anatolia. Bulletin of Minerals Research and Exploration Institute of Turkey. 66, 35-76.

- Avdan, U., & Jovanovska, G. (2016). Algorithm for automated mapping of land surface temperature using LANDSAT 8 satellite data. *Journal of sensors*, 2016.
- Dağlıyar, A., Avdan, U., & Uça Avcı, Z. D. (2015). Uzaktan Algılama Verileri Yardımıyla Kahramanmaraş İli Ve Çevresinin Yer Yüzey Sıcaklığının Belirlenmesi. TUFUAB VIII. Teknik Sempozyumu.
- DeVries, B., Huang, C., Armston, J., Huang, W., Jones, J. W., & Lang, M. W. (2020). Rapid and robust monitoring of flood events using Sentinel-1 and Landsat data on the Google Earth Engine. *Remote Sensing of Environment*, 240, 111664.
- Kumar, D., & Shekhar, S. (2015). Statistical analysis of land surface temperature-vegetation indexes relationship through thermal remote sensing. *Ecotoxicology and environmental safety*, 121, 39-44.
- Li, Z. L., Tang, B. H., Wu, H., Ren, H., Yan, G., Wan, Z., ... & Sobrino, J. A. (2013). Satellite-derived land surface temperature: Current status and perspectives. *Remote sensing of environment*, 131, 14-37.
- Ma, W., Chen, Y. H., Zhou, J., & Gong, A. (2008). Quantitative analysis of land surface temperature-vegetation indexes relationship based on remote sensing. In *Proc. 21st ISPRS Congress, Youth Forum* (pp. 261-264).
- Macarof, P., & Birlica, C. I. (2018). Investigating Land Surface Temperature and Vegetation Indices Changes Using Landsat Data: A Case Study of Iaşi County. *GEOREVIEW: Scientific Annals of Stefan cel Mare University of Suceava. Geography Series*, 28(1), 44-52.
- Malik, M. S., Shukla, J. P., & Mishra, S. (2019). Relationship of LST, NDBI and NDVI using landsat-8 data in Kandahimmat watershed, Hoshangabad, India.
- Mercan, Ç. (2020). Yer yüzey sıcaklığının termal uzaktan algılama görüntüleri ile araştırılması: Muş ili örneği. *Türkiye Uzaktan Algılama Dergisi*, 2(2), 42-49.
- MODIS Land-Surface Temperature Algorithm Theoretical Basis Document. (2020). <https://lpdaac.usgs.gov/products/mod11a2v006/>.
- Ndossi, M. I. (2016). ASTER ve Landsat görüntülerinden açık kaynak kod teknolojisi kullanılarak yüzey sıcaklık haritalarının üretilmesi (Master's thesis, Anadolu Üniversitesi).
- Reddy, S. N., & Manikiam, B. (2017). Land surface temperature retrieval from LANDSAT data using emissivity estimation. *International Journal of Applied Engineering Research*, 12(20), 9679-9687.



## 5<sup>th</sup> Intercontinental Geoinformation Days

igd.mersin.edu.tr



### Calculation of glacial area change at Cilo mountain with Google Earth Engine

Gonca Abdioğlu<sup>\*1</sup>, Yunus Kaya<sup>1</sup>, Nizar Polat<sup>1</sup>

<sup>1</sup>Harran University, Faculty of Engineering, Department of Geomatics Engineering, Sanliurfa, Türkiye

#### Keywords

Remote Sensing,  
Google Earth Engine  
Glaciation

#### Abstract

Global climate change has become an important natural phenomenon that threatens the world today, with the negative factors that occur in the ecosystem such as constantly developing cities, population growth and climatic conditions. Since active glacial areas are very sensitive to climate changes, it is one of the important areas that should be examined to reveal the extent of global warming. They grouped Turkey's current glaciers and regions of glaciation under three main groups: Taurus Mountains, Eastern Black Sea Mountains, Volcanoes and other independent mountains of Anatolia. Cilo Mountain, located in the Taurus Mountains group, constitutes one of the important glaciation areas with active glaciers and many glacial forms. In this study, the active glacier on Cilo Mountain is examined using Remote Sensing and Geographic Information Systems techniques. In the study, the numerical data used in the Normalized Difference Snow Index (NDSI) study were obtained with the Google Earth Engine tool and the analyzes created as a result of the algorithms made using satellite data.

#### 1. Introduction

Since glaciers cover a large part of the earth's surface, their effects on living life are also quite high. The polar and high mountain glaciers play a crucial role in maintaining and stabilizing the world's climate system, sea level and temperature, ocean currents, freshwater resources and all habitats. Considering the climatic and environmental factors, losses in glacial areas cause serious problems in economic and social life as well as negatively affecting ecosystems.

The catastrophic global warming, which we can say the biggest we face today, and the gradual increase in greenhouse gases in the troposphere layer of the atmosphere cause a chain of events that threaten the life of all living things (Galip et al., 2013). Global warming causes many disasters such as melting of glaciers, rising sea levels, drought, floods, landslides and erosion. One of the disasters that will cause great chaos in the world is the rapid melting of snow and glaciers in the poles and high mountains (Galip et al., 2013). It is of great importance that the data be used quickly and effectively in the studies carried out. Considering the importance of remote sensing and geographic information systems, the use of developing technologies is increasing. In parallel with this, geographic information system software is also

developing. Advances in remote sensing and geographic information systems have enabled detailed investigations using high-resolution data. These developments also enabled the data to be obtained numerically and to reach the user quickly and to use the data effectively. The use of data obtained from satellites and geographic information systems provide fast, comparable and updatable information about the changes that have occurred on the earth from past to present. In parallel with these developments, Google Earth Engine (N. Gorelick, 2017), which offers the opportunity to conduct research by combining large satellite images and data obtained from satellites, has provided a great advantage to users in recent years. Access to large data sets is made easy with Google Earth Engine. It contains a large number of data sets such as environment, climate, glacier, geology, population, disease, disaster. With this large data set, it provides the advantage of fast and effective change analysis and ease of use.

Cilo Mountain (37.5°N, 44°E, 4135m), which is the second highest mountain in Turkey after Ağrı Mountain in the study area, is located at the corner of the southeastern border of Turkey, on the highest peak of the Taurus-Zagros Mountains (Sarıkaya, 2009). The region draws attention with its height and snow masses that do

\* Corresponding Author

(goncatr61@gmail.com) ORCID ID 0000-0002-2021-9582  
(yunuskaya@harran.edu.tr) ORCID ID 0000-0003-2319-4998  
(nizarpolat@harran.edu.tr) ORCID ID 0000-0002-6061-7796

Cite this study

Abdioğlu, G., Kaya, Y., & Polat, N. (2022). Calculation of glacial area change at Cilo mountain with Google Earth Engine. 5<sup>th</sup> Intercontinental Geoinformation Days (IGD), 112-115, Netra, India

not melt in summer. With more than 20 large and small glaciers, Cilo Mountain (Erinç, 1953; Günal, 2013) is Turkey's most important glacier area, with hot and dry summers and harsh continental climate characteristics. Global warming in recent years and glacial losses in the region are among the reasons for choosing the region as a study area. In this context, the glacial area changes of the region between 2013-2022 were investigated by monitoring with Google Earth Engine.

## 2. Method

In the study, with the help of satellite products in the Google Earth Engine Library, data for the years 2013-2022 were obtained and the effects of the results on glacial losses were investigated. Google Earth Engine is a platform that contains more than forty years of data archives and scientific datasets updated daily. A large number of analyzes can be made with the help of algorithms developed using satellite data with the data catalog open to everyone. Thanks to open source data, analyzes can be made easily, various filters can be made on the image to be studied through the code editor, and work can be done on the desired date and in the area. The data used for the study were obtained through images obtained from different satellites.

In the study, data between 2013-2022 were obtained by making analyzes related to NDSI. The aim of the study is to investigate the effect of these data on glacial losses.

The majority of the analyzes in the study were obtained through the Google Earth Engine code editor. In the Google Earth Engine data library, there are studies and algorithms related to many areas such as glacier, climate, environment and atmosphere. Various algorithms created using satellite images form a basis for work in many areas. Algorithms developed on a global scale in each area can be developed and used by filtering according to the scale of work, the desired date, and the desired unit. In the study, each analysis was carried out between the dates determined by cutting according to the study area called roi with the algorithms selected according to the subject. In addition, while graphical data were obtained by using different code sequences, maps were also obtained.

### 2.1. Study area

The study area consists of 3 glaciation areas (Cilo Mountains, İkiyaka Mountains, Kavuşşahap Mountains) located in the Southeast Taurus range, and the area covering the border of the Cilo (Glacial) Mountains, which is the most important (Figure 1). The Cilo (Glacial) Mountains are the second highest peak of Turkey with an altitude of 4135 meters. In the Cilo Mountains Geographical Coordinate System, located in the north of the Turkey-Iraq border; It is located between 37°29'54.9996"N and 43°57'34.9956"E.

In the Universal Transverse Mercator (UTM) Coordinate System, it is located in the 38S Grid and is between the values of East 382363 - 437033 (meters) and North 4128843 - 4174418 (meters). (Reşat GEÇEN, 2017). It is located in the Eastern Anatolia Region of Turkey, Hakkari Section, within the borders of Hakkari province. Although the Cilo Mountains have many high

peaks, the most important peaks are Reşko (Uludoruk) 4135m and Erinç (Suppa Durek) 4060m. Active glaciers in the study area; Gelyaşın (İzbrak) Glacier, Mia Hvara Glacier, Suppa Durek (Erinç), Poyraz Hill glaciers. These are also the most important areas of glaciation.

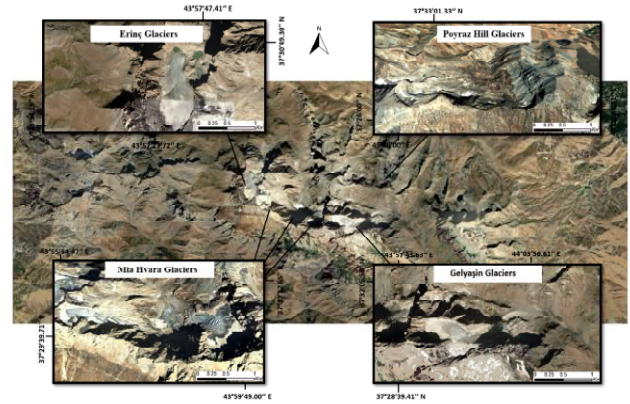


Figure 1. Study area

### 2.2. Google Earth Engine (GEE) system

Google Earth Engine (GEE) is a cloud computing platform designed to store and process large data sets (at petabyte scale) for analysis and final decision making. After the Landsat series became available for free in 2008, Google archived all datasets and linked them to its cloud computing engine for open source use. The current data archive includes Geographic Information Systems (GIS)-based vector datasets, social, demographic, weather, digital elevation models, and climate data layers, among other satellites.

The easily accessible and user-friendly front-end provides a suitable environment for interactive data and algorithm development. GEE provides a lot of data on a global scale over the last 40 years. The platform not only provides data but also includes very powerful tools that enable analysis.

Landsat 8 data was used in this study. Landsat8 data used in the study are presented in 3 different preprocessing levels; Surface Reflectance, Top of Atmosphere and raw images. In this study, atmospheric corrected surface reflectance data were used. In the study, the NDSI index was calculated.

### 2.3. Obtaining NDSI data

For the detection of glacial areas, NDSI data obtained by Landsat8 Satellite Collection 2 Tier 1 TOA Reflectance calibrated above-atmospheric reflection was used. NDSI is an index in which image transformation operations are performed using Band arithmetic operations. This method is obtained by dividing the green bands (GREEN) and short wave infrared (SWIR) bands of satellite images by the sum of their differences. Analysis was done with Google Earth Engine Code Editor. It is calculated with NDSI (1) equation.

$$NDSI = \frac{(Green - SWIR)}{(Green + SWIR)} \quad (1)$$

The values resulting from the formula are between -1 and +1, and areas with high index values are determined as areas with snow cover.

#### 2.4. Analysis of NDSI Values

The graph of NDSI values between 2013 and 2022 is given in Figure 2. When Figure 2 is examined, it is seen that the NDSI values are in a decreasing trend.

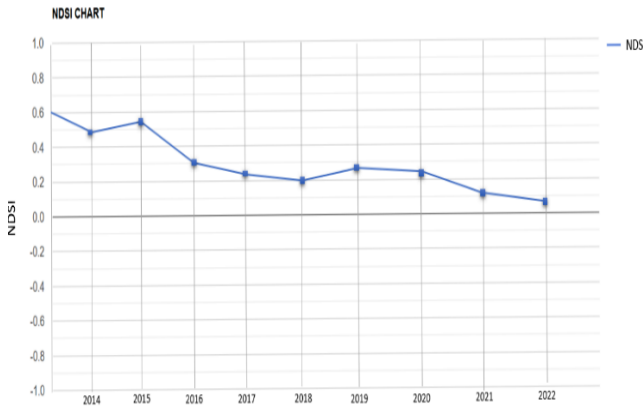


**Figure 2.** Hakkari Cilo Mountain NDSI Values Analysis Chart

#### 3. Results

In the study, the changes of the active glaciers in the Cilo Mountains between 2013 and 2022 were examined using the Geographical Information Systems and Remote Sensing techniques. With the NDSI used in this study, it is seen that snow surfaces are decreasing due to climate change and global warming (Figure 3,4). The calculated glacier area for 2013 is 1.82 km<sup>2</sup>. The calculated glacier area for 2022 is 1.22 km<sup>2</sup>.

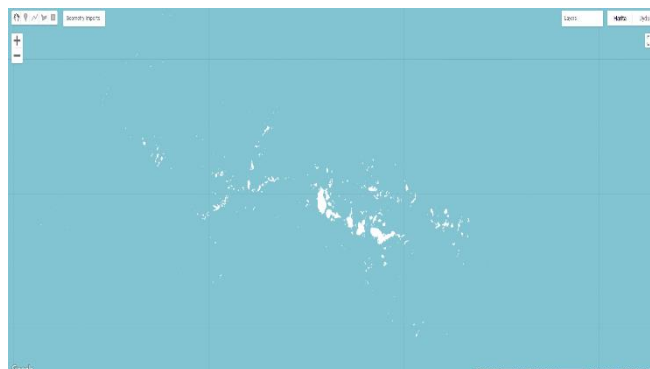


**Figure 3.** Hakkari-Cilo Mountain NDSI image (2013)



**Figure 4.** Hakkari-Cilo Mountain NDSI image (2022)

#### 4. Conclusion

Within the scope of the study, glacial losses due to global warming in Hakkari between the years 2013-2022 were examined and the criteria that could affect these losses were analyzed and evaluated through Google Earth Engine datasets and code editor. Within the scope of the study, NDSI data for the years 2013-2022 were calculated and graphics and visuals were revealed.

In this study, revealing the temporal changes in glacial areas is of great importance in terms of future planning. Along with monitoring the temporal changes of glacial areas, the causative factors should also be investigated. Changes and developments in geographic information systems and remote sensing methods are also important in the rapid and effective use of data in such studies. The rapid and effective use of the data that will form the basis for the planning to be made is possible with geographic information systems. Especially in recent years, increasing glacial losses underline the importance of the problem. It is of great importance to follow the increase in urban areas in the protection of the natural environment. Considering all these criteria affecting glacial losses in the study, it is of great importance to control these negativities for a livable nature. In the study, the lost glacier area for the Hakkari Cilo region between 2013-2022 is 0.6 km<sup>2</sup>. which means a meltdown of about 33%.

#### References

- Altınlı, İ. E. (1966). Geology of Eastern and Southeastern Anatolia (Part II). Bulletin of the Mineral Research and Exploration, 67(67).
- Bahadır, M., & Dikbaş, E. D. (2011). Türkiye'deki aktüel buzul alanlarının CBS ve UA ile değişim analizi (1990-2000). TMMOB Coğrafi Bilgi Sistemleri Kongresi, Antalya.
- Bobek, H. (1940). Die gegenwärtige und eiszeitliche Vergletscherung im zentralkurdischen Hochgebirge (Osttaurus, Ostanatolien). Bornträger.
- Çiner, A. (2003). Türkiye'nin güncel buzulları ve geç kuvaterner buzul çökelleri. Türkiye Jeoloji Bülteni, 46(1), 55-78.
- Mercan, Ç. (2020). Yer yüzey sıcaklığının termal uzaktan algılama görüntüleri ile araştırılması: Muş ili örneği. Türkiye Uzaktan Algılama Dergisi, 2(2), 42-49.
- Dağlıyar, A., Avdan, U., & Uça Avcı, Z. D. (2015). Uzaktan Algılama Verileri Yardımıyla Kahramanmaraş İli Ve Çevresinin Yer Yüzey Sıcaklığının Belirlenmesi. TUFUAB VIII. Teknik Sempozyumu.
- DeVries, B., Huang, C., Armston, J., Huang, W., Jones, J. W., & Lang, M. W. (2020). Rapid and robust monitoring of flood events using Sentinel-1 and Landsat data on the Google Earth Engine. Remote Sensing of Environment, 240, 111664.
- Eriñç, S. (1953). Van'dan Cilo Dağlarına. İstanbul Üniversitesi Coğrafya Enstitüsü Dergisi, 2, 84-106.
- Gorelick, N., Hancher, M., Dixon, M., Ilyushchenko, S., Thau, D., & Moore, R. (2017). Google Earth Engine: Planetary-scale geospatial analysis for everyone. Remote sensing of Environment, 202, 18-27.

- Günel, N. (2013). Türkiye’de kar yağışı, karın yerde kalma süresi ve daimi kar sınırı. *Acta Turcica*, Yıl, 5, 1-13.
- İzbrak, R. (1951). Cilo Dağı ile Van Gölü Çevresinde Coğrafya Araştırmaları. Ankara Üniversitesi, Dil ve Tarih-Coğrafya Fakültesi Yayınları, (67).
- Karabulut, M. (2005). Coğrafi bilgi sistemleri ve otomatikleşmiş coğrafya. EGE coğrafi bilgi sistemleri sempozyumu bildiri kitabı, 193-200.
- Özkök, M. K., Ezgi, T. O. K., Gündoğdu, H. M., & Demir, G. (2017). Arazi yüzey sıcaklığı farklılaşmalarının kentsel gelişim ve planlama süreçleri açısından uzaktan algılama verileri ile değerlendirilmesi: Çorlu/Çerkezköy/Ergene/Kapaklı alt bölgesi örneği. *Toprak Bilimi ve Bitki Besleme Dergisi*, 5(2), 69-79.
- Sarikaya, M. A. (2009). Late Quaternary glaciation and paleoclimate of Turkey inferred from cosmogenic chlorine-36 dating of moraines and glacier modeling. The University of Arizona.
- Yakar, M., Yılmaz, H. M., & Mutluoglu, O. (2014). Performance of Photogrammetric and Terrestrial Laser Scanning Methods in Volume Computing of Excavation and Filling Areas. *Arabian Journal for Science and Engineering*, 39(1), 387-394.
- Yeşilyurt, S., & Doğan, U. (2013). Cilo ve Sat dağlarında 1955'ten 2007'ye kadar iklim değişimi ve buzul gerilemesi. 66 Jeoloji Kurultayı, Ankara



## 5<sup>th</sup> Intercontinental Geoinformation Days

igd.mersin.edu.tr



### Automated vehicle detection and instance segmentation from high-resolution UAV imagery using YOLOv7 model

Esra Yildirim\*<sup>1</sup>, Umut Gunes Sefercik<sup>1</sup>, Taskin Kavzoglu<sup>1</sup>

<sup>1</sup>Gebze Technical University, Faculty of Engineering, Department of Geomatics Engineering, Kocaeli, Türkiye

#### Keywords

Deep learning  
UAV imagery  
Vehicle detection  
Instance segmentation  
YOLOv7

#### Abstract

Automatic vehicle detection from unmanned aerial vehicles (UAVs) is an important task in the remote sensing domain and plays a pivotal role in many applications such as traffic monitoring, parking lot management, search and rescue tasks. Inspired by the success of the deep learning paradigm in image processing applications, many object detection, and tracking approaches have been developed and successfully employed in UAV-based object detection studies. In this study, automatic vehicle detection and instance segmentation was conducted using YOLOv7, which is the latest version of the You Only Look Once (YOLO) model from high-resolution UAV data obtained from Gebze Technical University campus in Turkey. For this purpose, vehicle images were collected from the UAV data of the study area, and the vehicles in the images were manually annotated with the LabelMe annotation tool. With the created dataset, the YOLOv7 algorithm was trained and tested with a transfer learning approach on Google Colab's virtual machine. Experimental results revealed that the YOLOv7 model achieved the Precision, Recall, and mAP@0.50 values for the bounding boxes and masks of vehicles as 99.79%, 97.54%, and 99.46%, respectively.

#### 1. Introduction

Nowadays, there is a huge increase in the utilization of unmanned aerial vehicles (UAVs) for a wide range of applications, including disaster management, smart agriculture, transportation, and surveillance. Compared with conventional satellite systems, UAVs afford several capabilities such as high spatial resolution, a large field of view, low cost, flexible and effective data acquisition [Ammar et al. 2021]. Considering these unique capabilities, UAVs have become an indispensable technology in various image processing applications including automatic object detection, tracking, and image classification. In this context, the detection of numerous objects such as trees [Yildirim et al. 2022], vehicles [Tang et al. 2017a], buildings [Boonpook et al. 2018], and pedestrians [Shao et al. 2021] from UAV data has recently attracted increasing attention from researchers. Specifically, the recognition of vehicles from UAV data is a significant research topic as it has many useful applications including traffic management, surveillance, search and rescue tasks.

Traditional vehicle detection algorithms in aerial imagery mostly adopt sliding window search and hand-

crafted features (e.g., histogram of oriented gradients, local binary patterns). However, the sliding window search produces a large number of candidate windows, leading to high computational complexity. Moreover, manually extracted features have restricted representation power for the target object. Due to these drawbacks, it is arduous for traditional vehicle detection methods to achieve real-time performance and high detection accuracy [Tang et al. 2017b].

With the advent of the deep learning paradigm, many convolutional neural network-based object recognition architectures have been recently developed, and they have been increasingly employed in object detection applications from aerial images [Yildirim and Kavzoglu 2022]. Among these, YOLO models based on the "You Only Look Once" approach are the most well-known object detectors as they can achieve real-time performance and high detection accuracy [Redmon et al. 2016]. Furthermore, the YOLOv7, the latest version of YOLO, performs instance segmentation tasks as well as object detection [Wang et al. 2022].

The main objective of this study is to automatically detect vehicles from high-resolution UAV data and to

#### \* Corresponding Author

(esrayildirim@gtu.edu.tr) ORCID ID 0000-0002-4951-0488  
(sefercik@gtu.edu.tr) ORCID ID 0000-0003-2403-5956  
(kavzoglu@gtu.edu.tr) ORCID ID 0000-0002-9779-3443

#### Cite this study

Yildirim, E., Sefercik, U. G., & Kavzoglu, T. (2022). Automated vehicle detection and instance segmentation from high-resolution UAV imagery using YOLOv7 model. 5<sup>th</sup> Intercontinental Geoinformation Days (IGD), 116-119, Netra, India

obtain pixel-wise masks for each detected vehicle. To achieve this goal, the YOLOv7 model was employed in the vehicle dataset generated from the UAV data obtained from the Gebze Technical University (GTU) campus in Turkey. The performance of the model was investigated using Precision, Recall, and mAP evaluation metrics.

## 2. Method

### 2.1. Study area and UAV data acquisition

GTU Campus is located in Kocaeli province in the Northwest side of Turkey (Figure 1). The area is nearly 2.5 km<sup>2</sup> and covered by different land cover classes such as buildings, roads, and varied vegetation. The topography is mostly flat and orthometric elevation is between 2 m and 50 m.

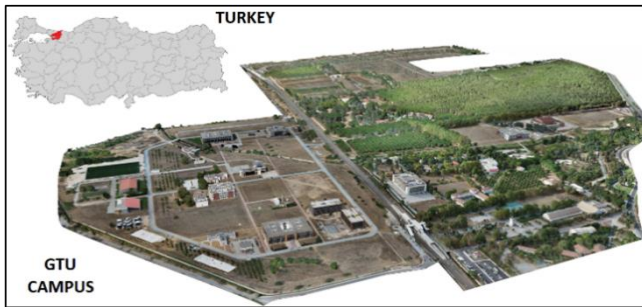


**Figure 1.** The UAV orthomosaic of GTU Campus

For the acquisition of high-resolution UAV orthomosaic, DJI Phantom 4 Pro V2 UAV was used. The geometry of the captured aerial photos was corrected by using 86 mobile ground control points (GCP) which were measured by CHC-i80 GNSS receiver. Table 1 shows the specifications of used materials for UAV data acquisition.

**Table 1.** Specifications of used materials

DJI Phantom IV Pro V2.0 UAV	
Specification	Value
Camera	4K, HD, 1080p, 1", effective pixel resolution 20 MP
Gimbal	3-axis (pitch, roll, yaw)
Hover accuracy range	± 0.1 m V, ± 0.5 m H (Vision) ± 0.3 m V, ± 1.5 m H (GPS)
Flight duration	Max. 30 minutes
Weight and speed	1375 g, Max. 20 m/s in S-mode
Operating temperature	0° to 40°C
CHC-i80 GNSS Receiver	
GNSS technology	GPS, GLONASS, GALILEO, BeiDou, SBAS, NavIC
Positioning accuracy RTK	± 0.8 cm H, ± 1.5 cm V with initialization reliability >99.9%
Network-RTK	Available

According to the land use and land cover in the Campus, the UAV flights were organized as polygonal, bundle-grid, and circular. While the nadir camera view is applied in polygonal flights, 70° was preferred for bundle-grid and circular flights. In all flights, minimum front and side overlap ratios were applied as 80% and 60%, respectively. The flying altitude was chosen as 80 m for polygonal and bundle grid flights and 30 m for circular flights. Totally, 8333 RGB aerial photos with ≤2.2 cm GSD were captured and used for orthomosaic generation [Sefercik et al. 2022].

### 2.2. Data preparation

To build a vehicle dataset, a total of 200 images with 512x512 pixel-sized were collected from the UAV data. The vehicles in each image were manually labeled with the polygon shape using the open-source image labeling tool LabelMe [Wada, 2016] and ground-truth masks were obtained. Figure 2 depicts the annotation process of a sample image in the dataset and the corresponding ground-truth instance segmentation mask. Unlike semantic segmentation, instance segmentation identifies each target as a different instance, regardless of its class. Thus, each vehicle in the image was masked in distinct colors as can be seen from the generated ground-truth mask. Afterward, the annotated dataset was divided into training, validation, and testing datasets at a ratio of 70:20:10, respectively.

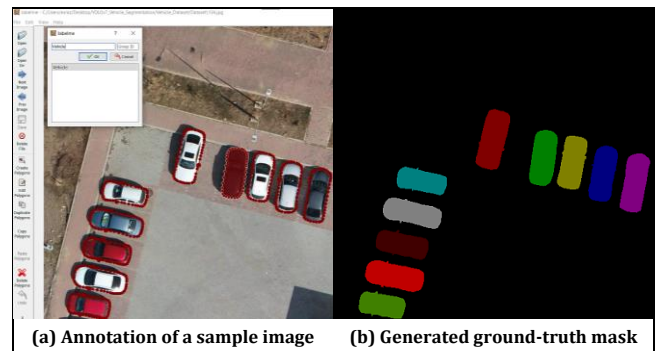


**Figure 2.** Dataset labeling process with LabelMe

In the implementation of deep learning models in object detection studies, a high-quality dataset containing a large number of images immensely enhances the training performance and prediction accuracy of the model. Therefore, different variations of the existing images were obtained in this study by utilizing several data augmentation techniques to boost the generalization capability of the model and prevent overfitting. For this aim, the training dataset was extended by horizontal flipping, randomly cropping 0 and 50 percent of the image, and adding salt and pepper noise to 5 percent of the pixels in the image. The samples of horizontally flipped, cropped and noise added images are illustrated in Figure 3.

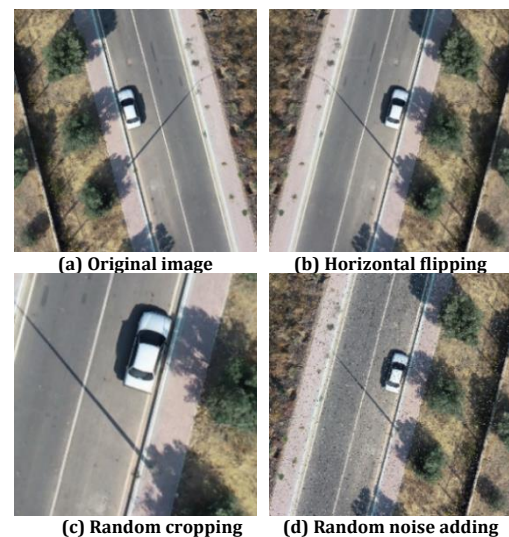


**Figure 3.** Data augmentation methods

### 2.3. YOLOv7 algorithm

In YOLOv7, the latest detector in the YOLO series, several changes were made in architecture to improve the detection accuracy and speed of the model. An extended efficient layer aggregation network (E-ELAN) based on the use of expanding, shuffling, and merging cardinality was proposed on its backbone. This network continuously improves the learning capability without losing the original gradient path. In addition, it was introduced the utilization of a compound model scaling approach to retain the features that the model had in the initial design and thereby maintain an optimal structure. Moreover, the planned re-parametrized convolution was proposed in YOLOv7. To improve training, label designers and soft labels were introduced. This process generates two types of soft labels, namely coarse labels and fine labels. This mechanism is significant because it enables fine and coarse labels to be dynamically adjusted during the training process [Wang et al. 2022].

In addition to the foregoing, there are brand-new features that were not available in the previous versions of YOLO. The first one is instance segmentation that enables YOLO to segment objects pixel-wise. The second is pose estimation, which is beneficial for understanding body movement.

### 2.4. Design and implementation

For the experiment, Python programming language and the PyTorch framework were utilized. The training and testing processes of the model were carried out on the cloud-based Google Colab environment, which provides access to the NVIDIA Tesla T4 GPU. In the study, the transfer learning approach was adopted because a relatively small data set was generated. That is, instead of training the model end-to-end from scratch, the training process of the YOLOv7 model was initialized from the pre-trained weights obtained on the COCO dataset. The hyperparameters utilized in the training phase of the model are given in Table 2.

**Table 2.** Experimental hyperparameter configuration

Hyperparameters	Values
Image size	640 x 640
Epochs	100
Batch size	16
Learning rate	0.01
Momentum	0.937
Weight decay	0.0005

## 3. Results

As a result of the training and validation process of YOLOv7, three types of losses were generated, namely bounding box loss, segmentation loss, and objectiveness loss. As can be seen from Figure 4, all loss values showed a decreasing trend during the training and no overfitting was observed in the model. The training loss converged in the early stages of the training while the validation loss converged at the end of the training. After 100 epochs of training, the minimum value was reached in the training and validation loss curves.

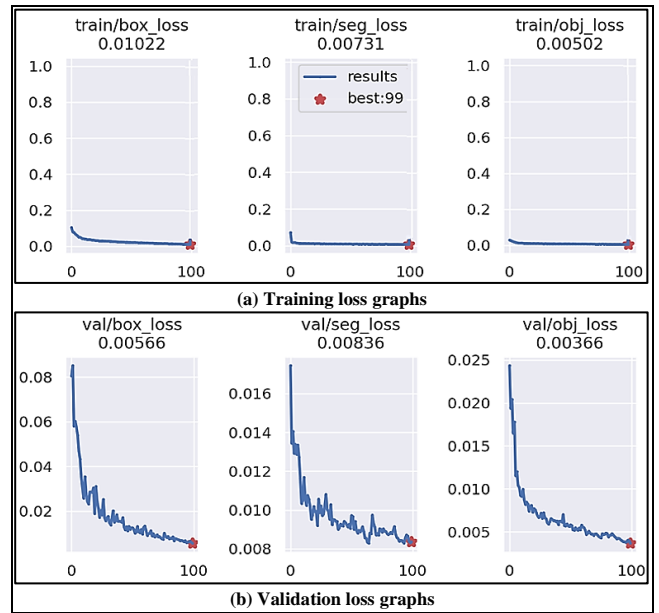


**Figure 4.** Convergence of the training and validation loss curves

To assess the performance of the trained model, Precision, Recall, and mean average precision (mAP), calculated at the intersection over union (IoU) threshold value of 0.50, accuracy metrics were utilized (Table 3). The model achieved the Precision, Recall, and mAP@0.50 values for both the bounding boxes and masks of vehicles as 99.79%, 97.54%, and 99.46%, respectively. Considering the computational burden, the model exhibited superior performance in detection and segmentation tasks with only training for about 49 minutes. Additionally, the prediction time of the model per test image is about 62.3 milliseconds.

**Table 3.** Performance evaluation of the YOLOv7 model

Metrics	Values
Precision (%)	99.79
Recall (%)	97.54
mAP@0.50 (%)	99.46
Training time	48 min 43 sec
Average detection speed (ms)	62.3

Apart from the accuracy assessment and computation time evaluation, the visual detection and segmentation results of the model on the testing dataset are given in Figure 5 to better investigate the performance of the model. It was observed that the YOLOv7 model successfully predicted the bounding boxes and segmentation masks of the vehicles, and they fitted the object boundaries correctly. Moreover, the model performed well in detecting vehicle objects with diverse backgrounds such as shadows, parking lots, and roads. It was also observed that the model gave remarkable results in identifying different vehicle types, orientations, and sizes. Even though many vehicle objects were located very adjacent to each other in the image, the model was able to accurately draw the boxes and masks of these objects. When the confidence scores in the upper left of the bounding box drawn for each vehicle were examined, it was obvious that the model detected each vehicle with a confidence score of more than 90%.



**Figure 5.** Examples of vehicle detection and instance segmentation results of the YOLOv7 model

#### 4. Conclusion

In this study, automatic vehicle detection from high-resolution UAV imagery was carried out using the state-of-the-art deep learning-based YOLOv7 object detector. Besides, pixel-wise masks of each detected vehicle were obtained by utilizing the instance segmentation feature of YOLOv7. Thanks to this feature, vehicle objects belonging to a single class in an image were segmented as distinct instances, thus each vehicle could be distinguished from the other. According to the experimental results, it was observed that the model could correctly identify vehicles from UAV data with mAP of about 99%. As a result of the study, it was concluded that YOLOv7 achieved satisfactory results in terms of accuracy and speed in detecting vehicles from UAV imagery.

#### References

- Ammar, A., Koubaa, A., Ahmed, M., Saad, A., & Benjdira, B. (2021). Vehicle detection from aerial images using deep learning: A comparative study. *Electronics*, 10(7), 820.
- Boonpook, W., Tan, Y., Ye, Y., Torteeka, P., Torsri, K., & Dong, S. (2018). A deep learning approach on building detection from unmanned aerial vehicle-based images in riverbank monitoring. *Sensors*, 18(11), 3921.
- Redmon, J., Divvala, S., Girshick, R., & Farhadi, A. (2016). You only look once: Unified, real-time object detection. *IEEE Conference on Computer Vision and Pattern Recognition*, 779-788, Las Vegas, USA.
- Sefercik, U. G., Kavzoglu, T., Nazar, M., Atalay, C., & Madak, M. (2022). Creation of a virtual tour .exe

utilizing very high-resolution RGB UAV data. *International Journal of Environment and Geoinformatics*, 9(4), 151-160.

- Shao, Z., Cheng, G., Ma, J., Wang, Z., Wang, J., & Li, D. (2021). Real-time and accurate UAV pedestrian detection for social distancing monitoring in COVID-19 pandemic. *IEEE Transactions on Multimedia*, 24, 2069-2083.
- Tang, T., Deng, Z., Zhou, S., Lei, L., & Zou, H. (2017a). Fast vehicle detection in UAV images. *International Workshop on Remote Sensing with Intelligent Processing*, 1-5, Shanghai, China.
- Tang, T., Zhou, S., Deng, Z., Zou, H., & Lei, L. (2017b). Vehicle detection in aerial images based on region convolutional neural networks and hard negative example mining. *Sensors*, 17(2), 336.
- Wada, K. (2016). Labelme: Image polygonal annotation with python.
- Wang, C. Y., Bochkovski, A., & Liao, H. Y. M. (2022). YOLOv7: Trainable bag-of-freebies sets new state-of-the-art for real-time object detectors. *arXiv preprint arXiv:2207.02696*.
- Yildirim, E., & Kavzoglu, T. (2022). Ship Detection in Optical Remote Sensing Images Using YOLOv4 and Tiny YOLOv4. *Innovations in Smart Cities Applications*, 913-924, Springer, Cham.
- Yildirim, E., Nazar, M., Sefercik, U. G., & Kavzoglu, T. (2022). Stone Pine (*Pinus pinea* L.) Detection from High-Resolution UAV Imagery Using Deep Learning Model. *IEEE International Geoscience and Remote Sensing Symposium (IGARSS)*, 441-444, Kuala Lumpur, Malaysia.



## 5<sup>th</sup> Intercontinental Geoinformation Days

igd.mersin.edu.tr



### Determination of rainwater harvesting potential in GIS using UAV imagery with machine learning classification

Abdulkadir Memduhoglu\*<sup>1</sup>

<sup>1</sup>Harran University, Faculty of Engineering, Department of Geomatic Engineering, Sanliurfa, Türkiye

#### Keywords

Rainwater Harvesting  
UAV  
Machine Learning  
Image Classification  
GIS

#### Abstract

The importance of water is increasing with the growing world population. Therefore, preserving and collecting water is essential for the continuation of life. Rainwater harvesting is one of the long-standing methods of water collection. With advances in Geographic Information Systems (GIS), Unmanned Aerial Vehicle (UAV) based remote sensing and Machine Learning (ML) image classification technologies, it has become easier to calculate rainwater harvesting potential. However, methods need to be customized for different man-made objects. In this study, the rainwater harvesting potential of a building complex with its surrounding marble ground surface located in the Harran University Osmanbey Campus was determined in GIS by using UAV imagery with ML classification techniques. The results showed that a 4153 m<sup>2</sup> grass area can be irrigated every day for a year from this potentially harvested rainwater.

#### 1. Introduction

Turkey is a water-stressed country in terms of the average amount of available water per person per year. It is below the world average with approximately 1500 m<sup>3</sup> (Alparslan et al., 2008; Şahin & Manioğlu, 2011; Yiğit et al., 2020). Therefore, preserving and collecting water is essential for the country.

Rainwater harvesting is a long-standing method used by people all over the world to collect water (Boers & Ben-Asher, 1982). In parallel with Geographic Information Systems (GIS) and Remote Sensing (RS) technologies, methods for calculating rainwater harvesting potential have also developed. In addition, image acquisition techniques such as Unmanned Aerial Vehicles (UAV) and Machine Learning (ML) image classification techniques have facilitated this process.

In literature, there are many studies using GIS and RS techniques to determine rainwater harvesting potential (Campisano et al., 2017; Hari et al., 2018; Mbilinyi et al., 2007; Mwenge Kahinda et al., 2009; Shokati et al., 2021). The majority of the rainwater harvesting potential calculations are based on urban building roofs only. However, different building complexes may need different methods.

In this study, the rainwater harvesting potential for a building complex located in the Harran University Osmanbey Campus was determined in GIS by using UAV imagery with ML classification techniques. The marble surface area on the ground between the building blocks was also taken into account for the rainwater harvesting potential calculation.

#### 2. Method

Calculating rainwater harvesting potential in terms of different impervious surfaces is achieved mainly in five phases: i. obtaining images of the study area from UAV, ii. generating orthophoto of the study area, iii. performing ML classification with the defined parameters, iv. calculating area based on classes and v. calculating rainwater harvesting potential (Fig 1).

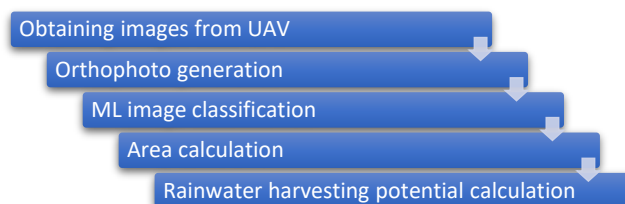


Figure 1. The overall methodology of the study

\* Corresponding Author

\*akadirm@harran.edu.tr ORCID ID 0000-0002-9072-869X

Cite this study

Memduhoglu A (2022). Determination of Rainwater Harvesting Potential Using in GIS UAV Imagery with Machine Learning Classification. 5<sup>th</sup> Intercontinental Geoinformation Days (IGD), 120-123, Netra, India

The images of the study area were obtained from a UAV (DJI Mavic 2 Pro) with 80 m altitude flight and 70 % overlap for both sides. Orthophoto generation from these images was performed using the Agisoft software package.

To classify image based on surface types, an image classification was needed. Although there are many different algorithms for image classification such as support vector machines, k-nearest neighbor and maximum likelihood, in our case, according to preliminary studies, the random forest algorithm performed the best in terms of time efficiency and visual comparison of accuracy. Therefore, the pixel-based random forest algorithm which is an ML classification method was applied to the orthophoto to identify four surface types of the study area. These classes are soil, green, metal roof, concrete and marble. While these surfaces have different behaviors in terms of rainwater flow, they need to be distinguished in order to calculate rainwater harvesting potential more accurately. However, green and soil areas which are not impervious surfaces were not considered for the rainwater harvesting potential. Thus, metal roof, concrete and marble areas have been calculated from the classified image. Concrete and marble classes were merged due to the similar spectral reflectance and same flow coefficient (see Table 1).

The rainwater harvesting potential for both metal roof and concrete&marble areas were calculated according to Equation 1.

$$\text{rainwater harvesting } p. (m^3) = \frac{\text{area} \times \text{precip} \times \text{coeff} \times \text{filter}}{1000} \quad (1)$$

To calculate *rainwater harvesting potential* in the equation, the *area* is the surface type area to be calculated, *precip* denotes the average precipitation amount in mm per year which is 460.1 for the Şanlıurfa region (TSMS, 2022), *coeff* is the coefficient for rainwater flow on surface types and the *filter* denotes the filter efficiency coefficient which is 0.9 according to the DIN (1989).

The rainwater flow coefficient for the surface types used in the study area were given in Table 1.

**Table 1.** The flow coefficients for surface types (DIN, 1989)

Class	Flow Coefficients
Metal Roof	0.9
Concrete	0.7
Marble	0.7

### 3. Results

The study area is a building complex consisting of the Faculty of Engineering and GAP YENEV (GAP Renewable Energy Research Center) on the Harran University Osmanbey campus (Fig 2).

A total of 172 images were obtained by a UAV flight with the given parameters in the methods section. These images were then used to generate an orthophoto of the study area (Fig 3).

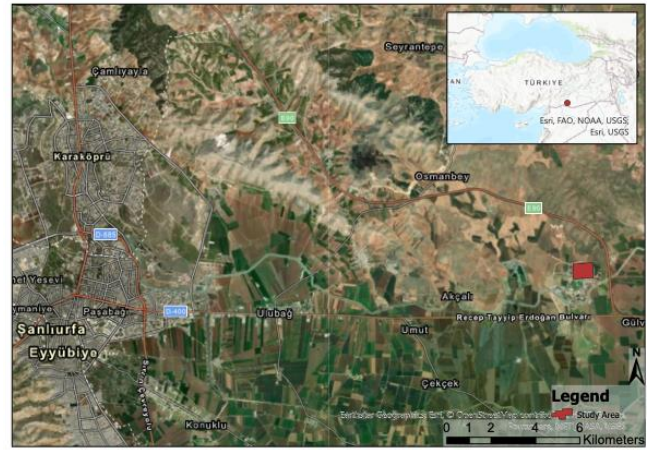


**Figure 2.** Location of the study area

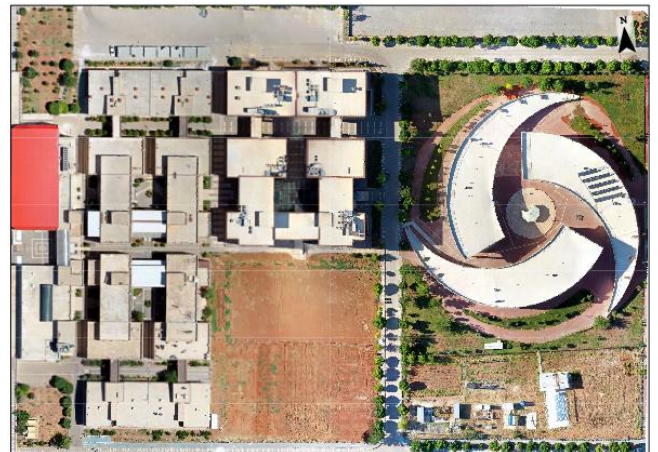


**Figure 3.** Orthophoto of the study area

As can be seen in Fig 3, the faculty of engineering consists of several blocks (right) and a circular building of GAP YENEV (left). The joints and gaps between blocks on the ground also are made of marble. This makes it possible to collect rainwater not only from the roofs of the building but also from the marble floor. In order to accurately calculate rainwater potential, surfaces need to be classified. Therefore, the random forest algorithm, one of the ML classification methods for geospatial images, was used. The method parameters were set: 80 for maximum number of trees, 40 maximum tree depth and 1500 maximum number of samples per class. The sample statistics for the training model are given in Table 2.

**Table 2.** The train samples statistics

Class	Num. of Samples	Pixels (%)
Green	12	13.23
Soil	11	4.79
Metal Roof	5	16.63
Concrete&Marble	42	65.34

The classification was performed with a training accuracy of 0.987. The image of the study area classified into the four surface types is given in Fig 4.

In order to find potential areas for rainwater harvesting, it is necessary to calculate the areas according to the surface types. For this reason, the areas of the surface types subject to the study were calculated from the classified image and given in Table 3.



**Figure 4.** The classified image of the study area

**Table 3.** The area and the ratio of the surface types

Class	Area (m <sup>2</sup> )	the ratio of total area (%)
Green	14613.62	22.2
Soil	11190.61	17.0
Metal Roof	1777.33	2.7
Concrete&Marble	38245.55	58.1
<b>TOTAL</b>	<b>65827.11</b>	<b>100</b>

According to Equation 1, the rainwater harvesting potential was calculated for concrete&marble and metal roof surface types. The result can be seen in Table 4.

**Table 4.** The rainwater potential

Class	Rainwater harvesting Potential (m <sup>3</sup> )
Metal Roof	662
Concrete & Marble	11086
<b>TOTAL</b>	<b>11748</b>

A total of 11748 m<sup>3</sup> of rainwater can potentially be collected from the study area. According to Erdoğan (2002) and Yiğit et al. (2020), 7.75 m<sup>3</sup>/day of water is needed for the irrigation of 1000 m<sup>2</sup> of grass area. Therefore, with the amount potentially collected, 4153 m<sup>2</sup> of grass can be irrigated every day for a year.

#### 4. Discussion

The images used for classification were acquired in the afternoon. Therefore, the shadows of the objects affect the classification results. Thus, it should be noted that the time of flight is an important factor and should be closer to noon to obtain images with fewer shadows.

The random forest algorithm can be used for the ML classification of geospatial images. However, it is a parametric method where these parameters can affect the result. These three parameters namely, maximum number of trees, maximum tree depth and maximum number of samples per class can be used by default (respectively: 50,30,1000) or empirically. In this study, these parameters were tested several times with different combinations and decided by a visual accuracy comparison. Although the area of the study is relatively small, the samples used for training are sufficient to cover the surface types and are suitable for application to larger areas.

Accuracy was not assessed in the study, as a visual accuracy comparison seems sufficient for the calculation of rainwater harvesting potential.

Collecting and storing rainwater on marble floors may not be as easy as on building roofs. Therefore, UAV imagery with a high-resolution digital elevation model makes it possible to determine runoff directions and accumulation for accurate storage planning.

#### 5. Conclusion

In this study, a UAV flight was conducted to acquire high-resolution image data of a building complex. These images were then used to generate an orthophoto of the study area. This orthophoto was classified by the random forest algorithm to obtain different surface types of the study area. Based on the classified image, the impervious surface areas were calculated not only for the building roofs but also for the ground marble area between the building blocks. As a result, the rainwater harvesting potential of the building complex was calculated according to different surface types.

Classification of UAV imagery with ML algorithms provides fast solutions in applications such as determining rainwater harvesting potential. In addition, many applications such as solar panel installation on roofs, landscape monitoring and land use/land cover detection can also benefit from this method.

#### Acknowledgment

This study was supported by Harran University Research Project Office (HUBAP) (Project Number: 22126).

#### References

- Alparslan, N., Tanık, A., & Dölgen, D. (2008). *Türkiye’de Su Yönetimi Sorunlar ve Öneriler*.
- Boers, T. M., & Ben-Asher, J. (1982). A review of rainwater harvesting. *Agricultural Water Management*, 5(2), 145–158. [https://doi.org/10.1016/0378-3774\(82\)90003-8](https://doi.org/10.1016/0378-3774(82)90003-8)
- Campisano, A., Butler, D., Ward, S., Burns, M. J., Friedler, E., DeBusk, K., Fisher-Jeffes, L. N., Ghisi, E., Rahman, A., Furumai, H., & Han, M. (2017). Urban rainwater harvesting systems: Research, implementation and future perspectives. *Water Research*, 115, 195–209. <https://doi.org/10.1016/j.watres.2017.02.056>
- DIN-1989-1. (1989). *Rainwater Harvesting Systems—Part 1: Planning, Installation, Operation and Maintenance*.
- Erdoğan, O. (2002). *Kocaeli İli Sahil Düzenlemesinin Sulama Sistemi Projelendirilmesi, Masters Thesis*. İstanbul Üniversitesi Fen Bilimleri Enstitüsü.
- Hari, D., Ramamohan Reddy, K., Vikas, K., Srinivas, N., & Vikas, G. (2018). Assessment of rainwater harvesting potential using GIS. *IOP Conference Series: Materials Science and Engineering*, 330(1). <https://doi.org/10.1088/1757-899X/330/1/012119>
- Mbilinyi, B. P., Tumbo, S. D., Mahoo, H. F., & Mkiramwinyi, F. O. (2007). GIS-based decision support system for identifying potential sites for rainwater harvesting.

- Physics and Chemistry of the Earth*, 32(15–18), 1074–1081.  
<https://doi.org/10.1016/j.pce.2007.07.014>
- Mwenge Kahinda, J., Taigbenu, A. E., Sejamoholo, B. B. P., Lillie, E. S. B., & Boroto, R. J. (2009). A GIS-based decision support system for rainwater harvesting (RHADESS). *Physics and Chemistry of the Earth*, 34(13–16), 767–775.  
<https://doi.org/10.1016/j.pce.2009.06.011>
- Şahin, N. I., & Manioğlu, G. (2011). Binalarda Yağmur Suyunun Kullanılması. *Tesisat Mühendisliği*, 125, 21–32.
- Shokati, H., Kouchakzadeh, M., & Noroozi, A. (2021). *Designing of Rainwater Harvesting Systems Using Drone*. 14(48), 73–85.  
<https://doi.org/10.30495/wej.2021.4590>
- TSMS. (2022). *Turkish State Meteorological Service*.  
<https://www.mgm.gov.tr/?il=Sanliurfa>
- Yiğit, A. Y., Orhan, O., & Ulvi, A. (2020). Investigation of The Rainwater Harvesting Potential at the Mersin University, Turkey. *Mersin Photogrammetry Journal*, 2(2), 64–75.  
<https://dergipark.org.tr/en/pub/mephoj/issue/58058/836719>



## 5<sup>th</sup> Intercontinental Geoinformation Days

igd.mersin.edu.tr



### Evaluation of Cutaneous Leishmaniasis cases in Şanlıurfa in 2019-2022 using geographic information systems

Ceren Arkant\*<sup>1</sup>, Abdullah İzzeddin Karabulut\*<sup>2</sup>, Yaşar Koçer\*<sup>1</sup>, Mehmet İrfan Yeşilnacar\*<sup>2</sup>

<sup>1</sup> Public Health Services Department, Şanlıurfa, Türkiye

<sup>2</sup> Harran University, Faculty of Engineering, Department of Environmental Engineering, Sanliurfa, Türkiye

#### Keywords

Cutaneous Leishmaniasis  
Environmental factors  
Geographic Information  
Systems

#### Abstract

Cutaneous leishmaniasis (CL) is one form of the Leishmaniasis disease causing skin sores that may leave scars. Majority of CL cases (%80) worldwide is in WHO Eastern Mediterranean Region. Rural areas rather than urban areas are of greater potential for the transmission of the disease. Major risk factors including socioeconomic conditions, , such as poverty, malnutrition, lack of waste management, population mobility, changes in urbanization, changes in temperature, rainfall and humidity can be classified as environmental factors that exacerbate the condition. Cutaneous Leishmaniasis cases diagnosed upon the application of the patients have been recorded on the health surveillance system in control of the Ministry of Health. Geostatistics analysis methods, which is a type of analysis of Geographical information systems (GIS), were used in order to map the obtained data. During the period of the study 2601 CL cases were reported in Sanliurfa in total. This study showed the potential of the already existing disease in the region. Crowded areas where the settlements are disorganized seem to have higher risk for the CL cases to occur.

#### 1. Introduction

Leishmaniasis is a tropical/sub-tropical disease caused by the Leishmania protozoa, transmitted through the bite of an infected sandfly. Cutaneous leishmaniasis (CL) is one form of the Leishmaniasis disease causing skin sores that may leave scars. CL is seen worldwide including the Mediterranean coast (European Centre for Disease Control and Prevention [ECDC], 2022).

CL is the most common form of leishmaniasis characterized by skin lesions and ulcers on the exposed parts of the body. This form of the disease may leave life-long scars and serious disability or stigma. Between 600 000 to 1 million new CL cases are estimated to occur worldwide annually. The transmission of *Leishmania* parasites is caused by the bite of infected female phlebotomine sandflies. Characteristics of the parasite and sandfly species, local ecological characteristics of transmission sites, current and past exposure of human population to the parasite, and human behaviour are some of the factors that determine the epidemiology of leishmaniasis. Natural reservoir hosts of *Leishmania* parasites consist of nearly 70 animal species including humans. Majority of CL cases (%80)

worldwide is in WHO Eastern Mediterranean Region (World Health Organization [WHO], 2022).

Rural areas rather than urban areas are of greater potential for the transmission of the disease. Climatic factors along with other environmental changes expand the geographic distribution of sand fly vectors and therefore CL cases. The most active periods of the sand fly vectors are evening, night-time and twilight. (Centers for Disease Control and Prevention [CDC], 2022).

Major risk factors including socioeconomic conditions, such as poverty, malnutrition, lack of waste management, population mobility, changes in urbanization, changes in temperature, rainfall and humidity can be classified as environmental factors that exacerbate the condition.

#### 2. Method

Şanlıurfa province is located in the southeastern of Turkey at 36°41'28"- 37°57'50" N, 37°49'12"- 40°10'00" E and with 18.765km<sup>2</sup> of surface area is the 7th largest city of the country. Sanliurfa province covers 13 counties. The study subjects are the inhabitants of the province. According to Turkstat data, the population of the

#### \* Corresponding Author

(cerenarkant@gmail.com) ORCID ID 0000-0001-8976-061X  
(karabulut6363@gmail.com) ORCID ID 0000-0002-9784-5549  
(koceryasar@gmail.com) ORCID ID 0000-0002-9565-4685  
(iyesilnacar@gmail.com) ORCID ID 0000-0001-9724-8683

#### Cite this study

Arkant C, Karabulut A İ, Koçer Y & Yeşilnacar M İ (2022). Evaluation of CL cases in Şanlıurfa in 2019-2022 using Geographic Information Systems. 5<sup>th</sup> Intercontinental Geoinformation Days (IGD), 124-127, Netra, India

province by the end of 2021 is 2.143.020 (Turkish Statistical Institute [Turkstat],2021).

Cutaneous Leishmaniasis cases diagnosed upon the application of the patients have been recorded on the health surveillance system in control of the Ministry of Health. The online surveillance system includes CL cases in 13 counties of Sanliurfa Province as of April 2019 and the period of this study ends with CL cases in the early July 2022.

Geostatistics analysis methods, which is a type of analysis of Geographical information systems (GIS), were used in order to map the obtained data. GIS, a large domain that provides a variety of capabilities designed to capture, store, manipulate, analyze, manage, and present all types of geographical data utilizes geospatial and hydrosatial analysis in a variety of contexts, operations and applications. GIS and the underlying geographic information science that advances these technologies have a strong influence on spatial analysis. The increasing ability to capture and handle geographic data means that spatial analysis is occurring within increasingly data-rich environments. GIS provide platforms for managing these data, computing spatial relationships such as distance, connectivity and directional relationships between spatial units, and visualizing both the raw data and spatial analytical results within a cartographic context (Karabulut et al 2022).

Spatial analysis method, which is a type of analysis of geographic information systems, was used to analyze and map the obtained data. With spatial analysis, surface creation tools from values taken from certain points, the user can easily obtain the most accurate surface using geostatistical methods. 13 counties were mapped according to numbers of the CL cases by years and in total.

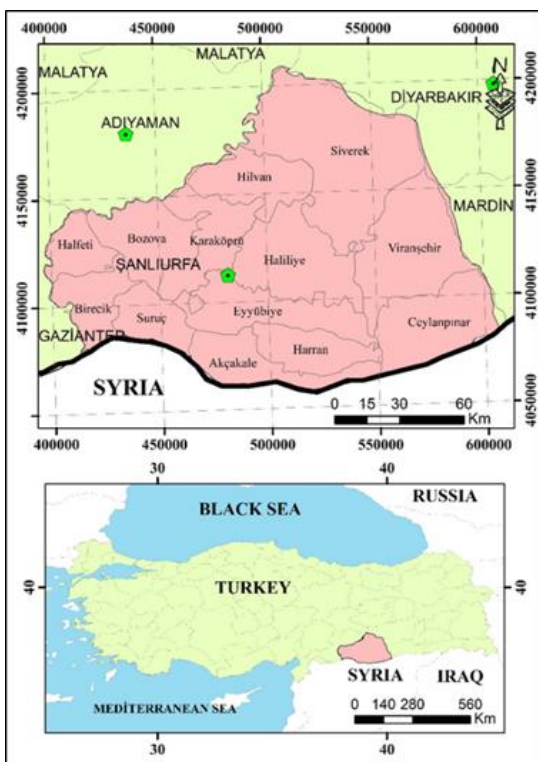


Figure 1. Map of Sanliurfa province indicating its location in the region

### 3. Results

During the period of the study 2601 CL cases were reported in Sanliurfa in total; consisting of 1404 (53,98%) children and 1197 (46,02%) adult patients. Of 2601 cases, 1292 (49,67%) were women and 1309 (50,33%) were men.

The cases were classified according to the date of diagnosis and presented in Table1. For 114 cases included in the study, no date of diagnosis was available and those 114 cases (4,38%) are excluded in the table. The distribution of the remaining cases by year is as follows: 136 cases (5,23%) in 2019; 345 cases (13,26%) in 2020; 1404 cases (53,98%) in 2021; 602 cases (23,14%) in 2022(first 7 months) respectively "Table1".

Table 1. Number of CL cases in the city of Şanlıurfa in each month during the period of study

	2019	2020	2021	2022
January		63	44	276
February		11	36	142
March			36	73
April	4	39	19	37
May		39	24	46
June	1	40	25	26
July	1	32	12	2
August		22	28	
September	1	18	89	
October	43	17	241	
November	35	22	418	
December	51	42	432	
Total	136	345	1404	602

Age distribution varied from age of 0 to age of 87. Mean age was calculated as 21,71 while median age was 15,00 and mode was 3.

As demonstrated in Table 2, among 13 counties, Eyyübiye has the highest number (n=882) of CL cases (33,91%) during the study period. Eyyübiye was followed by Ceylanpınar(n=456, %17,57) , Haliliye (n=293, 11,26%), Viranşehir (n=284, 10,91%) and Akçakale (n=275, 10,57%) "Table2".

Table 2. Number of CL cases in the 13 counties in the city of Şanlıurfa during the period of study

County Name	2019	2020	2021	2022	XXXX	Total
Akçakale	1	5	186	78	5	275
Birecik	1	10	8	19	3	41
Bozova	5	9	4	6		24
Ceylanpınar	2	3	289	160	3	457
Eyyübiye	96	244	333	139	70	882
Halifeti		3	2	4		9
Haliliye	20	36	161	60	16	293
Harran	1	5	122	73	4	205
Hilvan	2		12	1		15
Karaköprü	5	21	41	20	5	92
Siverek			12			12
Suruç		3	4	4	1	12
Viranşehir	3	6	230	38	7	284
Total	136	345	1404	602	114	2601

The distribution of CL cases in the 13 counties of Sanliurfa from 2019 to 2022 is demonstrated in Figure 2.

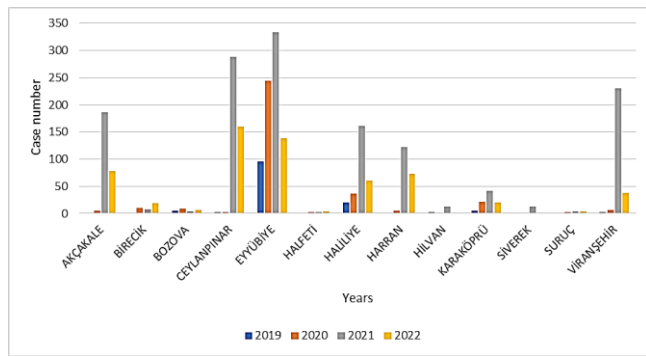


**Figure 2.** CL case numbers in the 13 counties of Sanliurfa from 2019 to 2022

#### 4. Discussion

During the study period, 2021 is the year in which CL cases reach the highest number. December and November are the months of highest case numbers. The climatic factors seem to cause changes in the accumulation of the case numbers. Many studies reveal the importance of the season on vector born diseases transmission (Caminade et al. 2014; Dhimal, Ahrens and Kuch 2015; Ostad et al. 2016).

Supporting our study, a systematic review concluded that for CL, probability of occurrence was

greater in years with greater average winter precipitation (Valero and Uriarte 2020).

Also, our study shows different distribution of cases in between the 13 counties. The population group, their socioeconomic factors and other environmental factors may have played role in this distribution. Considering the clustering of the cases in Eyyübiye county, reveals that Eyyübiye county is of the highest risk for its residents compared to other counties of the province. This variation was expected as different studies have shown variations in between different parts of the study areas. (Salimi, Jesri, and Javanbakht 2018).

#### 5. Conclusion

This study showed the potential of the already existing disease in the region. Children consist of more than half of the cases in the study period. Environmental factors play a significant role in the transmission of the disease. Crowded areas where the settlements are disorganized seem to have higher risk for the CL cases to occur.

#### Acknowledgement

The authors would like to appreciate Sanliurfa Public Health Services Department for the contribution to this study.

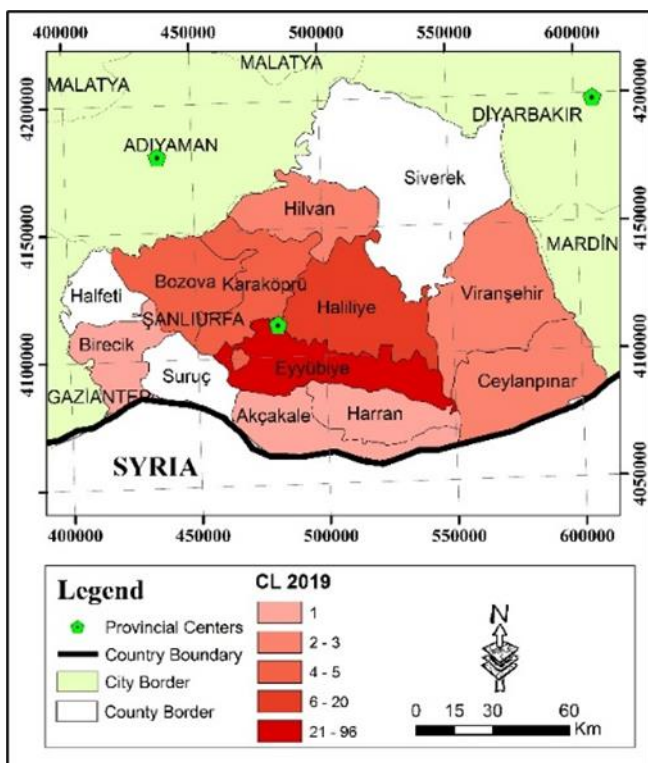


**Figure 3.** CL case numbers distributed in 13 counties of Sanliurfa in 2019

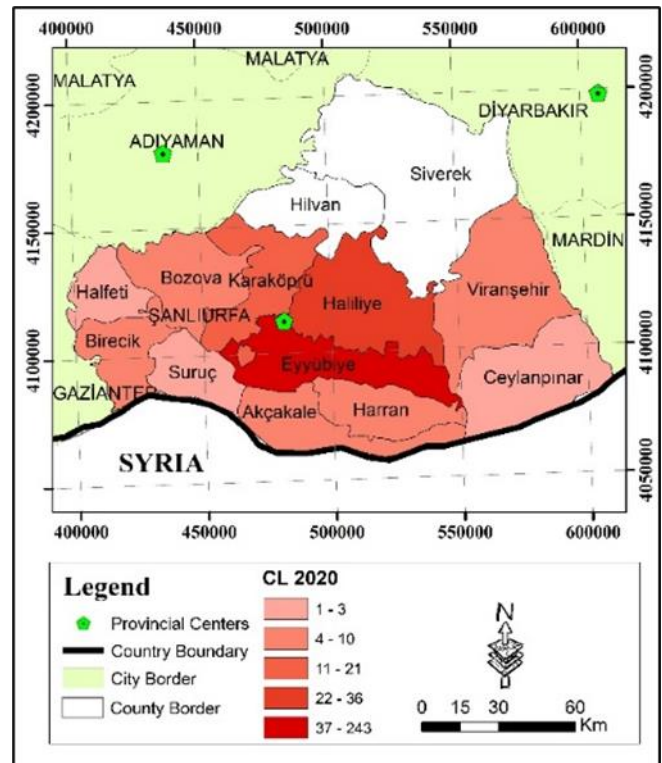


**Figure 4.** CL case numbers distributed in 13 counties of Sanliurfa in 2020

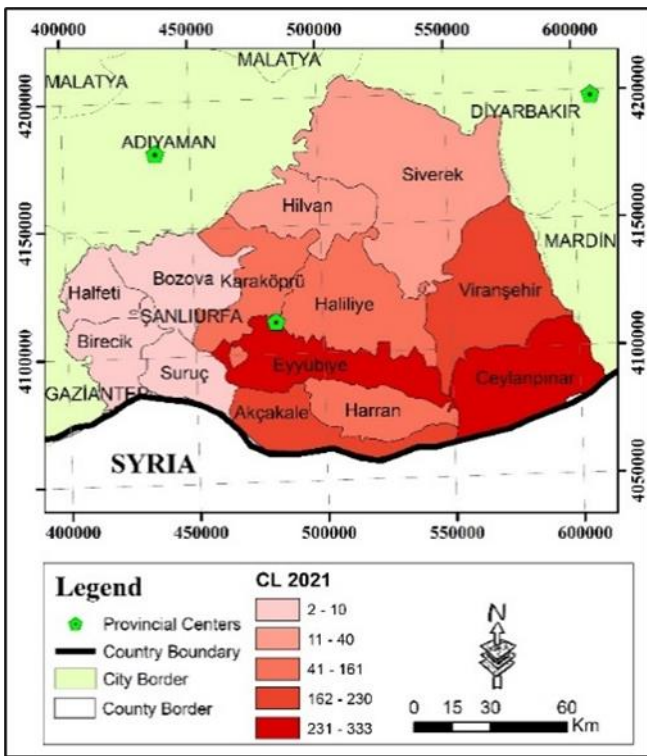


Figure 5. CL case numbers distributed in 13 counties of Sanliurfa in 2021

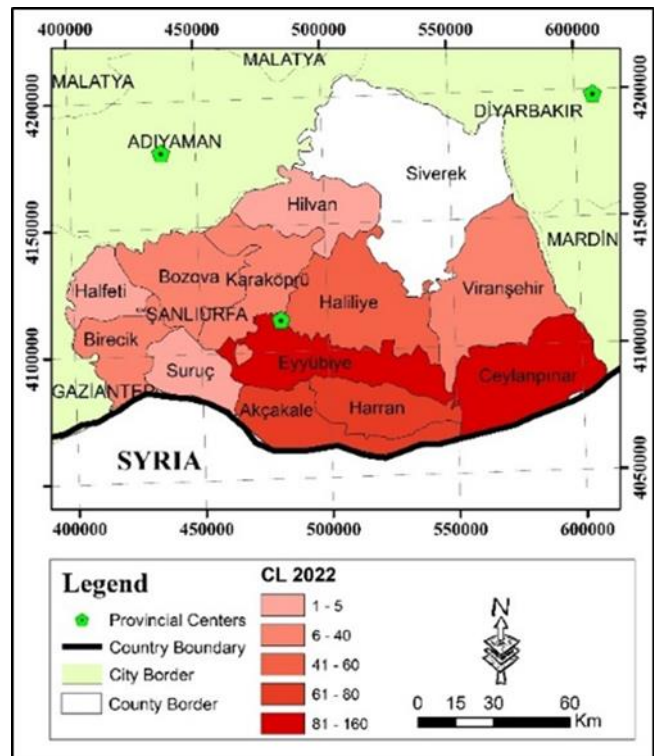


Figure 6. CL case numbers distributed in 13 counties of Sanliurfa in 2022

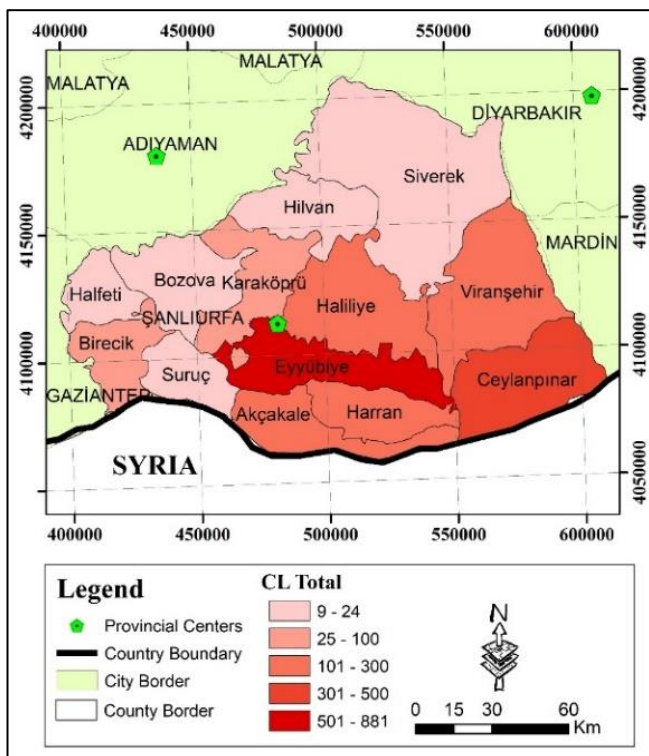


Figure 7. CL case numbers distributed in 13 counties of Sanliurfa in 2019-2022

## References

Caminade C, Kovats S, Rocklov J, Tompkins AM, Morse A P, Colón-González FJ, et al. (2014). Impact of climate change on global malaria distribution. *Proceedings of the National Academy of Sciences of the United States*

of America., 111: 3286–3291 doi: 10.1073/pnas.1302089111 PMID: 24596427

Dhimal M, Ahrens B, Kuch U. Climate Change and Spatiotemporal Distributions of Vector-Borne Diseases in Nepal—A Systematic Synthesis of Literature. *PLoS One*. 2015 18; 10(6), e0129869. doi: 10.1371/journal.pone.0129869 PMID: 26086887

Karabulut, A.İ., Yazici-Karabulut, B., Derin, P. Yesilnacar, M., İ., Çullu, M., A., (2022), Landfill siting for municipal solid waste using remote sensing and geographic information system integrated analytic hierarchy process and simple additive weighting methods from the point of view of a fast-growing metropolitan area in GAP area of Turkey. *Environ Sci Pollut Res* 29, 4044–4061. <https://doi.org/10.1007/s11356-021-15951-7>

Ostad M, Shirian S, Pishro F, Abbasi T, Ai A, Azimi F (2016) Control of Cutaneous Leishmaniasis Using Geographic Information Systems from 2010 to 2014 in Khuzestan Province, Iran. *PLoS ONE* 11(7): e0159546. doi:10.1371/journal.pone.0159546

Salimi, M., Jesri, N., Javanbakht, M. et al. Spatio-temporal distribution analysis of zoonotic cutaneous leishmaniasis in Qom Province, Iran. *J Parasit Dis* 42, 570–576 (2018). <https://doi.org/10.1007/s12639-018-1036-5>

Valero NN, Uriarte M. (2020). Environmental and socioeconomic risk factors associated with visceral and cutaneous leishmaniasis: a systematic review. *Parasitol Res*; 119:365–84., 2020



## 5<sup>th</sup> Intercontinental Geoinformation Days

igd.mersin.edu.tr



### Landslide Susceptibility Analysis with AHP and FUCOM; a case Study of Taşova

Melike Öcül<sup>1</sup>, Aziz Şişman<sup>2</sup>

<sup>1</sup> Ondokuz Mayıs University, Faculty of Engineering, Department of Geomatics, Samsun, Türkiye

<sup>2</sup> Ondokuz Mayıs University, Faculty of Engineering, Department of Geomatics, Samsun, Türkiye

#### Keywords

FUCOM  
AHP  
Landslide Susceptibility

#### Abstract

Various studies are carried out in order to minimize the loss of life and property that may occur after a disaster. One of these studies is disaster risk maps. In order to prepare disaster risk maps, first of all, the criteria affecting them according to the type of disaster should be determined well. Multi-Criteria Decision Making Methods (MCDM) and spatial analyzes are needed as it will be difficult to evaluate more than one criterion alone. MCDM methods help both to weight criteria and to rank among alternatives. The criteria determined for disaster risk maps are weighted with the help of criterion weighting methods, so that the analysis is performed according to these weights and the most optimum result is obtained. In this study, two different Landslide Susceptibility Maps were obtained for Taşova district of Amasya province by using Analytical Hierarchy Process (AHP) and Full Consistency Method (FUCOM). Twelve criteria were determined for map production and raster data was created by performing various spatial analyzes for these criteria. Two different landslide susceptibility maps were obtained by giving criterion weights to the generated raster data.

#### 1. Introduction

Today, studies are carried out to produce disaster risk maps due to the loss of life and property during disasters. There are many known disaster types and multiple criteria affecting these disasters. In order for these criteria to be evaluated simultaneously, the spatial analysis of the data is done first, and then weights are assigned to the criteria with MCDM methods. The criterion with the highest weight will affect the risk map more, while the criterion with the least weight will affect the risk map less. Thus, more reliable results will be obtained. One of the risk maps is the landslide susceptibility analysis.

Landslide is defined as a noticeable downslope or movement of landslide rock, soil or pieces of land due to gravity or external factors such as earthquakes and heavy rains (Disaster Management Dictionary). Although a landslide is a natural disaster, the human factor also triggers it. Examples of human factors such as unknowingly felling trees, unauthorized mining, inadequate retaining walls on the roadside. Therefore, it allows to determine the places with landslide risk and to act carefully in those areas. Thus, the loss of life and property is minimized.

In the studies, maps were generally made with the Analytical Hierarchy Process (AHP). In this study, it was desired to compare the Full Consistency Method (FUCOM) developed by Pamucar et al. in 2018 and the AHP method. For this, two different maps were created by using both methods of landslide susceptibility analysis for the Taşova district of Amasya province.

#### 2. Method

In this section, the methods are briefly explained and criteria for landslide susceptibility analysis are determined.

##### 2.1. Analytical hierarchy process (AHP) method

The Analytical Hierarchy Process is a method developed by Thomas Saaty in 1980 that provides a basis for comparing decision-making criteria in a mathematical structure by creating a hierarchical structure.

In the first stage, a hierarchical model is created that shows the relations between the aim, criteria and alternatives to be obtained by taking expert opinion for the solution of the problem.

Organizing goals, attributes, issues, and stakeholders in a hierarchy serves two purposes. Provides an

\* Corresponding Author

(e-mail: 20281655@stu.omu.edu.tr) ORCID ID – 0000 – 0001 – 9949 – 0115  
(e-mail: asisman@omu.edu.tr) ORCID ID – 0000 – 0001 – 6936 – 5209

Cite this study

Öcül M & Şişman A (2022). Landslide Susceptibility Analysis with AHP and FUCOM; a case Study of Taşova. 5<sup>th</sup> Intercontinental Geoinformation Days (IGD), 128-133, Netra, India

overview of the complex relationship vessels inherent in the situation; and helps the decision maker to assess whether the problems at all levels are of the same magnitude, so that they can accurately compare these homogeneous elements (Saaty 1994).

In the second stage, each criterion is compared with other criteria and values are assigned according to the importance scale in Table.1 prepared by Saaty. With these values, nxn dimensional pairwise comparison matrix is created for n criteria.

**Table 1.** Saaty Significance Scale

Importance Values	Value Definitions
1	Equal Importance
3	A little more important
5	Quite Important
7	Very Important
9	Highly Important
2,4,6,8	Intermediate values

The third step is to determine the weights of the criteria. In the pairwise comparison matrix, the sum of each column is taken and divided by each element in the column and matrix B is obtained. If we divide the row sum of matrix B by the number of criteria, that is, if the arithmetic average of the row is taken, the weights of each criterion will be found (Equation 1).

$$W_i = \frac{\sum_{j=1}^{n-1} b_{i,j}}{n} \quad (i=1,2,3,\dots,n ; j=1,2,3,\dots,n) \quad (1)$$

In the last step, the consistency ratio (CR) of the measures is calculated. If the consistency ratio (CR) according to Saaty is less than 0.1, the comparisons are consistent, if it is greater than 0.1, the comparisons are inconsistent.

No matter how mathematically consistent the AHP has in itself, the realism of the results will depend on the consistency of the judgment of the decision maker in the one-to-one comparison between the criteria (Yilmaz 2010).

$$[C_{ij}]_{n \times 1} = [a_{ij}]_{n \times n} \times [W_{ij}]_{n \times 1}$$

$$[d_{ij}]_{n \times 1} = [C_{ij}]_{n \times 1} / [W_{ij}]_{n \times 1}$$

$$\lambda = \frac{\sum_{i=1}^n d_i}{n} \quad (i=1,2,3,\dots,n)$$

a<sub>ij</sub>: Pairwise comparison matrix

w<sub>ij</sub>: Weight vector of criteria

C<sub>ij</sub>: Column Vector

d<sub>ij</sub>: Consistency Vector

λ: Base value

Finally, the randomness indicator (R1) prepared by Saaty, determined according to the number of criteria, is selected from the table and the consistency ratio (CR) is calculated (Equation 2).

**Table 2.** Hourly Randomness Indicator

n	1	2	3	4	5	6	7	8	9	10	11	12	13	14	15
RI	0.00	0.00	0.58	0.90	1.12	1.24	1.32	1.41	1.45	1.49	1.51	1.48	1.56	1.57	1.59

$$CR = \frac{\lambda - n}{(n-1)RI} \quad (2)$$

## 2.2. Full consistency method (FUCOM)

The Full Consistency Method (FUCOM) is one of the criteria weighting methods based on expert opinion, developed by Pamucar, Stevic and Sremac in 2018.

FUCOM selections have pairwise comparisons of criteria for which only n – 1 comparisons are required in the model. The model implies the implementation of a simple algorithm capable of validating the model by determining the deviation from the full consistency of comparison (DFC). (Pamucar et al,2018)

The FUCOM method takes place in three stages. At the first stage, decision makers are asked to rank n criteria from the most important to the less important criteria (Equation 3).

$$C_j(1) > C_j(2) = C_j(3) > \dots > C_j(n) \quad (3)$$

In the second stage, the comparative priorities of the criteria ranked by the decision makers in order of importance (φ n/(n+1)) The comparative priority vector (Equation 4) with n-1 elements is obtained.

$$\varphi = \{\varphi_{1/2}, \varphi_{2/3}, \dots, \varphi_{n/(n+1)}\} \quad (4)$$

In the FUCOM method, the decision maker(s) can use integers, decimals or values of certain scales for comparisons of criteria. This provides flexibility to decision makers in the evaluation of criteria. (Aycin 2021)

In the last stage, the following two conditions must be met in order to calculate the criteria weights.

Condition 1: The ratio of the weights of the two criteria to each other should be equal to the priority value in the pairwise comparison. (Equation 5)

$$\frac{w_n}{w_{n+1}} = \varphi_{n/(n+1)} \quad (5)$$

Condition 2: The final values of the weight coefficients must satisfy the mathematical transitivity condition.

Since φ n/(n+1) × φ (n+1)/(n+2) = φ n/(n+2) and

φ<sub>n/(n+1)</sub> =  $\frac{w_n}{w_{n+1}}$  are  $\frac{w_n}{w_{n+1}} \times \frac{w_{n+1}}{w_{n+2}} = \frac{w_n}{w_{n+2}}$  must satisfy the mathematical equation. If we combine the two equations, we get Equation 6.

$$\varphi_{n/(n+1)} \times \varphi_{(n+1)/(n+2)} = \frac{w_n}{w_{n+2}} \quad (6)$$

If the conditions in Equation 2.5 and Equation 2.6 are met, the expressions in Equation 2.7 are used to find the criterion weights, and solutions are made with simple codes with programs such as Excel Solver or MATLAB with a linear programming model. As a result of the solution, the consistency deviation (min (DFC(X))) being zero (0) indicates that full consistency is achieved.

$$\begin{aligned} & \text{Min } X \\ & \left| \frac{w_j(n)}{w_j(n+1)} - \varphi_{n/(n+1)} \right| \leq X \cdot \forall j \\ & \left| \frac{w_j(n)}{w_j(n+2)} - \varphi_{n/(n+1)} \times \varphi_{(n+1)/(n+2)} \right| \leq X \cdot \forall j \\ & w_j > 0, \forall j \\ & \sum_j w_j = 1 \end{aligned} \quad (7)$$

### 2.3. Study area

The study was carried out for the town of Taşova in Amasya. Taşova District. The district has an area of 1051 km<sup>2</sup>. The lowest altitude is 170 m where Karlık Stream meets Yeşilirmak. The highest altitude is Cami Hill, located in the South of ESENÇAY Village, 1956 m. is A certain part of it is sloped and a certain part of it is plain with high altitude difference. In the landslide density map of Turkey published by MTA, it has been seen that Taşova district carries a landslide risk. Regional landslides have been observed during times of heavy rainfall. Therefore, this study area was chosen.

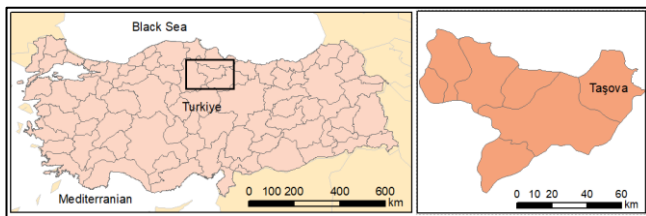


Figure 1. Study area

### 2.4. Determination of criteria and criterion maps

The criteria are the decision components used in the evaluation of alternatives to reach the goals, so it is necessary to be meticulous in the determination of the criteria. It should be known that each criterion included in the decision problem is effective in the decision process, as well as the criteria not addressed in the problem have an indirect effect on the decision output. (Yildirim, 2019)

Regardless of the method used in the preparation of landslide susceptibility maps, or whatever the geographical location, there is a general tendency to use parameters such as slope, lithology, land use potential or vegetation, slope direction, distance to main faults, drainage and relative height. (Gokceoglu and Ercanoglu 2001)

The criteria used for this study are as follows: slope shape, slope, elevation, aspect, lithology, precipitation, proximity to the river, proximity to the road, ndvi (vegetation), land use, soil type, fault line, a total of twelve criteria were used. The raster data of each criterion were prepared by performing various spatial analyzes with the ArcGIS program.

#### a) Elevation

It has been reported that the height conditions of the topography are also an effective factor in the formation of landslides. (Ozsahin 2015) The highest value of the region is 1956, and the lowest value is 170. A total of five classes were created in these value ranges.

#### b) Slope

The general tendency among researchers is that as the slope increases, the sensitivity to landslides will also increase (Gokceoglu and Ercanoglu 2001). The slope in the region varies between 0-62°.

#### c) Slope shape

In the studies, the effect of the shape of the slope on the landslide susceptibility was examined, but some researchers said that more landslides occurred on concave slopes, while some researchers suggested that more landslides occurred on convex slopes.

In addition, statistical evaluation of this parameter is quite difficult. Because during a landslide, the initial appearance of the slope is often distorted and this may lead to erroneous assessments during data collection. (Gokceoglu and Ercanoglu 2001). This study was carried out by accepting the statement “more landslides occur on concave slopes”.

#### d) Aspect

The slope direction (aspect) indicates the direction of the land surface and is expressed by the direction of the tangent plane at any point on the surface. Slope direction is an important parameter that is frequently used in studies related to the preparation of landslide susceptibility maps (Dag 2007).

The map of these four criteria was obtained using Digital Elevation Model (DEM) data in the '3D ANALYST TOOLS' analysis. (Figure-2 elevation, slope, slope shape, aspect maps)

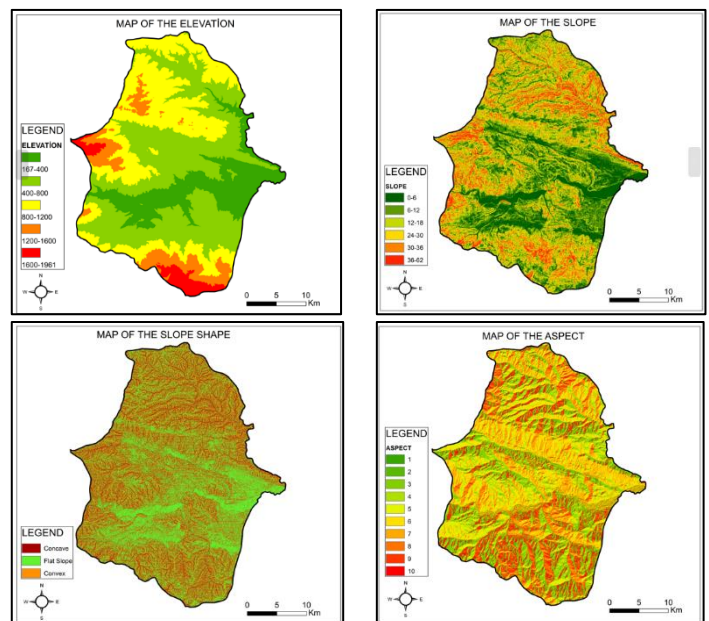


Figure 2. Elevation-Slope-Slope Shape-Aspect Maps

#### e) Proximity to the Fault Line

Proximity to the fault line increases the risk of landslides. The landslide analysis was carried out by considering the faults remaining in the study area in the fault line map published by MTA.

f) Proximity to the Stream

Since being close to the stream will increase the water saturation of the soil, the risk of landslide increases as you get closer to the stream.

g) Proximity to the Road

The roads opened on the slopes cause a load reduction in both the topography and the slope toe. The change in topography and the decrease in load cause stress increases behind the slope and this causes the development of stress cracks (Yalcin, 2007).

The maps of these three criteria were obtained by using the multiple ring buffer analysis of the proximity tool. (Figure-3 Distance to fault line, distance to streams, distance to roads)

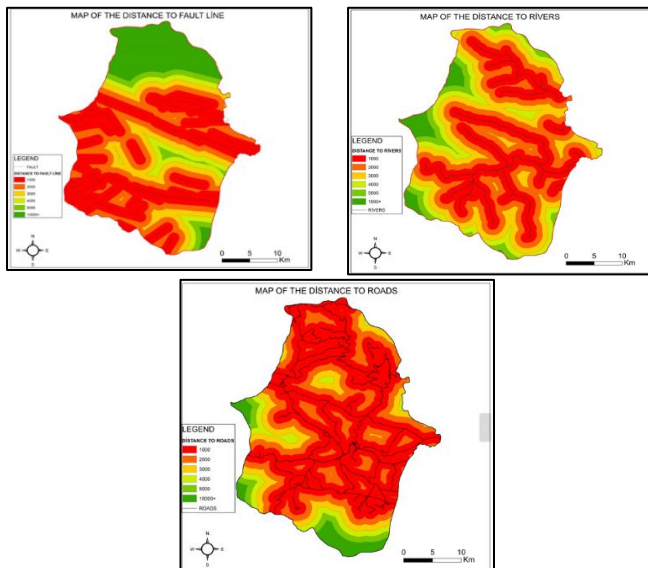


**Figure 3.** Distance to fault line-Distance to rivers-Distance to roads Maps

h) Lithology

Lithology is one of the important parameters affecting landslide formation and plays an important role in landslide susceptibility studies. Because different lithological units have different sensitivities for active geomorphological processes such as landslides. Using the earth sciences website published by MTA, it was determined that there are five different lithologies in the region.

i) Land Use

Although the land use situation includes a part of the NDVI (vegetation) analysis such as forest, meadow, swamp, residential area, agricultural area, pasture, etc. It was used as a separate criterion as it would affect the landslide in certain situations.

j) Soil type

The type of soil the ground is also important for landslides. The soil mass covering the ground of the topography also causes the formation of landslides. In fact, soils affect landslide formation according to grain size, arrangement and types (Ozsahin, 2015).

The lithology map was taken from the earth sciences site of MTA and the soil types map was taken from the agriculture portal site. The land use map was obtained from the Copernicus page by classifying the CORINE 2018 vector data and they are shown in Figure-4.

k) NDVI (Vegetation)

Landslide risk increases in areas with low vegetation density. Therefore, the NDVI map was produced and the places with low vegetation were determined.

l) Precipitation

Annual average precipitation is considered as an important factor for landslide susceptibility analysis. Because, as a result of precipitation, the ground becomes saturated with water, the groundwater level rises and the leakage forces reach their maximum value (Ozsahin,2015). The annual precipitation of Taşova district is 967mm.

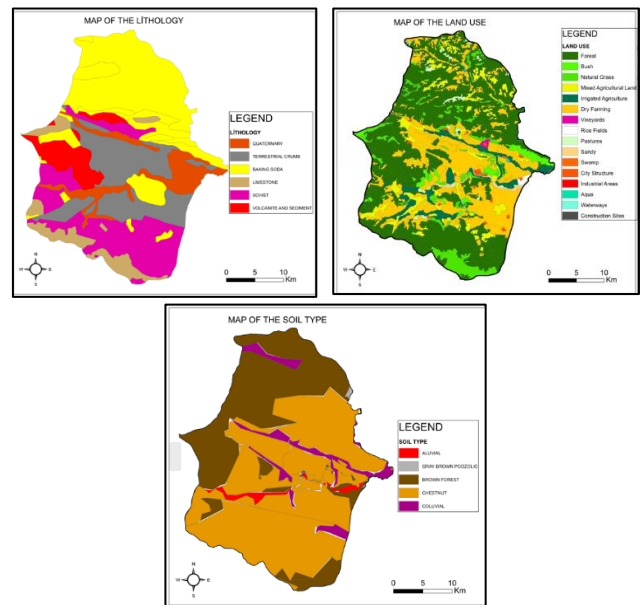


**Figure 4.** Lithology-Soil Type-Land Use Maps

The last two criteria maps were made as follows: NDVI (vegetation) data was calculated with the help of band4 and band5 in the lansat satellite image ((band5-band4)/(band5+band4)). The precipitation map is produced at the end of the calculations made with the help of climate data. (Figure 5. NDVI (vegetation), Precipitation)

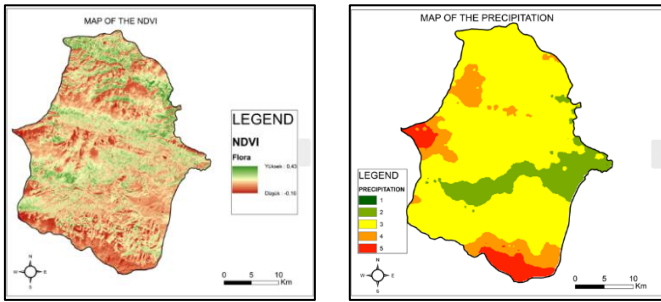


Figure 5. NDVI (vegetation), Precipitation Maps

### 3. Results And Discussion

The criteria weighting steps above were carried out sequentially and the criteria weights were calculated for both methods. The criteria weights obtained by the AHP method and the FUCOM method are shown in Table 4.

When we look at the table, the most important weights found by AHP were lithology, while the least important criterion was vegetation. The consistency calculated in the AHP was found to be 0.02 and since it was less than 0.1, the measurements were considered consistent.

When we look at the weights found with FUCOM, the most important criterion was lithology, while the least important criterion was vegetation. Since the FUCOM method is based on full consistency, the consistency deviation (DFC(X)) was found to be 0 as a result of the calculations and full consistency was obtained in the measurements.

When we compared the two methods, a total of 144 comparisons were made with AHP, while 11 comparisons were made with FUCOM. Consistency was found to be 0.02 with AHP, while full consistency was obtained by finding 0 with FUCOM.

Table 3. AHP and FUCOM criterion weights

CRITERIA	Weights with AHP	Weights with FUCOM
Lithology	0.204	0.2473
Slope	0.162	0.1236
Slope Shape	0.150	0.1236
Precipitation	0.125	0.0824
Aspect	0.093	0.0618
Prox. to Fault Line	0.072	0.0618
Prox. to the Stream	0.061	0.0618
Distance to Road	0.043	0.0618
Land Use	0.032	0.0495
Soil Type	0.025	0.0495
Elevation	0.019	0.0495
Ndvi (Vegetation)	0.013	0.0275

By using the weights obtained from the raster data produced separately for each criterion, 'Weighed Sum' analysis was performed in both methods and landslide susceptibility maps were obtained. Figure 6 shows the map made with the FUCOM method, while Figure 7 shows the map made with the AHP method.

The area of each class was calculated with the help of the pixels of the classes from the maps obtained. Percentages were made by dividing the total area by the area of each class. As can be seen in Table 5, while risk-

free, low-risk and high-risk areas gave similar results, medium-risk areas and risky areas gave different results in the two methods.

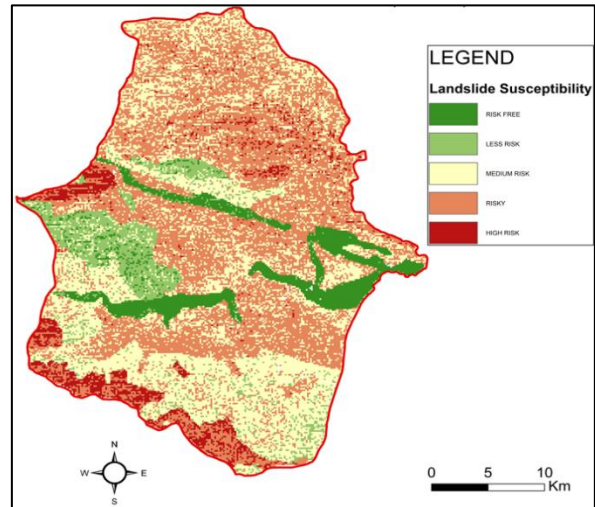


Figure 6. Landslide Susceptibility Map with FUCOM

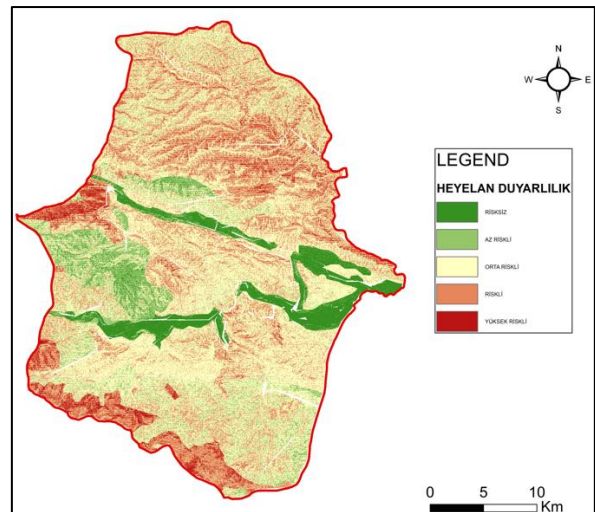


Figure 7. Landslide Susceptibility Map with AHP

Table 5. Percentages of Map Classes Made with AHP and FUCOM

	Ratios found with AHP (%)	Ratios found with FUCOM (%)
Risk-Free Area	7.25	7.89
Low Risk Area	10.75	8.08
Medium Risk Area	50.60	35.97
Risk Area	27.95	42.98
High Risk Area	3.45	5.08

### 4. Conclusion

In the study, two different landslide susceptibility maps of Taşaova district were created by using AHP and FUCOM criterion weighting. The maps are divided into five classes and the risk-free areas are green and the high-risk areas are red. By making area calculations from pixels according to colors, ratio calculations were made over the total area.

As a result of the calculations, the risky area was found to be 27%, and the high-risk area was 3%,

according to AHP. According to the FUCOM method, the risky area was 42% and the high-risk area was 5%. The percentage of risky areas in the map made with the FUCOM method was higher than the AHP method.

We said that the FUCOM method differs from the AHP method with less pairwise comparison and full consistency. With fewer comparisons, the effect of expert opinion is reduced. As a result, the FUCOM method, which is the version developed in 2018 of the AHP method, which is frequently used in the literature, can also be preferred and used in map production studies.

In general, when we look at both maps, it is seen that high-risk areas are in the same places. These high-risk areas are seen as areas where the slope is high and the vegetation is low.

Finally, landslide susceptibility maps can be prepared with various methods and criteria data. The aim of this study is to examine the similarity and dissimilarity between the two methods.

## References

- Ayçin, E., & Aşan, H. (2021). Determining The Importance Weights Of The Criteria In The Selection Of Business Intelligence Applications By FUCOM Method. *KOCATEPEİİBFD*, 23(2), 195-208
- Dağ S. (2007) Çayeli And Its Surroundings With Statistical Methods For Landslide Susceptibility Analysis, Trabzon, KTÜ, Phd Thesis, RİZE
- Gökçeoğlu, C., & Ercanoğlu, M. (2001). Uncertainties Regarding The Parameters Used In The Preparation Of Landslide Susceptibility Maps. *Geosciences* , 22 (23), 189-206.
- Özşahin E., (2015) "Landslide Susceptibility Analysis With The Help Of Geographic Information Systems: The Example Of Mount Ganos (Tekirdağ)" *Electronic Journal Of Map Technologies* 2015, 7(1) 47-63, Doi: 10.15659/Hartek.15.04.68
- Pamuçar, D., Stević, Ž. & Sremac, S., (2018). A New Model For Determining Weight Coefficients Of Criteria In Mcdm Models: Full Consistency Method (FUCOM). *Symmetry*, 10(9)
- Saaty, T L, (1994), "How To Make A Decision: The Analytic Hierarchy Process", *Interfaces*, 24 (6), November-December,
- Varnes, DJ (1978). Slope Movement Types and Processes. *Special Report*, 176, 11-33.
- Yalçin, A. (2007). Usage Of Analytical Hierarchy Method and Gis In Generation Of Landside Sensitivity Maps. *Selcuk University Journal of Engineering, Science And Technology*, 22 (3), 1-14.
- Yildirim B, (2019). Blog Post Bahadiryildirim.Com/Blog/Serie/Cok-Kriterli-Karar-Verme/



## 5<sup>th</sup> Intercontinental Geoinformation Days

igd.mersin.edu.tr



### Use of GIS in macro planning, interdisciplinary collaboration: Konya – Isparta environmental master plans

İrem Yurday<sup>\*1</sup> Mehmet Tunçer<sup>2</sup>

1Konya Technical University, Graduate School of Education, MA in Surveying Engineering Konya, Türkiye  
2Çankaya University, Faculty of Architecture, Department of City and Regional Planning Ankara, Türkiye

#### Keywords

GIS  
Environmental Plan  
Map Engineer  
City and Regional Planner  
Konya  
Isparta

#### Abstract

In this study; one of the most common usage areas of Geographic Information Systems (GIS) in recent years, 1/100 000 and 1/25 000 scale "Environmental Plans" and how these plans are handled in cooperation with GIS and interdisciplinary will be explained. The relationship between "Provincial Environmental Plans (ÇDP) and Geographic Information Systems (GIS)", which is a reform work of the public administration, which has been in search of high-scale planning and environmental control since the beginning of the 2000s, will be discussed. In this Paper, as examples of these studies; "Konya - Isparta Planning Region 1/100 000 Scale Environmental Master Plan" was discussed. Analysis sheets, SWOT and synthesis sheets were prepared by supporting the Geographic Information System with literature studies, thesis studies, interviews, meetings held in the region.

#### 1. Introduction

From the spatial information at the regional and/or provincial level produced with GIS, in line with the benefits of science and society; In MACRO PLANNING, human and environment-centered ENVIRONMENTAL PLANS and FUTURE STRATEGY and SCENARIOS are produced for "to provide benefit with maximum effect" and "sharing".

These strategies and scenarios and the 1/100 000 / 1/25 000 Scale Environmental Plans they are reflected in; "In The Entire Province" and/or in "The Planning Zone Including Several Provinces"; earthquake, epidemic disease, global warming, climate crisis, mucilage, fire, water, air pollution, reducing the urban heat island effect, establishing the protection-use balance, protecting the natural environment, determining land use decisions to ensure sustainable development, evaluating urban and rural developments and redirect, traffic etc. are used to develop solutions.

Within the scope of this paper; In order to provide information sharing for the benefit of society, it is aimed to reveal the spatial informatics (common) research/study topics that are of interest to the

disciplines of "map engineering" and "city and regional planning", science and social sciences, and to contribute to the decision makers to make the right decisions with the final products. This study will shed light on the need for interdisciplinary cooperation and GIS at the level of strategic planning and management.

#### 2. Method

By examining the data related to the 1/100 000 Scale Konya Isparta Environmental Plans and the method of preparation with the ArcGIS program, the intersection between survey engineering and City and Regional Planning will be evaluated. By giving the cooperation and communication of the Survey Engineers and City Planners working in the creation and use of "Satellite Photographs", which is the most basic database used in these plans, and the prepared Provincial Entire GIS, the resulting products (analysis, synthesis and plan) are given.

#### 3. Results

Spatial planning and decision making is a complex and interdisciplinary task with an infinite number of

\* Corresponding Author

(yurdayirem@gmail.com) ORCID ID 0000-0003-2960-0926  
(mtuncer@cankaya.edu.tr) ORCID ID 0000-0002-1591-6383

Cite this study

Yurday İ, Tunçer M (2022). Use Of GIS In Macro Planning, Interdisciplinary Collaboration: Konya – Isparta Environmental Master Plans. 5<sup>th</sup> Intercontinental Geoinformation Days (IGD), 134-135, Netra, India

solutions. Noting that during the planning process, *“better planning can be achieved through better information and that better information”* will necessarily flow through an information system; integration of geographic information systems into planning; It has contributed to a clearer understanding of real planning problems as well as planning scenarios.

Slope analyzes were made by using satellite images and elevation charts called YÜKPAF, apart from the data storage in the database, the plan drawing. In addition, apart from ARCGIS, for example, a separate software was used for the classification of forest areas, and classification studies of forest areas and non-forest areas were made from satellite images. During the implementation of Environmental Plans prepared on the basis of a province or "Planning Region", which includes several provinces, rapid access to data and plan, updating and monitoring of information (monitoring) of many local and central public institutions/organizations are of great importance. Evaluation of the "Performance" of the plan and its addition and revision, when necessary, can only be healthier if the GIS environment is prepared effectively -web-based- and its access is facilitated.

#### 4. Conclusion

As a result, the contribution of GIS to urban planning problems in both macro and micro level planning and decision-making processes, the opportunities it offers to evaluate alternative solutions, has shown that it is an invaluable tool. As the details will be explained in this paper, the use of GIS and the resulting Environmental Plans in line with the "Public Benefit" and the protection

of natural, cultural and historical values, as a result of the continuous cooperation and coordination of the Survey Engineer and the City and Regional Planner, are one of the most important legal tools used today.

#### References

- Konya Isparta Planlama Bölgesi, Çevre Düzeni Planı, 2005, Araştırma Raporu, UTТА Planlama Ltd. Geotek Ltd. İşortaklığı, Çevre ve Şehircilik Bakanlığı.
- Keskin, S., Usul, M., Bayramin, İ., Beek, K.J. , Bre, K. , Drressen, P., D-Bre, K. 1997. Land information and land evaluation for land planning and sustainable land management. Land Chatharn.1:1,27-44, Netherland.
- Rossiter, D., Bouma, J., Bregt, A.K. 1989. Land qualities in space and time, 113-116, Procceding of a symposium organized by the ISSS at Wageningen, Netherlands. 22-26 August.
- ÖÇKK Başkanlığı, K.H.Gn. Md.lüğü Ankara Araştırma Enstitüsü, Tuz Gölü ÖÇK Bölgesi'nin Toprak ve Arazi Kalite Sınıflaması ile Alternatif Tarımsal Uygulamaların Belirlenmesi Projesi Sonuç Raporu, Ankara, 2004
- Konya İl Çevre ve Orman Müdürlüğü, Konya Atık su Envanteri, Konya, 2003
- Konya İl Çevre ve Orman Müdürlüğü, Konya İli'nin Sulak Alanları, Konya, 2003
- Yüksel Proje, Ankara-Konya Demiryolu (Polatlı – Konya Kesimi) Çevresel Etki Değerlendirmesi Ana Rapor, Mart 2006, Ankara-Konya



## 5<sup>th</sup> Intercontinental Geoinformation Days

igd.mersin.edu.tr



### The ultimate vertical accuracy assessment of the third generation Turkish 1:25000 quad maps; under canopy vs. no canopy

Arif Oguz Altunel<sup>1\*</sup>, Oytun Emre Sakici<sup>1</sup>

<sup>1</sup>Kastamonu University, Forest Engineering Department, Faculty of Forestry, Kastamonu, Türkiye

#### Keywords

Photogrammetry  
Quad Maps  
DEM  
Raster Resolution

#### Abstract

Elevation, vertical accuracy of any topographic Earth representation, e. g. stereo surface models, topo maps, DEMs, etc., is important if such data will be the base of further projects or development plans. The main form of these types of data in Türkiye is “1:25000” scaled quad maps. The third generation such maps were produced via digital stereo air-photo capture and photogrammetry capabilities as opposed to the previous two analogue based releases. Through this long-adapted scale, land cover types, hydrological formations, surface features, down to house rooftops, can be depicted in these maps. Elevation integration are also provided through the contour lines drawn in 10 m elevation difference showing intervals. They are the most frequently addressed topographic data type in forestry education as well as in profession. With the establishment of county-wide active GNSS network, very high precision elevation verification has become available for multitude of purposes. In this study, four dam reservoirs intensively surveyed using CORS-GPS were used to assess the vertical accuracies of the corresponding quad-map based DEMs produced in different resolutions. RMSEs ranged from 5.49 m to 14.22 m when the entire quad sheets were used while they ranged from 2.58 m to 8.95 m when the quads were purposely cut. Canopy closure apparently worsened the results.

#### 1. Introduction

Although there were earlier attempts in site-specific (Sahin et al. 2022) or country-wide (Dagdas and Bilge 2015) scales, depicting target land cover type, forests, topography related map production, undertaken by Turkish Mapping Command in Türkiye started revealing the first country-wide coverage around 1959-1960.

Relatively similar to 7.5 minute, 1:24000 US quadrangle maps, 1:25000 Turkish quads can be considered as the country’s main elevation integrated, forest cover and type prioritizing topographic maps. Repeated with a second coverage around 1992-1993, they were produced via stereo air-photo capture and photogrammetric analyses and interpretation capabilities. These two coverages were produced with analogue means.

Since elevation has been embedded into such maps in contour line fashion, they have been accepted as the first set of reliable datasets to produce surface models, DEMs, in cartographic studies using GIS software(s), starting from the 1980s onward (Taud et al. 1999; Ardiansyah and Yokoyama 2002; Guth 1999).

Although everybody has started using them in all sorts of projects, reports, theses, etc. to generate surface models and their inherent derivatives e.g., slope, aspect, hillshade, roughness, hydrology, etc. not very many studies looking into the actual vertical accuracy of those maps surfaced until the late 2000s. Based on a verification established over 1:16000 stereo air photo driven models, Ozturk and Kocak (2007) found out that 1:25000 Turkish quad maps had RMSEs in the range of  $\pm 2$  m. Then, Bildirici et al. (2009) used them to assess the practicality of the newly released 3 arc-second SRTM and showed that SRTM’s absolute height error was actually better than the mission stated 16 m.

Although there have been even more subsequent coverages in places where frequent land-cover/land-use changes occur, finally, the third and current country-wide coverage produced with digital means, was started to be released around 2009-2010. Around the same in 2009, Türkiye also established and started effectively using the indigenous active GNSS system, TUSAGA-Active (TA) network (Yildirim et al. 2011). Using this new achievement, it’s been possible to acquire positional coordinates, x, y, z, in millimeter accuracy in much of the country as well as in Northern Cyprus.

#### \* Corresponding Author

(aoaltunel@kastamonu.edu.tr) ORCID ID 0000-0003-2597-5587  
(oesakici@kastamonu.edu.tr) ORCID ID 0000-0003-4961-2991

#### Cite this study

Altunel, A. O., & Sakici, O. E. (2022). The ultimate vertical accuracy assessment of the third generation Turkish 1:25000 quad maps; under canopy vs. no canopy. 5<sup>th</sup> Intercontinental Geoinformation Days, 136-140, Netra, India

In the scope of this study, four dam reservoirs, two to be transformed from agricultural fields, one to be transformed from >%90 forest cover and one to be transformed from <%30 forest cover were surveyed utilizing CORS GPS constantly communicating with TA network, and the results were compared to those extracted from quad map(s) generated different resolution DEMs; purpose-cut, entire sheet, 10 m resampled, 30 m resampled.

**2. Study Area and Methodology**

**2.1. Study Area**

Four dam reservoirs chosen previously by the State Hydraulic Works (DSI) for hydro-electric and irrigation purposes in Kastamonu province, were meticulously surveyed in 2014-2015 period by independent surveyors for engineering and hydrologic calculations, yet to come in the following years (Figure 1). Two of the dam reservoirs (Incebogaz and Hasanli) were planned over agricultural areas with occasional single-story dwellings for living and livestock storage. One of them (Arac) had <%30 forest cover with human habitation signs and the last one (Obrucak) had >90% forest cover with no habitations.

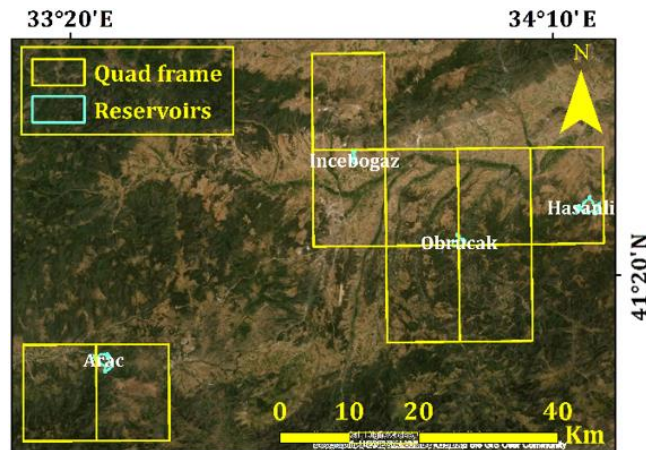


**Figure 1.** Locations of the studied dam reservoirs

**2.2. Methodology**

GCPs were recorded using ITRF-96 coordinate system meaning 3<sup>o</sup> Transverse Mercator projection. An

illustration of GCP set acquired in Obrucak Reservoir can be seen in Figure 2. Elevation measurements were based upon GRS80 vertical datum. Elevation readings were subsequently transformed into orthometric heights by subtracting the respective geoid heights from the recorded ellipsoidal heights (Simav et al. 2015). After the elevation correction, all GCP records were transformed into 6<sup>o</sup> Universal Transvers Mercator projection over WGS84 datum for easier comparison with the elevations to be extracted from different versions of the quad map generated DEMs. Tested quad coverage was also produced adopting the same projection and datum. ArcGIS 10.8 was used in the analyses.

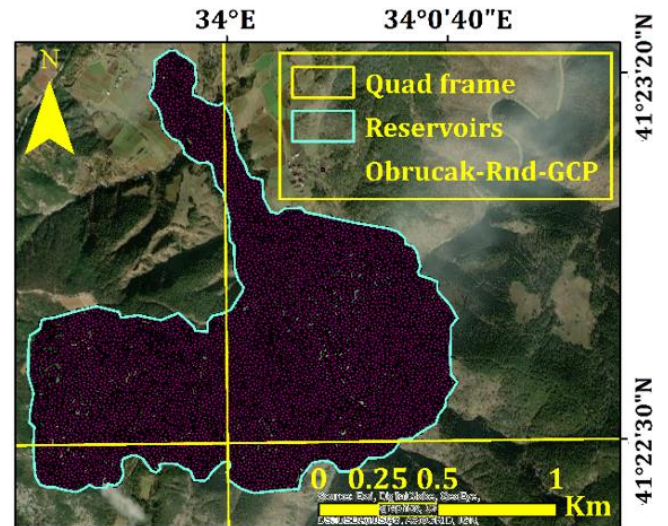


**Figure 2.** Random GCPs within Obrucak dam reservoir

Vectorized quad sheets were used. Sheets were first purposely cut using the polygons housing the GCPs, Second, TIN surfaces were generated for each site within the designated polygons. Then, a TIN to raster conversion was performed for each site preserving the ArcGIS recommended default cell sizes. Thus, four site-specific DEM datasets, “Purpose-Cut Quad Sheet” were generated.

The same sequence was repeated to create four more DEM datasets utilizing the quad sheets as whole, “Entire Quad Sheet”. 10 m and 30 m cell size preferences were dictated during entire sheet TIN to raster conversion phases of the third and fourth DEM dataset creations, “10 and 30 m Resampled Entire Quad Sheet” (Table 1).

**Table 1.** Summary statistics

Raster Resolution	Arac Dam Reservoir	Obrucak Dam Reservoir	Hasanli Dam Reservoir	Incebogaz Dam Reservoir
From Purpose-cut Quad Sheet (m)	11.2	7.5	12.3	7.5
From Entire Quad Sheet (m)	84.4	112.4	56.3	111.8
From 10 m Resampled Entire Quad Sheet (m)	10	10	10	10
From 30 m Resampled Entire Quad Sheet (m)	30	30	30	30
Number of GCPs	41181	26716	14894	11226
Acreage (ha)	339.7	160.5	394.9	64.1
Number of quad sheets per site (tying)	2	4	1	2
Quad sheet line-up sequence	West-East	All around	None	North-South

A total of 16 DEM datasets was generated to test how quad sheet generated DEM resolution would differ in elevation accuracy against precisely measured GPS GCPs. To do this, each random GCP dataset was placed on the

generated DEM(s) and the respective elevation record of each GCP was extracted from four different DEM datasets. Root mean square error (RMSE), mean error (ME), mean absolute error (MAE) and standard deviation

(STD) were calculated (Satge et al. 2016). They were then placed as input into Poudel and Cao (2013) approach to get a collective comparison result. The respective equations are as followed;

$$RMSE = \sqrt{\frac{\sum_{i=1}^n (x_i - y_i)^2}{n}} \quad (1)$$

$$ME = \frac{\sum_{i=1}^n (x_i - y_i)}{n} \quad (2)$$

$$MAE = \frac{\sum_{i=1}^n (|x_i - y_i|)}{n} \quad (3)$$

$$STD = \sqrt{\frac{1}{n-1} \sum_{i=1}^n [(x_i - y_i) - ME]^2} \quad (4)$$

where  $n$  is the number of GCPs,  $x$  is the measured elevation value (m) of the GCPs, while  $y$  is the elevation value extracted from DEM datasets.

$$R_i = 1 + \frac{(m-1)(S_i - S_{min})}{(S_{max} - S_{min})} \quad (5)$$

where  $R_i$  is the relative rank of the DEM datasets ( $i$ =purpose-cut, entire sheet, 10 m resampled and 30 m resampled),  $S_i$  is the basis of error values produced by each DEM dataset,  $S_{min}$  is the minimum value of  $S_i$  and  $S_{max}$  is the maximum value  $S_i$ ,  $m$  is the number of questioned DEM datasets. The equation produced a ranking score ranging from 1 to  $m$ . The remaining ranks were produced in real numbers between 1 and  $m$ .

### 3. Results and Discussion

As apparent from many studies based on both active and passive-sensor produced surface models, DEMs, the vertical accuracy performance of the end product is highly correlated with the land cover type and topographic uncertainties within the target during the

actual image acquisition (Shortridge 2006; Wechsler and Kroll 2006; Hebel and Purves 2009; Altunel 2018; Gonzalez and Rizzoli 2018;). Although smaller in caliber in terms of investment, coverage and know-how, aerial stereo image capture, today, is not entirely different from those of the satellite-based ones. Tested third generation quad coverage was produced from stereo captured color infrared air-photos, better defined as air-imagery. Imagery-wise, Yilmaz and Erdogan (2018) showed that RMSE of DEMs produced from new stereo air-photos captured at 45 cm ground sampling distance were  $\pm 2.51$  m,  $\pm 1.38$  m and  $\pm 1.3$  m within Uşak, Aksaray and Dogu Beyazit designated quad sheets. They said a 5 m GRID spaced DEM could very well be produced for the entire country, utilizing the new generation air-photos.

While the building blocks of the third and later version(s) country-wide quad sheets have been this strong, it is perfectly logical to think that elevation accuracy of the quad sheets must also be close to above mentioned figures.

Arac, Obrucak, Hasanli and Inceogaz reservoir areas extended across 435-1710 m, 580-1750 m, 555-1280 m and 680-1375 m elevations, respectively. In Arac, Hasanli and Inceogaz reservoirs, bulk of the slope facades was on sloping to very steep slopes, 5% < - <150%, whereas in Obrucak they were on moderately steep to very steep slopes, 15% < - <200% (FAO, 2006). These figures amounted to 93% of Arac reservoir, 99.6% of Hasanli reservoir, 95% of Inceogaz reservoir and 91% of Obrucak reservoir land area being on steep topography. This could be understood when water storage was intended. Random, but rather tightly, recorded GCPs allowed us to reach the results presented in this study.

RMSE-wise, the results were as followed: in Arac reservoir, purpose-cut and 10 m resampled DEMs were clearly similar and better than 30 m resampled DEM, entire sheet-based DEM produced the least favorable elevation performance; in Hasanli reservoir, the situation was the same, but the gain was marginal; Inceogaz reservoir, same results with better gain were observable and in Obrucak reservoir, same results again with more than 2 times better gain was obvious (Table 2).

**Table 2.** Ranking results based on individually calculated errors

Reservoir	Canopy Closure	Raster Making Method	RMSE	ME	MAE	STD	Total Rank	Overall Rank
Arac	Partial canopy (<30%)	Purpose-cut Quad Sheet	4.73 (1.00)	-0.77 (1.26)	3.42 (1.00)	4.67 (1.00)	4.26	1.07
		Entire Quadrangle Sheet	7.02 (4.00)	-1.08 (4.00)	5.13 (4.00)	6.94 (4.00)	16.00	4.00
		10 m Resampled Entire Quad Sheet	4.73 (1.00)	-0.74 (1.00)	3.42 (1.00)	4.67 (1.00)	4.00	1.00
		30 m Resampled Entire Quad Sheet	5.08 (1.46)	-0.77 (1.26)	3.70 (1.49)	5.02 (1.46)	5.68	1.42
Obrucak	Full canopy (>90%)	Purpose-cut Quad Sheet	6.77 (1.03)	0.07 (1.28)	4.95 (1.00)	6.67 (1.00)	4.31	1.00
		Entire Quadrangle Sheet	14.22 (4.00)	-0.56 (4.00)	10.6 (4.00)	14.21 (4.00)	16.00	4.00
		10 m Resampled Entire Quad Sheet	6.70 (1.00)	0.07 (1.28)	4.98 (1.02)	6.70 (1.01)	4.31	1.00
		30 m Resampled Entire Quad Sheet	7.54 (1.34)	0.02 (1.00)	5.54 (1.31)	7.54 (1.35)	4.99	1.18
Hasanli	Agriculture (no canopy)	Purpose-cut Quad Sheet	8.95 (1.32)	-0.14 (1.00)	4.25 (1.29)	8.91 (1.29)	4.78	1.00
		Entire Quadrangle Sheet	9.12 (4.00)	-0.19 (4.00)	4.53 (4.00)	9.07 (4.00)	16.00	4.00
		10 m Resampled Entire Quad Sheet	8.93 (1.00)	-0.18 (3.40)	4.22 (1.00)	8.90 (1.00)	6.40	1.43
		30 m Resampled Entire Quad Sheet	8.97 (1.63)	-0.18 (3.40)	4.30 (1.77)	8.92 (1.77)	8.34	1.95
Inceogaz	Agriculture (no canopy)	Purpose-cut Quad Sheet	2.58 (1.00)	0.81(4.00)	2.05 (1.00)	2.45 (1.00)	7.00	1.22
		Entire Quadrangle Sheet	5.49 (4.00)	0.08 (1.00)	4.04 (4.00)	5.49 (4.00)	13.00	4.00
		10 m Resampled Entire Quad Sheet	2.59 (1.01)	0.68 (3.47)	2.05 (1.00)	2.49 (1.04)	6.52	1.00
		30 m Resampled Entire Quad Sheet	2.94 (1.37)	0.61 (3.18)	2.32 (1.41)	2.88 (1.42)	7.38	1.40

Although the tendency in terms of elevation performance was towards purpose-cut and 10 m

resampled DEMs in all reservoirs, the results were not the same one another despite the fact that they were all

located within same geographical region. Location-wise, Incebogaz reservoir produced nearly the same results of Ozturk and Kocak (2007) and Yilmaz and Erdogan (2018), however the rest was worse. Even though their results were basing upon direct air photography photogrammetric calculations, it was nice to see that a secondary product fabricated using the same photography would match their original precision. Closed canopy in Obrucak reservoir must have been the reason that entire sheet-based DEM produced the overall worse RMSE, 14.2 m. Besides, this high RMSE was also triggered by the DEM acquired, combining four quad sheets together. Partial canopy closure in Arac reservoir did not tarnish the RMSE as much as that of Obrucak reservoir. Additionally, MAE values calculated over all questioned DEMs were the overall highest just like those of the RMSEs in the same reservoir.

In three out of four reservoirs, Arac, Obrucak, Incebogaz, purpose cutting the quad map clearly improved the DEM making performance of the quad maps compared to that of the entire sheet-based DEM. The gains were close to more than two times. However, the fact that no such improvement was observed in Hasanli reservoir convinced us that it would be impossible to get the same elevation precision from all quad maps. Nevertheless, it is possible to say that a less than 10 m quad specified contour interval precision can be achieved in the third generation 1:25000 Turkish quad maps.

Resampling clearly improved the DEM making performance of the quad maps. Both of the tested GRID spacing, 10 m and 30 m, were better in Arac, Obrucak and Incebogaz reservoirs, 10 m DEM being the better one in each, than the entire sheet-based DEM, but no noticeable difference was observed in Hasanli reservoir. Sorensen and Seibert (2007) showed that high resolution DEM provided better TWI distribution while Tan et al. (2015) said the most sensitive SWAT model DEM parameter was DEM resolution so higher the resolution better the outcome. Quad line-up sequence did not have any detectable effect over the calculated error values, however, although not certainly conclusive, it was obvious that quad tying worsened the error values.

The remaining error calculations, ME, MAE and STD behaved the same so detailed explanations were deemed unnecessary to elaborate, however they were nice additions to achieve the overall ranking results for each reservoir area.

#### 4. Conclusion

Quad, topographic, maps are important geographical assets of a country. Türkiye has long had a meticulous tradition of producing them systematically. Three nation-wide coverages have been released as of 2022, and they have been produced through photogrammetric calculations performed over tens of thousands of stereo-captured air photos. Topography is depicted via elevation embedded contour lines, which yielded the above results for the third and current coverage in four dam reservoirs in Kastamonu province. This study showed that a less than 10 m vertical accuracy can be attained directly from 1:25000 Turkish national quads,

and the results can be further improved if secondary products such as resampled DEMs, are produced.

#### References

- Altunel, A. O. (2018). Suitability of open-access elevation models for micro-scale watershed planning. *Environmental Monitoring and Assessment*, 190(512).
- Ardiansyah, P. O. D., & Yokoyama, R. (2002). DEM generation method from contour lines based on the steepest slope segment chain and monotone interpolation function. *ISPRS Journal of Photogrammetry and Remote Sensing*, 57(1-2), 86-101.
- Bildirici, O. I., Ustun, A., Selvi, Z. H., Abbak, A. R., & Bugdayci, I. (2009). Assessment of shuttle radar topography mission elevation data based on topographic maps in Turkey. *Cartography and Geographic Information Science*, 36(1), 95-104.
- Dagdas, S., & Bilge, S. (2015). Türkiye Cumhuriyetinin orman alanlarını gösteren ilk haritası ve orman varlığımız üzerine-(1926). *Orman Mühendisliği Dergisi*, 52, 28-36. (in Turkish)
- FAO. (2006). *Guidelines for soil description (Fourth edition)*. Food and Agriculture Organization of the United Nations, Rome.
- Gonzalez, C., & Rizzoli, P. (2018). Landcover-dependent assessment of the relative height accuracy in TanDEM-X DEM products. *IEEE Geoscience and Remote Sensing Letters*, 15(12), 1892-1896.
- Guth, P. L. (1999). Contour line "Ghosts" in USGS Level 2 DEMs. *Photometric Engineering and Remote Sensing*, 65(3), 289-296.
- Hebeler, F., & Purves, R. S. (2009). The influence of elevation uncertainty on derivation of topographic indices. *Geomorphology*, 111, 4-16.
- Ozturk, E., & Kocak, E. (2007). Farklı kaynaklardan değişik yöntem ve ölçeklerde üretilen sayısal yükseklik modellerinin doğruluk araştırması. *Harita Dergisi*, 73(137), 25-41. (in Turkish)
- Poudel, K. P., & Cao Q. V. (2013). Evaluation of methods to predict Weibull parameters for characterizing diameter distribution. *Forest Science*, 59(2), 243-252.
- Sahin, A., Caglayan, I., Buyuk, H., Karademir, H., Aksu, A., & Sahin, H. (2022). Türkiye'nin ilk orman planlama ünitesindeki teknik ve yapısal değişimlerin 100 yıllık değerlendirilmesi. *Turkish Journal of Forestry Research*, 9(1), 12-34. (in Turkish)
- Satge, F., Denezine, M., Pillco, R., Timouk, F., Pinel, S., Molina, J., Garnier J., Seyer, F., & Bonnet, M. (2016). Absolute and relative height-pixel accuracy of SRTM-GL1 over South American Andean Plateau. *ISPRS Journal of Photogrammetry and Remote Sensing*, 121, 157-166.
- Shortridge, A. (2006). Shuttle radar topography mission elevation data and its relationship to land cover. *Cartography and Geographic Information Science*, 33(1), 65-75.
- Simav, M., Yıldız, H., Cingöz, A., Sezen, E., Demirsoy, N. S., Akpınar, İ., ..., & Doğan, U. (2015, March 25-28). Türkiye Yükseklik Sisteminin Modernizasyonu ve Gravite Altyapısının İyileştirme Projesi. 15<sup>th</sup> Türkiye Harita Bilimsel ve Teknik Kurultayı, Ankara, Türkiye.

- Sorensen, R., & Seibert, J. (2007). Effect of DEM resolution on the calculation of topographical indices: TWI and its components. *Journal of Hydrology*, 347(1-2), 79-89.
- Tan, M. L., Ficklin, D. L., Dixob, B., Yusop, Z., & Chaplot, V. (2015). Impacts of DEM resolution, source and resampling technique on SWAT-simulated streamflow. *Applied Geography*, 63, 357-368.
- Taud, H., Parrot, J., & Alvarez, R. (1999). DEM generation by contour line dilation. *Computers and Geosciences*, 25(7), 775-783.
- Wechsler, S. P., & Kroll, C. N. (2006). Quantifying DEM uncertainty and its effect on topographic parameters. *Photogrammetric Engineering and Remote Sensing*, 72(9), 1081-1090.
- Yildirim, O., Mekik, C., & Bakici, S. (2011). TUSAGA-Aktif CORS-TR sisteminin Tapu ve Kadastro Genel Müdürlüğüne katkıları. *Jeodezi ve Jeoinformasyon Dergisi*, 104(2), 134-139.
- Yilmaz, A., & Erdoğan, M. (2018). Designing high resolution countrywide DEM for Turkey. *International Journal of Engineering and Geosciences*, 3(3), 98-107.



## 5<sup>th</sup> Intercontinental Geoinformation Days

igd.mersin.edu.tr



### Analysis of three hydro-meteorological parameters for the East Mediterranean Basin with GLDAS data

Cihangir Koycegiz<sup>\*1</sup>, Meral Buyukyildiz<sup>2</sup>

<sup>1,2</sup>Konya Technical University, Faculty of Engineering and Natural Sciences, Department of Civil Engineering, Konya, Türkiye

#### Keywords

GLDAS  
East Mediterranean  
Trend  
Spatial analysis  
Remote sensing

#### Abstract

In this study, precipitation, actual evapotranspiration and potential evapotranspiration in the East Mediterranean Basin were investigated temporally and spatially. The data of this study, in which January 2000-July 2022 was determined as the study period, was obtained from the Global Land Data Assimilation System (GLDAS). According to the results obtained, it was determined that precipitation has a decreasing slope and evapotranspiration parameters have an increasing slope during the study period. In addition, it has been determined that the basin has spatial variability in terms of the investigated hydro-meteorological parameters.

#### 1. Introduction

Hydro-climatological difficulties that occur with global warming cause many disasters all over the world (IPCC 2021). However, some regions are more affected by this phenomenon than others regions. The Mediterranean Basin comes first among these regions (Talu and Özütlü 2011). In addition to its socio-economic importance, its historical background is one of the reasons why it has been preferred by many people as a settlement for years. Along with drought, deteriorating ecosystems damage biodiversity, leading to the gradual loss of natural riches. In geographies with a sensitive hydrological balance, precipitation is one of the important water inputs of the basin. In addition, evaluation together with evapotranspiration is frequently used in the comprehensive examination of precipitation.

Depending on the development of remote sensing and land cover models, global observations can be made with the data provided by many data sets. The Global Land Data Assimilation System (GLDAS) is one of these data sets (Rodell et al. 2004). There are many studies in the literature using these data sets (Awange et al. 2014; Lv et al. 2017; Mo et al. 2016). Studies are using hydro-meteorological analysis tools related to the East Mediterranean Basin, which is located within the borders of Turkey, which is determined as the study area. Oğuz et al. (2017) conducted a drought analysis for

the East Mediterranean Basin using ERA-Interim data. It was stated that there was variation in precipitation in the results obtained. They also reported that drought had the most negative impact on crop production. Özfıdaner et al. (2015) calculated the streamflow drought index from the streamflow data of the flow observation station no 1712 in the East Mediterranean Basin. According to the results obtained, they determined that the drought had an effect during the 1967-2007 periods. Koçyiğit et al. (2021) performed a flood risk analysis for the East Mediterranean Basin based on the river morphology. According to the results obtained, it was stated that the flood risk is located along the basin, with variability depending on the size of the sub-basin. There are other studies in which drought analysis is done for the East Mediterranean Basin (Altın and Altın 2021; Simsek 2021).

According to the information obtained from the literature review, no study was found in which the GLDAS dataset was used in the analysis of hydrological parameters for the East Mediterranean Basin. From this point of view, it is aimed to examine the three hydro-meteorological parameters (precipitation, actual evapotranspiration and potential evapotranspiration) obtained from the GLDAS dataset for the East Mediterranean Basin. Spatial and temporal averages of the basin were obtained from the raw data obtained from GLDAS. In addition, a linear trend is applied spatially.

#### \* Corresponding Author

(ckoycegiz@ktun.edu.tr) ORCID ID 0000 – 0002 – 0510 – 1164  
(mbuyukyildiz@ktun.edu.tr) ORCID ID 0000 – 0003 – 1426 – 3314

#### Cite this study

Koycegiz C & Buyukyildiz M (2022). Analysis of three hydro-meteorological parameters for the East Mediterranean Basin with GLDAS data. 5<sup>th</sup> Intercontinental Geoinformation Days (IGD), 141-144, Netra, India

## 2. Material and Method

### 2.1. Study area and data

The East Mediterranean Basin, determined as the study area, is one of Turkey's 25 main basins with a surface area of 21800 km<sup>2</sup>. It constitutes 3% of Turkey's surface area. The East Mediterranean Basin is located between the coordinates 36°00'-37°28'N and 32°06'-35°09'E (Fig. 1). The altitude of the basin mainly varies between 0-2000 m. However, the altitude of the basin rises above 3000 m on the ridges of the Taurus Mountains (Altin and Altin 2021). The drainage area is bounded by the Sedir River on the west and the Tarsus River on the east. The study area, which has a typical Mediterranean climate, is a flood-risk basin with sharp slopes. The summers are hot and the winters are experienced as the months when precipitation occurs predominantly. In the mountainous parts of the basin, the climate is shifting from the Mediterranean climate to the continental climate. Annual average precipitation is 745 mm (Altin and Altin 2021). Agricultural areas of the basin are evaluated in the crop production class with 63%. Other areas consist of areas used for vegetable and fruit production, especially olive groves (Koçyiğit et al. 2021).



**Figure 1.** Location map of the East Mediterranean Basin

GLDAS, a project that aims to bring together the information obtained as a result of integrating satellite and observations with advanced land surface modeling techniques, provides data with 0.25° spatial resolution (Beaudoin et al. 2021; Rodell et al. 2004). Aiming to provide high-resolution data, GLDAS supports water resources, climate and weather research and global land surface analysis studies with the data it provides. GLDAS brings together the results of Noah, Variable Infiltration Capacity (VIC), Mosaic, Common Land Model (CLM) and Catchment land surface models. Many hydro-meteorological parameters are available from the GLDAS dataset. Within the scope of this study, data were obtained from GLDAS for precipitation, actual evapotranspiration and potential evapotranspiration parameters for the 2000 January-2022 July period.

### 2.2. Simple Linear Regression Model (SLRM)

Within the scope of the study, Simple Linear Regression Model (SLRM) was used to determine the

monotonic trends of spatially distributed hydro-meteorological parameters. This model, which is frequently used in hydrological studies, provides a general view of the entire time series. In addition, it gives insight into the general behavior of the determined study area in terms of ease of application. SLRM is applied by determining the slope and constant coefficients of the linear equation including the dependent and independent variables. The slope of the equation contains trend information about the overall behavior of the data set. Accordingly, depending on the studied parameter and period, if the slope value of the SLRM is close to zero, it is stated that the parameter has a constant slope, if it is positive, it has an increasing slope, and if it is negative, it has a decreasing slope. Within the scope of the study, SLRM was applied not only to the time series of the determined parameters but also to the spatially distributed maps. Each grid (0.25°x0.25°) contains a time series of that area. When SLRM is applied for all grids in the study area and the slopes obtained are mapped, spatially scattered trend information is obtained. There are many studies in the literature in which SLRM is used in spatial and temporal analyzes of hydro-meteorological parameters (Zhang et al. 2017; Patel et al. 2016; Sriram and Rashmi 2014; Dimitriadou and Nikolakopoulos 2022; Mogaji and Lim 2020; Zhang et al. 2018).

## 3. Results

For the period January 2000-July 2022, the spatial average of the precipitation (P), actual evapotranspiration (aET) and potential evapotranspiration (PET) parameters for the East Mediterranean Basin obtained from GLDAS was obtained, and the time series was obtained. The obtained time series is given in Fig. 2. Accordingly, it is observed that precipitation has a negative slope and evapotranspiration parameters have a positive slope. In addition, precipitation in winter and evapotranspiration reach peak values in summer.

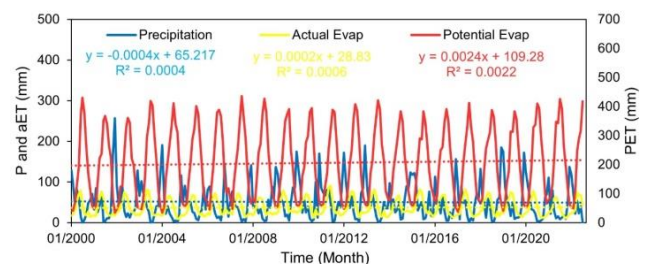


**Figure 2.** Average time series of P, aET and PET for East Mediterranean Basin

The difference between precipitation and evapotranspiration is frequently used in the interpretation of hydro-meteorological parameters. In practice, it is aimed to interpret the net water entering the basin. In addition, the ratio of the actual evapotranspiration to the potential indicates how close the actual evaporation and transpiration are to the basin potential. P-aET and aET/PET time series were obtained from the time series obtained by taking the spatial averages of the East Mediterranean Basin. These

time series are given in Fig. 3. Here, the decreasing slope of the P-aET is an indication that the net water inflow of the basin may be under threat. P-aET reached low values in the last years of the study period. When aET/PET ratios are examined, although an increasing trend is observed in recent years, the slope of the study period is very close to zero.

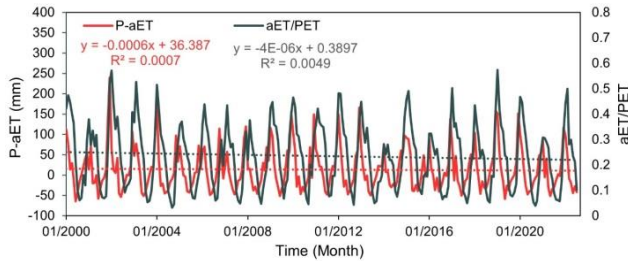


**Figure 3.** Monthly average P-aET and aET/PET time series for East Mediterranean Basin

In addition to examining the time series, hydro-meteorological analysis of the basin was made with the help of spatially distributed maps. In Fig. 4, temporal averaged maps for the three parameters are given. It is observed that precipitation reaches the highest values (690 mm) in the southwestern parts of the basin. The lowest precipitation (566 mm) was detected on the southeast coast of the basin. When the evapotranspiration parameters were examined, it was determined that there were higher values in the coastline compared to the interior. Maximum values of 572 mm for actual evapotranspiration and about 3000 mm for potential evapotranspiration were observed.

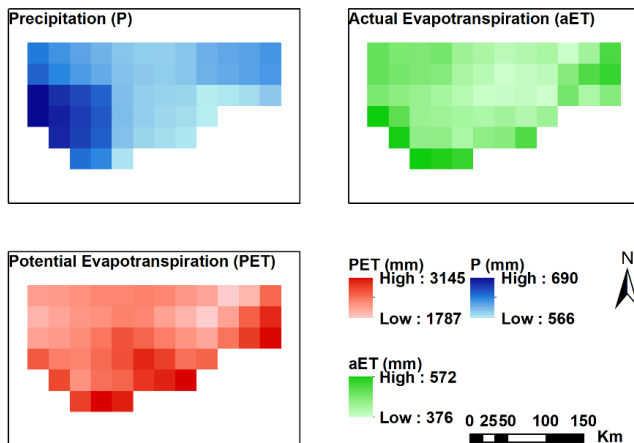


**Figure 4.** Study period average for P, aET and PET

The temporal averaged maps of P-aET and aET/PET are given in Fig. 5. According to Fig. 5, net precipitation has the highest values in the western parts of the basin. Due to the high evapotranspiration values on the coastline, net precipitation has been relatively low in these areas. Net precipitation decreases from west to east of the basin. When the aET/PET ratio is examined, it is quite interesting that extreme values were observed at the western and eastern borders of the basin. Low rates were determined in the central parts of the basin. The highest rate is 0.24 while the lowest rate is 0.14.

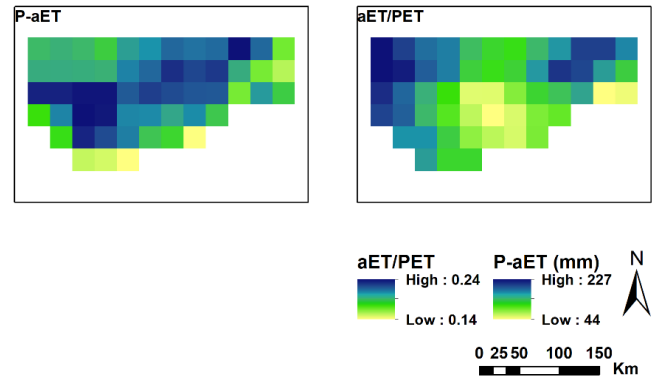


**Figure 5.** P-aET and aET/PET maps for East Mediterranean Basin

Spatial distributed linear trend maps for the three parameters (P, aET and PET) determined within the scope of the study are given in Fig. 6. It is quite remarkable that precipitation has a high linear trend along a steep grid series from south to north. The highest increasing slope of precipitation in the basin starts from the southernmost grids and progresses to the inner parts. However, the western boundary of the basin has a decreasing slope. When the actual evapotranspiration is examined, there is an increasing slope in the inner parts of the basin in the north. However, the central inner sections have increasing slopes in the potential evapotranspiration parameter. Accordingly, the western and eastern borders of the basin and the middle and coastline sections have different hydro-meteorological characteristics.

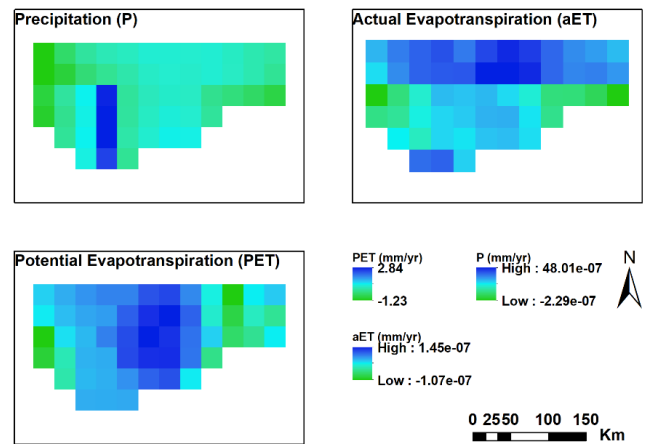


**Figure 6.** Linear trend map for P, aET and PET

#### 4. Conclusion

Within the scope of this study, the data obtained from the GLDAS data set for the East Mediterranean Basin were examined. These data are limited by precipitation, actual evapotranspiration and potential evapotranspiration parameters. The period of January 2000-July 2022 has been determined as the study period. The obtained data were analyzed spatially and temporally. In addition, linear slopes were investigated throughout the study period.

In light of the research findings, it was determined that evapotranspiration increased and precipitation decreased during the study period. If this trend

continues, it is thought that the significant decrease in net precipitation in the basin may lead to droughts. It has been determined that the hydro-meteorological parameters examined spatially differ in the coastline and inland areas. The increasing continentality as it moves toward the interior reduces evapotranspiration along with precipitation. It is thought that evapotranspiration values on the coastline reach high values with the presence of water depending on the temperature. It is quite remarkable that the potential evapotranspiration has an increasing slope in the middle parts, while the actual evapotranspiration increases in the north of the basin.

It is thought that examining the Eastern Mediterranean Basin by dividing it into temporal sub-periods can provide information that monotonic slopes do not provide, to provide an idea for future studies. In addition, it was considered that it would be very important to examine the spatial variability at higher resolutions by using the station data.

## References

- Altin, T. B., & Altin, B. N. (2021). Response of hydrological drought to meteorological drought in the eastern Mediterranean Basin of Turkey. *Journal of Arid Land*, 13, s. 470-486.
- Awange, J. L., Gebremichael, M., Forootan, E., Wakbulcho, G., Anyah, R., Ferreira, V. G., & Alemayehu, T. (2014). Characterization of Ethiopian mega hydrogeological regimes using GRACE, TRMM and GLDAS datasets. *Advances in Water Resources*, 64-78.
- Beaudoing, H., & Loeser, C. (2021). Readme Document for NASA GLDAS Version 2 Data Products. [https://hydro1.gesdisc.eosdis.nasa.gov/data/GLDAS/GLDAS\\_NOAH025\\_M.2.1/doc/README\\_GLDAS2.pdf](https://hydro1.gesdisc.eosdis.nasa.gov/data/GLDAS/GLDAS_NOAH025_M.2.1/doc/README_GLDAS2.pdf) adresinden alındı
- Dimitriadou, S., & Nikolakopoulos, K. G. (2022). Multiple Linear Regression Models with Limited Data for the Prediction of Reference Evapotranspiration of the Peloponnese, Greece. *Hydrology*, 9(7), s. 124.
- IPCC. (2021). *Climate Change 2021: The Physical Science Basis*. Contribution of Working Group I to the Sixth. Cambridge University Press. <https://www.ipcc.ch/report/ar6/wg1/> adresinden alındı
- Koçyiğit, M. B., Akay, H., & Babaiban, E. (2021). Evaluation of morphometric analysis of flash flood potential of Eastern Mediterranean Basin using principle component analysis. *Journal of the Faculty of Engineering and Architecture of Gazi University*, 36 (3), s. 1669-1685.
- Lv, M., Ma, Z., Yuan, X., Lv, M., Li, M., & Zheng, Z. (2017). Water budget closure based on GRACE measurements and reconstructed evapotranspiration using GLDAS and water use data for two large densely-populated mid-latitude basins. *Journal of Hydrology*, 547, 585-599. doi:<https://doi.org/10.1016/j.jhydrol.2017.02.027>
- Mo, X., Wu, J., Wang, Q., & Zhou, H. (2016). Variations in water storage in China over recent decade from GRACE Observations and GLDAS. *Nat. Hazards Earth Syst. Sci. Discuss.*, 3251-2015.
- Mogaji, K. A., & Lim, H. S. (2020). A GIS-based linear regression modeling approach to assess the impact of geologic rock types on groundwater recharge and its hydrological implication. *Modeling Earth Systems and Environment*, 6, s. 183-199.
- Oğuz, K., Pekin, M. A., Gürkan, H., Oğuz, E., & Coşkun, M. (2017). Analyses of drought in Eastern Mediterranean basin with era-interim data. *Anadolu Journal of Agricultural Sciences*, 32 (2), s. 229 - 236.
- Özfidaner, M., Topaloglu, F., Baydar, A., & Ucan, D. S. (2015). Hydrological Drought Analysis of Monthly Streamflows in Doğu Akdeniz Basin. 4. Uluslararası Katılımlı Toprak ve Su Kaynakları Kongresi. Kahramanmaraş.
- Patel, S., Hardaha, M. K., Seetpal, M. K., & Madankar, K. K. (2016). Multiple Linear Regression Model for Stream Flow Estimation of Wainganga River. *American Journal of Water Science and Engineering*, 1-5. doi:10.11648/j.ajwse.20160201.11
- Rodell, M., P.R. Houser, U., Jambor, J., Gottschalck, K., Mitchell, C., Meng, K., . . . Toll, D. (2004). The Global Land Data Assimilation System. *Bull. Amer. Meteor. Soc.*, 85, 381-394. doi:10.1175/BAMS-85-3-381
- Simsek, O. (2021). Hydrological drought analysis of Mediterranean basins, Turkey. *Arabian Journal of Geosciences*, 14, s. 2136.
- Sriram, A. V., & Rashmi, C. N. (2014). Estimation of Potential Evapotranspiration by Multiple Linear Regression Method. *IOSR Journal of Mechanical and Civil Engineering*, 65-70. doi:10.9790/1684-11246570
- Talu, N., & Özüt, H. (2011). *Strategic Steps to Adapt to Climate Change in Seyhan River Basin*. Ankara: T.R. Ministry of Environment and Urbanization General Directorate of Environmental Management Department of Climate Change.
- Zhang, J., Zhang, Y., Song, J., Cheng, L., Gan, R., Shi, X., . . . Zhao, P. (2017). Comparing hydrological modelling, linear and multilevel regression approaches for predicting baseflow index for 596 catchments across Australia. *Hydrol. Earth Syst. Sci. Discuss.* doi:<https://doi.org/10.5194/hess-2017-737>
- Zhang, Y., Chiew, F. H., Li, M., & Post, D. (2018). Predicting Runoff Signatures Using Regression and Hydrological Modeling Approaches. *Water Resources Research*, 54 (10), s. 7859-7878.



## 5<sup>th</sup> Intercontinental Geoinformation Days

igd.mersin.edu.tr



### Classification of Jilin-1 GP01 hyperspectral image using machine learning techniques with explainable artificial intelligence

Elif Ozlem Yilmaz\*<sup>1</sup>, Taskin Kavzoglu <sup>1</sup>

<sup>1</sup>Gebze Technical University, Faculty of Engineering, Department of Geomatics Engineering, Kocaeli, Türkiye

#### Keywords

Machine learning  
Hyperspectral image  
Explainable AI  
Image classification  
Jilin-1 GP01

#### Abstract

Machine learning (ML) techniques have been significant potential for the image classification; however, they behave as a black box because of the use of unknown descriptors in model construction. Thus, explainable Artificial Intelligence can assist with comprehending the prediction process of a model. In this study, XgBoost and Random Forest were utilized to generate LULC maps for the Özbağ district of Krişehir, a highly forested through the valley, using Jilin-1 GP01 hyperspectral image. Accordingly, the overall accuracies of thematic maps produced by XgBoost and Random Forest were estimated as 93.17% and 91.98%, respectively. Moreover, the Shapley additive explanations (SHAP) technique is employed to understand the output of the models. After SHAP analysis of the ML models, the feature importance of each spectral band was determined. Therefore, given the trained by both algorithms, Band 7 was determined the most important of the hyperspectral bands used in this study. According to the Shapley values, band 5 in the Xgboost model and Band 7 in the random forest model are efficient in class-based evaluations for identifying the bare soil class with the highest F-score value. Although the differences were obtained in the SHAP analysis according to some spectral bands since the working principles of the classification algorithms are different.

#### 1. Introduction

Hyperspectral imaging technology has expanded, thanks to its extensive variety of applications and specialties. It provides digital images composed of tens/hundreds of spectral bands which has a tiny range (Kavzoglu and Yilmaz 2022). With the ability to recognize short spectral ranges, hyperspectral images have commonly used widespread applications in numerous fields (Moharram and Sundaram 2022). Particularly, HSI has been utilized extensively in agricultural environmental studies (i.e., land use land cover (LULC) mapping), biology and mineral exploration. Each pixel in HSI relies on characteristics from a small area surrounding the pixel, rather than attributes directly associated with the pixel itself (Liu et al. 2019).

Many techniques used in the early stages of HSI analysis research focused on using the spectral signatures of hyperspectral images for classification. For this purpose, many pixel-wise classification techniques (e.g., Support Vector Machine, Maximum Likelihood, Decision Tree, Random Forest, and eXtreme Gradient Boosting-XgBoost) have been employed for the classification of HSIs (Sothe et al.2020). Furthermore, these techniques have demonstrated outstanding

success in the classification of hyperspectral images according to the recent studies (Gore et al. 2021; Moharram and Sundaram 2022).

Because of the variability of band spectrum, hyperspectral image classification has been recognized in the literature as a complex issue. Consequently, machine learning (ML) approaches have been developed as a useful method for analyzing hyperspectral images. However, ML approaches operate as black boxes despite their considerable capacity in this area (Arrieta et al. 2020).

Artificial intelligence (AI), including machine learning (ML) techniques, can be employed to construct powerful models that provide remarkable prediction or classification performance in a massive variety of difficult areas. Nevertheless, they often have a complex system (i.e., black-box structure), which may impair to ability to comprehend the data. At this point, ML models with explainable AI approaches can be rendered more transparent and interpretable, and consequently their inferences can be helped generate to improve model performance (Arrieta et al. 2020). For instance, SHAP (SHapley Additive exPlanations) algorithm is a commonly employed approach for interpreting black box models (Kavzoglu et al. 2021).

\* Corresponding Author

(eoyilmaz@gtu.edu.tr) ORCID ID 0000-0002-6853-2148  
(kavzoglu@gtu.edu.tr) ORCID ID 0000-0002-9779-3443

Cite this study

Yilmaz EO & Kavzoglu T (2022). Classification of Jilin-1 GP01 hyperspectral image using machine learning techniques with explainable artificial intelligence. 5<sup>th</sup> Intercontinental Geoinformation Days (IGD), 145-148, Netra, India

The aim of this work is to evaluate the performance of XgBoost, and Random Forest classifiers using Jilin-1 GP01 hyperspectral image. Besides, this study demonstrates how to interpret the predictions of the aforementioned classification models using an explainable AI method, namely SHAP.

## 2. Methodology

### 2.1. XgBoost Algorithm

XgBoost is a gradient-boosted decision tree method, which consecutive decision trees are generated (Chen and Guestrin 2016). The weights are significant parameters because they play a crucial role in this algorithm. In other words, all independent variables that are supplied into the decision tree that used predict outcomes are allocated weights. The weight of variables for which the tree produced incorrect predictions is enhanced, and these variables are then supplied to a second decision tree. Thus, the ensemble of these independent classifiers yields a robust and more accurate model.

### 2.2. Random Forest Algorithm

Random Forest has become a popular ensemble learning technique for developing predict rules based on multiple types of characteristics without initial assumptions about the relationship amongst dependent features. The success of the algorithm depends on how the decision trees are generated. This technique includes two main steps. In the first step, each tree is created using random samples. Also, whole trees are the same size although being trained in different ways. Two-thirds of the training data is used to train the trees and one-third to evaluate the model. It maintains tree strength while reducing correlation. The second stage uses predictor variables to separate all tree nodes. It is crucial to select few features with enough predictive capacity and minimal correlation (Breiman 2001).

### 2.3. Interpretation of ML Model

The complex structure of ML algorithms (i.e., XgBoost and Random Forest) makes them difficult to explain and evaluate their outcomes. Explaining model outputs helps to identify the features that affect the model, providing more reliable and robust prediction performance. For this aim, SHapley Additive exPlanations (SHAP) method was utilized to explain and interpret ML model outputs (Lundberg and Lee 2017). It is one of the approaches used for explainable artificial intelligence and is based on the game-theory explaining the performance of a machine learning model. It utilizes the strategy of additive feature importance, which the output of model is stated as the linear addition of parameters of the model input to construct an interpretable method (Kavzoglu et al. 2021).

Tree SHAP is a quick and accurate method for computing SHAP values for tree-based approach including ensemble methods, considering a variety of possible feature dependence assumptions. In this manner, two tree-based ML algorithms (i.e., XGboost and

Random Forest) were employed for HSI classification in this study. In addition, Tree SHAP was implemented for explaining the model predictions considering the tree-based architecture of these algorithms.

## 3. Study Area and Dataset

The Özbağ district of Kirsehir province in Turkey was chosen as the study area (Fig.1.). The Jilin1-GP01 hyperspectral image of June 30, 2021, was used to produce a thematic map of the study area that is a highly forested through the valley.



**Figure 1.** The study area of Kirsehir in Turkey.

Jilin1-GP01, launched in 2019, is a satellite system with a 12-bit radiometric resolution capable of hyperspectral sensing. The image has three spatial resolutions (5m, 10m and 20m) and consist of a total of 20 spectral bands, including one panchromatic band (Table 1.).

**Table 1.** Technical specifications of the hyperspectral Jilin1-GP01 satellite image.

Band No	Spectral Range (nm)	Spatial Reso. (m)	Band No	Spectral Range (nm)	Spatial Reso. (m)
B_0	450-800	>5	B_10	698.75-718.75	10
B_01	403-423	5	B_11	732.5-747.5	10
B_02	433-453	5	B_12	773-793	10
B_03	450-515	5	B_13	855-875	20
B_04	525-600	5	B_14	660-670	20
B_05	630-680	5	B_15	677.5-685	20
B_06	784.5-899.5	5	B_16	750-757.5	20
B_07	485-495	10	B_17	758.75-762.5	20
B_08	615-625	10	B_18	935-955	20
B_09	650-680	10	B_19	1000-1040	20

It should be stated that all bands of Jilin-1 GP01 image atmospherically and geometrically corrected before image processing stage. The Gram-Schmidt pansharpener technique was used to resample 10- and 20-m spatial resolution bands to a 5 m resolution.

According to characteristics of study area, five LULC classes, including impervious surface, soil bare, rock, forest, and vegetation, were used in the classification process to generate thematic maps. In order to implement supervised classifications, the ground-reference dataset was splitted into training and testing

samples. To be more specific, 500 pixels from each LULC class were collected for the training stage while 300 pixels were gathered for the testing stage. Furthermore, the classification application was executed employing Jupyter Notebook with the Python programming language.

#### 4. Results

In this study, pixel-based XgBoost and Random Forest classifiers were used to produce thematic maps. The thematic maps produced with XgBoost and Random Forest classification algorithms are shown in Figure 2.

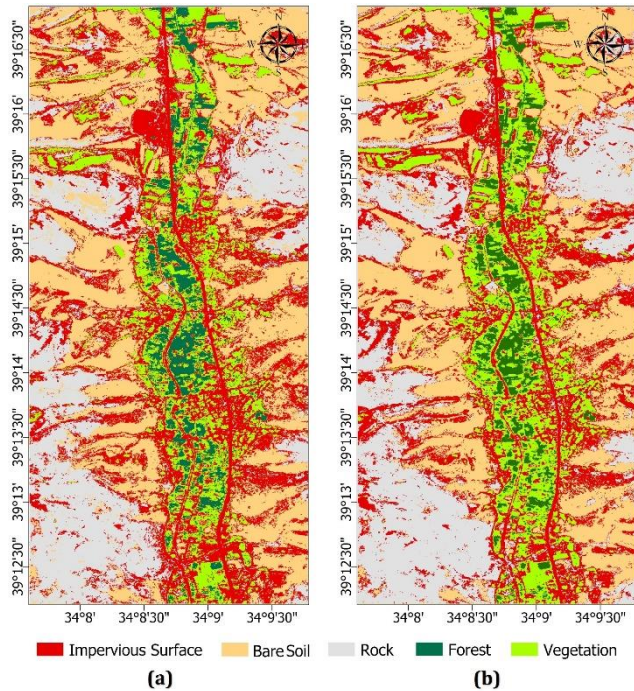


**Figure 2.** Thematic maps generated with XgBoost classifier (a) and Random Forest classifier (b)

At the end of the classification stage, confusion matrices were estimated (Tab. 3). It should be noted that, equal number of pixels (300 pixels) per LULC class were used in generation of confusion matrices to avoid bias between classes.

The overall accuracies and Kappa coefficients were estimated to analyze the accuracy of the thematic maps. In accordance with this purpose, the overall accuracies of thematic maps produced by XgBoost and Random Forest were estimated as 93.17% and 91.98%, respectively. In addition, the Kappa coefficients were determined as 0.91 and 0.90 for both classifiers (Tab. 3). Besides, F-score values were generated to assess the predicted accuracy of LULC class-specific. The highest F-score values (97.10% with XgBoost classifier and 96.20% with Random Forest classifier) were computed for the bare soil class in two thematic maps, according to Table 3. On the other hand, lowest F-Score values (87.60% with XgBoost classifier and 85.90% with Random Forest classifier) for both thematic maps were calculated for vegetation class. The confusion matrix indicates that the vegetation class is particularly mixed with the forest class. The primary reason of this situation could be

related to spectrally similar characteristics of vegetation and forest class.

**Table 3.** Predictive performances of XgBoost and Random Forest methods

LULC Class	XgBoost (%)	Random Forest (%)
Impervious Surface	93.30	91.25
Bare Soil	97.10	96.20
Rock	95.55	93.00
Forest	92.30	92.30
Vegetation	87.60	85.90
Overall Acc. (%)	93.17	91.98
Kappa Coef.	0.91	0.90

Combining local interpretations from the SHAP tree explanation function, the SHAP graph scored the most significant spectral bands by importance. In other words, The SHAP method forecasts the estimated marginal contribution of each characteristic. According to Figures 3 and 4, the y-axis shows spectral bands in the hyperspectral dataset, the x-axis depicts the estimated Shapley value, and the color (i.e., blue, purple, pink, orange and green) shows how much of an effect the spectral bands have on the LULC classes.

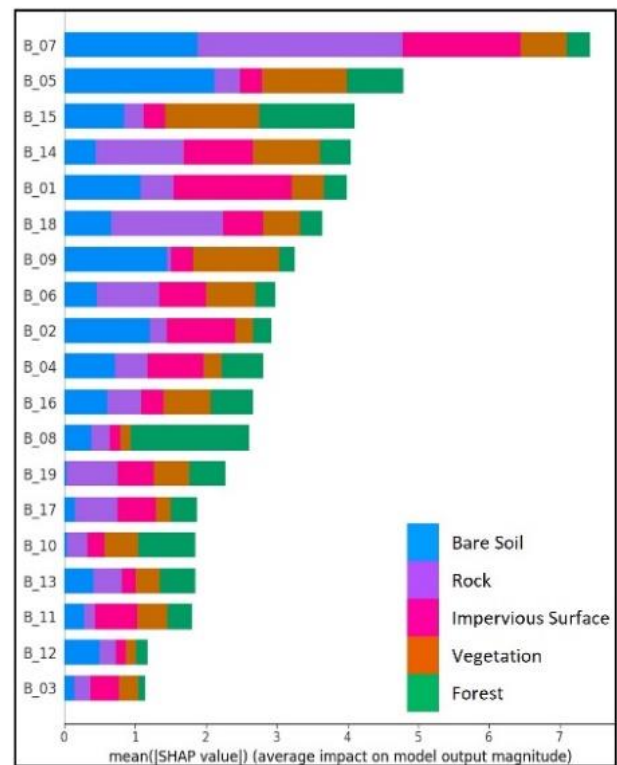


**Figure 3.** SHAP chart illustrating the feature importances for XgBoost model

The effect of Band 7 of Jilin-1 GP01 image exhibited a more considerable effect on the model output than the other spectral bands, demonstrating that changes to this band can have a significant effect on the outcomes for both ML classifier (Fig. 3). Besides, Band 7 contributes more to the bare soil, rock, and impervious surface classes than the others. On the other hand, it can be said that the first 3 spectral bands affecting the model in the SHAP analysis are located in the visible region. In the

trained Xgboost model, the effect of Band 5 and Band 7 on identifying the bare soil and rock class, respectively, was found to be remarkably considerable.

When Figures 3 and 4 are compared, there are several similarities; yet there are also a few differences. In the SHAP graph for Random Forest, the feature importance of the first four spectral bands is close (Fig. 4.). Furthermore, as in the other SHAP graph for XgBoost classifier, it is observed that the bare soil class is highly affected by Band 7 (Fig. 4.). The difference between the SHAP graphs can be attributed to that XgBoost and Random Forest classifier algorithms work with different principles during hyperspectral classification.

When both graphs were analyzed, the common bands with low significance were identified as 11, 12 and 13 Band. It was observed that the study area contains bare soil and rock classes and infrared bands affect the classifier less in the detection of them.

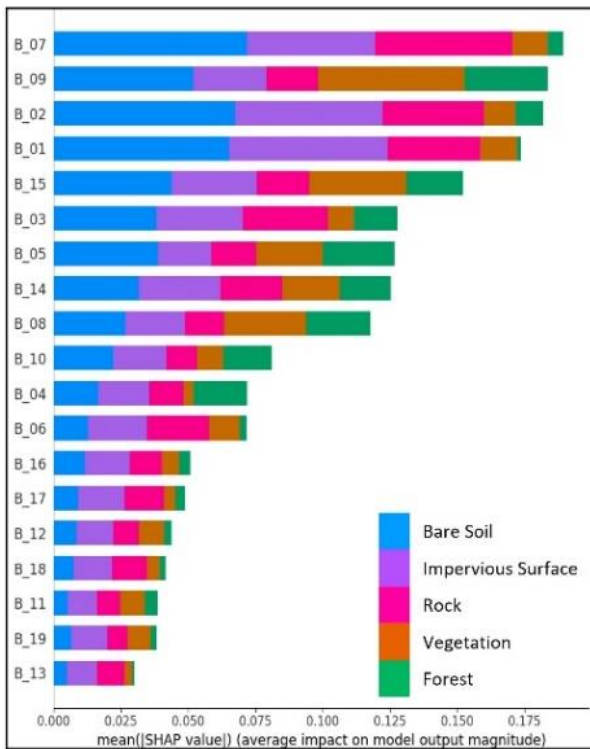


**Figure 4.** SHAP chart illustrating the feature importance for Random Forest model

## 5. Conclusion

ML approaches which have been commonly implemented in remote sensing applications were used to create LULC maps in this study. In detailed, it can be said that the performance of XgBoost classifier increased overall accuracy by approximately 1%, compared to performance of Random Forest classifier. On the other hand, to examine the performance of the ML algorithms in detail, that is to say, to understand the actions taken by the model and the non-linear relations that exist inside the model, explainable AI approaches are required. Therefore, the SHAP technique was used to interpret the classifier outputs and analyze the importance of spectral bands. Hereby, predicated on the trained by both algorithms, Band 7 was considered the most significant

among the other spectral bands utilized in this study. Consequently, SHAP allows in-depth analysis of hyperspectral data and can guide in selecting the appropriate spectral bands and AI model for LULC classification.

## References

- Arrieta A. B., Díaz-Rodríguez, N., Ser, J. D., Bennetot, A., Tabik, A., Barbado, A., Garcia, S., Gil-Lopez, S., Molina, D., Benjamins, R., Chatila, R., & Herrera, F. (2020). Explainable Artificial Intelligence (XAI): Concepts, taxonomies, opportunities and challenges toward responsible AI, *Information Fusion*, 58, 82-115. <https://doi.org/10.1016/j.inffus.2019.12.012>.
- Breiman, L. (2001) Random Forests. *Machine Learning*, 45, 5-32. <https://doi.org/10.1023/A:1010933404324>
- Chen, T., & Guestrin, C. (2016) Xgboost: A scalable tree boosting system. In *Proceedings of the 22nd ACM SIGKDD International Conference on Knowledge Discovery and Data Mining*, 785-794. <https://doi.org/10.1145/2939672.2939785>
- Gore, R. W., Mishra, A. D., Deshmukh, R. R. (2021). Hyperspectral Image Classification using Machine Learning, 261, 265. <https://doi.org/10.1145/3484824.3484883>
- Kavzoglu, T., Teke, A., & Yilmaz ,E. O. (2021). Shared block-based ensemble deep learning for shallow landslide susceptibility mapping. *Remote Sensing*, 13(25), 4776. <https://doi.org/10.3390/rs13234776>
- Kavzoglu, T. & Yilmaz E., O. (2022). Analysis of patch and sample size effects for 2D-3D CNN models using multiplatform dataset: hyperspectral image classification of ROSIS and Jilin-1 GP01 imagery. *Turkish Journal of Electrical Engineering and Computer Sciences*, 30(6), 2124-2144. <https://doi.org/10.55730/1300-0632.3929>
- Liu, S., Marinelli, D., Bruzzone L., & Bovolo, F. (2019). A review of change detection in multitemporal hyperspectral images: Current techniques, applications, and challenges. *IEEE Geoscience and Remote Sensing Magazine*, 7(2), 140-158. <https://doi.org/10.1109/MGRS.2019.2898520>.
- Lundberg, S. M. & Lee, S. (2017). A unified approach to interpreting model predictions. *Advances in Neural Information Processing Systems*, 2017,47-4775.
- Moharram, M. A. & Sundaram, D. M. (2022). Dimensionality reduction strategies for land use land cover classification based on airborne hyperspectral imagery: a survey. *Environmental Science and Pollution Research*. <https://doi.org/10.1007/s11356-022-24202-2>
- Sothe, C., De Almeida, C. M., Schimalski, M. B., La Rosa, L. E. C., Castro, J. D. B., Feitosa, R. Q., Dalponte, M., Lima, C. L., Liesenberg, V., Miyoshi G. T., & Tommaselli A. M. G. (2020) Comparative performance of convolutional neural network weighted and conventional support vector machine and random forest for classifying tree species using hyperspectral and photogrammetric data. *GIScience & Remote Sensing*, 57(3), 369-394. <https://doi.org/10.1080/15481603.2020.1712102>



## 5<sup>th</sup> Intercontinental Geoinformation Days

igd.mersin.edu.tr



### Measuring changes in spatio-temporal LST variations and evaluating their relationship between greenhouses and their surroundings

Serdar Selim<sup>\*1</sup>, Buket Eyiletlen<sup>2</sup>

<sup>1</sup>Akdeniz University, Faculty of Science, Department of Space Sciences and Technologies, Antalya, Türkiye

<sup>2</sup>Akdeniz University, Institute of Science, Department of Remote Sensing and Geographical Information Systems, Antalya, Türkiye

#### Keywords

Greenhouse  
LST  
Land cover  
Thermal Infrared  
Remote sensing

#### Abstract

Thermal infrared (TIR), frequently used in remote sensing studies, allows the analysis, modeling, collection, and evaluation of environmental parameters. Land surface temperature (LST) algorithms are used to detect urban heat islands and, accordingly, to identify concrete indicators of global warming resulting from urban heat islands. In this study, the land surface temperature change in agricultural land use where greenhouses occupy a dense area was determined in a time-dependent manner. To provide a suitable growing environment for the development of plants in greenhouses, the environment inside the greenhouse is kept warmer than its surroundings, especially in the winter. The investigation of the effect of this internal temperature on the external surface temperature constituted the motivation for this study. For this purpose, the determination and analysis of the land surface temperature change were carried out in the relevant region. The study material consists of agricultural fields containing greenhouses in the Kumluca district of Antalya province obtained from Landsat 8 satellite images between 2013-2019. LST analyzes were performed on images taken at 3-year intervals, and the results were compared. The results demonstrated that the surface temperatures of the greenhouses increased by about 1°C in the relevant period. Moreover, similar temperature increases were observed in other land cover classes. As a result, it has been concluded that while the surface temperatures of the greenhouses were generally lower than the building surface temperatures, they were higher than the green cover surface temperatures.

#### 1. Introduction

Land surface temperature (LST) is of fundamental importance for ecological and climatic studies (Liu and Wang 2018). LST values are an important indicator for monitoring vegetation condition, and evaluating ecological demands of agricultural areas in line with the information obtained from them (Rashid et al. 2021). LST measurements made with remote sensing can provide a wealth of regional and global data based on a variety of available temporal and spatial resolutions available (Yu et al. 2018). With the use of data in agricultural areas, information about the plant's existence, diversity, and health can be obtained (Ardahanlioğlu et al. 2017; Maroni et al. 2021; Selim et al. 2022).

In addition, the land surface temperature increase also affects the relevant region's air temperature (Yang et al. 2021). An area covered with vegetation has a lower surface temperature than the surrounding artificial structures since it can absorb radiation from

the sun (Deng et al. 2018; Tan et al. 2021). Similarly, agricultural products grown in open fields have a cooling effect on the air temperature of that region (Aram et al. 2019; Karakuş and Selim 2022; Yu et al. 2020). However, this situation differs in indoor agricultural applications, namely in greenhouses (Kim et al. 2022). Greenhouses play an essential role in producing high-yield foods, as they control various climatic parameters such as temperature, humidity, CO<sub>2</sub> concentration, and light (Amani et al. 2021). Temperature of the greenhouses are critical to growing quality crops and increasing yield, especially during the off-season (Tang et al. 2020). Materials used for greenhouse covers, such as glass, nylon, and the like, are expected to keep the internal temperature balanced by preventing heat loss inside (Papadakis et al. 2000). In order to provide a suitable growing environment for four seasons in the greenhouse interior, artificial heating and cooling are often necessary. Furthermore, due to economic reasons and to ensure optimum energy use, greenhouse cover materials are expected to interact

\* Corresponding Author

(serdarselim@akdeniz.edu.tr) ORCID ID 0000-0002-5631-6253  
(buketeyiletlen@gmail.com) ORCID ID 0000-0001-5010-5781

Cite this study

Selim S & Eyiletlen B (2022). Evaluation of the land surface temperature relationship and spatio-temporal variation of greenhouses and its surroundings. 5<sup>th</sup> Intercontinental Geoinformation Days (IGD), 149-152, Netra, India

well with solar radiation (Kim et al. 2018). In addition, they should be in a structure that allows the sun's radiation to pass through and be capable of trapping the heat inside (Teitel et al. 2019; Yan et al. 2020). In this context, it has been expected that the surrounding land cover surface temperature is likely to be different from the greenhouse surface temperature.

Current technological developments in remote sensing and Geographical Information Systems (GIS) make it possible to determine the surface temperatures of the land cover with LST analyses (Çoşlu et al. 2021). This technology is an important source of data for possible applications such as monitoring the relevant region's Spatio-temporal land surface temperature changes (Shen et al. 2020) and planning residential (Ardahanlıoğlu et al. 2020) and agricultural areas (Ghosh et al. 2019). This study aims to monitor the temporal variation of land surface temperatures of greenhouse areas, to determine the variations in these temperatures, and to evaluate their relationship with the surrounding land uses in Kumluca district, which is one of the important greenhouse cultivation centers of Antalya and even Turkey. Between 2013 and 2019, the change in surface temperature in greenhouses in the study area and adjacent land covers at 3-year intervals was analyzed with remote sensing and GIS technologies. It is anticipated that the results obtained can guide local and central governments in the planning of greenhouses and their surroundings.

## 2. Method

The study consists of the primary stages of obtaining data, performing data preprocessing, performing LST analyses, and finally interpreting the findings. The main material of the study is the sample area in Antalya province Kumluca district where greenhouses are densely located.

### 2.1. Study area

The study area is located in the southwest of Turkey at 36°19'56.65"N and 30°18'1.54"E coordinates (Fig. 1). The surface coverage of the greenhouses within the relevant land boundaries is mainly made of plastic material. Greenhouses are built adjacent to each other, with an average width of 5-10 m and various lengths, which can reach up to 200 m in length.



Figure 1. Aerial photograph of the study area

### 2.2. Data sets

The basic data set of the study consists of Landsat 8 Operational Land Imager (OLI) and Thermal Infrared Sensor (TIRS) satellite images of December for the years of 2013-2016 and 2019. For LST analysis, Band 4 (Red) and Band 5 (Near Infrared) with 30 m spatial resolution and Band 10 (Thermal Infrared 1) with 100 m spatial resolution of Landsat 8 were used.

#### 2.2.1. Pre-processing and LST analysis

Satellite images covering the study area for the relevant years were obtained from the official and free website of USGS Earth Explorer (<https://earthexplorer.usgs.gov/>). Atmospheric corrections were performed using QGIS software to remove the images' noise. Then, the LST analysis, whose 6-step formula is given below, was carried out in ArcGIS 10.4.1 software using Landsat 8's red (Band 4), near-infrared (Band 5), and thermal bands (Band 10).

#### Calculation of TOA (Top of Atmosrefic) (1)

$$TOA(L): M_L * Q_{cal} + A_L$$

#### Convert radiance into BT in Celcius (2)

$$BT = \left( \frac{K2}{\ln\left(\frac{K1}{L}\right)+1} \right) - 273.15$$

#### Calculation of NDVI (3)

$$NDVI_i = \left( \frac{Band\ 5 - Band\ 4}{Band\ 5 + Band\ 4} \right)$$

#### Calculation of proportion of vegetation (4)

$$P_V = \text{Square} ((NDVI - NDVI_{MIN}) / (NDVI_{MAX} - NDVI_{MIN}))$$

#### Calculation of emissivity (5)

$$\epsilon = 0.004 * P_V + 0.986$$

#### Calculation of LST (6)

$$LST = (BT / (1 + (0.00115 * BT / 1.4388) * \ln(\epsilon)))$$

$M_L$  = Band – spesific multiplicative rescaling factor

$Q_{CAL}$  = Corresponds to Thermal Band

$A_L$  = Band – spesific additive rescaling factor

$K1$  = Band specific thermal conversion constant 1 (774,8853)

$K2$  = Band specific thermal conversion constant 2 (1321.0789)

$L$  = TOA

Following these processes, on the LST maps, points are assigned randomly to the areas of greenhouses and its surroundings. Then, the obtained LST value of corresponding to each point were carried over to the table. In this context, the temperature values on the greenhouse surface and the land surfaces adjacent to the greenhouses were evaluated in line with the international literature and suggestions were developed.

### 3. Results

In this study carried out in Kumluca/Antalya, which has a very dense land use cover in terms of greenhouses, the difference between the surface temperatures of the greenhouse surfaces and other land covers and the time-dependent variation of the temperatures of these surfaces were determined. LST maps produced for the years 2013, 2016, 2019 confirm that the surface temperatures differ spatio-temporally (Fig. 2).

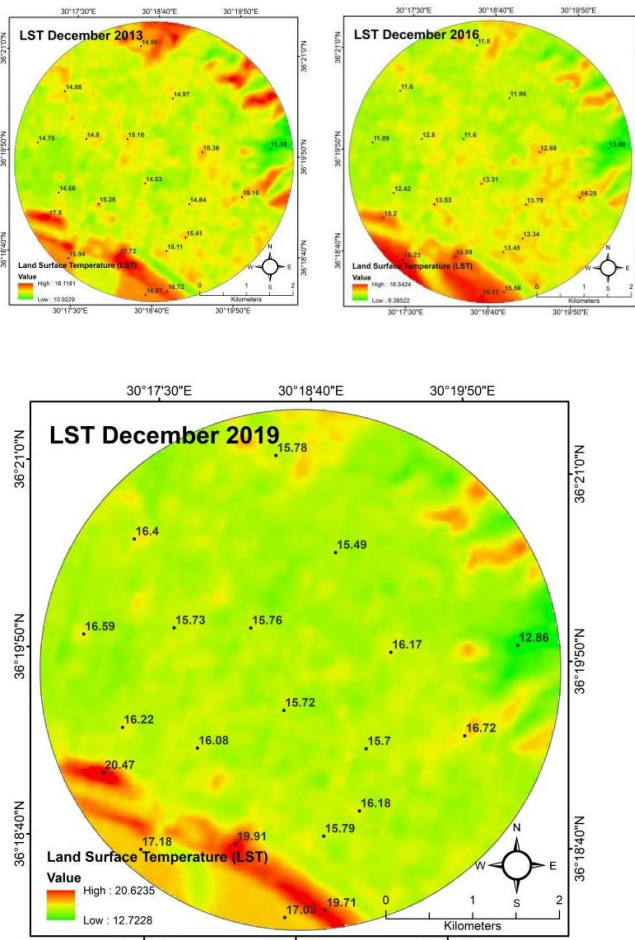


**Figure 2.** LST Maps of the relevant years

According to the findings obtained from the 2013 LST values, the average greenhouse surface temperature is 14.98 °C. In the same year, the average surface temperature for green areas is 13.15 °C, water is 16.00 °C, the building is 15.01 °C, and non-vegetation is 17.40 °C. In 2016, it was observed that the average greenhouse surface temperature decreased to 13.62 °C. Similarly, there was a temperature decrease in other land covers except for the water surface. In 2019, the average surface temperature of greenhouses increased significantly and reached 15.94 °C. Likewise, the mean surface temperatures increased for all other land covers. The data for 2019 shows that the highest surface temperature is in non-vegetation, which is followed by water, building, greenhouse and vegetation cover surfaces, respectively. According to the findings, in 2013, the highest surface temperature was measured at 17.80 °C in non-vegetation areas. Similarly, the highest value was measured again in non-vegetation in 2019.

However, in 2016, it was obtained from the water surface. In all three years, the lowest temperature values were measured in green areas. On the other hand, water surface temperature was found to be the highest in all three years compared to other land cover classes.

### 4. Discussion and Conclusion

For the relevant years, the surface temperature values in the greenhouses increased by about 1 °C depending on the micro climatic conditions. This surface temperature increase was similarly measured in other land covers. As seen in Table 1, all land cover surface temperatures partially decreased in 2016 but increased in 2019, depending on the micro climatic climate data.

**Table 1.** Average LST values of land covers

Land_cover_type	LST_2013	LST_2016	LST_2019
ve. water temperature (C°)	16.00	16.17	17.01
ve. non_vegetation temperature (C°)	17.40	15.54	17.18
ve. building temperature (C°)	15.01	12.91	16.56
ve. vegetation temperature (C°)	13.15	12.82	14.31
ve. temperature of greenhouses (C°)	14.98	13.62	15.94

In parallel with the related studies in the literature, the green areas showed a cooling effect on the surface temperatures (Song et al. 2018). The same situation was partially observed on water surfaces (Yang et al. 2021). Although greenhouses are artificial structures like buildings, their external surface temperatures were measured 1-2 °C higher than the buildings surface temperatures due to their internal temperature values (Saberian, and Sajadiye, 2019). On the other hand, the reason why the surface temperature values of greenhouses are lower than the surface temperature value of non-vegetation areas is thought to be due to the fact that greenhouses absorb some of the radiation and reflect the radiation less (Bonachela et al. 2020). It is also estimated that the increase in the surface temperature in greenhouses is due to global warming and micro climatic events (Haque et al. 2019), like the increase in other land cover surface temperatures.

### Acknowledgement

We would like to state our appreciation to Akdeniz University, the Institute of Natural and Applied Sciences, Remote Sensing and Geographic Information Systems Department for the contribution of the means of production and the data.

### References

Amani, M., Foroushani, S., Sultan, M., & Bahrami, M. (2020). Comprehensive review on dehumidification strategies for agricultural greenhouse applications. *Applied Thermal Engineering*, 181, 115979.

Aram, F., García, E. H., Solgi, E., & Mansournia, S. (2019). Urban green space cooling effect in cities. *Heliyon*, 5(4), e01339.

Ardahanlıoğlu, Z. R., Karakuş N., Selim S., Çınar, İ. ve Türkkan, H. R. (2017). Kentsel Tarım Alanlarının CBS Teknolojileri Kullanılarak Dağılımının

- Değerlendirilmesi Seydikemer Örneği. Fen, Matematik, Mühendislik ve Doğa Bilimleri Araştırmaları, Publisher: Çizgi Kitabevi Yayınları, 1, 198-205
- Ardahanlıoğlu, Z. R., Selim, S., Karakuş, N., & Çınar, İ. (2020). GIS-based approach to determine suitable settlement areas compatible with the natural environment. *Journal of Environmental Science and Management* 23-1: 71-82
- Bonachela, S., López, J. C., Hernández, J., Granados, M. R., Magán, J. J., Cabrera-Corral, F. J., ... & Baille, A. (2020). How mulching and canopy architecture interact in trapping solar radiation inside a Mediterranean greenhouse. *Agricultural and Forest Meteorology*, 294, 108132.
- Çoşlu, M., Karakuş, N., Selim, S., Sönmez, N.K. (2021). Evaluation of the Relationship Between Land Use and Land Surface Temperature in Manavgat Sub-Basin. *Planning, Design and Management in Landscape Architecture*, Altuntaş A., Editor, Iksad International Publishers, Ankara, pp.3-34, 2021
- Deng, Y., Wang, S., Bai, X., Tian, Y., Wu, L., Xiao, J., ... & Qian, Q. (2018). Relationship among land surface temperature and LUCC, NDVI in typical karst area. *Scientific reports*, 8(1), 1-12.
- Ghosh, S., Chatterjee, N. D., & Dinda, S. (2019). Relation between urban biophysical composition and dynamics of land surface temperature in the Kolkata metropolitan area: a GIS and statistical based analysis for sustainable planning. *Modeling Earth Systems and Environment*, 5(1), 307-329.
- Haque, U., Da Silva, P. F., Devoli, G., Pilz, J., Zhao, B., Khaloua, A., ... & Glass, G. E. (2019). The human cost of global warming: Deadly landslides and their triggers (1995–2014). *Science of the Total Environment*, 682, 673-684.
- Karakuş, N., & Selim, S. (2022). Dış Mekân Termal Konfor Koşullarının Zamansal ve Mekânsal Dağılımı: Konyaaltı-Antalya Örneği. *Mehmet Akif Ersoy Üniversitesi Fen Bilimleri Enstitüsü Dergisi*, 13(2), 259-269.
- Kim, H. K., Kang, G. C., Moon, J. P., Lee, T. S., & Oh, S. S. (2018). Estimation of thermal performance and heat loss in plastic greenhouses with and without thermal curtains. *Energies*, 11(3), 578.
- Kim, H. K., Lee, S. Y., Kwon, J. K., & Kim, Y. H. (2022). Evaluating the effect of cover materials on greenhouse microclimates and thermal performance. *Agronomy*, 12(1), 143.
- Liu, Y., Peng, J., & Wang, Y. (2018). Efficiency of landscape metrics characterizing urban land surface temperature. *Landscape and Urban Planning*, 180, 36-53.
- Maroni, D., Cardoso, G. T., Neckel, A., Maculan, L. S., Oliveira, M. L., Bodah, E. T., ... & Santosh, M. (2021). Land surface temperature and vegetation index as a proxy to microclimate. *Journal of Environmental Chemical Engineering*, 9(4), 105796.
- Nugraha, A. S. A., Gunawan, T., & Kamal, M. (2019). Comparison of Land Surface Temperature Derived from Landsat 7 ETM+ and Landsat 8 OLI/TIRS for Drought Monitoring. In *IOP Conference Series: Earth and Environmental Science*, 313(1), p. 012041.
- Papadakis, G., Briassoulis, D., Mugnozza, G. S., Vox, G., Feuilloley, P., & Stoffers, J. A. (2000). Review Paper (SE—Structures and Environment): Radiometric and thermal properties of, and testing methods for, greenhouse covering materials. *Journal of Agricultural Engineering Research*, 77(1), 7-38.
- Rashid, K. J., Hoque, M., Esha, T. A., Rahman, M., & Paul, A. (2021). Spatiotemporal changes of vegetation and land surface temperature in the refugee camps and its surrounding areas of Bangladesh after the Rohingya influx from Myanmar. *Environment, Development and Sustainability*, 23(3), 3562-3577.
- Saberian, A., & Sajadiye, S. M. (2019). The effect of dynamic solar heat load on the greenhouse microclimate using CFD simulation. *Renewable Energy*, 138, 722-737.
- Selim, S., Sönmez, N.K., Çoşlu, M. (2022). The Effect of Temporal Variation in Land Surface Temperature on Land Cover Classes and Agricultural Areas. *Recent Studies in Planning and Design*, Iksad International Publishing, 183-207.
- Shen, Y., Shen, H., Cheng, Q., & Zhang, L. (2020). Generating comparable and fine-scale time series of summer land surface temperature for thermal environment monitoring. *IEEE Journal of Selected Topics in Applied Earth Observations and Remote Sensing*, 14, 2136-2147.
- Song, Z., Li, R., Qiu, R., Liu, S., Tan, C., Li, Q., ... & Ma, M. (2018). Global land surface temperature influenced by vegetation cover and PM<sub>2.5</sub> from 2001 to 2016. *Remote Sensing*, 10(12), 2034.
- Tan, X., Sun, X., Huang, C., Yuan, Y., & Hou, D. (2021). Comparison of cooling effect between green space and water body. *Sustainable Cities and Society*, 67, 102711.
- Tang, Y., Ma, X., Li, M., & Wang, Y. (2020). The effect of temperature and light on strawberry production in a solar greenhouse. *Solar Energy*, 195, 318-328.
- Teitel, M., Barak, M., & Antler, A. (2009). Effect of cyclic heating and a thermal screen on the nocturnal heat loss and microclimate of a greenhouse. *Biosystems engineering*, 102(2), 162-170.
- Yan, S. R., Fazilati, M. A., Samani, N., Ghasemi, H. R., Toghraie, D., Nguyen, Q., & Karimipour, A. (2020). Energy efficiency optimization of the waste heat recovery system with embedded phase change materials in greenhouses: a thermo-economic-environmental study. *Journal of Energy Storage*, 30, 101445.
- Yang, J., Ren, J., Sun, D., Xiao, X., Xia, J. C., Jin, C., & Li, X. (2021). Understanding land surface temperature impact factors based on local climate zones. *Sustainable Cities and Society*, 69, 102818.
- Yu, Y., Y. Liu, and P. Yu. (2018). Land surface temperature product development for JPSS and GOES-R missions. *Comprehensive Remote Sensing*, 5, 284-303.
- Yu, Z., Yang, G., Zuo, S., Jørgensen, G., Koga, M., & Vejre, H. (2020). Critical review on the cooling effect of urban blue-green space: A threshold-size perspective. *Urban Forestry & Urban Greening*, 49, 126630



## 5<sup>th</sup> Intercontinental Geoinformation Days

igd.mersin.edu.tr



### Scene classification of Google Earth Images with different deep learning models

Şaziye Özge Atik\*<sup>1</sup>

<sup>1</sup> Gebze Technical University, Faculty of Engineering, Department of Geomatics Engineering, Kocaeli, Türkiye

#### Keywords

Scene Classification  
Algorithms  
Automatic Labeling  
CNN  
Google Earth

#### Abstract

Deep Convolutional Neural Networks are widely used for the automatic labeling of satellite imagery. Four different CNN models were trained using the AID dataset, which is an openly shared dataset, and the performances of the trained models were tested using the general accuracy metric. Test performances of ESA models were compared with similar studies in the literature on the same data set. At the same time, the model transferability of the trained models with the domain-shift application was tested with the help of different images obtained from the Google Earth platform. In this way, it is aimed to expand the application of automatic labeling of land use and land cover classes with deep CNN models in different data. The test results also support that the use of semantic scene classification algorithms is becoming more and more promising with the developing technology and opportunities.

#### 1. Introduction

A large number of research and studies are carried out for many purposes, such as monitoring the natural resources in the world, determining and monitoring the land use classes, and regional environmental monitoring programs. Remotely sensed scene classification applications are carried out with many different deep learning architectures in the literature (Chaib et al. 2017, Liu et al. 2018, Marmanis et al. 2016, Nogueira et al. 2017, Othman et al. 2016, Yu et al. 2018, Zhao et al. 2018). It is essential to use open shared and, free data in many studies carried out for environmental monitoring. The type and quality of the data used in the study are essential for these analyses carried out for large areas in the globalizing world and the applications are repeated at specific periods. For this purpose, it is aimed to use the free images provided by the Google Earth (GE) platform in the classification of aerial images. In this study, the performance of the models was tested on GE images of other regions with the help of ESA models trained on the openly shared data set. This study is also a proposal on determining the land use classes of the images of any region that need to be classified at any time. In the study, the AID dataset was used to train the algorithms. Densenet201, Resnet18, VGG16, and Alexnet were used as ESA models in the implementation phase. The classification results of these models were compared over the overall accuracy metric. At the same time, the

results of this study were compared with other similar studies in the literature. Finally, the automatic classification performances of the models trained on GE images selected from different regions of İstanbul were also tested.

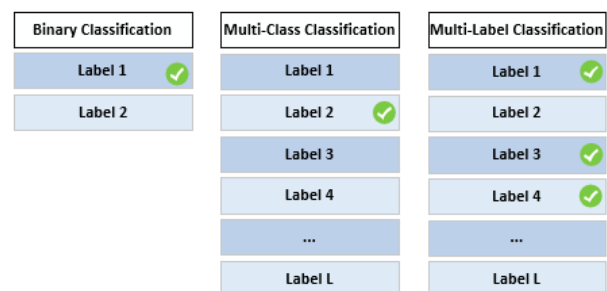


Figure 1. Types of scene classification

In Fig.1 the types of scene classification were illustrated. All classes are grouped under automatic labeling.

#### 2. Data and Methodology

The AID dataset (Xia et al. 2017) contains 10000 GE images in 600 x 600 size, between 200-400 for 30 different classes, with larger capacity among similar datasets (UC Merced, WHU-RS19 and EuroSat). This is because GE images consist of a mosaic of images detected

\* Corresponding Author

(soatik@gtu.edu.tr) ORCID ID 0000-0003-2876-040X

Cite this study

Atik, S. O. (2022). Scene Classification of Google Earth Images with Different Deep Learning Models 5<sup>th</sup> Intercontinental Geoinformation Days (IGD), 153-155, Netra, India

by multiple sensors for different regions. For this reason, the AID data set consists of images with many other properties (resolution) detected by different sensors. This situation also significantly differs from datasets obtained with a single sensor, such as the UC Merced dataset. In this way, the study also considers the need to apply Geographic Information Systems (GIS) studies in different places and at other times.

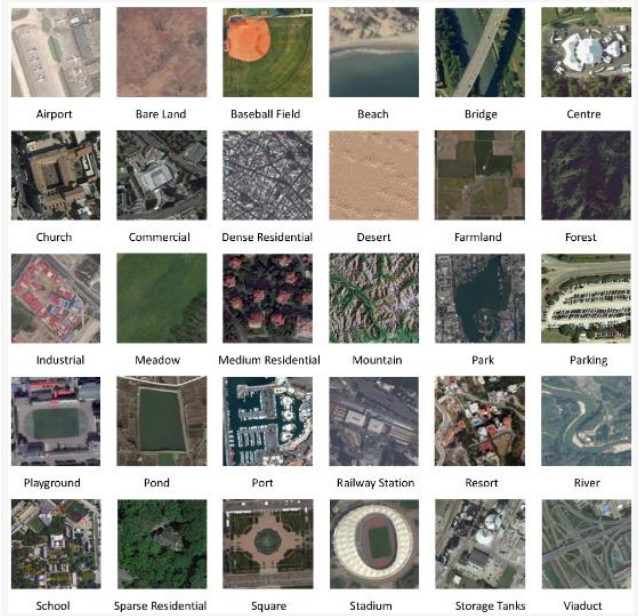


**Figure 2.** Selected sample images of the AID dataset (Zhang et al. 2020)

Convolutional Neural Networks (ESA) architectures have been used to classify images. AlexNet architecture (Krizhevsky et al. 2012) and validated in ImageNet and CIFAR da, is a widely used model. ResNet architecture (He et al. 2016) is another preferred algorithm with multiple convolution layers in many fields. The architecture takes names such as ResNet18 and 50, 101 according to the number of layers it contains. VGG was put there by Simonyan and Zisserman (Simonyan and Zisserman 2014) as ConvNet architecture with 1000 classes. VGG ,11,16 and 19 models are used according to their weight layers. DenseNet (Huang et al. 2017) is another architecture built as a Dense Convolutional Network and its performance was tested in CIFAR-10, CIFAR-100, SVHN, and ImageNet competitions.

$$Overall\ Accuracy = \left( \frac{TN + TP}{N} \right) \quad (1)$$

In the Eq.1, TP is True Positive, TN is True Negative, N is the total number of samples.

### 3. Experiment

The pre-trained weights of the ESA networks used were used as the starting weight. The number of epochs used in the training of ESA models was determined experimentally and selected as 20. The AID dataset is randomly divided into 50% training and 50% testing. However, after this segmentation, the performances of the ESA models were tested with the help of the same training and test images. A system equipped with i7-

11800H, a 2.30 GHz processor, GTX 3070 graphics card, and 32 GB RAM was used in the applications.

**Table 1.** The overall accuracy of the CNN models

Model	Overall Accuracy
DenseNet-201	93,18
VGG-16	92,84
ResNet-18	89,72
AlexNet	87,04

The overall accuracy values of the models used are shown in Table 2. Accordingly, the highest accuracy value was obtained with the DenseNet201 model at 93.18%. The lowest accuracy value belongs to AlexNet model with, 87.04%. At the same time, the highest accuracy in the GE images selected for this study from different regions was again obtained with the DenseNet 201 model. The overall accuracy values are illustrated in Fig.3.

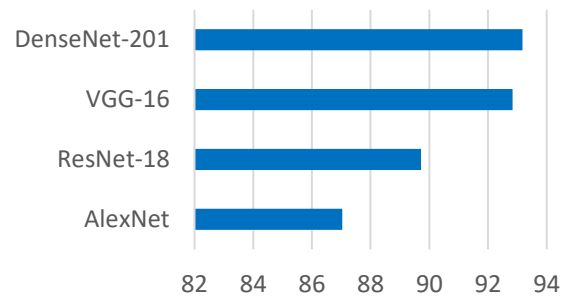


**Figure 3.** Overall accuracy values of CNN models

### 4. Results and Discussion

The test performances of the models used in this study were compared with similar studies in the literature. Accordingly, higher performance was obtained in the general accuracy criterion compared to other studies (Anwer et al. 2017, Xia et al. 2017). However, although similar accuracy values could not be reached on different images selected on Google Earth, the relevant land use class was determined correctly in many images. It is due to the model transfer process. Transferring the models to other data can decrease accuracy, as expected.

The models are used in the second test phase used for testing GE sample images. Classes of the AID dataset were collected on the GE platform from different regions of İstanbul. In Fig.3 and Fig.4, several samples are shown for false negative and true positive results. Alexnet model gave the worst test performances and DenseNen201 model provided the best performances for GE test images.

In future projections, this study can be enriched by testing models trained on a single dataset using images from different datasets. In this way, by measuring the model transfer capacity, semantic scene classification applications can be used by many experts in more expansive areas.

At the same time, then is that the models' data-based functionality areas, one of the main problems of deep

learning, which is the data-based functionality of the models, will be able to go beyond.



**Figure 3.** False Positive Samples (Left: GT Pond and Predicted Park; Right: GT Park and Predicted: Bridge)



**Figure 4.** True Positive Samples (Left: GT and Predicted: Bareland, Right: GT and Predicted: Square)

## 5. Conclusion

Automatic classification has the potential to become very popular soon, as in many different applications, in the automatic detection of land use classes from aerial images. However, realizing such applications with images of free and continuous image-sharing platforms such as GE will be one of the main pillars of widespread use. From planning automatic multi-label applications to due diligence, it can be preferred in many subjects, from environmental analysis to future simulations.

## References

Anwer, R.M.; Khan, F.S.; van deWeijer, J.; Monlinier, M.; Laaksonen, J. (2017) Binary patterns encoded convolutional neural networks for texture recognition and remote sensing scene classification. arXiv:1706.01171.  
 Chaib, S.; Liu, H.; Gu, Y.; Yao, H. (2017) Deep feature fusion for VHR remote sensing scene classification. IEEE Trans. Geosci. Remote Sens., 55, 4775–4784.

He, K., Zhang, X., Ren, S., & Sun, J. (2016). Deep residual learning for image recognition. In Proceedings of the IEEE conference on computer vision and pattern recognition (pp. 770-778).  
 Huang, G., Liu, Z., Van Der Maaten, L., & Weinberger, K. Q. (2017). Densely connected convolutional networks. In Proceedings of the IEEE conference on computer vision and pattern recognition (pp. 4700-4708).  
 Krizhevsky, A., Sutskever, I., & Hinton, G. E. (2012). Imagenet classification with deep convolutional neural networks. Advances in neural information processing systems, 25, 1097-1105.  
 Liu, Y.; Zhong, Y.; Fei, F.; Zhu, Q.; Qin, Q. (2018) Scene Classification Based on a Deep Random-Scale Stretched Convolutional Neural Network. Remote Sens. 2018, 10, 444.  
 Marmanis, D.; Datcu, M.; Esch, T.; Stilla, U. (2016) Deep learning earth observation classification using ImageNet pretrained networks. IEEE Geosci. Remote Sens. Lett., 13, 105–109.  
 Nogueira, K.; Penatti, O.A.B.; dos Santos, J.A. (2017) Towards better exploiting convolutional neural networks for remote sensing scene classification. Pattern Recognit. 61, 539–556.  
 Othman, E.; Bazi, Y.; Alajlan, N.; Alhichri, H.; Melgani, H. (2016) Using convolutional features and a sparse autoencoder for land-use scene classification. Int. J. Remote Sens., 37, 2149–2167.  
 Simonyan, K., & Zisserman, A. (2014). Very deep convolutional networks for large-scale image recognition. arXiv preprint arXiv:1409.1556.  
 Xia, G. S., Hu, J., Hu, F., Shi, B., Bai, X., Zhong, Y., ... & Lu, X. (2017). AID: A benchmark data set for performance evaluation of aerial scene classification. IEEE Transactions on Geoscience and Remote Sensing, 55(7), 3965-3981.  
 Yu, Y.; Liu, F. (2018) A two-stream deep fusion framework for high-resolution aerial scene classification. Comput. Intell. Neurosci., 8639367.  
 Zhang, S., Wu, G., Gu, J., & Han, J. (2020). Pruning convolutional neural networks with an attention mechanism for remote sensing image classification. Electronics, 9(8), 1209.  
 Zhao, L.; Zhang, W.; Tang, P. (2018) Analysis of the inter-dataset representation ability of deep features for high spatial resolution remote sensing image scene classification. Multimed. Tools Appl.



## 5<sup>th</sup> Intercontinental Geoinformation Days

igd.mersin.edu.tr



### 3D modeling of cultural heritage: Commagene Kingdom funerary monument

Cem Erol\*<sup>1</sup>, Nizar Polat<sup>2</sup>

<sup>1</sup>Harran University, Engineering Faculty, Department of Surveying Engineering, Sanlıurfa, Türkiye

<sup>2</sup>Harran University, Engineering Faculty, Department of Photogrammetry, Sanlıurfa, Türkiye

#### Keywords

Cultural Heritage  
3D Modelling  
Photogrammetry

#### Abstract

Our historical and cultural assets are undergoing deformations day by day. With today's technology and science, these historical structures can be processed and stored in three dimensions. These three-dimensional data; It provides the opportunity to work without damaging the architectural texture of the building during the visualization, restoration works and reproduction phases. Historical buildings have a significant contribution to the city's economy. These contributions are; It can keep the city economy alive for many reasons such as visiting that historical building, staying in the city, tasting the food culture of that region, shopping. One of the most important factors is to make a project that will attract the attention of domestic and foreign tourists in order to introduce our cultural assets by presenting them in digital environment for individuals who will not be able to visit those historical structures and to make them a center of attraction. In this study, a 3D (three-dimensional) model of this artifact was obtained with 60 photographs taken by the terrestrial photogrammetry method in the Karakuş Tumulus of Adıyaman Province, Kâhta District, with approximately 3.5 million point clouds, and it was possible to present it in digital environment.

#### 1. Introduction

Historical artifacts are cultural heritages that host hundreds of years of information, and this information should be passed on to future generations. While these historical heritages reflect the lifestyle and aesthetic understanding of the ancient civilization; They have changed over time due to natural and artificial effects such as wars and earthquakes. Documenting and preserving the natural texture of historical artifacts without damage is an indispensable element for transferring them to future generations (Varol et al. 2021). It is a fact that cultural heritage is damaged not only in our country but also in many parts of the world. For this reason, the documentation of cultural heritage is among the popular topics all over the world (Polat et al. 2021).

Documenting historical sites and cultural heritage is a complex and multifaceted process. Documentation of a historical or cultural building includes all the steps of study, process, storage and presentation necessary to determine the current state (shape and location) of the building in three-dimensional (3D) space. There are

several techniques for documenting cultural heritages. Photogrammetry and scanning methods are at the forefront of these very important and necessary techniques. At this point, it is a great advantage that photogrammetry can provide reliable information in a short time (Polat et al. 2021).

Today, documentation of cultural assets is done quickly and reliably with photogrammetry technique. With the digital photogrammetric method, the documentation, presentation, protection of historical buildings, and the detection of deteriorations that may occur in the works during and after the restoration works can be determined by the conservation experts. Another important advantage of photogrammetry is that it allows 3D representation of objects by modeling them in accordance with their originals (Uslu et al. 2016).

Cultural heritages are in danger of extinction due to natural or human reasons (Cömert et al. 2012; Tercan, 2017). As technology advances and human beings do more detailed studies on science, the interest in these unique areas and structures increases and the studies to protect them are developing day by day. One of the most

\* Corresponding Author

(cemerol0234@gmail.com) ORCID ID 0000 – 0001 – 8781 – 1890  
(nizarpolat@harran.edu.tr) ORCID ID 0000 – 0002 – 6061 – 7796

Cite this study

Erol, C., & Polat, N. (2022). 3D Modeling of Cultural Heritage: Commagene Kingdom Funerary Monument. 5<sup>th</sup> Intercontinental Geoinformation Days (IGD), 156-159, Netra, India

important studies that emerged as a result of these developments is the documentation of cultural artifacts. Different and many techniques have been used for many years to document and digitize historical artifacts, but no technique used so far has offered more practical solutions than taking photographs (Ulvi et al. 2019; Şasi and Yakar 2017). For this reason, it is very important that the cultural heritage values that can survive, cannot be reproduced, and cannot be returned should be documented in a non-destructive way down to the smallest point (Hamal et al. 2020; Kanun et al., 2022).

In this study, the 'Lion Statue', which was destroyed over time and detached from its column, in the Karakuş Tumulus located in the borders of the Kâhta District of Adıyaman Province, was modeled in three dimensions by making measurements with the terrestrial photogrammetric method.

## 2. Method

Information about the study area, the equipment used and the methodology are explained in this section. The characteristics of the camera used in the study are given.

### 2.1. Study Area

Karakuş Tumulus located in Adıyaman Province, Kahta District has been determined as the study area.



Figure 1. Study area

Karakuş Tumulus is a mausoleum belonging to the Kingdom of Commagene, whose history dates back to the 1st century BC. Eagle on the column in the south, Lion and Bull on the columns on the east, and a mausoleum belonging to the Commagene Kingdom family on the column on the west (1st century BC). Although four columns were built in the east, west and south directions, only 4 columns remain today. Two of them are in the East and one is in the West. Karakus is located in the south (Internet Source).

Since there is no information about the lion head statue found in the study, it was not mentioned. The visual of the lion head sculpture is shown in Fig. 2.

Canon EOS 2000D camera with 24.1 mega pixels, 6000\*4000 maximum image resolution and 475 g weight was used in the study.



Figure 2. The image of the Lion Sculpture



Figure 3. The digital camera used in the study

### 2.2. Using photogrammetric methods in 3D modeling of cultural heritage

Photogrammetry means measuring with the help of photographs. Photogrammetry is a branch of science in which reliable information about objects and the environment is obtained as a result of recording, measuring and interpreting the photographic images shaped by the rays emanating from the objects and the environment they form, and the electromagnetic energy they emit (Senol et al. 2021).

Classical two-dimensional photogrammetric applications are insufficient for many applications. For this reason, the three-dimensional calculation, questioning, analysis, simulation and visualization of the geographical area have gained importance. With today's CAD technology, a perspective view of a geographical area can be obtained, three-dimensional visualization is possible, it is possible to fly over the land in the virtual environment and to wander around the city (Uslu et al. 2016).

In digital photogrammetry, sequential and overlay images must be taken from different stations in order to obtain three-dimensional data and achieve high accuracy. In order to realize this condition, it is necessary to design the camera layout well and to choose the most suitable mathematical model for the operation. In addition, reaching high measurement accuracy, how many cameras can be placed, called camera network design, where and how, the number of control points on the object and how their positions

should be, are provided by using the appropriate optimization method (Uslu et al. 2016).

Photogrammetry is divided into branches by terrestrial and aerial photogrammetry methods. These methods have advantages and disadvantages relative to each other. In terrestrial photogrammetry, the objects are equipped with a denser point cloud, since the overlapping ratio is higher with the images taken consecutively, and thus the zoomed and zoomed model can be viewed with better quality. However, aerial images are needed because images of high-rise buildings cannot be taken with terrestrial photogrammetry. Roof, minaret, etc. with aerial images. Measuring tall buildings has become easier.

In addition to documenting with traditional methods, today unmanned aerial vehicles, terrestrial photogrammetry, laser scanning, etc. techniques are developing (Yakar et al., 2015; Şenol et al., 2020; Karataş et al., 2022). Although laser scanning, GPR (Ground Penetrating Radar), aerial photogrammetry, model creation with classical measurement methods etc. for the detection and documentation of archaeological sites. In this study, historically important objects extracted from archaeological sites were modeled with terrestrial photogrammetry technique (Polat et al. 2020; Alptekin & Yakar, 2021).

### 3. Results

In order to model the historical building in three dimensions, 62 photographs were taken around the model as overlay. Two of these photographs were not considered appropriate, so they were not processed. Processing of the photos was carried out in Agisoft PhotoScan software. Agisoft Photoscan; It is a software that provides fast, reliable and quality results in image processing and works with an interface that offers ease of operation.

Three-dimensional models were produced with point cloud, compacted dense point cloud and texture overlay by processing the photographs of the working area. Approximately 3.5 million points were produced in the model, which was textured with the terrestrial photogrammetry technique. In Figure 2, the image with texture coating is given, and in Figure 3, the image of the solid model.

The study area was visited before noon, and attention was paid to produce a smooth model by combining the common details in each photograph so that the image becomes clear without being exposed to sunlight and the model produced has a void-free structure.

### 4. Discussion

The study has many important contributions in terms of the tourism sector. Considering these contributions, it can be a guide for future studies. First of all, many destroyed, forgotten or neglected cultural heritage artifacts can be brought back to life by performing the most accurate restoration works with 3D modeling techniques and offered to the service of tourism sector stakeholders. In addition, virtual tours can be made around and inside cultural structures with

the most realistic 3D modeling. 3D applications in cultural heritage sites will help visitors improve their learning experiences by visualizing historical events in their minds. Thus, it will be possible to contribute to tourist guides and virtual museum applications for tourists

Unfortunately, as a guide model that will lead and guide these studies is not undertaken in our country, our cultural heritage cannot be recorded sufficiently and sufficient preliminary studies cannot be carried out in restoration works. Only with this study and similar studies, virtual museology is becoming widespread and digital archiving of historical artifacts is carried out.



**Figure 4.** The image of the Lion Sculpture in the study area in the raw dataset

### 5. Conclusion

In this study, the modeling of the lion head statue in the Karakuş Tumulus was carried out by terrestrial photogrammetric method. The digital record that emerged as a result of the modeling will contribute both to the digital recording of the works and to the creation of the virtual museum archive.

With the protection of the lion head sculpture in the study, it will provide the opportunity to work on the sculpture sensitively in case it deforms in the following years, or it will be possible to reproduce it with a model to be taken from the digital archive in case the sculpture is destroyed.

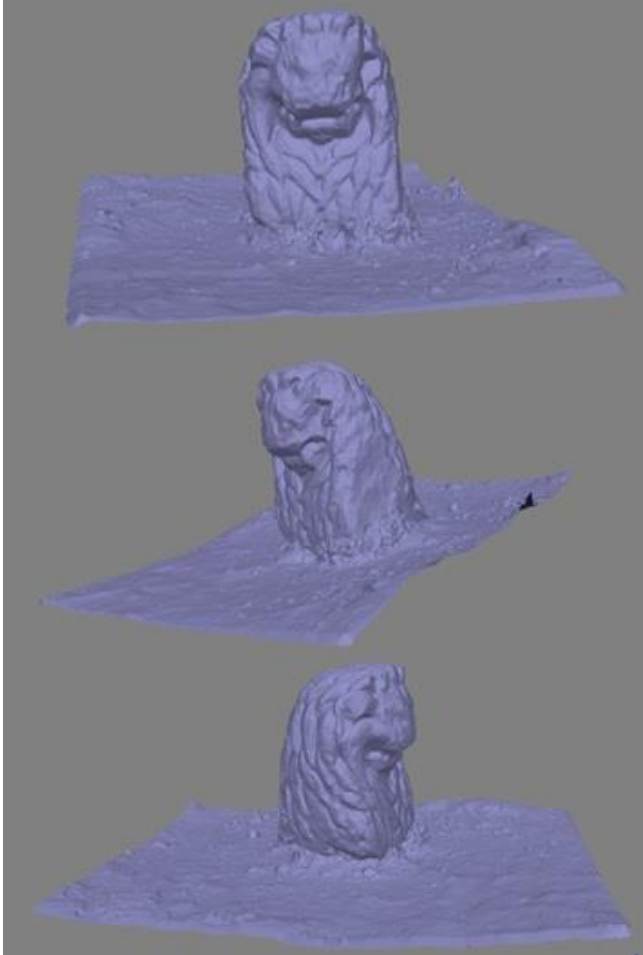


**Figure 5.** Image of 3D solid model obtained in Agisoft Photoscan software

## References

- Alptekin, A., & Yakar, M. (2021). 3D model of Üçayak Ruins obtained from point clouds. *Mersin Photogrammetry Journal*, 3(2), 37-40.
- Cömert, R., Avdan, U., & Şenkal, E., (2012). İnsansız Hava Araçlarının Kullanım Alanları ve Gelecekteki Beklentiler. IV. Uzaktan Algılama ve Coğrafi Bilgi Sistemleri Sempozyumu (UZAL-CBS 2012), 16-19, Zonguldak.
- Hamal, S. N. G., Sarı, B. & Ulvi, A. (2020). Using of Hybrid Data Acquisition Techniques for Cultural Heritage a

- Case Study of Pompeiopolis. *Türkiye İnsansız Hava Araçları Dergisi*, 2(2), 55-60.
- Kaya, Y., Polat, N., Şenol, H. İ., Memduhoğlu, A., & Ulukavak, M. (2021). Arkeolojik kalıntıların belgelenmesinde yersel ve İHA fotogrametrisinin birlikte kullanımı. Harran Üniversitesi, Mühendislik Fakültesi, Harita Mühendisliği Bölümü, Şanlıurfa, Türkiye.
- Kanun, E., Alptekin, A., Karataş, L., & Yakar, M. (2022). The use of UAV photogrammetry in modeling ancient structures: A case study of "Kanytellis". *Advanced UAV*, 2(2), 41-50.
- Karataş, L., Alptekin, A., Kanun, E., & Yakar, M. (2022). Tarihi kârgir yapılarda taş malzeme bozulmalarının İHA fotogrametrisi kullanarak tespiti ve belgelenmesi: Mersin Kanlıdivane ören yeri vaka çalışması. *İçel Dergisi*, 2(2), 41-49.
- Polat, N., Önal, M., Ernst, F. B., Şenol, H. İ., Memduhoğlu, A., Mutlu, S., Mutlu, S. İ., Budan, M. A., Turgut, M., & Kara, H., Harran Ören Yeri Arkeolojik Kazı Alanınının Çıkarılan Bazı Küçük Arkeolojik Buluntuların Fotogrametrik Olarak 3B Modellenmesi. E-ISSN: 2687-6590
- Polat, N., Önal, M., Kaya, Y., Memduhoğlu, A., Kaya, N., Ulukavak, M., Mutlu, S. İ., & Mutlu S. (2021). Harran Ören Yeri Kazısında Bulunan Kabartma Yazıların Üç Boyutlu Olarak Modellenmesi. *BEÜ Fen Bilimleri Dergisi* 10 (2), 594-601, 2021.
- Şasi, A., & Yakar, M. (2017). Photogrammetric modelling of sakahane masjid using an unmanned aerial vehicle. *Turkish Journal of Engineering*, 1(2), 82-87.
- Şenol, H. İ., Yiğit, A. Y., Kaya, Y., & Ulvi, A. (2021). İHA ve yersel fotogrametrik veri füzyonu ile kültürel mirasın 3 boyutlu (3B) modelleme uygulaması: Kanlıdivane Örneği.
- Ulvi, A., Yakar, M., Yiğit, A. ve Kaya, Y. (2019). The Use of Photogrammetric Techniques in Documenting Cultural Heritage: The Example of Aksaray Selime Sultan Tomb. *Universal Journal Of Engineering Science*, 7(3), 64-73. doi: 10.13189/ujes.2019.070303
- Uslu, A., Polat, N., Toprak, A. S., & Uysal, M., (2016). Kültürel Mirasın Fotogrametrik Yöntemle 3B Modellenmesi Örneği. e-ISSN: 1309-3983
- Varol, F., Yiğit, A. Y., & Ulvi, A., (2021). Kültürel Mirasın Dijital Ortamda 3B Arşivlenmesi: Magoki Attar Cami Sanal Model Örneği
- Web, Karakuş Tümülsü Tarihi. <https://www.azbibak.com/karakustumulusu->
- Yakar, Murat, Orhan O., Ulvi, A., Yiğit, A. Y., & Yüzer, M. M., "Sahip Ata Külliyesi Rölöve Örneği." TMMOB Harita ve Kadastro Mühendisleri Odası 10 (2015).



## 5<sup>th</sup> Intercontinental Geoinformation Days

igd.mersin.edu.tr



### Automatic Building Extraction using Kernel-based Deep Learning Approach from VHR Imagery

Tolga Bakirman\*<sup>1</sup>, Mahmut Oğuz Selbesoğlu <sup>1</sup>

<sup>1</sup>Yıldız Technical University, Civil Engineering Faculty, Department of Geomatics Engineering, İstanbul, Türkiye

<sup>2</sup>Istanbul Technical University, Civil Engineering Faculty, Department of Geomatics Engineering, İstanbul, Türkiye

#### Keywords

Deep Learning  
Building Extraction  
VHR  
K-Net

#### Abstract

Monitoring and analyzing the rapidly changing and growing cities in terms of buildings has become an important demand today. Deep learning approach has been widely used recently in the automatic extraction of buildings, which are important inputs for smart city systems. The recent studies demonstrate that the deep learning approaches greatly improve the accuracy of building extraction from the high-resolution images. The purpose of the study is to investigate the performance of K-Net architecture for building extraction from VHR imagery. In this context, The Wuhan University (WHU) Aerial Building Dataset was used for training, validation and testing. The outcomes of the study demonstrate that the extraction of buildings based on deep learning architectures provides sufficient results with 98.17 % Accuracy, 92.29 % Precision, 91.20 % Recall, 84.74 % IoU and 91.74 % F1-Score.

#### 1. Introduction

Building information is of great importance for urban planning, monitoring engineering structures, and building deformation monitoring. In the last decade, automatic building extraction from high spatial resolution maps has become a very effective way based on recent deep learning approaches. In building extraction studies, there are three widely used platforms which are satellite remote sensing, aerial photogrammetry (Chen et al., 2017), and close-range photogrammetry based on unmanned aerial vehicles (UAV) (Zhuo et al., 2018). These systems have some advantages and disadvantages. Although remote sensing satellites can provide images with spatial panchromatic band resolution up to 0.30 m (Boonpook et al., 2021), it is affected by the orbital period and atmospheric interference. However, the mentioned systems above may have limitations in temporal resolution and cannot respond to emergency monitoring purposes. Furthermore, based on aerial platforms, approximately

centimeters high-resolution orthoimages in red, green, blue (RGB) bands (U.S. Department of Interior 2011) can be produced. Widely used recent aerial imagery has many advantages of low flight cost, high accuracy, and real-time monitoring capability.

The uncertainty for extracting buildings caused by the variations in building structure and texture is a challenging factor for conventional methods such as Maximum Likelihood Classification (MLC) and Support Vector Machine (SVM) (Zhong et al. 2018) and object-based classification (Liu and Xia, 2010, Wang et al., 2004). Recently, automatic segmentation of buildings based on deep learning (DL) plays a significant role and provides efficient results especially based on high resolution datasets. The DL approaches can learn complex features depending on the given dataset and classify objects with high accuracy (Li et al., 2017). There have been various architectures throughout the years implemented for building extraction such as U-Net (Guo et al., 2020, Wang and Miao, 2022), DeepLabv3+ (Atik et al., 2022, Li and Dong, 2022), FPN (Sariturk and Seker,

\* Corresponding Author

(bakirman@yildiz.edu.tr) ORCID ID 0000-0001-7828-9666  
(selbesoglu@itu.edu.tr) ORCID ID 0000-0002-1132-3978

Cite this study

Bakirman T & Selbesoglu M. O. (2022). Automatic Building Extraction using Kernel-based Deep Learning Approach from VHR Imagery. 5<sup>th</sup> Intercontinental Geoinformation Days (IGD), page numbers, 160-163, Netra, India

2022), PSPNet (Yuan et al., 2022), U-net++ (Bakirman et al., 2022), etc. In this study, we aim to automatically extract building footprints using recently proposed kernel-based architecture K-Net using high resolution WHU aerial building dataset.

## 2. Material and methods

In this study, The Wuhan University (WHU) building open access dataset including aerial images was used (Ji et al., 2019). The featured of the dataset is given in Table 1.

**Table 1.** Dataset features

Image Size	512 × 512 pixels
Number of images	8189 natural image tiles
Overlap	no overlaps
Resolution	0.30 meter spatial resolution
Raw resolution	0.075 meter original data.
Number of labels	187,000 independent buildings.

Original vector data provided by land information service which covers rural, residential, cultural and industrial areas of the area. The labels were improved with manually editing. A sample image tile with corresponding labels is given in Figure 1.



**Figure 1.** sample image tile with labels

In the study, WHU dataset separated as training, validation and test sets consisting of 4736, 1036, and 2416 image tiles, respectively.

K-Net architecture (Zhang et al., 2021) is built on a collection of convolutional kernels that have been randomly initialized and may be applied to panoptic, semantic, and instance segmentation. The semantic kernels use convolutions to produce the corresponding segmentation predictions. Globally, the kernels are dynamically modified to enhance their capacity for better discrimination. The bipartite matching approach is used to recognize objects that create a one-to-one mapping between kernels and instances in an image. K-Net architecture can be implemented for semantic segmentation, instance segmentation and panoptic segmentation. In this study, we exploited the K-Net architecture for semantic segmentation of building footprints from VHR aerial imagery. The general structure of the K-Net architecture can be seen in Figure 2.

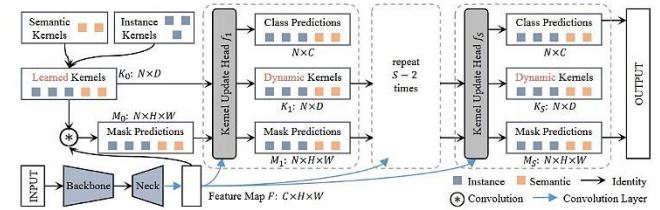


**Figure 2.** The general structure of K-Net (Zhang et al., 2021)

## 3. Results and discussion

In this study, K-Net architecture is trained on a workstation equipped with 11th Gen Intel(R) Core(TM) i9-11900 @ 2.50GHz processor and NVIDIA Quadro RTX 5000 16 GB graphic processor unit. The architecture is implemented with the MMsegmentation library for PyTorch in the Python environment. The hyperparameters used in the training are given in Table 2. We have also used pretrained weights from ADE20K dataset.

**Table 2.** Hyperparameters for K-Net training

Number of Images (Training)	4736
Number of Images (Validation)	1036
Number of Images (Testing)	2416
Backbone	Swin Transformer
Image Size	512 x 512
Iterations	5000
Loss Function	Cross Entropy Loss
Optimizer	AdamW
Learning Rate	0.00006
Weight Decay	0.0005
Batch Size	2
Augmentation	Random Flip, Photo Metric Distortion

We report accuracy, precision, recall, intersection over union (IoU) and F1-score in order to evaluate the results. The accuracy metrics were calculated on pixel level based on True-Positive (TP), True-Negative (TN),

False-Positive (FP) and False Negative (FN). Accuracy metrics is ratio of correctly predicted pixels to total count of all predicted pixels which is shown in Equation 1. In the case of class imbalance between the target class and background, accuracy metric may provide misleading results. In order to overcome this issue, the IoU, also known as the Jaccard Index, was calculated by the ratio of overlap area between the prediction and the ground truth divided by the area of union between the prediction and the ground truth. Precision is the ratio of pixels predicted as buildings to all pixels predicted as buildings. As can be seen in Equation 2, the precision is highly affected by FP pixels. On the other hand, recall is the ratio of pixels predicted as buildings to all pixels that are labeled as buildings in ground truth (Equation 3). Similarly, the recall metric is heavily dependent on FN pixels which are classified as background instead of building. Naturally, there is a trade-off between precision and recall. Therefore, F1-score, also known as Dice coefficient, provides a more balanced metric through harmonic mean of precision and recall which was calculated by Equation 4.

$$Accuracy = \frac{TP+TN}{TP+TN+FP+FN}$$

$$Precision = \frac{TP}{TP+FP}$$

$$Recall = \frac{TP}{TP+FN}$$

$$F1 - Score = \frac{Precision \times Recall}{Precision + Recall}$$

The evaluation results that were calculated with the test set of the WHU dataset are given in Table 3. All accuracy metrics are above 90% except IoU. However, considering that IoU metric is quite essential for semantic segmentation studies, more experiments should be conducted to obtain a more efficient solution.

**Table 3.** Performance of the K-Net DL method

Accuracy	98.17 %
Precision	92.29 %
Recall	91.20 %
IoU	84.74 %
F1-Score	91.74 %

Figure 3 shows prediction examples from the test dataset. The visual inspections show that even though the used architecture can extract general structure of the buildings, it fails to preserve edge details of the buildings. Figure 3 also reveals that the DL method is more successful on larger buildings. It can be seen that the morphological features are lost especially in small sized buildings. On the other hand, the architecture is able to detect both residential and industrial buildings.

#### 4. Conclusion

Monitoring of rapidly changing and growing cities today can be carried out by advanced remote sensing technologies based on recent deep learning approaches. It has been seen that automatic building extraction with recent kernel-based deep learning approach used in the

study produces sufficient results. However, the architecture still fails to predict building edges efficiently which may require post-processing. Future studies, it is planned to perform more experiments and analyze the region with different patterns using different deep-learning techniques.



**Figure 3.** Prediction examples from the dataset. Top Row: Test Image, Middle Row: Ground Truth, Last Row: Predictions

#### Acknowledgment

The authors would like to acknowledge the Group of Photogrammetry and Computer Vision (GPCV) at Wuhan University for providing the WHU building dataset.

#### References

- Atik, S. O., Atik, M. E. & Ipbuker, C. J. J. O. A. R. S. (2022). Comparative research on different backbone architectures of DeepLabV3+ for building segmentation. 16, 024510.
- Bakirman, T., Komurcu, I. & SERTEL, E. (2022). Comparative analysis of deep learning based building extraction methods with the new VHR Istanbul dataset. *Expert Systems with Applications*, 202, 117346.
- BOONPOOK, W., TAN, Y. & XU, B. 2021. Deep learning-based multi-feature semantic segmentation in building extraction from images of UAV photogrammetry. *International Journal of Remote Sensing*, 42, 1-19.

- CHEN, K., FU, K., GAO, X., YAN, M., SUN, X. & ZHANG, H. Building extraction from remote sensing images with deep learning in a supervised manner. 2017 IEEE International Geoscience and Remote Sensing Symposium (IGARSS), 2017. IEEE, 1672-1675.
- GUO, M., LIU, H., XU, Y. & HUANG, Y. J. R. S. 2020. Building extraction based on U-Net with an attention block and multiple losses. 12, 1400.
- JI, S., WEI, S. & LU, M. 2019. Fully Convolutional Networks for Multisource Building Extraction From an Open Aerial and Satellite Imagery Data Set. *IEEE Transactions on Geoscience and Remote Sensing*, 57, 574-586.
- LI, Y., HE, B., LONG, T. & BAI, X. Evaluation the performance of fully convolutional networks for building extraction compared with shallow models. 2017 IEEE International Geoscience and Remote Sensing Symposium (IGARSS), 2017. IEEE, 850-853.
- LI, Z. & DONG, J. J. R. S. 2022. A Framework Integrating DeeplabV3+, Transfer Learning, Active Learning, and Incremental Learning for Mapping Building Footprints. 14, 4738.
- LIU, D. & XIA, F. J. R. S. L. 2010. Assessing object-based classification: advantages and limitations. 1, 187-194.
- SARITURK, B. & SEKER, D. Z. 2022. Comparison of Residual and Dense Neural Network Approaches for Building Extraction from High-Resolution Aerial Images. *Advances in Space Research*.
- WANG, H. & MIAO, F. J. E. J. O. R. S. 2022. Building extraction from remote sensing images using deep residual U-Net. 55, 71-85.
- WANG, L., SOUSA, W. & GONG, P. 2004. Integration of object-based and pixel-based classification for mapping mangroves with IKONOS imagery. *International journal of remote sensing*, 25, 5655-5668.
- YUAN, W., WANG, J. & XU, W. J. R. S. 2022. Shift Pooling PSPNet: Rethinking PSPNet for Building Extraction in Remote Sensing Images from Entire Local Feature Pooling. 14, 4889.
- ZHANG, W., PANG, J., CHEN, K. & LOY, C. C. K-net: Towards unified image segmentation. *Advances in Neural Information Processing Systems*, 2021. 10326-10338.
- ZHUO, X., FRAUNDORFER, F., KURZ, F. & REINARTZ, P. J. R. S. 2018. Optimization of OpenStreetMap building footprints based on semantic information of oblique UAV images. 10, 624.



## 5<sup>th</sup> Intercontinental Geoinformation Days

igd.mersin.edu.tr



### Comparison of CSF and SMRF filtering methods for airborne LiDAR point cloud data

Ramazan Alper Kuçak\*<sup>1</sup>

<sup>1</sup>Niğde Ömer Halisdemir University, Engineering Faculty, Geomatics Engineering Department, Niğde, Türkiye

#### Keywords

Ground Filtering  
LiDAR  
DTM  
CSF  
SMRF  
Point Cloud

#### Abstract

Airborne LiDAR System (ALS) technologies are widely used for rapid data collection in a wide range of applications, including cultural heritage, Geography Information Systems (GIS), geodesy applications, 3D city modeling, and deformation analysis systems, and the generation of Digital Terrain Models (DTM). Filtering bare soil from point cloud data is critical for archaeologists, architects, and geomatics professionals employing airborne Light Detection and Ranging (LiDAR). Cloth Simulation Filtering (CSF) and Simple Morphological Filtering (SMRF), both ground filtering techniques, are discussed in this study. Airborne LiDAR point cloud data were split into the ground and non-ground point clouds for evaluation. A thorough evaluation of filtering accuracy necessitates comparing all point cloud data. However, because the data is so huge, this seems implausible. To adequately measure classification success, data manually identified as ground and non-ground was used as a reference. The performance of the CSF and SMRF approaches is enough, but it is impacted by point cloud type, slope, and vegetation type, according to our findings.

#### 1. Introduction

Airborne LiDAR methods are used in geomatics applications for quick data collecting on a broad spectrum of topographic land surveys. In addition, various applications have also employed elevation and geomorphological data from digital elevation models created using these approaches (Erol S. et al.,2020). DTMs, on the other hand, are used to confirm the physical surface and depict the bare soil. As a result, point clouds generated by these measuring methods have become increasingly popular in developing DTMs. To filter DTMs, airborne LiDAR point cloud data are filtered as ground and non-ground point clouds. However, point cloud filtering (removing bare soil from point cloud data) remains a significant problem when creating DTMs.

Over the past two decades, various ground filtering algorithms have been offered in various GIS or Lidar software solutions (e.g., ArcGIS, QGIS, LASTools, PDAL, PCL, and ALDPAT). However, each method of dealing with different terrains has pros and cons, and the benefits of these filtering algorithms vary from landscape to landscape. Therefore, performance evaluation among filtering algorithms is beneficial for selecting appropriate filters, especially for inexperienced users (Chen, C., 2021). Such algorithms are increasingly used to filter

point cloud data (Klápště, P., et al. 2021). However, most algorithms are designed for filtering ALS data (Klápště, P., et al. 2021; Meng, X., Currit, N., & Zhao, K., 2010; Susaki, J., 2012; Rashidi, P., & Rastiveis, H., 2017). The ALS records the sequence of multiple laser pulse returns. Therefore, the ground filter algorithm uses these momentum properties to represent the ground.

This study's primary purpose is to evaluate these algorithms' performance on LiDAR point cloud data using the Cloth Simulation Filter (CSF) and Simple Morphological Filter (SMRF) methods. In addition, it is used to analyze the effects of filtering methods applied to various point clouds once the ground surface has been obtained.

#### 2. Method

The case study area is located in the Bergama test site for aerial LiDAR data west of Turkey (Figure 1). The land size is 200 m in length and 100 m in width. After obtaining the point cloud data with Lidar for this study area, the point cloud data were filtered, and the DTMs were gained with CSF and SMRF algorithms. In addition, the performances of the filter algorithms in DTM generation were evaluated and discussed.

\* Corresponding Author

<sup>\*</sup>(e-mail) ORCID ID xxxx – xxxx – xxxx – xxxx

Cite this study

Kuçak R, A. (2022). Comparison of CSF and SMRF filtering methods for airborne LiDAR point cloud data. 5<sup>th</sup> Intercontinental Geoinformation Days (IGD), 164-167, Netra, India

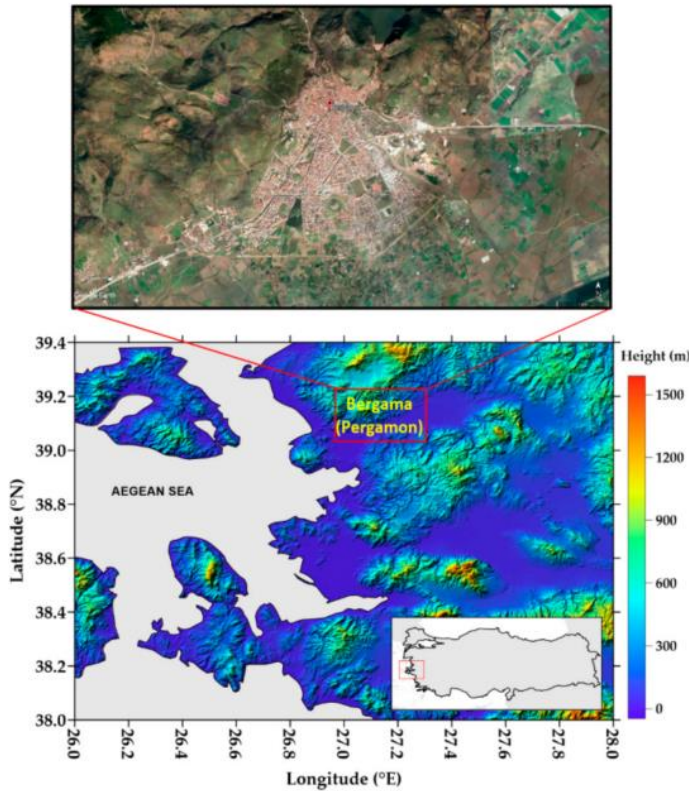


**Figure 1.** Google Earth image (top) and SRTM DTM (bottom) of Bergama test area (Erol, S. et al., 2021)

In this study, LiDAR point cloud data were obtained by making test flights from 1200 m heights with the Riegl LMS-Q1560 LiDAR system provided by the general directorate of mapping of Turkey. For the performance of filtering, a manual accuracy assessment approach was preferred. The primary purpose of this study is to evaluate the performance of CSF and SMRF methods in different point clouds in the same area.

### 2.1. Filtering

Filtering is the process of determining whether data belongs to the ground or non-ground surface in digital terrain model development. There are several filtering algorithms, which may be classified into five types. [Štular, B., & Lozić, E., 2020; Pfeifer, N. and G. Mandlbürger, 2018; Süleymanoğlu, B. and Soycan, M., 2019):

- morphological filtering (PMF, SBF, SMRF),
- progressive densification (PTIN),
- surface-based filtering (WLS, CSF),
- segmentation-based filtering (SegBF),
- other (MCC), and hybrid (BMHF).

The point cloud data were filtered in this case study using the CSF and SMRF algorithms, and DTMs were produced. The foundation of SMRF is mathematical morphology. By figuring out the height of nearby locations, morphological filtering algorithms maintain the characteristics of the landscape [Pfeifer, N. and G. Mandlbürger, 2018; Buján, S., Cordero, M. and Miranda, D., 2020). A morphological abrasion with the core function and a test for the difference between a point's original height and the eroded height are the two

fundamental phases in the filtering process (Figure 3). Surface-based filtering techniques are the foundation of CSF. They initially acknowledge that all points are ground points and gradually eliminate all non-ground points. Using basic kriging, the surface is typically defined utilizing all of the points in the first stage. Then, an average surface is created between the ground and non-ground locations. The distance from the mean surface determines the residual value (Pingel, T. J., 2013; Süleymanoğlu, B. and Soycan, M., 2019).

In this study, ground and non-ground data were utilized to examine the effectiveness of filtering techniques using a manually edited methodology (Visual inspection). When ground truth data are unavailable, visual inspection is a manual accuracy evaluation method that is frequently utilized. In addition, three indices based on a confusion matrix were used: error type I, II, and accuracy (Table 1). Equations (1), (2), and (3) demonstrate these equations (Susaki, J., 2012).

$$\text{error type I} = b/(a+b), \quad (1)$$

$$\text{error type II} = c/(c+d), \quad (2)$$

$$\text{accuracy} = (a+d)/(a+b+c+d), \quad (3)$$

**Table 1.** Structure of Confusion Matrix

		Ground Points	Non-Ground Points
Reference Points	Ground Points	a	b
	Non-Ground Points	c	d

### 3. Results

DTM filtering (CSF and SMRF) was implemented to LiDAR data (the experimental field) using Cloud Compare and Matlab software. The accuracy of filtering algorithms was checked manually using reference data.

#### 3.1. SMRF Algorithm

The SMRF algorithm was applied to Lidar point clouds and filtered ground and non-ground points in this case study. For the study area, approximately 215.000 points were filtered as ground points. Also, approximately 45.900 points were filtered as non-ground points (Figure 2).

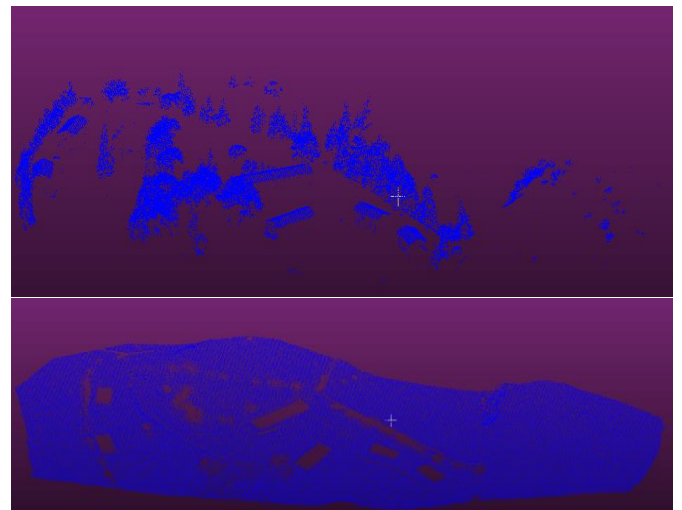


**Figure 2.** The ground (bottom) and the non-ground (top) points of Bergama test area with SMRF

### 3.2. CSF Algorithm

In this case study, the CSF algorithm was applied to Lidar point clouds and filtered ground and non-ground points. For the study area, approximately 206.000 points were filtered as ground points. Also, approximately 55.000 points were filtered as non-ground points (Figure 3).

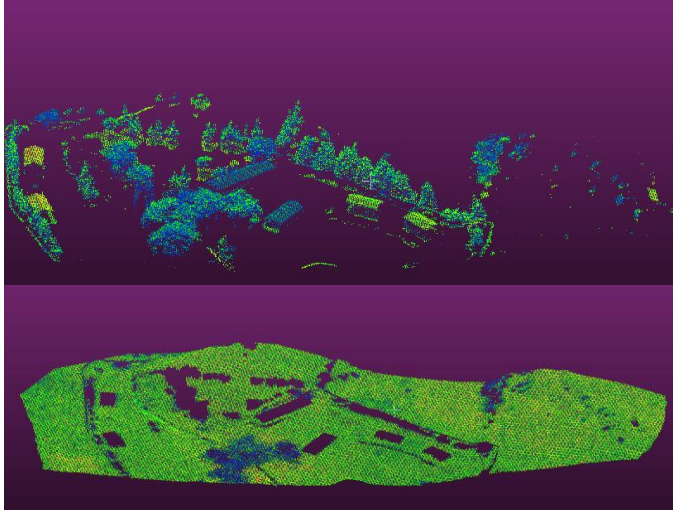


**Figure 3.** The ground (**bottom**) and the non-ground (**top**) points of Bergama test area with CSF

### 3.3. Evaluation of Filtering Data

During DTM filtering, Matlab and Cloud Compare software was used. Ground data and non-ground data were utilized as references for the filtering procedures, which were performed using manually edited reference data (Table 1). For the SMRF filtering approach, the filtered point cloud's accuracy achieved 94% accurate segmentation. The accuracy for LiDAR data was 94% when measured using the CSF algorithm (Table 2). In conclusion, both algorithms' accuracy is the same, proving that the approach used to filter the LiDAR data is adequate. Table 2 displays the outcomes of the filtering strategies.

**Table 2.** The Confusion Matrix of the filtering methods

Sample Dataset	Type Error I (%)	Type Error II (%)	Accuracy
Lidar CSF	5	11	94
Lidar SMRF	1	25	94

Confusion Matrix has performed a visual evaluation. The SMRF algorithm has produced the most trustworthy findings compared to the CSF approach. The computed type I, type II, and accuracy for the test samples are shown in Table 2. Lidar SMRF, in contrast, has the most significant type II error (%25). The LiDAR point cloud filtering techniques, however, produced identical findings.

### 4. Discussion

The reference data chosen with the manually edited methodology was utilized for the performance of filtering

methods, including both ground and non-ground data. For the SMRF filtering approach, the accuracy of the filtered point cloud achieved 94% correct segmentation. Likewise, the accuracy of LiDAR data was 94% when examined using the CSF algorithm. Finally, the accuracy of both methods is the same, indicating that the implemented method has a favorable effect on filtering LiDAR data.

The SMRF set of rules was designed to be aggressive with different ground filtering algorithms for LiDAR data, particularly in city environments on enormously varied topography. The SMRF algorithm is successful when optimized and even when using a single set of parameters, suggesting that novice users can achieve good results. Also, SMRF establishes a baseline performance for a progressive morphological filter implemented in its simplest form. The essence of the SMRF algorithm requires the input of a minimum surface and two parameters – a maximum window radius that corresponds to the most significant feature to be removed and a single slope parameter that governs the cell-based ground / non-ground flagging at each iteration. To categorize the original LiDAR points as bare earth (BE) or object, the SMRF creates a provisional ground surface (DTM) using these two characteristics and a provided minimum surface (OBJ). The primary benefit of SRMF is that it offers a straightforward conceptual and computational foundation for achieving effective outcomes. (Pingel, T. J., 2013)

### 5. Conclusion

This paper presents an experimental investigation of existing methods for ground filtering on point clouds. Two ground filtering approaches were compared for the same point cloud data, and the trials revealed several of the methods' properties. Bergama was chosen as the case study location for airborne LiDAR data. The accuracy values for both datasets and methods are sufficient for ground filtering, indicating that the provided approach effectively filters LiDAR data. Additionally, topographic features such as houses and trees are filtered when the ground point cloud is created. As a result, these items are the result of filtering failures. As a result, existing algorithms must be improved.

In future Lidar filtering applications, new filtering algorithms will be tested for large fields, and the influence of UAV point cloud quality on filtering outcomes will be examined.

### Acknowledgement

I acknowledge the General Directorate of Mapping. The General Directorate of Mapping in Turkey collected the LiDAR data used in this study.

### References

- Buján, S., M. Cordero, and D. Miranda, (2020). Hybrid Overlap Filter for LiDAR Point Clouds Using Free Software, 12(7): p. 1051.
- Chen, C., Guo, J., Wu, H., Li, Y., & Shi, B., (2021). Performance Comparison of Filtering Algorithms for

- High-Density Airborne LiDAR Point Clouds over Complex LandScapes. *Remote Sensing*, 13(14), 2663.
- Erol, S., Özögel, E., Kuçak, R. A., & Erol, B., (2020). Utilizing Airborne LiDAR and UAV Photogrammetry Techniques in Local Geoid Model Determination and Validation. *ISPRS International Journal of Geo-Information*, 9(9), 528.
- Klápště, P., Fogl, M., Barták, V., Gdulová, K., Urban, R., & Moudrý, V., (2020). Sensitivity analysis of parameters and contrasting performance of ground filtering algorithms with UAV photogrammetry-based and LiDAR point clouds. *International Journal of Digital Earth*, 13(12), 1672-1694.
- Meng, X., Currit, N., & Zhao, K. (2010). Ground filtering algorithms for airborne LiDAR data: A review of critical issues. *Remote Sensing*, 2(3), 833-860.
- Pfeifer, N. and G. Mandlbürger, (2018). LiDAR data filtering and digital terrain model generation, in *Topographic Laser Ranging and Scanning*. CRC Press. p. 349-378.
- Pingel, T. J., Clarke, K. C., & McBride, W. A. (2013). An improved simple morphological filter for the terrain classification of airborne LIDAR data. *ISPRS Journal of Photogrammetry and Remote Sensing*, 77, 21-30.
- Rashidi, P., & Rastiveis, H. (2017). Ground filtering lidar data based on multi-scale analysis of height difference threshold. *Int. Arch. Photogramm. Remote Sens. Spat. Inf. Sci*, 225-229.
- Štular, B., & Lozić, E. (2020). Comparison of Filters for Archaeology-Specific Ground Extraction from Airborne LiDAR Point Clouds. *Remote Sensing*, 12(18), 3025.
- Susaki, J. (2012). Adaptive slope filtering of airborne LiDAR data in urban areas for digital terrain model (DTM) generation. *Remote Sensing*, 4(6), 1804-1819.
- Süleymanoğlu, B. and M. Soycan, (2019). Comparison of filtering algorithms used for DTM production from airborne lidar data: A case study in Bergama, Turkey.



## 5<sup>th</sup> Intercontinental Geoinformation Days

igd.mersin.edu.tr



### Point cloud classification using machine learning algorithms and selection of relevant features

Muhammed Enes Atik\*<sup>1</sup>, Zaide Duran <sup>1</sup>

<sup>1</sup>Istanbul Technical University, Faculty of Civil Engineering, Department of Geomatics Engineering, Istanbul, Turkey

#### Keywords

Point cloud  
Machine learning  
Classification  
Feature selection  
Geometric features

#### Abstract

3D scene classification has become an essential task in photogrammetry, remote sensing, computer vision, and robotics. Point clouds are a data source containing geometric information for 3D world representation. Successful classification results are obtained using the point cloud's geometric information. Machine learning approaches are widely used for point cloud classification. In this study, point cloud classification was performed using random forest (RF) and support vector machine (SVM) algorithms. Geometric features are used to describe each point in the point cloud. However, not every feature may have the same effect on classification. For this reason, the most effective features were determined by applying the filter-based feature selection algorithm. As a result of feature selection, the F1-score value obtained with RF increased by 5.7%, and the F1-score value obtained with SVM increased by 16%.

## 1. Introduction

Three-dimensional (3D) point clouds are widely used in many applications such as urban geometry mapping, autonomous driving, virtual reality, cultural heritage, augmented reality, as they present the 3D representation of the environment with high precision (Bello et al., 2020; Atik and Duran, 2022). In particular, they provide more information about the structure of objects than 2D images, thanks to the 3D geometric information they contain.

Point cloud classification has become a focus of researchers over the past decade. Machine learning approaches have come to the fore because traditional rule-based approaches are insufficient for classification of complex and large point clouds. Machine learning algorithms provide powerful mathematical tool that can be used to segment large and complex point clouds. The discriminating rules are learned automatically from the training data in machine learning (Atik et al., 2021).

For machine learning approaches, features that define a point must be provided as input. Geometric features produced using the 3D geometry of the point cloud distinguish a point. However, not every input feature has the same effect on classification. Many feature selection algorithms have been proposed in the

literature to identify the most relevant features (Wu et al., 2013). Thus, it is aimed to improve the point cloud classification performance of machine learning approaches.

In this study, point cloud semantic segmentation was performed by machine learning using geometric features. Experiments were carried out using the mobile LiDAR dataset Oakland3D. Random Forest (RF) and Support Vector Machine (SVM), two popular machine learning algorithms, are preferred as classifiers. Filter-based Information Gain (IG) algorithm is used as a feature selection algorithm.

## 2. Data and Method

### 2.1. Oakland3D Dataset

Oakland3D dataset (Munoz et al., 2009) is one of the most used datasets obtained from mobile platform and includes urban environment. The Oakland dataset consists of 36,932 training points, 91,579 validation points and 1.3 million testing points, which include 5 classes, namely ground, vegetation, façade, wire and pole/trunk. The wire and pole/trunk classes were removed, so they contain a few points. A sample from the dataset is shown in Fig. 1.

\* Corresponding Author

(atikm@itu.edu.tr) ORCID ID 0000-0003-2273-7751  
(duranza@itu.edu.tr) ORCID ID 0000-0002-1608-0119

Cite this study

Atik, M.E. & Duran, Z. (2022). Point Cloud Classification Using Machine Learning Algorithms and Selection of Relevant Features. 5<sup>th</sup> Intercontinental Geoinformation Days (IGD), 168-171, Netra, India

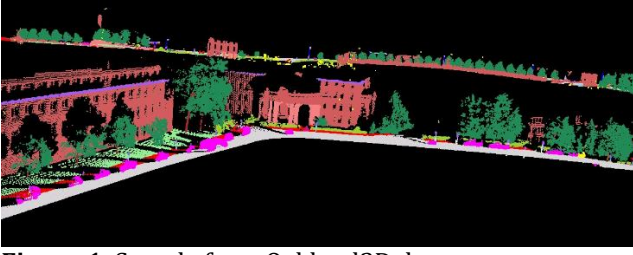


Figure 1. Sample from Oakland3D dataset

## 2.2. Random Forest

Random Forest (RF) (Breiman, 2001) is a machine learning approach that consists of uncorrelated trees and averages these trees. In many problems, the performance of random forests is easily increased. Each tree generates a prediction, and the class with the most votes is assigned the model's prediction. A sub-dataset is assigned to each tree for training in the bagging algorithm.

Two parameters are required to generate a tree with the RF classifier. These parameters are the number of variables used in each node and the number of trees to develop to determine the best split.

## 2.3. Support Vector Machine

Support Vector Machines (SVM) (Cortes and Vapnik, 1995) is a supervised machine learning algorithm used for both classification and regression. The main purpose of SVM is to classify the data by finding the hyperplane with the maximum distance between the data points of both classes. The optimal hyperplane can be obtained by using Eq. 1. For a given set of a sample  $x_i$  ( $i=1,2,\dots, N$ ):

$$f(x) = w^T x + b = \sum_{j=1}^N w_j x_j + b = 0 \quad (1)$$

where  $w$  is an  $N$ -dimensional vector and  $b$  is a scalar, and they are used to define the hyperplane.

## 2.4. Extraction of Geometric Features

Geometric features are used to describe the local geometry of a point in the point cloud. Geometric features are calculated by the eigenvalues ( $\lambda_1, \lambda_2, \lambda_3$ ) of the eigenvectors ( $v_1, v_2, v_3$ ) derived from the covariance matrix of any point  $p$  of the point cloud:

$$cov(S) = \frac{1}{S} \sum_{p \in S} (p - \bar{p})(p - \bar{p})^T \quad (2)$$

where  $\bar{p}$  is the centroid of the support  $S$  (Weinmann et al., 2015). Calculated features are the sum of eigenvalues, omnivariance, eigenentropy, anisotropy, planarity, linearity, surface variation, sphericity, and verticality.

## 2.5. Feature Selection with Information Gain

Some features have a greater impact on the semantic segmentation of the algorithm, while others do not. Feature selection is defined as the task of determining the minimum number of features that will accurately

represent the data. Feature selection methods can be grouped as filter-based, wrapper-based, and embedded methods. Both wrapper-based and embedded methods depend on classifier algorithms. Filter-based methods are independent of the classifier (Weinmann et al., 2015).

Information Gain (IG) is an entropy-based feature selection algorithm and measures the amount of information provided by features. It is widely used in the literature for text classification (Lei, 2012).

## 2.6. Experiment

Geometric features were calculated for the training and test data. Geometric features are calculated using neighboring points falling into the sphere with a certain radius around the point. In this study, the sphere radius was determined as 1.5 m. This value is the optimum value determined for the Oakland3D data set in previous studies.

The training parameters determined for RF are maximum depth 100, random state 100 and minimum sample split 80. The parameters determined for SVM are kernel radial basis function (RBF) and decision function one-vs-rest (ovr). Values were determined experimentally.

Classification was performed using all features with RF and SVM algorithms. Then, the semantic segmentation process was repeated using 5 features determined by IG. F1 score was used as evaluation metrics. For the experiments, i7-11800H, 2.30 GHz processor, GTX 3070 graphics card, and 32 GB RAM hardware was used.

## 3. Results and Discussion

Feature importance values were calculated with IG using the entire training set. A threshold value of 0.7 has been determined for feature selection. Five features with importance greater than 0.7 were selected as the most relevant feature: surface variation, normal change rate, sphericity, anisotropy and verticality. Feature importance values and selected features are shown in Fig. 2.

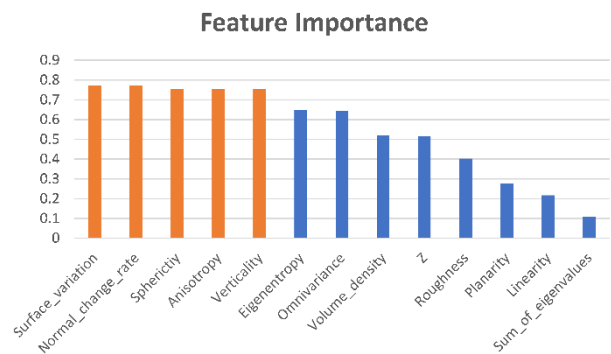


Figure 2. Calculated feature importances with IG. Selected features are marked as orange

When all features were used, 86.6% and 77.4% F1-scores were obtained with RF and SVM, respectively. With both algorithms, less accuracy was obtained in the building than in vegetation and ground. When Table 1 is

examined, it is revealed that feature selection significantly improves the semantic segmentation performance of RF and SVM. The average F1-score of the RF increased by 5.7%, while the average F1-score of the SVM increased by 16%. Feature selection provided the highest improvement in the building class. It was concluded that not all geometric features have the same effect. The results are presented in Table 1. Classified point clouds are shown in Fig. 3.

**Table 1.** F1-score of the algorithms based on features.

Class	All Features		Selected Features	
	RF	SVM	RF	SVM
Building	73.6	67.0	85.9	88.3
Vegetation	87.5	83.2	91.6	92.6
Ground	98.6	82.0	99.3	99.3
Average	86.6	77.4	92.3	93.4

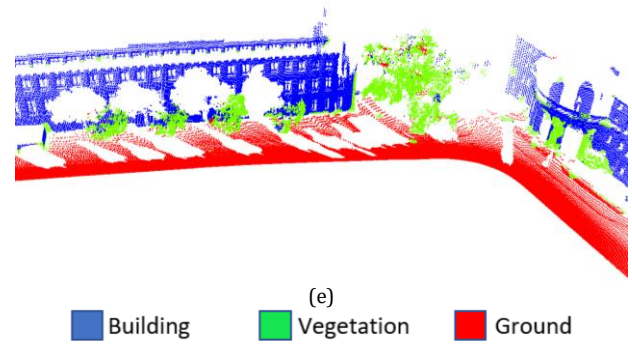
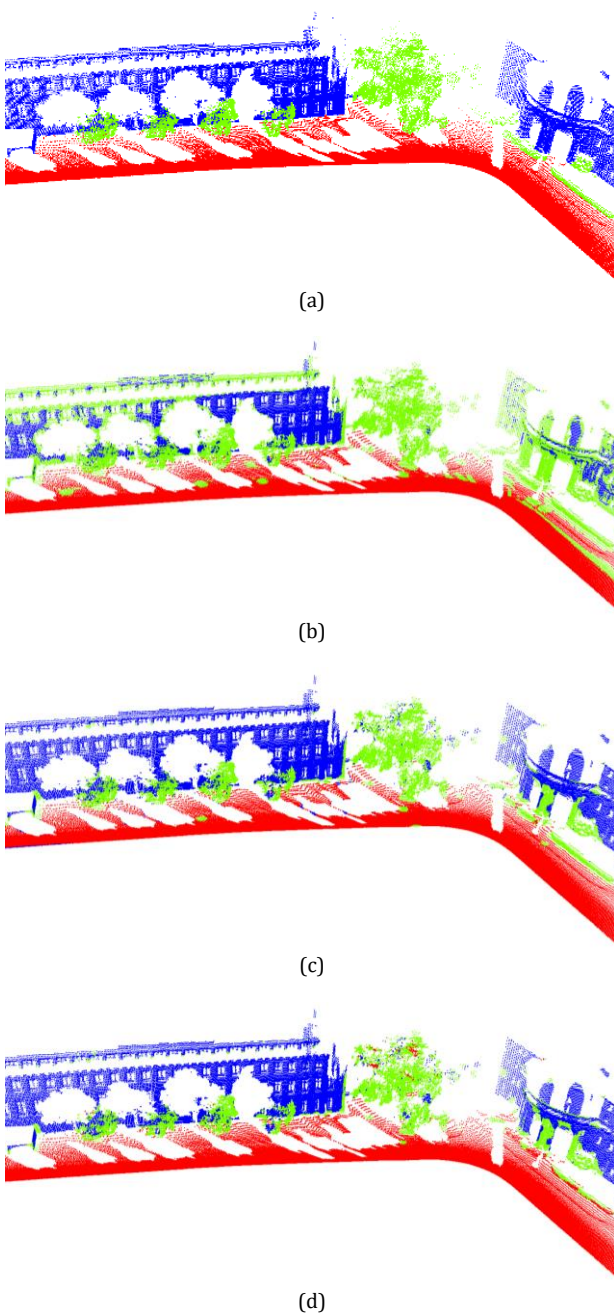


**Figure 3.** Classified point clouds. (a) Ground truth Prediction with RF using all features; (c) Prediction with SVM using all features; (d) Prediction with RF using selected features; (e) Prediction with SVM using selected features

#### 4. Conclusion

In this study, research on improving the point cloud classification performance of machine learning algorithms by feature selection is presented. The most effective geometric features on classification were determined by the filter-based IG algorithm. Classification performances of RF and SVM algorithms have increased thanks to feature selection.

In future studies, datasets and algorithms obtained from different sensors can be used. In addition, feature selection algorithms can be integrated with deep learning networks.

#### Acknowledgement

This research was funded by Istanbul Technical University Scientific Research Office (BAP) grant number MDK-2021-42992.

#### References

- Bello, S. A., Yu, S., Wang, C., Adam, J. M., & Li, J. (2020). Deep learning on 3D point clouds. *Remote Sensing*, *12*(11), 1729.
- Atik, M. E., & Duran, Z. (2022). Selection of Relevant Geometric Features Using Filter-Based Algorithms for Point Cloud Semantic Segmentation. *Electronics*, *11*(20), 3310.
- Atik, M. E., Duran, Z., & Seker, D. Z. (2021). Machine learning-based supervised classification of point clouds using multiscale geometric features. *ISPRS International Journal of Geo-Information*, *10*(3), 187.
- Wu, B., Chen, C., Kechadi, T. M., & Sun, L. (2013). A comparative evaluation of filter-based feature selection methods for hyper-spectral band selection. *International Journal of Remote Sensing*, *34*(22), 7974-7990.
- Munoz, D., Bagnell, J. A., Vandapel, N., & Hebert, M. (2009, June). Contextual classification with functional max-margin markov networks. In *2009 IEEE Conference on Computer Vision and Pattern Recognition* (pp. 975-982). IEEE.
- Breiman, L. (2001). Random forests. *Machine learning*, *45*(1), 5-32.
- Cortes, C., & Vapnik, V. (1995). Support-vector networks. *Machine learning*, *20*(3), 273-297.

Weinmann, M., Jutzi, B., Hinz, S., & Mallet, C. (2015). Semantic point cloud interpretation based on optimal neighborhoods, relevant features and efficient classifiers. *ISPRS Journal of Photogrammetry and Remote Sensing*, 105, 286-304.

Lei, S. (2012, March). A feature selection method based on information gain and genetic algorithm. In *2012 international conference on computer science and electronics engineering* (Vol. 2, pp. 355-358). IEEE.



## 5<sup>th</sup> Intercontinental Geoinformation Days

igd.mersin.edu.tr



### Documentation of stone material deterioration on the facades of historical masonry buildings by terrestrial laser scanning: A case study of a Mansion in Mardin

Lale Karataş<sup>\*1</sup>, Aydın Alptekin<sup>2</sup>, Murat Yakar<sup>3</sup>

<sup>1</sup>Mardin Artuklu University, Mardin Vocational School, Department of Architecture and Urban Planning, Mardin, Türkiye

<sup>2</sup>Mersin University, Faculty of Engineering, Department of Geological Engineering, Mersin, Türkiye

<sup>3</sup>Mersin University, Faculty of Engineering, Geomatics Engineering Department, Mersin, Türkiye

#### Keywords

Terrestrial Laser Scanning  
Material Deterioration  
Stone Material  
Orthophoto  
Sustainability

#### Abstract

The traditional house design in Mardin has been determined by some local criteria in parallel with the complex historical process. These are yellow limestone, which is abundant in the region and obtained from quarries in the region, continental climate and topography. Except for the joinery, the only material used in architecture is stone. The subject of this research is an example of civil architecture located in Şar Neighborhood in the Artuklu district of Mardin. The mansion was built in the area where the historical city walls, which no longer exist today, surround the city from the south, in the Sar District of Mardin. The building, which was built on a wide area, carries the characteristics of the historical buildings in the region with its construction technique, plan features and materials. The aim of the study is to detect the stone material deteriorations of the facades of the mansion, which is a traditional masonry building, by terrestrial laser scanning method, and to ensure that this example of civil architecture is transferred to future generations as original. As a result of the study, many types of stone material deterioration were encountered on the facades of the building, such as surface loss, contamination-blackening, plant formation, melting, joint loss and salinization.

## 1. Introduction

Moisture content in the atmosphere, heat, rain, wind, temperature changes, chemical reactions and corrosion are factors of deterioration for the building blocks. Exposure of building materials to atmospheric conditions for a long time causes various types of deterioration in building facades. This deterioration turns into physical and chemical wear of building materials in later stages. Physical and chemical weathering, on the other hand, causes the formation of chemical and mechanical processes that cause damage to the microstructure and the expansion of micro cracks (Karataş, 2016; Karataş, 2022; Karataş et al., 2022).

The rich architectural heritage of our Turkey is also manifested in stone monuments. The building, which is the subject of the study, is located in the Şar Neighborhood of the Artuklu district of Mardin Province which has the characteristics of historical buildings in the region with its construction technique, plan features and materials. As in many buildings in the region as construction material, there is an intense use of stone

materials in the historical building examined. The aim of the study is to detect the stone material deteriorations in the building by terrestrial laser scanning method and to ensure that this civil architectural example is transferred to future generations as original.

## 2. Method

In the study, literature review, archive research and terrestrial laser scanning method were used. First of all, the information about the building was compiled from the archive of the Mardin Metropolitan Municipality. Afterwards, field research was carried out and the structure was scanned with a terrestrial laser scanner (Faro Focus Laser Scanner) (Figure 1).

Point clouds were obtained in the scanning process. The point clouds obtained in the laser scanning process were transferred to the software called PointCab Origins 4.0. In the next stage, orthophotos of the structure were produced by taking sections from the desired places on the 3D images of the structure using the software called PointCab Origins 4.0 (Figure 2-5).

#### \* Corresponding Author

<sup>\*</sup>(lalekaratas@artuklu.edu.tr) ORCID ID 0000-0001-8582-4612  
(aydinalptekin@mersin.edu.tr) ORCID ID 0000-0002-5605-0758  
(myakar@mersin.edu.tr) ORCID ID 0000-0002-2664-6251

#### Cite this study

Karataş, L, Alptekin, A., & Yakar, M. (2022). Documentation of stone material deterioration on the facades of historical masonry buildings by terrestrial laser scanning: A case study of a Mansion in Mardin. 5<sup>th</sup> Intercontinental Geoinformation Days (IGD), 172-175, Netra, India

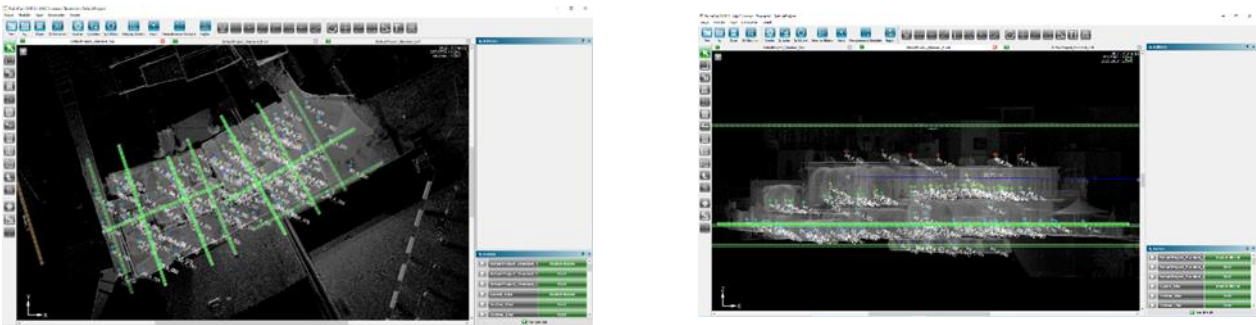


Figure 1. Stations used in scanning

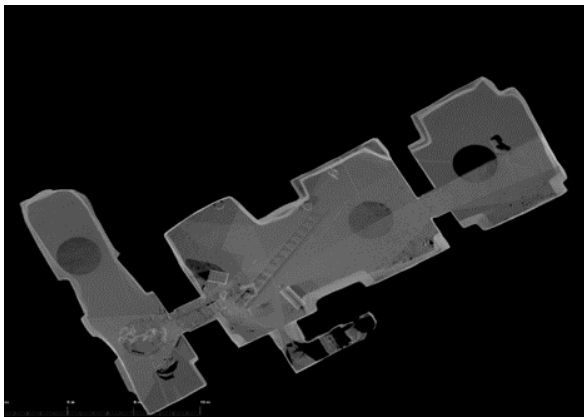


Figure 2. Orthophoto of the Layout Plan

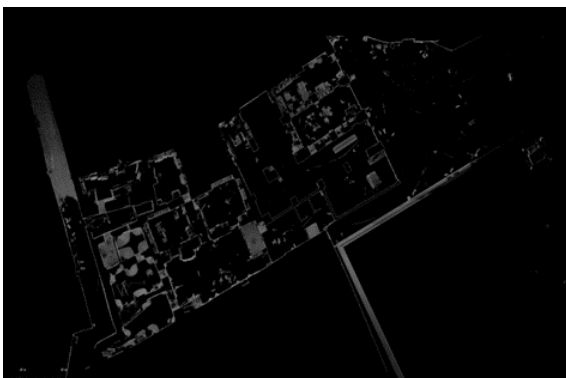


Figure 3. Orthophoto of the Ground Floor Plan



Figure 4. Orthophoto of the Western Front



Figure 5. Orthophoto of the Eastern Front

### 3. Results

After comparative evaluation of the analytical drawings obtained from the orthophotos obtained from the laser scanning made in the previous section, the following findings were reached. Relief drawings of the floor plans and facades of the building were created from the orthophotos obtained from the scanning. Material deteriorations were analyzed on the facade surveys created. The building consists of basement, ground floor and 1st floor and covers a total area of 623 m<sup>2</sup>. The building itself consists of different parts. The analysis was made by considering these sections. The ground floor was divided into 5 sections and examined. 3 separate courtyards and spaces associated with the courtyard are grouped. In addition, the stores and warehouses facing the east façade were separated and analyzed. The 1st floor plan, like the ground floor, was analyzed in 5 separate sections.

#### 3.1. Floor Plans

The building consists of basement, ground floor and first floor. The basement floor area is 72 m<sup>2</sup> and consists of 3 separate spaces. The spaces are made of rubble stone. The floor covering is concrete screed. The ceiling is in the form of a vault. The building consists of 5 separate sections on the ground floor and the 1st floor, and each section is functional in itself (Figure 6-8).

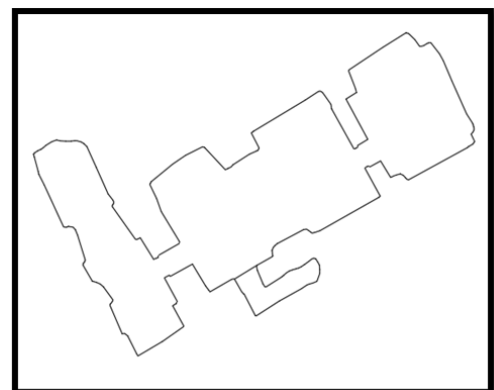


Figure 6. Basement Floor Plan

#### 3.2. Western Front

The western façade of the building is the side entrance façade and has a total length of 23 m. The building facade height is 3.51 m at the lowest and 9.45 m at the highest. The façade wall of the building was built with rubble stone and faceted stone (Figure 9).

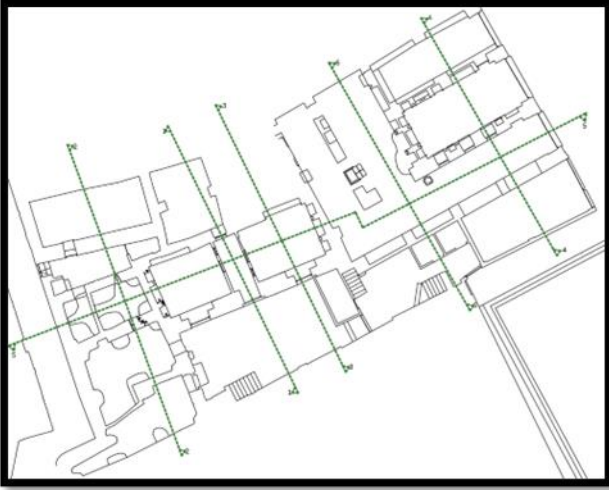


Figure 7. Ground Floor Plan

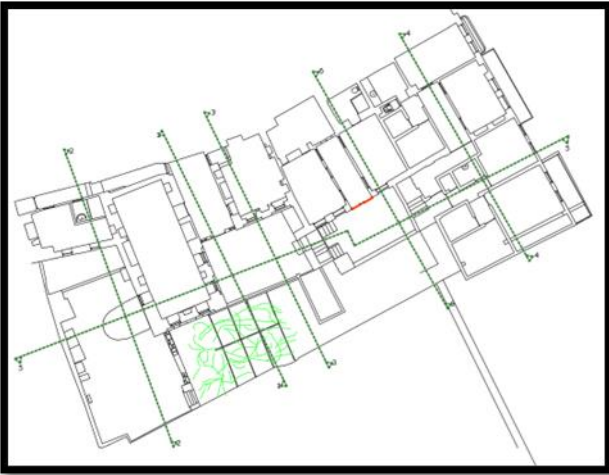


Figure 8. First Floor Plan



Figure 9. Western Front

### 3.3. Eastern Front

The eastern façade of the building is the entrance façade of spaces such as workshops and shops. Its total length is 17 m and the facade height is 9.10 m. The facade wall is covered with stone and rubble stone, and some of it is plastered with cement-based mortar (Figure 10).



Figure 10. Eastern Front

### 4. Conclusion

The study, based on terrestrial laser scanning research, combines the data obtained from laser scanning with various techniques for the analysis of material deterioration of stone facades with data obtained from on-site inspection, focusing on the documentation of material deterioration of stone facades. The study is important in that it systematically exemplifies the methods of creating a base for documenting material deterioration by converting the data obtained from laser scanning into orthophotos, which are necessary for the preservation of original materials in historical buildings. With the study, the material deterioration of the building was determined and the information reflecting the original state of the building was transferred and it was aimed to transfer these civil architectural examples to future generations as originals. As a result of the study, many types of stone material deterioration were encountered on the facades of the building, such as surface loss, contamination-blackening, plant formation, melting, joint loss and salinization.

It is seen that the structures that have similar features with our construction in Mardin Province were generally built in the 19th and 20th centuries. During the preparation and implementation of the renovation and restoration project, emphasis should be placed on preserving the original qualities, minimizing the interventions, and applying the traditional material, technique and construction system. Building elements with wear and deterioration should be repaired by adhering to the original condition.

### References

- Karataş, L., Alptekin, A., Kanun, E., & Yakar, M. (2022). Tarihi kârgir yapılarda taş malzeme bozulmalarının İHA fotogrametrisi kullanarak tespiti ve belgelenmesi: Mersin Kanlıdivane ören yeri vaka çalışması. *İçel Dergisi*, 2 (2), 41-49
- Karataş, L. (2016). Mardin Kentsel Sit Alanındaki İbadet Yapılarında Malzeme Kullanımı ve Sorunları Üzerine Bir Araştırma. Master's Thesis, Uludağ University, Fen Bilimleri Enstitüsü, Bursa, 340p (in Turkish).

- Karatas, L. (2023). Investigating the historical building materials with spectroscopic and geophysical methods: A case study of Mardin Castle. *Turkish Journal of Engineering*, 7(3), 266-278
- Karataş, L., Alptekin, A., & Yakar, M. (2022). Creating Architectural Surveys of Traditional Buildings with the Help of Terrestrial Laser Scanning Method (TLS) and Orthophotos: Historical Diyarbakır Sur Mansion. *Advanced LiDAR*, 2(2), 54–63.
- Karataş, L., Alptekin, A. & Yakar, M. (2022). Determination of Stone Material Deteriorations on the Facades with the Combination of Terrestrial Laser Scanning and Photogrammetric Methods: Case Study of Historical Burdur Station Premises. *Advanced Geomatics*, 2(2), 65-72.
- Karataş, L., Alptekin, A., & Yakar, M. (2022). Detection and documentation of stone material deterioration in historical masonry structures using UAV photogrammetry: A case study of Mersin Aba Mausoleum. *Advanced UAV*, 2(2), 51–64.
- Karataş, L., Alptekin, A, & Yakar, M. (2022). Detection of materials and material deterioration in historical buildings by spectroscopic and petrographic methods: The example of Mardin Tamir Evi. *Engineering Applications*, 1(2), 170-187
- Karatas, L. (2022). Integration of 2D mapping, photogrammetry and virtual reality in documentation of material deterioration of stone buildings: Case of Mardin Şeyh Çabuk Mosque. *Advanced Engineering Science*, 2, 135-146
- Karataş, L., Alptekin, A. & Yakar, M. . (2022). Analytical Documentation of Stone Material Deteriorations on Facades with Terrestrial Laser Scanning and Photogrammetric Methods: Case Study of Şanlıurfa Kışla Mosque. *Advanced LiDAR*, 2(2), 36–47.
- Karataş, L., Alptekin, A., & Yakar, M. (2022). Investigation of Molla Hari (Halil) Süleyman Paşa Mosque’s material deteriorations. 4th Advanced Engineering Days, 55-57
- Karataş, L., Alptekin, A., & Yakar, M. (Year). Restitution suggestion for Mardin TatlıDede Mansion. 4th Advanced Engineering Days, 61-63



## 5<sup>th</sup> Intercontinental Geoinformation Days

igd.mersin.edu.tr



### Can we “see” the neighborhood-built environments from a UAV?

Xin Hong\*<sup>1</sup>

<sup>1</sup>Koç University Research Center for Anatolian Civilizations, Türkiye

#### Keywords

Sidewalk-homogenous neighborhood  
UAV  
Built environments  
Deep learning  
Public health

#### Abstract

Health-related built environments in a neighborhood are significant to the health of the residents. In order to quantitatively examine built environments at the neighborhood scale, the operational unit *neighborhood* should be clearly defined in advance. This paper assessed a newly developed neighborhood concept, *sidewalk-homogenous neighborhood*, which corresponds to the economic profile and the health behaviors of residents. This study examined the applicability of the sidewalk-homogenous neighborhood in the process of detecting and evaluating built environments at the street level in four study sites. Sidewalks and greenery as the representations for built environments were classified on UAV images using the combined applications of geographic information systems (GIS) and deep learning. The study addressed that the sidewalk-homogenous neighborhood is a practical, operational unit to identify the spatial disparities of built environments at the neighborhood scale. In addition, the study revealed the inequality in Unmanned Aerial Vehicle (UAV) research opportunities between rich and poor neighborhoods.

#### 1. Introduction

In quantitative analysis of neighborhood effects, census geography is often used as a surrogate neighborhood due to its simplicity and low cost (Clapp and Wang 2006). However, census geography can hardly respect the social and behavioral relationships among residents in the real world. Researchers may need to move beyond census geography and develop a neighborhood concept that maximizes sociological reality and statistical measurability for targeted research.

This study examined the applicability of *sidewalk-homogeneous neighborhood*, a newly proposed neighborhood concept for health-related built environment research. Four sidewalk-homogenous neighborhoods with different economic levels were used to examine the neighborhood effects in health-related built environments. Images captured by an Unmanned Aerial Vehicle (UAV) were processed with the combined applications of geographic information systems (GIS) and deep learning in the detection of spatial distribution of sidewalk and greenery at the neighborhood scale.

#### 2. Method

This study was to further expand the concept of sidewalk-homogenous neighborhood, which had been initially proposed in Hong (2021) and Hong et al. (2022). The applicability of the proposed neighborhood concept was tested at four study sites in Northeast Ohio, USA. Sidewalks and greenery detected using the combined methods of GIS and deep learning on UAV imagery in Hong et al. (2022) were further utilized to examine the sidewalk-homogenous neighborhood concept in this paper.

##### 2.1. Defining the sidewalk-homogenous neighborhoods

There are two defining criteria for a sidewalk-homogenous neighborhood: 1) house prices within the neighborhood are similar; and 2) all the streets of the neighborhood are residential (local) roads as defined by the road classification system in Ohio Department of Transportation (2020). The first factor suggests the economic component of a neighborhood, indicating that the residents are in a similar economic background. The second factor respects the habit of sidewalk usage.

\* Corresponding Author

(xhong21@ku.edu.tr) ORCID ID 0000-0001-9266-9307

Cite this study

Hong, X. (2022). Can we “see” the neighborhood built environments from a UAV? 5<sup>th</sup> Intercontinental Geoinformation Days (IGD), 176-178, Netra, India

People are more likely to use sidewalks that are by local roadways due to a lower speed and less traffic (Teff 2011).

Four study sites in Northeast Ohio, USA with different economic levels were demarcated in Hong et al.'s (2022) study based on the criteria defined in the sidewalk-homogenous neighborhood. They were named *River Bend*, *North Cherry*, *Sandy Lake*, and *Summit Mall*. The ranges of house prices from the lowest to the highest and the area of each neighborhood are listed in Table 1. The boundaries of the four neighborhoods and the UAV flight paths are displayed in Figure 1. The house price in each sidewalk-homogenous neighborhood is in the same level of price range and the roadways within the neighborhood are all residential roads where the speed limits are below either 25 or 30 miles per hour. The difference in the house price range between neighborhoods was to examine how sidewalk-homogenous neighborhoods with different economic components may differ from each other in terms of built environments.

**Table 1.** House prices and area of neighborhoods (Hong et al. 2022)

Neighborhood	House price (Thousand US \$)	Area (sq km)
North Cherry	70 - 150	0.8
Sandy Lake	170 - 300	4.48
Summit Mall	220 - 500	1.13
River Bend	300 - 900	0.61

### 3. Results and Discussion

Figures 2 and 3 demonstrate the sidewalk density and greenery ratio at the street level of each neighborhood, respectively. By visual observation, we may see that the neighborhoods at the higher economic level (*River Bend* and *Summit mall*) have greater sidewalk density and greenery ratio than the neighborhoods at the lower economic level (*Sandy Lake* and *North Cherry*). In addition, the intra-neighborhood differences are more remarked in the lower-economic neighborhoods.

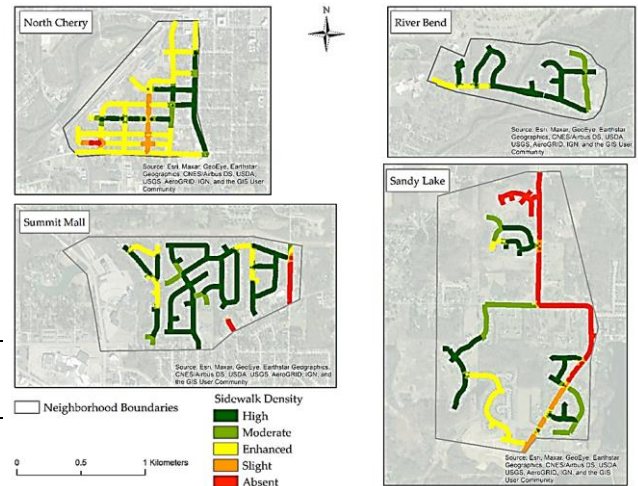


**Figure 2.** Sidewalk density at the street level of the sidewalk-homogenous neighborhood (Hong et al. 2022)

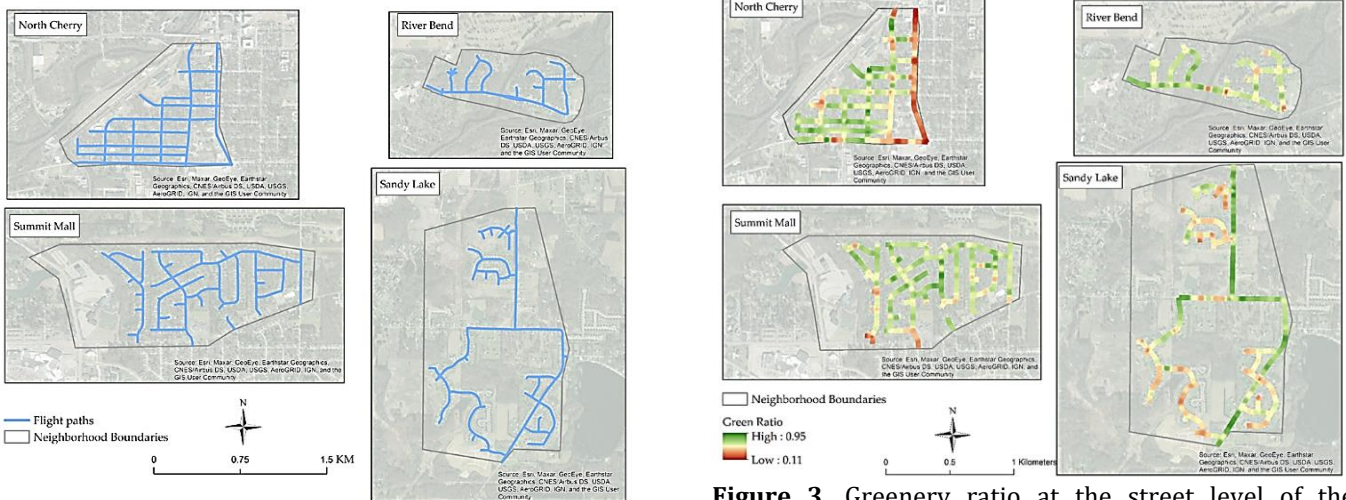


**Figure 3.** Greenery ratio at the street level of the sidewalk-homogenous neighborhood (Hong et al. 2022)

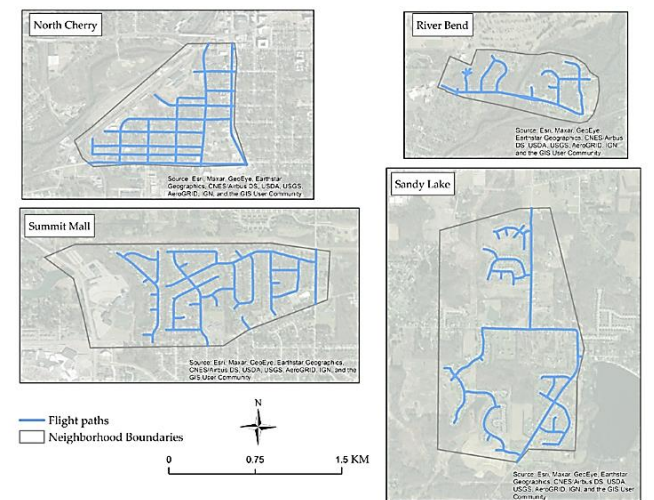


**Figure 1.** The boundaries of the neighborhoods and the UAV flight paths

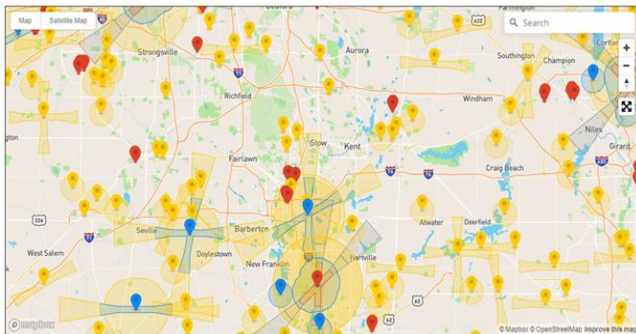
#### 2.2. The built environments revealed in the sidewalk-homogenous neighborhood

The densities of sidewalks and greenery in each street were detected and classified using deep learning methods and GIS in processing UAV imagery. Please refer to Hong et al. (2022) for details on the workflow.

From the field experience of collecting images using a UAV, I realized that data collection over certain neighborhoods is restricted from autonomous flight mode over areas that are classified as either restricted, authorization, or warning zones by the Federal Aviation Administration (FAA). In the original plan for the study, two more neighborhoods with lower economic levels were planned as the study sites. However, they are located in the warning zone where the autonomous flight mode is not allowed. Although the manual flight mode is

permitted, the scenes would be hardly captured with consistent configurations when flying the UAV manually. For instance, in the manual flight mode, it would be hard to ensure that the entire video or all the photos are captured at the same flying altitude, the same perspective, and the constant speed.

Figure 4 displays restricted/ authorization/ warning zones around my study sites (the Greater Akron region). Many marginalized neighborhoods in the Greater Akron region are within the warning zones of airspace (see yellow zones in Figure 4). The airspace from the ground of either an airport or a prison up to a certain distance is a warning zoom. It turns out that on one hand, most residential neighborhoods around an airport or a prison are economically marginalized. On the other hand, most neighborhoods with higher economic levels tend to be far away from those facilities and in airspace that UAVs are free to fly. The inequality in research opportunities between economically advantaged and disadvantaged neighborhoods may exacerbate the existing gap in built environment quality between the rich and the poor.



● Restricted Zones      ● Authorization Zones      ● Warning Zones

**Figure 4.** The restricted/authorization/warning zones in the Greater Akron region. Locators (in red, blue, or yellow) are the facilities (e.g., airports, prisons) that their airspace from the ground up to a certain distance are the restricted, authorization, or warning zones (DJI 2021)

#### 4. Conclusion

This paper attempted to move beyond the traditional neighborhood concepts and examined applicability of the newly developed concept of sidewalk-homogenous n for

health-related built environment studies at the neighborhood scale. The measurability of sidewalk-homogenous neighborhood was tested in four residential neighborhoods with different economic levels in Northeast Ohio, USA. Sidewalk density and greenery ratio at the street level in each neighborhood were examined and compared with the combined applications of deep learning and GIS in processing UAV imagery. The results indicated that the spatial differences between and within neighborhoods can be revealed in the spatial unit operated by the sidewalk-homogenous neighborhood. In addition, the results also addressed the inequality in research opportunity between the rich and the poor neighborhoods.

#### Acknowledgement

This research was supported by the Research / Scholarly Activity Support from the University Research Council, Kent State University; the Research Award from the Graduate Student Senate, Kent State University; and the Norah Henry Award from the Department of Geography, Kent State University.

#### References

- Clapp, J. M., & Wang, Y. (2006). Defining neighborhood boundaries: are census tracts obsolete? *Journal of Urban Economics* 59: 259-284.
- DJI, (2021). *Fly safe geo zone map*. Retrieved June 15, 2021. Retrieved June 15, 2021.
- Hong, X. (2021). A convolutional neural network for detecting and mapping built environment at neighborhood scale. Doctoral Dissertation, Kent State University, Kent, Ohio, USA.
- Hong, X., Sheridan, S., & Li, D. (2022). Mapping built environments from UAV imagery: a tutorial on mixed methods of deep learning and GIS. *Computational Urban Science*, 2(1), 1-15. <https://doi.org/10.1007/s43762-022-00039-w>
- Ohio Department of Transportation. (2020). *Ohio roadway functional class*. Retrieved June 15, 2021.
- Tefft, B.C. (2011). Impact speed and a pedestrian's risk of severe injury or death [Technical report]. AAA Foundation for Traffic Safety. Washington, D.C..



## 5<sup>th</sup> Intercontinental Geoinformation Days

igd.mersin.edu.tr



### Development of Open-Source Applications Using WebGIS Technology

Mehmet Alper Şahin<sup>\*1</sup>, Murat Yakar<sup>1,2</sup>, Ali Ulvi<sup>1</sup>, Abdurahman Yasin Yiğit<sup>2</sup>

<sup>1</sup>Mersin University, Institute of Sciences, Department of Remote Sensing and Geographic Information Systems, Mersin, Türkiye

<sup>2</sup>Mersin University, Faculty of Engineering, Department of Geomatics Engineering, Mersin, Türkiye

#### Keywords

Internet based GIS  
GIS  
Open-source  
Application development  
GeoServer

#### Abstract

In this day and age of technology advancing at a rapid pace, it is very important for people to understand the world they live in and know where in the world they are. With the support of rapidly developing technology, it is much easier for humans to access spatial information than it used to be. Geographic information systems (GIS) can now be used with inexpensive mobile devices. These devices can be GPS, handheld computers, tablets, or even cell phones. With the spread of the Internet, the importance of geospatial information systems became much better understood. Today, such powerful geographic information systems can be used via the Internet (Yandex Maps, Bing Maps, Google Maps, OpenStreet, etc.). In the present day when Web-based GIS applications rapidly spread, and commercial or free source-coded GIS infrastructures can be found easily, a GIS application that has the basic GIS functions that hold the information of historic places and buildings' information by using a GeoServer can be realized. This study including the documentation of this application will supply basic and general information about how a GIS system is and how it works to those concerned about it. The web application that is a part of the study has been developed by Python, GeoServer, and PostgreSQL Server and has been designed and realized to be able to keep a historic place's geographic and written information. The application can be seen in two parts; the first part is the part that keeps the written data. Written data is kept through PostgreSQL Server. And the second part is the part that keeps the geographic data. Geographic data is kept through map source files and published through GeoServer. Those maps that are published through Python can be viewed through the web pages. Several basic GIS operations can be done via a web page. Besides the detailed information on GIS, wide information about the technologies necessary for developing the GIS applications via the internet and internet technologies are included within the documentation of the study.

#### 1. Introduction

Location is the key to understanding the world in which humanity lives. Knowing and using the location increases the rhythm of life. Thus, people want to know their surroundings and where they are. Electronic device manufacturers and software technology companies (such as mobile phones, PDAs, handheld GPS, Google Maps, Google Earth, and Microsoft Virtual Earth) use technology and science to meet people's demands. These technologies become habitual for the people who use them. They do not go to unfamiliar places without

looking on the internet, or they send their location or meeting point to their friends using the GPS features of their phones. Today, GIS technologies or related technologies are entering our lives at an increasing rate, and we welcome these technologies sincerely.

The aim of this study is to show how to develop web GIS software and use it with an ordinary internet browser. In the next chapters, the problems, and difficulties that I encountered during the work will be presented. Anyone who develops GIS software within the framework I have made can use these solutions.

#### \* Corresponding Author

(mehmetalpersahin@engineer.com) ORCID ID 0000-0003-0133-5278  
(myakar@mersin.edu.tr) ORCID ID 0000-0002-2664-6251  
(aliulvi@mersin.edu.tr) ORCID ID 0000-0003-3005-8011  
(abdurahmanyasinyigit@gmail.com) ORCID ID 0000-0002-9407-8022

#### Cite this study

Şahin, M. A., Yakar, M., Ulvi, A. & Yiğit, A. Y. (2022). Development Of Open-Source Applications Using WebGIS Technology. 5<sup>th</sup> Intercontinental Geoinformation Days (IGD), 179-182, Netra, India

## 2. Method

### 2.1. GIS Applications using the Internet

The Internet is an endless interactive medium and source of information. Someone needs to produce this information and present it on the internet so that others can access it and use it for their own purposes. Several online GIS software has appeared in recent years (Google Maps, Yandex Maps, Bing Maps, OpenStreet, etc.). These online apps are indeed quite useful in our daily life. These powerful GIS applications convert GIS data into basic images and HTML code and serve in this form so that an ordinary internet browser can easily interpret the code and display output maps and graphs. Internet technology has reinvented itself and taken to an incredibly different level, but underneath all that, programming languages are no different than they were 5 or 6 years ago. We used HTML and Javascript back then, and we still use HTML and Javascript today. Although we use the same programming languages, our usage patterns have changed a lot over the years. In this section, internet technologies and internet programming languages will be explained as broadly as possible.

### 2.2. Network Technologies

The basic components of the Internet are "packet networks" (called "nets" for short in the rest of this section). This term refers to any technology capable of transferring data packets from one computer to another; Figure 3.1 shows an abstract view of such a network. Usually, many computers are connected to the network, providing them with "addresses" that can be used to specify the source and destination of packets. Most computers connected to networks are classified as "hosts". These are computers rather than running programs; desktop computers and servers fall into this category. Few computers provide functions related to network operation only. For example, "gateways", "routers" and "bridges" transfer packets between networks. There is a wide variety of technologies that fit into this general pattern. For example, LANs such as Ethernet (Şahin & Yakar, 2021) use medium access control (MAC) addresses. These are 48-bit addresses allocated by manufacturers of interface cards installed in hosts. The "network service" provided by a LAN is simple: a computer creates a packet containing the destination MAC address and asks the network to deliver it, just like sending a letter. This is called a "connectionless" (CL) service. For example, a quite different style of service is provided by asynchronous transfer mode (ATM) (Yakar et al., 2014) networks. In these networks, there is an initial negotiation phase where the computer tells the network what type of data it wants to send and the address of the destination. This gives the computer the opportunity to determine the quality of service (QoS) it needs (throughput limits, transfer latency, etc.). The network must decide whether it can meet the demand. If it can, it tells the computer that a "connection" has been established with the target, and data transfer can begin. This is like making a phone call, where the person dials a number and makes a call before

the conversation begins and is called a "connection-oriented" (CO) service. Addresses in CO networks are used only during the connection establishment phase (Farrel, 2004).

Almost all network technologies provide services similar to those just described, although the mechanisms they use to implement the service are radically different. However, there are many strange differences within these broad categories: each technology imposes its own limit on the size of a packet that can be sent, each has its own unique addressing scheme, some technologies allow fine control of QoS, others do not, and so on. . These differences create difficulties for network interconnection. We cannot receive packets from one network and forward them to another; any kind of subtle transformation will be required. The solution is "convergence". We invent an abstract network service and provide "convergence functions" to implement the abstract service for each network technology. In this way, we make all networks look the same and the interconnection problem becomes manageable (Anderberg, 2002).

## 3. Results

The aim of this study is to develop a web-based geographic information application to publish historical property data using Python, GeoServer, PostGRE SQL Server, and PostGIS. The web application consists of two independent parts, the first is the internet map application and the second is the common database application. Map application was developed on GeoServer. The second part is developed in Python, this application uses PostGRE SQL Server as its database. The map application stores the geographic features of the point or area, and the database application stores text data about a point or terrain feature. With these two data types, all properties of the property can be stored and presented to users. Basic calculations or analyzes such as distance and area measurement can be made with Javascript. The phases of the project can be written as application design, coding, and development.

### 3.1. GeoServer

GeoServer is an open-source software server written in Java that allows users to share and edit geographic data. Designed for interoperability, it publishes data from any large spatial data source using open standards. As a community-driven project, GeoServer has been developed, tested, and supported by various individuals and organizations from around the world (Alptekin & Yakar, 2021). GeoServer is the reference implementation of the Open Geospatial Consortium (OGC) Web Feature Service (WFS) and Web Coverage Service (WCS) standards as well as the compliant Web Map Service (WMS) with high-performance certification. GeoServer forms a core component of the Geospatial Web.

### 3.2. Postgres SQL Server

PostgreSQL is an object-relational database management system (ORDBMS) based on POSTGRES,

Version 4.2, developed at the University of California, Berkeley Department of Computer Science (Erener & Yakar, 2015). POSTGRES pioneered many concepts that only became available in some commercial database systems much later. PostgreSQL is an open-source descendant of this original Berkeley code.

### 3.3. PostGIS

PostGIS is a spatial extension of the PostgreSQL relational database created by Refrations Research Inc as a geodatabase technology research project. Refrations is a GIS and database consulting firm headquartered in Victoria, British Columbia, Canada, specializing in data integration and custom software development. PostGIS is now a project of the OSGeo Foundation and is developed and funded by many FOSS4G developers and organizations around the world who benefit greatly from its functionality and versatility (Tona et al., 2022). The PostGIS project development group plans to support and develop PostGIS to better support a range of key GIS functionality in the data source areas for OGC and SQL/MM spatial standards, advanced topological structures (scopes, surfaces, meshes), and desktop UI tools.

### 3.4. Application Design

Enterprise applications deal with huge amounts of data. With this type and amount of data, performance is the first problem that comes to mind. When performance has to be considered, the architecture of the application becomes more important. The design of the database and the design of the application must be compatible with each other. Both main parts of the application should be designed with the other in mind. When developing such an application, the application must be divided into smaller parts, these parts are called layers. Enterprise applications mostly consist of three layers; The database layer where database operations are performed, the business layer where calculations and data transformations are made, and the interface layer where the user interacts with the system. As seen in Figure 1, the layers are placed in order and data operations should occur in this order. The first user places a command from the website, which is the top layer. The business layer processes the inputs and converts the input to the required object type and calls the function in the data layer and passes the inputs to the data layer function. The data layer function connects the database and sends query sentences to the database engine and the database engine runs the statements on the database and if there are return values passed to the business layer.

The homepage image of the application is shown in Figure 2.

The Frontend codes of the application homepage are shown in Figures 3 and 4.

DLL List Written for Application: In order for the application to work healthily and quickly, the libraries I wrote were created as DLLs. DLL (Dynamic Link Library) are libraries that contain functions and that these functions can be run, which are specially written in the

project to which they are added. The list of DLLs I wrote specifically for the application is given in Figure 5.

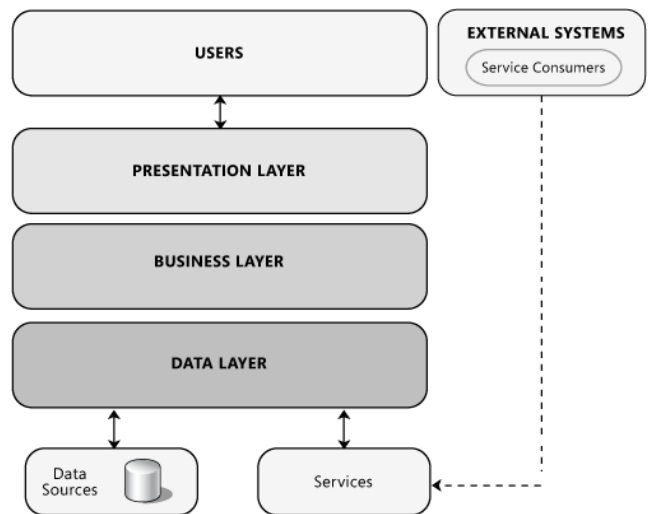


Figure 1. The main layers of the application.

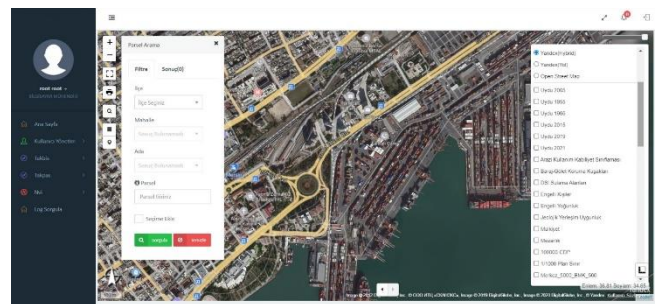


Figure 2. The main page image of the application.

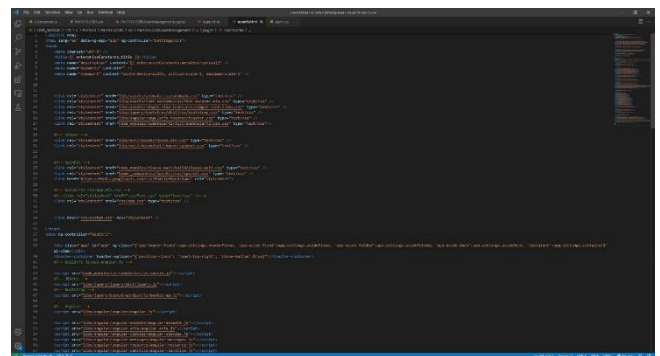


Figure 3. Frontend codes of the application home page.

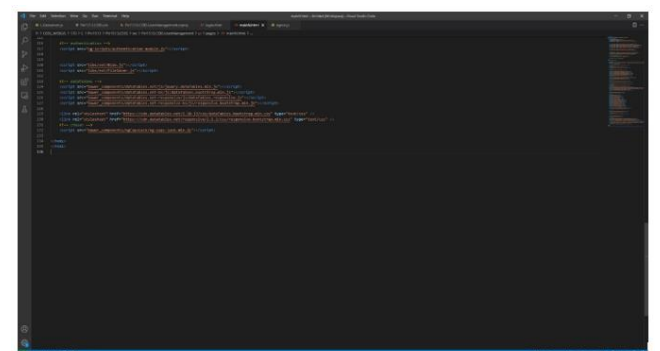


Figure 4. Frontend codes of the application home page.

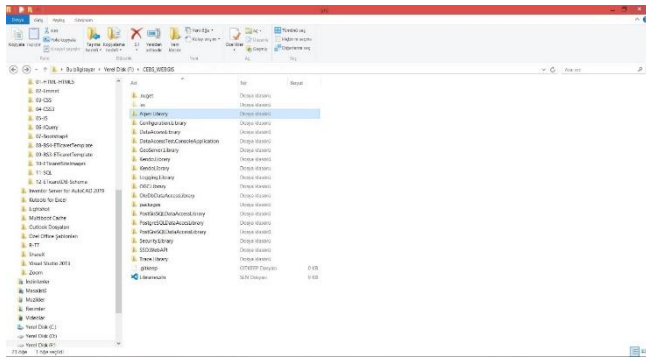


Figure 5. DLL list.

#### 4. Conclusion

The main purpose of the study is to create a web-based geographic information systems application and by realizing this purpose, to create a website that publishes parcels, plans, various maps, and structures within the provincial border of Mersin. This website contains text-based information as well as geographic information. Geographical information is stored in the PostGIS server, published maps are stored in the GeoServer server, and non-graphical information is stored in Postgres SQL. The website is built on Python, Javascript, and HTML 5.0. Python is one of the best solutions for rapid application development. Ready-to-use components, easy debugging, and debugging are the outstanding features of Python. A mapping website was created using all these contemporary technologies, the site is quite large and comprehensive, but has the capabilities of most known GIS web applications. It also has a scalable infrastructure.

Every software project has its problems and challenges, that's the nature of software development. The success of a software project lies in balancing the cost and quality of the software. There were several problems encountered during the development phase of the project. The first problem encountered while configuring the GeoServer is that the GeoServer server is difficult to configure, and some points are easily overlooked. Another difficulty is the processing of spatial and text-based data hosted in the PostGIS server on the map that is associated and presented. Unfortunately, the documentation of these processes is quite inadequate. Another serious issue is performance. Performance and fast loading are very important considerations for websites as it is well known that the average internet user only takes sixteen seconds to load a web page in the browser. A web page must load instantly and must be accurate. The database and ArcGIS server must be installed and run on different computers. Another performance-related issue has to do with client-side components and javascript. When working with image

data the browser has to deal with large image files, XML, and javascript. These large files cause the browser to run slowly and sometimes freeze. Optimization is crucial for this type of application. Application codes should be optimized for the purpose. The sensitivity should also be at optimum, higher sensitivity introduces extra data overhead.

If we bring all the suggestions together, a GIS application should be installed on a three-node cluster system, Active-Active-Passive, and it is absolutely necessary for this cluster system to have redundant internet and power lines. All these data should be backed up by taking full backup instantaneously at the end of the incremental day in backup units, one on-site and the other off-site, hosted in different locations. The level of GIS data detail must be precisely determined. Extra high detailed data will reduce the performance of the application, but low detailed data that cannot meet the needs of people will not work.

#### Acknowledgement

This study forms a part of Mehmet Alper Şahin's thesis and was supported by Mersin University Scientific Research Projects with the project number 2022-1-TP2-4644.

#### References

- Farrel, A. (2004). "The Internet and Its Protocols." Elsevier
- Anderberg, A. (2002). "History of the Internet and Web." <http://www.anderbergfamily.net/ant/history>.
- Şahin, M. A., & Yakar, M. (2021). WebGIS Technology and Architectures. *Advanced GIS*, 1(1), 22–26.
- Yakar, M., Yılmaz, H. M., & Mutluoglu, O. (2014). Performance of photogrammetric and terrestrial laser scanning methods in volume computing of excavation and filling areas. *Arabian Journal for Science and Engineering*, 39, 387-394. <https://doi.org/10.1007/s13369-013-0853-1>
- Alptekin, A. & Yakar, M. (2021). Mapping of local soil conditions in GIS environment: A case study in Çukurkeşlik village. 2<sup>nd</sup> Intercontinental GeoinformationDays (IGD), 64-67, Mersin, Turkey
- Erener, A., & Yakar, M. (2015). Uzaktan Algılama ve CBS Teknolojileri ile Kıyı Sınır Değişim Analizi: Meke Gölü Örneği. *TUFUAB VIII. Teknik Sempozyumu, Konya*, 1, 193-197.
- Tona, A. U., Demir, V., Kuşak, L. & Yakar, M. (2022). Su Kaynakları Mühendisliğinde CBS'nin Kullanımı. *Türkiye Coğrafi Bilgi Sistemleri Dergisi*, 4 (1), 23-33.



# MERSIN UNIVERSITY



ISBN: 978-605-72800-1-5

<https://igd.mersin.edu.tr/>